

**MICROSTRUCTURE AND RHEOLOGY OF CONCENTRATED
SUSPENSIONS OF NEAR HARD-SPHERE COLLOIDS**

by

Dennis P Kalman

A thesis submitted to the Faculty of the University of Delaware in partial fulfillment of the requirements for the degree of Doctor of Philosophy of Degree in Chemical Engineering

Summer 2010

Copyright 2010 Dennis P Kalman
All Rights Reserved

**MICROSTRUCTURE AND RHEOLOGY OF CONCENTRATED
SUSPENSIONS OF NEAR HARD-SPHERE COLLOIDS**

by

Dennis P Kalman

Approved:

Norman J. Wagner, Ph.D.
Chair of the Department of Chemical Engineering

Approved:

Michael J. Chajes, Ph.D.
Dean of the College of Engineering

Approved:

Debra Hess Norris, M.S.
Vice Provost for Graduate and Professional Education

I certify that I have read this dissertation and that in my opinion it meets the academic and professional standard required by the University as a dissertation for the degree of Doctor of Philosophy.

Signed:

Norman J. Wagner, Ph.D.
Professor in charge of dissertation

I certify that I have read this dissertation and that in my opinion it meets the academic and professional standard required by the University as a dissertation for the degree of Doctor of Philosophy.

Signed:

Eric M. Furst, Ph.D.
Member of dissertation committee

I certify that I have read this dissertation and that in my opinion it meets the academic and professional standard required by the University as a dissertation for the degree of Doctor of Philosophy.

Signed:

Michael E. Mackay, Ph.D.
Member of dissertation committee

I certify that I have read this dissertation and that in my opinion it meets the academic and professional standard required by the University as a dissertation for the degree of Doctor of Philosophy.

Signed:

Eric D. Wetzel, Ph.D.
Member of dissertation committee

ACKNOWLEDGEMENTS

Completion of this dissertation would not have been possible without the assistance from numerous people. Professor Norman Wagner deserves high praise for his unending enthusiasm, as well as his creativity and his own hard work contributing to this research. Meetings with Norm always filled me with newly found excitement to pour into my studies. I also benefitted significantly from regular discussions with Eric Wetzel at the Army Research Lab. I owe an enormous debt of gratitude to a number of other graduate students, post-docs, scientists, and undergraduates who either worked with me on some of the projects presented here, taught me about the science, provided useful discussions regarding these and other topics, and helped me in other ways, including Ron Egres, Lakshmi Krishnamurthy, Florian Nettesheim, Matt Liberatore, Matt Helgeson, Jason McMullan, Armin Opitz, Don Kessler, Kate Hollabaugh, Joe Houghton, Manish Kelkar, Ben Schiffman, and others I am sure I am forgetting. Special thanks go to Dick Merrill for performing many of the experiments with ballistic fabrics shown here and Liz Adams for directly assisting in the AFM measurements. The neutron scattering measurements and analysis could never have been done without tireless efforts from many people at NIST, especially Lionel Porcar, Paul Butler, Jeff Krzywon, and Cedric Gagnon. I also would like to thank my parents, Herb and Jill, for all of their love and support over the years and for the values they instilled in me.

Graduate school is an arduous experience which is alternately challenging and fun, and is often frustrating. Through this experience, I developed great personal relationships which I know I will always cherish. In particular, graduate school is

worth all the pain and trouble alone purely for the benefit of bringing me together with my love, Rebecca Brummitt.

TABLE OF CONTENTS

LIST OF TABLES.....	iv
LIST OF FIGURES	v
ABSTRACT	xv
Chapter	
1	INTRODUCTION 1
	1.1 Motivation 1
	1.2 Background..... 3
	1.3 Thesis Objectives and Overview 7
2	EXPERIMENTAL TECHNIQUES..... 12
	2.1 Introduction 12
	2.2 Particle Characterization..... 12
	2.2.1 Particle Size 12
	2.2.2 Density Measurements..... 13
	2.2.3 Atomic Force Microscopy Nano-indentation of Particles 14
	2.3 Suspension Preparation 17
	2.3.1 Preparation of Suspensions from Dry Particles 17
	2.3.2 Synthesis of Spherical, Monodisperse PMMA Particles 18
	2.3.3 Coating of Silica Particles with Octadecyl Chains 18
	2.4 Rheometry 20
	2.4.1 Steady-State Rheological Measurements 20
	2.4.2 Stress Jump Measurements..... 21
	2.4.3 Normal Stress Measurements 22
	2.4.4 Determination of Rheological Slip 24
	2.4.5 Small Amplitude Oscillatory Shear Measurements..... 26
	2.4.6 Critical Stress Determination 27
	2.5 Neutron Scattering Techniques 27
	2.5.1 Flow-Ultra Small Angle Neutron Scattering (Flow-USANS)..... 27
	2.5.2 Flow- and Rheo- Small Angle Neutron Scattering (Flow-SANS/Rheo-SANS) 29
	2.5.3 Small Angle Neutron Scattering Theory and Analysis..... 32
	2.6 Application Testing of Shear Thickening Fluid/Fabric Composites 45
	2.6.1 Yarn Pull-Out 45
	2.6.2 Single-Layer Quasi-static Spike Puncture 49
	2.6.3 Single-Layer Ballistic V_{50} Testing..... 52
3	RHEOLOGY OF SPHERICAL, NEAR HARD-SPHERE, COLLOIDAL SILICA PARTICLE SUSPENSIONS 54
	3.1 Introduction 54

3.2	Background.....	55
3.3	Suspension Preparation and Characterization	59
3.4	Experimental.....	61
3.4.1	Particle Size and Particle Interactions	61
3.4.2	Rheology.....	61
3.5	Results and Discussion	63
3.5.1	Particle Size and Interactions	63
3.5.2	Dilute Suspension Rheology	72
3.5.3	Steady Shear Viscosity	74
3.5.4	The Effects of Suspending Medium Viscosity	100
3.5.5	Critical Stress for Onset of Shear Thickening	106
3.5.6	Normal Stress Measurements	110
3.5.7	Step Rate/Stress Measurements.....	115
3.5.8	Dynamic Rheology Measurements	119
3.5	Conclusions	122
4	RHEO-SANS EXPERIMENTS ON NEAR HARD-SPHERE COLLOIDAL SUSPENSIONS	124
4.1	Introduction	124
4.2	Experimental.....	126
4.3	Results	131
4.3.1	Flow-SANS in the Shear Plane (Flow-Gradient or 1-2 Plane)..	134
4.3.1.1	Microstructure Measurements of Strongly Shear- Thickening ($\phi \sim 0.5$) Suspensions	134
4.3.1.2	Microstructure Measurements of Moderately Shear- Thickening ($\phi \sim 0.4$) Suspensions	148
4.3.1.3	Microstructure Measurements of Low Concentration ($\phi \sim 0.2$), Shear-Thinning Suspension	153
4.3.1.4	Microstructure Measurements of Non-Thickening, High Concentration ($\phi_{\text{core}} \sim 0.5$), Polymer Coated Sticky Hard-Sphere Particle Suspension.....	158
4.3.2	Radial (1-3 Plane) Rheo-SANS Microstructure Measurements	165
4.3.2.1	Microstructure Measurements of Strongly Shear- Thickening ($\phi \sim 0.5$) Suspensions	165
4.3.2.2	Microstructure Measurements of Moderately Shear- Thickening ($\phi \sim 0.45$) Suspensions	179
4.3.3	Micromechanics Calculations via the Stress-SANS Law.....	188
4.4	Discussion.....	225
4.5	Confirmation of Scattering and Flow Field in 1-2 Plane Shear Cell	237
4.6	Conclusions	243

5	FLOW-USANS EXPERIMENTS ON NEAR HARD-SPHERE SILICA DISPERSIONS	245
	5.1 Introduction	245
	5.2 Experimental.....	246
	5.2.1 Flow-USANS Experiment.....	246
	5.2.2 Suspension Properties.....	247
	5.3 Flow-USANS Data.....	250
	5.4 Discussion.....	255
	5.4.1 Analysis of Flow-USANS Results	255
	5.4.2 Experimental Limitations	262
	5.4.2.1 Anisotropy Limitations from 1-d Detection	262
	5.4.2.2 Multiple Scattering Effects	262
	5.5 Conclusions	263
6	EFFECTS OF PARTICLE SOFTNESS ON CONCENTRATED SUSPENSIONS RHEOLOGY	265
	6.1 Introduction	265
	6.2 Experimental.....	268
	6.3 Results	269
	6.3.1 PMMA Particle Characterization	269
	6.3.2 Rheology.....	270
	6.3.3 Particle Modulus.....	272
	6.4 Elastohydrodynamic Model.....	277
	6.4.1 Model Development	277
	6.4.2 Elastohydrodynamic Model Predictions and Comparison to Data.....	280
	6.4.3 Discussion.....	291
	6.5 Conclusions	296
7	THE EFFECT OF PARTICLE HARDNESS ON SHEAR THICKENING FLUID COMPOSITES WITH PROTECTIVE FABRICS	299
	7.1 Introduction	299
	7.2 Experimental.....	301
	7.3 Results	307
	7.3.1 Yarn Pull-Out Testing	307
	7.3.2 Spike Puncture Testing.....	313
	7.3.3 Ballistic V_{50} Testing	317
	7.4 Discussion.....	320
	7.5 Conclusions	329
8	CONCLUSIONS	331
Appendix		
A	NOMENCLATURE	338
B	ANALYSIS OF RHEOLOGICAL SLIP	343

C	EVALUATION OF STRUCTURE HOMOGENEITY ACROSS THE GAP VIA 1-2 PLANE FLOW-SANS	349
D	ADDITIONAL PICTURES AND MICROGRAPHS OF FABRIC COMPOSITES	351
	BIBLIOGRAPHY.....	357

LIST OF TABLES

Table 3.1	TGA results.	61
Table 3.2	Summary of particle property measurements.	65
Table 3.3	Solvent properties.	65
Table 3.4	Parameters from USANS fitting of 260 nm silica dispersions.	68
Table 3.5	Dilute viscosity measurements and fit to Einstein equation.	74
Table 3.6	Fitting parameters and results from Cross model fits to rheology of 60 nm silica spheres in PEG-200.	82
Table 3.7	Fitting parameters and results from Cross model fits to rheology of 130 nm and 260 nm silica spheres in PEG-200.	86
Table 3.8	Fitting parameters and results from Cross model fits to rheology of 60 nm silica spheres in solvent mixture of PEG-600 and ethylene glycol.	105
Table 4.1	Details of samples tested in SANS experiments.	128
Table 4.2	Transmission values from $\phi \sim 0.5$ samples in 1-2 plane flow SANS. ...	147
Table 4.3	Transmission data from $\phi = 0.40$ sample in 1-2 plane flow SANS.	151
Table 4.4	Transmission measurements from $\phi = 0.20$ sample in 1-2 plane flow SANS.	157
Table 4.5	Transmission values for low concentration samples in 1-2 plane flow-SANS.	164
Table 4.6	Transmission values for strongly thickening samples in radial Rheo-SANS.	178
Table 4.7	Transmission values for mildly thickening samples in radial Rheo- SANS.	187
Table 4.8	Parameters used to correlate viscosity from SANS using spherical harmonic decomposition to the measured rheology.	198
Table 5.1	System properties and data.	248
Table 5.2	Suspension properties.	248
Table 5.3	Transmission measurements from USANS experiments.	263
Table 6.1	Particle shear modulus data.	277
Table 6.2	Summary of particle types, moduli, and solvent viscosities used in elastohydrodynamic model comparisons to data.	290
Table 7.1	Tabulated rheological parameters for suspensions used.	302
Table 7.2	Data table of fabric treatment add-on and test results.	306

LIST OF FIGURES

Figure 2.1	Representative force versus displacement data from atomic force microscope (AFM) nano-indentation experiments.....	16
Figure 2.2	Normal stress measurements for 60 nm silica in PEG-200	23
Figure 2.3	Creep measurement after a peak hold at 300 Pa and before a peak hold at 200 Pa on 60 nm silica in PEG used to determine zero normal force value.....	24
Figure 2.4	Diagram of rheological slip behavior in parallel plate rheometry.	26
Figure 2.5	Schematic of Flow-USANS experiment.....	29
Figure 2.6	Various planes of shear available for scattering measurements	31
Figure 2.7	SANS data analysis averages.....	34
Figure 2.8	Projections of the pair distribution function, showing the sign on the contribution to the Brownian or thermodynamic component to the normal stress difference from particle concentrations in that region.....	35
Figure 2.9	Geometry for 1-2 plane flow-SANS analysis.....	37
Figure 2.10	Yarn pull-out (YPO) testing apparatus.....	47
Figure 2.11	Typical yarn pull-out results.....	48
Figure 2.12	Spike puncture testing apparatus.....	49
Figure 2.13	Typical spike puncture results.....	51
Figure 2.14	Ballistic V_{50} testing frame and witness configuration.....	52
Figure 3.1	SEM micrographs of three sizes of silica particles.....	60
Figure 3.2	Static USANS form factor measurement of suspension of 260 nm SiO_2 in PEG with Schultz sphere model fit.....	67
Figure 3.3	Static USANS measurements of suspensions of 260 nm SiO_2 in PEG with core-shell model fits.....	67
Figure 3.4	Static SANS form factor measurement of suspension of 60 nm SiO_2 in D_2O with Schultz sphere model fit.....	69
Figure 3.5	Static SANS measurements of suspensions of 60 nm SiO_2 in PEG-200	70
Figure 3.6	Depiction of a particle with surface coating.....	72
Figure 3.7	Newtonian viscosity measurements of various suspensions.....	74
Figure 3.8	Steady-shear rheology of 60 nm silica dispersions in PEG-200.....	76
Figure 3.9	Steady-shear rheology of 130 nm silica dispersions in PEG-200.....	78
Figure 3.10	Steady-shear rheology of 260 nm silica dispersions in PEG-200.....	79
Figure 3.11	Steady shear data and fits to Cross model for 60 nm particle suspensions.....	80
Figure 3.12	Reduction of data using Cross model for 60 nm particle suspensions.....	81
Figure 3.13	Steady shear data and fits to Cross model for 130 nm particle suspensions.....	84

Figure 3.14	Reduction of data using Cross model for 130 nm particle suspensions.	84
Figure 3.15	Steady shear data and fits to Cross model for 260 nm particle suspensions.	85
Figure 3.16	Reduction of data onto Cross model for 260 nm particle suspensions.	85
Figure 3.17	Summary of zero and infinite shear viscosities from Cross model fitting compared based on calculated volume fraction	87
Figure 3.18	Summary of zero and infinite shear viscosities from Cross model fitting compared based on volume fraction with an additional excluded volume shell scaled for the particle radius	89
Figure 3.19	Summary of zero and infinite shear viscosities from Cross model fitting compared based on an alternate effective volume fraction with the assumption of an excluded volume shell of constant thickness for all three particle sizes	90
Figure 3.20	Values of the Baxter sticky parameter, τ_b , determined from fitting to the zero shear rheology	91
Figure 3.21	Deviation in effective volume fraction calculated from zero or infinite shear viscosity, relative to volume fraction.....	93
Figure 3.22	Cross model exponent m and critical stress τ_{Cross} plotted against the effective volume fraction using the 5.6% layer thickness excluded volume shell.....	93
Figure 3.23	Values of the yield stress (dimensionless) plotted against the effective volume fraction using the 5.6% layer thickness excluded volume shell.....	95
Figure 3.24	Steady-shear rheology data for suspensions of three sizes of spherical silica particles on a common shear rate axis.	96
Figure 3.25	Steady-shear rheology data for suspensions of three sizes of spherical silica particles on a common shear stress axis.	98
Figure 3.26	Steady-shear rheology data for suspensions of three sizes of spherical silica particles on a common axis of Péclet number.	99
Figure 3.27	Steady-shear rheology data for selected volume fractions of suspensions of three sizes as a function of Péclet number.	100
Figure 3.28	Steady-shear rheology of 60 nm silica spheres dispersed in a 70/30 mixture by volume of PEG-600 and ethylene glycol.....	101
Figure 3.29	Comparison of the steady shear rheology of dispersions of 60 nm silica spheres in PEG-200 and a mixture of PEG-600 and ethylene glycol.	102
Figure 3.30	Steady shear data and fits to Cross model for 60 nm particle suspensions in solvent mixture of PEG-600 and ethylene glycol.....	104
Figure 3.31	Reduction of data onto Cross model for 60 nm particle suspensions in solvent mixture of PEG-600 and ethylene glycol.....	104

Figure 3.32	Comparison of the steady shear rheology of dispersions of 60 nm silica spheres in a mixture of PEG-600 and ethylene glycol to those in a mixture of PEG-600 and deuterated ethylene glycol	106
Figure 3.33	Values of the critical stress for shear thickening for various silica suspensions as a function of volume fraction.	107
Figure 3.34	Log of the dimensionless critical stress versus volume fraction for various suspensions, used in fitting	109
Figure 3.35	Correlation of the critical stress with volume fraction with a radius squared dependence for various suspensions, used in fitting.	110
Figure 3.36	First normal stress difference rheological measurements for 60 nm silica dispersion at $\phi=0.515$ in solvent mixture of PEG-600 and ethylene glycol (70% ethylene glycol by weight)	112
Figure 3.37	First normal stress difference rheological measurements for 130 nm silica dispersion at $\phi=0.517$ in PEG-200	114
Figure 3.38	Stress jump measurements on the $\phi=0.500$ suspension of 60 nm SiO ₂ in PEG-600 and ethylene glycol solvent mixture	116
Figure 3.39	Stress jump measurements on a log-time axis, from the $\phi=0.500$ suspension of 60 nm SiO ₂ in PEG-600 and ethylene glycol solvent mixture	118
Figure 3.40	Stress jump measurements on the $\phi=0.391$ suspension of 260 nm SiO ₂ in PEG-200	119
Figure 3.41	Small amplitude oscillatory shear data for suspensions of 60 nm silica in PEG-200	121
Figure 3.42	Small amplitude oscillatory shear data for suspensions of 130 nm silica in PEG-200	121
Figure 3.43	Plateau elastic modulus, loss modulus minimum, and frequency at the loss modulus minimum	122
Figure 4.1	Steady-state rheology of partly-deuterated samples used in SANS experiments, compared to non-deuterated samples	127
Figure 4.2	Steady shear rheological behavior for $\phi=0.515$ sample in partly deuterated solvent mixture used in following SANS experiments	134
Figure 4.3	Small angle neutron scattering spectra from experiments on $\phi=0.515$ silica in partly deuterated solvent mixture sample in 1-2 plane flow-SANS	136
Figure 4.4	Evolution of microstructure in 1-2 Plane Flow-SANS for $\phi=0.515$ sample	137
Figure 4.5	1-2 plane flow-SANS measurements exhibit varied scattering from changing the rotation direction.	138
Figure 4.6	Annular averaged SANS spectra from 1-2 plane flow-SANS on $\phi=0.515$ sample	140
Figure 4.7	Circular averaged 1-2 plane flow-SANS data on $\phi=0.515$ sample	140

Figure 4.8	Steady shear rheological behavior for $\phi=0.522$ sample in partly deuterated solvent mixture tested in following SANS experiments...	141
Figure 4.9	SANS scattering spectra from $\phi=0.522$ sample in 1-2 plane flow-SANS with additional high shear rate data.....	143
Figure 4.10	SANS subtraction pattern – shear thickened state minus pre-thickened state (100 s^{-1}) from $\phi=0.522$ sample in 1-2 plane flow-SANS.....	144
Figure 4.11	Annular averaged SANS spectra from 1-2 plane flow-SANS on $\phi=0.522$ sample.....	145
Figure 4.12	Circular averaged SANS data from $\phi=0.522$ sample in 1-2 plane flow SANS at various shear rates.....	146
Figure 4.13	Steady shear rheological behavior for $\phi=0.40$ sample in partly deuterated solvent mixture tested in following SANS experiments...	148
Figure 4.14	Small angle neutron scattering spectra from experiments on $\phi=0.40$ silica in partly deuterated solvent mixture sample in 1-2 plane flow-SANS.	149
Figure 4.15	Annular averaged SANS spectra from 1-2 plane flow-SANS on $\phi=0.40$ sample.....	150
Figure 4.16	Circular averaged SANS data from $\phi=0.40$ sample in 1-2 plane flow SANS at various shear rates.....	152
Figure 4.17	Steady shear rheological behavior for $\phi=0.20$ sample in partly deuterated solvent mixture tested in following SANS experiments...	153
Figure 4.18	Small angle neutron scattering spectra from experiments on $\phi=0.20$ silica in partly deuterated solvent mixture sample in 1-2 plane flow-SANS.	154
Figure 4.19	Annular averaged SANS spectra from 1-2 plane flow-SANS on $\phi=0.20$ sample.....	156
Figure 4.20	Circular averaged SANS data from $\phi=0.20$ sample in 1-2 plane flow SANS at various shear rates. The line is included on the highest rate data to guide the eye.....	156
Figure 4.21	Steady-shear rheology comparison of octadecyl-coated 60 nm silica in mineral solvent mix to standard 60 nm silica in PEG-600 and ethylene glycol solvent mix	158
Figure 4.22	Rheology comparison of reduced viscosity versus Péclet number for coated, thickening-suppressed suspensions compared to uncoated suspension	160
Figure 4.23	Small angle neutron scattering spectra from experiments on octadecyl-coated silica in partly deuterated solvent mixture sample in 1-2 plane flow-SANS	161
Figure 4.24	Annular averaged SANS spectra from 1-2 plane flow-SANS on octadecyl-coated silica sample	162

Figure 4.25	Circular averaged SANS data from octadecyl-coated silica sample in 1-2 plane flow SANS at various shear rates	163
Figure 4.26	Steady shear rheological behavior for $\phi=0.531$ sample tested in following SANS experiments	166
Figure 4.27	Small angle neutron scattering spectra from experiments on $\phi=0.531$ sample in radial Rheo-SANS	167
Figure 4.28	Diagram of angular averaging on radial SANS data and definition of θ_{rad}	168
Figure 4.29	Annular averaged SANS spectra from radial Rheo-SANS on $\phi=0.531$ sample	169
Figure 4.30	Circular averaged SANS data from $\phi=0.531$ sample in radial Rheo-SANS at various shear stresses	170
Figure 4.31	Steady shear rheological behavior for $\phi=0.53$ sample tested in following SANS experiments	171
Figure 4.32	Small angle neutron scattering spectra from experiments on $\phi=0.53$ sample in radial Rheo-SANS	172
Figure 4.33	Small angle neutron scattering spectra from experiments on $\phi=0.53$ sample in radial Rheo-SANS	173
Figure 4.34	SANS subtraction pattern – shear thickened state minus pre-thickened state (100 Pa) from $\phi=0.53$ sample in radial Rheo-SANS .	174
Figure 4.35	Circular averaged SANS data from $\phi=0.53$ sample in radial Rheo-SANS at various shear rates	175
Figure 4.36	Circular averaged SANS data from $\phi=0.53$ sample in radial Rheo-SANS at various shear rates	175
Figure 4.37	Annular averaged SANS spectra from radial Rheo-SANS on $\phi=0.53$ sample	177
Figure 4.38	Annular averaged SANS spectra from radial Rheo-SANS on $\phi=0.53$ sample	177
Figure 4.39	Steady shear rheological behavior for $\phi=0.436$ sample tested in following SANS experiments	179
Figure 4.40	Small angle neutron scattering spectra from initial experiments on $\phi=0.436$ sample in radial Rheo-SANS	181
Figure 4.41	Annular averaged SANS spectra from radial Rheo-SANS on $\phi=0.436$ sample	182
Figure 4.42	Circular averaged SANS data from $\phi=0.436$ sample in radial Rheo-SANS at various shear rates	182
Figure 4.43	Steady shear rheological behavior for $\phi=0.44$ sample tested in following SANS experiments	183
Figure 4.44	Small angle neutron scattering spectra from initial experiments on $\phi=0.44$ sample in radial Rheo-SANS	185

Figure 4.45	Annular averaged SANS spectra from radial Rheo-SANS on $\phi=0.44$ sample.....	186
Figure 4.46	Circular averaged SANS data from $\phi=0.44$ sample in radial Rheo-SANS at various shear rates	186
Figure 4.47	Circular averaged static SANS data in shear cells for hard-sphere suspensions	190
Figure 4.48	Circular averaged static SANS data in 1-2 plane shear cell for coated sticky hard-sphere suspension compared to hard-sphere suspension.....	191
Figure 4.49	Harmonic weighted difference spectra ($I_{\text{shear}}-I_{\text{static}}$) data from $\phi=0.522$, 1-2 plane flow-SANS.	193
Figure 4.50	Harmonic weighted SANS data normalized by static data ($I_{\text{shear}}/I_{\text{static}}$), or W terms, from $\phi=0.522$, 1-2 plane flow-SANS.....	194
Figure 4.51	Structurally weighted harmonics calculated from $\phi=0.522$, 1-2 plane flow-SANS.....	195
Figure 4.52	Harmonic integrals calculated from micromechanics analysis of SANS data in 1-2 plane measurements of $\phi=0.522$ hard-sphere silica.....	197
Figure 4.53	Comparison of thermodynamic and hydrodynamic components of the viscosity from SANS microstructure measurements to viscosity from rheometry for 1-2 plane measurements of $\phi=0.522$ hard-sphere silica.	198
Figure 4.54	Comparison of thermodynamic and hydrodynamic components of the first normal stress difference, N_1 , from SANS microstructure measurements to N_1 from rheometry for 1-2 plane measurements of $\phi=0.522$ hard-sphere silica.....	199
Figure 4.55	Harmonic weighted, circular averaged difference spectra ($I_{\text{shear}}-I_{\text{static}}$) from $\phi=0.40$ sample in 1-2 plane flow-SANS.....	202
Figure 4.56	Harmonic weighted SANS data normalized by static data ($I_{\text{shear}}/I_{\text{static}}$), or W terms, from $\phi=0.40$, 1-2 plane flow-SANS.....	203
Figure 4.57	Structurally weighted harmonics calculated from $\phi=0.40$, 1-2 plane flow-SANS	204
Figure 4.58	Harmonic integrals calculated from micromechanics analysis of SANS data in 1-2 plane measurements of $\phi=0.40$ hard-sphere silica.....	205
Figure 4.59	Comparison of thermodynamic and hydrodynamic components of the viscosity from SANS microstructure measurements to viscosity from rheometry for 1-2 plane measurements of $\phi=0.40$ hard-sphere silica.....	206
Figure 4.60	Harmonic weighted, circular averaged difference spectra ($I_{\text{shear}}-I_{\text{static}}$) from $\phi=0.20$ sample in 1-2 plane flow-SANS.....	207

Figure 4.61	Harmonic weighted SANS data normalized by static data ($I_{\text{shear}}/I_{\text{static}}$), or W terms, from $\phi=0.20$, 1-2 plane flow-SANS.....	208
Figure 4.62	Structurally weighted harmonics calculated from $\phi=0.20$, 1-2 plane flow-SANS	209
Figure 4.63	Harmonic integrals calculated from micromechanics analysis of SANS data in 1-2 plane measurements of $\phi=0.20$ hard-sphere silica.	210
Figure 4.64	Comparison of thermodynamic and hydrodynamic components of the viscosity from SANS microstructure measurements to viscosity from rheometry for 1-2 plane measurements of $\phi=0.20$ hard-sphere silica.....	211
Figure 4.65	Harmonic weighted, circular averaged difference spectra ($I_{\text{shear}}-I_{\text{static}}$) from $\phi\sim 0.5$ coated sticky hard-sphere sample in 1-2 plane flow-SANS.	212
Figure 4.66	Harmonic weighted SANS data normalized by static data ($I_{\text{shear}}/I_{\text{static}}$), or W terms, from $\phi\sim 0.5$ coated sticky hard-sphere sample in 1-2 plane flow-SANS.....	213
Figure 4.67	Structurally weighted harmonics calculated from $\phi\sim 0.5$ coated sticky hard-sphere sample in 1-2 plane flow-SANS.....	214
Figure 4.68	Harmonic integrals calculated from micromechanics analysis of SANS data in 1-2 plane measurements of $\phi\sim 0.5$ coated sticky hard-sphere sample	215
Figure 4.69	Comparison of thermodynamic and hydrodynamic components of the viscosity from SANS microstructure measurements to viscosity from rheometry for 1-2 plane measurements of $\phi\sim 0.5$ coated sticky hard-sphere sample	216
Figure 4.70	Harmonic weighted, circular averaged difference spectra ($I_{\text{shear}}-I_{\text{static}}$) from $\phi=0.53$ sample in radial Rheo-SANS.	217
Figure 4.71	Harmonic weighted SANS data ($I_{\text{shear}}/I_{\text{static}}$), from $\phi\sim 0.53$ sample in radial Rheo-SANS.....	218
Figure 4.72	Harmonic integrals calculated from micromechanics analysis of SANS data in radial Rheo-SANS measurements of $\phi=0.53$ hard-sphere silica	219
Figure 4.73	Comparison of hydrodynamic component of the viscosity from SANS microstructure measurements to viscosity from rheometry for radial Rheo-SANS measurements of $\phi=0.53$ hard-sphere silica... ..	220
Figure 4.74	Harmonic weighted, circular averaged difference spectra ($I_{\text{shear}}-I_{\text{static}}$) from $\phi=0.44$ sample in radial Rheo-SANS.	221
Figure 4.75	Harmonic weighted SANS data ($I_{\text{shear}}/I_{\text{static}}$), from $\phi\sim 0.44$ sample in radial Rheo-SANS	222

Figure 4.76	Harmonic integrals calculated from micromechanics analysis of SANS data in radial Rheo-SANS measurements of $\phi=0.44$ hard-sphere silica	223
Figure 4.77	Comparison of hydrodynamic component of the viscosity from SANS microstructure measurements to viscosity from rheometry for radial Rheo-SANS measurements of $\phi=0.44$ hard-sphere silica... ..	224
Figure 4.78	SANS spectra from 1-2 plane Flow-SANS experiment, compared to expectation radial distribution function data from Stokesian dynamics simulations ($\phi\sim 0.45$) of Foss and Brady [24]	226
Figure 4.79	Comparisons of angular dependent SANS data to literature radial distribution at contact data.....	229
Figure 4.80	Snapshots of particle configuration from Stokesian Dynamics simulations of Melrose and Ball [99] at $Pe=3000$	231
Figure 4.81	Comparison of circular averaged 1-2 plane data between static and high shear for three concentrations of near hard-sphere suspensions and a high concentration sticky hard-sphere suspensions.	232
Figure 4.82	SANS spectra from radial Rheo-SANS experiment, compared to expectation radial distribution function data from Stokesian dynamics simulations ($\phi\sim 0.45$) of Foss and Brady [24]	234
Figure 4.83	Comparison of unweighted harmonic, W_0 , between radial and 1-2 plane SANS experiments on comparable high concentration suspensions.	236
Figure 4.84	Comparison of SANS data from various path length static cells compared to 1-2 plane shear cell.	239
Figure 4.85	Velocity contour plot of cross-section of gap in shear cell.....	240
Figure 4.86	Velocity profile across the gap of the cell for a Newtonian fluid at a shear rate of 0.01 s^{-1}	241
Figure 4.87	Velocity profile along the shear cell height for the Newtonian fluid at a shear rate of approximately 0.01 s^{-1}	242
Figure 5.1	SEM micrograph of silica particles.	249
Figure 5.2	Steady-shear viscosity of a suspension of silica in PEG.	250
Figure 5.3	Flow-USANS measurements suspensions of SiO_2 in PEG.....	252
Figure 5.4	Particle form factor and measured effective smeared structure factors under static conditions	253
Figure 5.5	Effective steady-shear structure factors measured via USANS and static structure factor with equilibrium structure factor subtracted to show growth of cluster peaks.	254
Figure 5.6	Rectangular and circular averaged scattered intensity as a function of wave vector from the $\phi=0.44$ sample of 60 nm suspensions tested in radial Rheo-SANS.....	259

Figure 6.1	Viscosity versus shear rate data for concentrated suspensions of 1.25 μm diameter PVC spherical particles in di-octyl phthalate (DOP) from Hoffman [37].	267
Figure 6.2	SEM micrograph of PMMA particles.	269
Figure 6.3	Steady shear rheological data for suspensions of 1.05 μm diameter PMMA spheres in PEG-200	270
Figure 6.4	Comparison of steady shear rheology for PMMA particles in PEG-200 between cone and plate geometry and roughened parallel plates.	272
Figure 6.5	Raw force versus tip displacement AFM data for PMMA and SiO_2 spheres	273
Figure 6.6	AFM deflection force versus indentation distance data used to calculate particle modulus	274
Figure 6.7	Proposed elastohydrodynamic deformation between two particles within a hydrocluster in a concentrated suspension.	278
Figure 6.8	Elastohydrodynamic model compared to rheology data of 1.05 μm diameter PMMA spherical particle suspensions	281
Figure 6.9	Elastohydrodynamic model prefactor fit to PMMA-PEG suspension data at various volume fractions.	283
Figure 6.10	Elastohydrodynamic model compared to rheology data of 520 nm diameter silica spheres in PEG-200	284
Figure 6.11	Elastohydrodynamic model compared to rheology data of SiO_2 sphere suspension rheology data	285
Figure 6.12	Elastohydrodynamic model compared to rheology data of 1.25 μm PVC particles in di-octyl phthalate (DOP)	286
Figure 6.13	Elastohydrodynamic model compared to rheology data of poly(styrene/ethyl acrylate) spheres in water.	287
Figure 6.14	Elastohydrodynamic model compared rheology data of plate-like kaolin clay particle suspensions in water.	288
Figure 6.15	Elastohydrodynamic model compared rheology data of rod-like precipitated calcium carbonate (CaCO_3)	289
Figure 6.16	Elastohydrodynamic model compared rheology data of fumed silica suspensions in PPG	291
Figure 6.17	Steady shear rheology of concentrated suspensions of agar microgel particles of varying particle hardness	294
Figure 6.18	Steady shear rheology of Pickering emulsions	296
Figure 7.1	Steady shear rheology of shear-thickening suspensions and SEM micrographs of commercial SiO_2 particles and lab produced PMMA particles	302
Figure 7.2	All curves of force versus crosshead displacement for yarn pull-out testing.	309

Figure 7.3	Typical force versus crosshead displacement curves from yarn pull-out testing for various fabric treatments.	310
Figure 7.4	Yarn pull-out testing data for various fabric treatments.....	311
Figure 7.5	SEM micrographs of fabric from pull-out testing	312
Figure 7.6	SEM micrographs of fabric from pull-out testing	313
Figure 7.7	Force versus crosshead displacement for all curves in spike puncture testing.....	315
Figure 7.8	Typical force versus crosshead displacement curves for quasistatic spike puncture testing for various fabric treatments.....	316
Figure 7.9	Spike puncture testing data for various fabric treatments.	316
Figure 7.10	Optical micrographs of fabric from spike puncture testing.	317
Figure 7.11	Ballistic V_{50} testing data for various fabric treatments.....	319
Figure 7.12	Front faces of fabric after ballistic testing.	320
Figure 7.13	Diagram of shear stress calculations from pull-out experiment.	327
Figure B.1	Apparent viscosity measurements of a certified viscosity standard, Cannon S8000, used to validate slip measurements.....	344
Figure B.2	Apparent shear rate versus reciprocal gap height for S8000 viscosity standard at a constant value of $\tau_R=10$ Pa yield the slip velocity and true shear rate.	345
Figure B.3	Apparent viscosity versus applied stress for 60 nm silica dispersions at $\phi=0.521$ in solvent mixture of PEG-600 and ethylene glycol	346
Figure B.4	Apparent shear rate at various values of the rim shear stress, plotted against reciprocal gap height for 60 nm silica dispersions at $\phi=0.521$ in solvent mixture of PEG-600 and ethylene glycol.....	347
Figure B.5	True shear rate and slip velocity for 60 nm silica suspension in PEG-200 at various rim shear stresses.	348
Figure B.6	Slip lengths as a function of rim shear stress.....	348
Figure C.1	Steady-shear rheology of $\phi=0.5$ SiO_2 sample tested in gap-resolved 1-2 plane flow-SANS experiments.....	349
Figure C.2	Gap-resolved 1-2 plane Flow-SANS of concentrated suspensions at $\phi\sim 0.50$	350
Figure D.1	Additional fabric photos from ballistic testing.....	351
Figure D.2	Additional fabric photos from ballistic testing.....	352
Figure D.3	Additional fabric photos from ballistic testing.....	353
Figure D.4	Additional fabric scanning electron micrographs from spike testing.	354
Figure D.5	Additional fabric scanning electron micrographs from yarn pull out testing.	355
Figure D.6	Additional fabric scanning electron micrographs from spike testing.	356

ABSTRACT

The relationship between colloidal suspension microstructure and rheology is investigated to provide a solid understanding of the nonlinear rheology of concentrated suspensions, with a focus on shear thickening. These suspensions are also studied as a treatment to woven fabric in body-armor applications, where the insight from microstructural measurements is used to attempt to improve the application.

The colloid and suspension properties are characterized via SEM, DLS, SANS, USANS, and rheometry. The rheology is mapped onto an effective hard-sphere model with the addition of a yield stress. An additional excluded volume shell, as measured by SANS and USANS structural measurements, accounts for interparticle interactions due to surface forces arising from the stabilizing layer on the particles.

The microstructure of these near hard-sphere concentrated, shear-thickening colloidal dispersions are measured via SANS and USANS as a function of volume fraction, shear rate, and particle size. Special Rheo-SANS, flow-SANS, and flow-USANS instruments are developed and validated to measure microstructure in flowing systems. Structures measured via USANS show a cluster peak that arises from hydrocluster formation in concentrated, shear thickening suspensions. Structure measurements in SANS via 1-d averaged analysis and analysis of the 2-d structure corresponds to that expected from Stokesian Dynamics simulations. Micromechanics theory via a Stress-SANS law is used to calculate rheology from the microstructure for comparison. As the rheology calculated from the SANS data qualitatively agrees with that of the suspension and the structures seen correspond to those expected from simulations, strong confirmation of the hydrocluster mechanism for shear thickening is observed.

This improved knowledge of the hydrocluster structure is used to develop an elastohydrodynamic theory for the limiting viscosity at high shear stresses due to particle deformations in the hydrocluster. Measurements of particle modulus give consistent application of this elastohydrodynamic model to suspensions studied in this thesis. In addition, the model is applied to widely varying suspensions, including those of hard mineral particles, polymer particles, microgels, and emulsions and consistent results are seen. The results of these fundamental studies of how particle size, concentration, and hardness affect suspension microstructure and rheology are used to engineer shear thickening fluid treated textiles, suitable for various types of protective devices.

Chapter 1

INTRODUCTION

1.1 Motivation

Concentrated particle suspensions are encountered in many situations including industrial processes, such as paper coating, mechanical polishing, and mining, products such as food and consumer products, and natural processes such as the flow of blood [1]. More recently, concentrated silica suspensions have been used with ballistic fabrics to improve the protective properties of the composite [2-5]. The dispersions seen in these different processes can show widely varying, nonlinear rheological behavior such as shear thinning, shear thickening, yielding, thixotropy, and shear-induced aggregation [1, 6, 7].

The nonlinear rheology of colloidal dispersions is a direct response of flow-induced microstructural rearrangements. One of the most significant changes evident in stable, colloidal dispersion is shear thickening [1], which is ubiquitous and marked by a shear viscosity that increases with increasing applied shear rate or shear stress. Shear thickening complicates and limits processes with high shear rates and high particle concentrations, such as paper coating, spraying, and the efficient pumping of slurries as well as the use of concrete [8]. However, it can be harnessed for benefit in novel electrorheological fluids [9], unique materials that can simultaneously stiffen and dampen [10], stab and puncture resistant flexible composites [11], as well as enhanced body armor [12]. Shear thickening has been shown to be a very sensitive

probe of the nanoscale forces operational in controlling dense suspension rheology [13].

Understanding the mechanisms of these various rheological phenomena is critical to predicting and controlling them. In particular, shear thickening can have numerous detrimental effects such as damaging processing equipment or causing poor coating. In addition, discontinuous shear thickening has been linked to improved performance in the fabric composites. The tunable non-linear behavior and liquid-solid transition in jamming can potentially have numerous applications in sandwich structures and other composites [14]. The rational design of new composites utilizing shear thickening fluids requires accurate and robust constitutive equations for the rheology with parameters that can be determined from measurable properties of the particles, solvent, and other additives. Such constitutive equations require an accurate, fundamental understanding of the underlying mechanisms in flowing suspensions. In addition, control over the rheology through control of the particle properties and interactions would yield improvements in a wide variety of other industrial processes and applications.

Currently, there is some predictive control of concentrated suspension rheology based on theory and empirical relationships [1, 15-20]. Experimental microstructure measurements have previously combined with simulations to provide significant insight into the underlying mechanisms for shear thinning and shear thickening [21-23]. The understanding of this structure-property relationship has been limited because the microstructure has not been successfully measured in the flow-gradient (1-2) plane of shear, where the most dominant structural rearrangements are apparent [23-25].

1.2 Background

Typical hard-sphere suspensions, which only have excluded volume interactions, show both shear thinning, where the viscosity decreases with increasing applied shear stress or rate, and shear thickening, where the viscosity increases with increasing shear stress or rate. This varying rheological behavior comes as a result of the spatial rearrangements of the particles in the suspension under flow, generally termed the fluid “microstructure”. This microstructure can change drastically based on the applied shear and interparticle interactions, causing behavior such as shear thinning, shear thickening, yielding, and thixotropy. In the absence of significant microstructure changes, such as in dilute suspensions or at very low applied shear stresses in moderately concentrated suspensions, the steady-shear rheology is Newtonian. Much prior work has been done to connect the observed rheology to the interparticle interactions and the fluid microstructure experimentally, as well as connect the experimental rheology and microstructure to those from simulations and theory. However, prior microstructure measurements by SANS were limited to the radial direction, or 1-3 plane of shear, and the tangential direction, or 2-3 plane of shear [22, 23]. The most dominant structural rearrangements occur in the 1-2 plane of shear. This work will use further development of a 1-2 plane shear cell to measure these most dominant structural rearrangements and compare them to theory and simulations.

Shear-thinning in hard-sphere dispersions is known to occur through spatial rearrangements among the particles that are exhibited as anisotropic deformations in the microstructure away from the equilibrium arrangement. Specifically, an elastic component of the stress, termed the thermodynamic component of the stress, drives shear thinning as further increases in the shear stress do not lead to

linear increases in the shear rate. Alternatively as the particle microstructure gets further deformed from the equilibrium state, increasing the shear rate does not increase the stress linearly. The Brownian motion provides the driving force to move the microstructure back to equilibrium. This component of the stress is known to be elastic through step-rate rheological experimental measurements [26, 27], rheo-optical experiments [21], and simulations [28-31].

The mechanism for reversible shear thickening in stable colloidal dispersions is understood to be driven by the dominance of short range lubrication hydrodynamic interactions, which lead to particle clustering [30]. These flow-induced particle density fluctuations, denoted as “hydroclusters”, first predicted by Stokesian Dynamics simulations, were then observed experimentally by rheo-optical [21, 32] and neutron scattering methods [15, 23, 33]. Specifically, as the particles come into close contact at high stresses, the lubrication hydrodynamics cause two or more particles to begin moving together as a cluster. These clusters are not permanent aggregates and quickly dissipate, although permanent particle aggregation could be confused for reversible shear thickening. A fundamental theoretical understanding of hydrocluster formation has been developed via suspension micromechanics [34, 35]. Understanding the formation and structure of these hydroclusters is fundamental to understanding suspension rheology [31]. As noted by Brady and Bossis in their seminal review of the Stokesian Dynamics method [36]: “Thus the importance of cluster formation, which results from the lubrication forces and excluded volume, cannot be underestimated in understanding suspension behavior.”

The hydrocluster theory for shear-thickening can be broken down into three distinct questions for scientific study. First, are there clusters in a shear-

thickening fluid? Second, do the clusters cause the shear-thickening? And third, is the shear thickening hydrodynamic in origin? Separately, one should determine if evidence supports or disproves alternate theories. In this case, the only alternative theory of shear thickening in literature is the order-disorder transition theory, originally proposed by Hoffman, which is also hydrodynamic in origin but has an elastic contribution to the stress as the cause of thickening [37, 38].

There is much evidence of particle clustering in a shear thickening fluid. Experimental measures of turbidity changes at the onset of shear thickening provide strong evidence of clustering as a density fluctuation [21, 26, 27]. In addition, clustering has been seen in simulations of hard-spheres [25, 28, 30, 39, 40]. SANS measurements of the microstructure of shear thickening fluids have also seen structures corresponding to clustering by increased scattering at low q indicative of increased particle correlations at large length scales [23]. Also, studies of anisotropic (non-spherical) particle suspensions have been seen to exhibit clustering via SANS [16, 22, 41]. The relationship between clustering and rheological thickening cannot be expressly proven experimentally. Regardless, a strong link has been established through simulations showing clustering necessary for shear thickening [25, 28, 30, 39, 40].

Some evidence that shear-thickening is of hydrodynamic origin comes from Stokesian dynamics simulations. Specifically, Brownian dynamics simulations which do not include hydrodynamics do not show thickening, whereas Stokesian dynamics simulations which include hydrodynamics do show shear thickening [42]. In addition, the microstructures are vastly different between the two methods. In addition, stress jump measurements have shown that, as expected from the hydrodynamic origin

of shear thickening, there is an elastic component of the viscosity which is typically shear thinning and a viscous component of the viscosity which is shear thickening (although at very high concentrations, the elastic component of the stress was also shear thickening) [26, 27]. Alternatively, simple molecular fluids should not show shear thickening under the hydrocluster theory due to the lack of a coupling fluid – only the interparticle potential is necessary to understand the flow characteristics. Typically, shear thickening is not seen experimentally in molecular fluids, although one study does show thickening and clustering in molecular dynamics simulations of a simple fluid [43].

The alternative, order-disorder transition theory of shear thickening was originally proposed by Hoffman [37, 38]. In this theory, a layered, ordered structure drives the shear-thinning to a lower than expected viscosity in the absence of this ordering. As the imposed shear rate increases, hydrodynamic disruptions to the flow cause a transition to a disordered state, imposing a requisite increase in the viscosity concurrent with the order-disorder transition. Many experimental studies have shown that an order-disorder transition is neither necessary nor sufficient for shear thickening [21-23, 32, 33, 44].

Experimental and theoretical work has provided much predictive insight into the rheological scaling of concentrated suspensions. Barnes identified numerous factors influencing shear thickening of suspensions, such as particle concentration, particle size polydispersity, particle shape, interparticle interactions (such as electrostatics and van der Waals dispersion forces), and the properties of the solvent [1]. Suspensions of monodisperse spheres typically begin to show non-Newtonian flow behavior at volume fractions above 0.20. Discontinuous shear thickening begins

to appear at volume fractions in excess of 0.50. Polydispersity is known to increase the required concentration for these non-Newtonian effects [15], and anisotropy is known to decrease the required concentration or increase the severity of the non-Newtonian flows at a given concentration [16, 22, 41]. In addition, the behavior is known to be a strong function of particle size [15, 17, 19], with the hydrocluster theory giving a scaling of critical stress proportional to the particle size cubed for Brownian hard-spheres [15, 18-20]. Also, the steady shear rheology is known to scale with the suspending medium viscosity, as long as the interparticle potential remains similar [45].

1.3 Thesis Objectives and Overview

The objective of this dissertation is to systematically investigate the structure and rheology of near hard-sphere, concentrated, colloidal suspensions of spherical silica particles. The term near hard-sphere means that the behavior is dominated by the hard-sphere interactions and, while there are additional non hard-sphere interactions, these interactions are known, accounted for, and generally negligible. As discussed above, there is significant evidence for the hydrocluster theory of shear thickening, but few direct measurements of the structure of the hydroclustered fluid. The experiments previously mentioned have a number of limitations which will be addressed by this thesis. First, the microstructure of concentrated suspensions has only been measured in detail in the radial (1-3 or flow-vorticity plane of shear) and tangential (2-3 or gradient-vorticity plane of shear) before [20, 23]. However, theory [46, 47] and simulations [24] show that the dominant structural rearrangements occur in the 1-2 (or flow-gradient) plane of shear, which has been difficult to access experimentally. Consequently, the 1-2 plane of shear provides

the necessary structural features required to calculate the specific stress components from micromechanics theory: including the thermodynamic, or shear thinning, component of the viscosity and the hydrodynamic, or shear thickening component of the normal stress differences [23]. This thesis will also probe the microstructure of flowing colloidal suspensions on longer length scales with the new technique of flow-USANS to explore longer-range correlations that may arise in the hydroclustered fluid.

To elucidate the structure-property relationships, the steady shear rheology (i.e., viscosity and first normal stress differences) will be presented for suspensions of three different size particles in various solvents. The particle properties and equilibrium microstructure for a range of concentrations from dilute to concentrated are determined for suspensions of the smallest particles using SANS and for the largest particles using USANS. The first SANS measurements in the plane of shear (1-2 plane) will be presented on suspensions of the smallest particles. These experimental measurements, combined with measurements in the radial direction (1-3 plane) will provide a complete experimental understanding of the microstructural rearrangements that drive shear thinning, shear-thickening, and the first normal stress difference. The first flow-USANS measurements on a concentrated, shear thickening colloidal dispersion provides evidence for hydrocluster formation and correlations in the hydroclustered fluid. When these measurements are compared to SANS measurements on the smaller particles and those in literature, they show that the microstructure-rheology relationship is independent of particle size. The structure of the hydroclustered fluid is used within the framework of elastohydrodynamics to predict the existence of a second shear thinning regime that is governed in part by the particle

hardness. Finally, a practical application of the knowledge developed within this thesis is made to develop ballistic and puncture resistant materials.

Chapter 2 will discuss the experimental techniques used in this thesis, including small angle neutron scattering, suspension preparation, rheological measurements, and test methods for ballistic fabrics with concentrated suspension treatments.

Chapter 3 will present a full characterization of the particle size, particle interactions, and rheology of the commercial silica particles used in this study, dispersed in various solvents. Theoretical scaling laws will be tested and used to compare the data across the various systems. The effects of particle size on the shear-thinning and shear-thickening is examined in detail. In addition, the first normal stress difference of these suspensions will be measured. These rheological and particle size characterizations are used in later chapters to develop and test structure-property relationships.

Chapter 4 will present a complete characterization via SANS of nominally 60 nm radius spherical silica dispersed in a Newtonian mixture of poly(ethylene glycol) and ethylene glycol (deuterated ethylene glycol is used in some cases). Microstructures in two planes of shear will be presented and compared to simulations, giving a full 3-dimensional characterization of the microstructure. Theory will be used to calculate rheological parameters from the SANS data via a stress-SANS law. These are the first measurements of the microstructure of concentrated suspensions directly in the plane of shear (1-2 plane), which allows for calculating from theory both the thermodynamic and the hydrodynamic components of the shear stress. In addition, the thermodynamic and hydrodynamic component of the normal stress can be calculated

and will be compared to experimental measurements for the first time. A suspension which does not shear thicken, due to a polymer brush grafted onto the particle surface, is also studied and the microstructure evolution under shear is compared at equivalent Péclet number to the shear-thickening suspensions.

Chapter 5 will utilize ultra-small angle neutron scattering (USANS) in the 1-3 plane of shear, or radial direction, to characterize microstructural rearrangements of nominally 260 nm radius spherical silica dispersed in Newtonian poly(ethylene glycol). These are the first published flow-USANS measurements [48]. While the USANS technique does not measure anisotropy which is important in these systems, it can provide proof that the structure is length-scale independent over the size range studied here. In addition, these measurements give further information about the structure in the hydrocluster.

Chapter 6 will examine a seemingly anomalous phenomenon reported in the experimental literature where the viscosity of a concentrated suspension will transition to shear-thinning at high stresses, beyond the shear-thickening regime. We use the understanding of hydrocluster microstructure and develop an elastohydrodynamic model that gives a simple, predictive explanation of this post-thickening transition. Monodisperse PMMA particles nominally 500 nm in radius are synthesized and dispersed in poly(ethylene glycol) to test this theory. These suspensions show this post-thickening shear-thinning, which is shown to not be caused by wall slip or permanent particle deformations. Particle modulus measurements, necessary for the scaling law are done via contact-mode atomic force microscopy (AFM). In addition, the elastohydrodynamic model is applied to various concentrated suspensions in literature.

Chapter 7 will present a study on the use of concentrated suspensions as a treatment for improving the ballistic and puncture resistance of Kevlar fabric. The effect of particle hardness is studied by comparing the hard silica particles, studied in Chapters 3 and 5, to the softer PMMA particles studied in Chapter 6. In addition, the effect of viscous stress transfer, or the rheological effect of such a treatment is investigated by studying both dry particle treatments and concentrated, shear-thickening particle-fluid suspensions.

Finally, conclusions for this dissertation are presented in Chapter 8 along with suggestions for future research.

Chapter 2

EXPERIMENTAL TECHNIQUES

2.1 Introduction

In this chapter, the experimental techniques used to characterize particle and suspension physical properties are explained. The methods of preparing the particles and suspensions used are discussed. The procedures for measuring rheological properties are included. The SANS and USANS techniques are discussed as well as the methods of data analysis. The preparation of fabric composites and test methods for yarn pull-out, spike puncture, and ballistic testing are also included.

2.2 Particle Characterization

2.2.1 Particle Size

Particle size was measured via three different techniques and compared. Scanning electron microscope (SEM) (JEOL 7400) micrographs were taken of each type of particles, after dispersing in water and drying on a metal stub. Two perpendicular measurements per particle for over 40 particles give a measure of the particle size, polydispersity, and asphericity. In addition, the sample was scanned for anomalous particles such as exceptionally large particles, broken particles, or dicolloids.

Dynamic light scattering measurements of the particles suspended in either ethanol or water was also used to determine the hydrodynamic particle radius via

measurements of the diffusion coefficient and the Stokes-Einstein-Sutherland relationship, Equation 2.1 [49]:

$$D_0 = \frac{k_b T}{6\pi\mu_s R_h} . \quad (2.1)$$

In this equation, k_b is Boltzmann's constant, T is temperature, D_0 is the diffusion coefficient, μ_s is the solvent viscosity, and R_h is the particle hydrodynamic radius. A Brookhaven Zeta-PALS with a 635nm laser was used and the data analyzed by cumulant analysis with the BI-9000 correlator.

Finally, small angle neutron scattering measurements (SANS) or ultra small angle neutron scattering (USANS) measurements on dilute ($\phi \sim 0.01$) suspensions, with a fit to a polydisperse (Schultz distribution) spherical particle form factor using standard procedures [50] were used as a third measurement of size. Additional details can be found in section 2.5.2.

2.2.2 Density Measurements

Particle density was determined by solution densitometry. Where possible, the density was measured in the standard suspending fluid used in this thesis, polyethylene glycol (PEG-200). Measuring particle density in the suspending medium was preferred so as to eliminate effects of particle settling and interactions between the particles and solvent, such as absorbed solvent. In addition, since the silica particles used were available dry, it was straightforward to accurately measure particle and solvent masses when preparing the suspensions. For PMMA particles prepared in water, solution density measurements were made in the suspending water and used to check the volume fraction of suspensions transferred into PEG. The densities of a dilution series from a known stock solution were measured by a liquid density meter

(DMA 48 or DMA 4500 M, Anton Paar). This device measures density based on the oscillating tube principle to an accuracy of $\pm 0.0001 \text{ g/cm}^3$. In addition, it has temperature control to an accuracy of $\pm 0.05^\circ\text{C}$. Particle weight fractions, x , were determined by measurement of the dry particles added to the suspension (or by drying of the particle suspension in water, in the case of PMMA suspensions discussed in Chapters 6 and 7). Particle densities were determined based on assuming ideal mixing, using equation 2.2.

$$\frac{1}{\rho_{\text{particle}}} = x \left[\frac{1}{\rho_{\text{suspension}}} - \frac{1}{\rho_{\text{solvent}}} \right] + \frac{1}{\rho_{\text{solvent}}} \quad (2.2)$$

A range of particle weight fraction samples were measured via solution densitometry and a linear least-squares fit to equation 2.2 provided the density of the solvent, ρ_{solvent} , and that of the particle, ρ_{particle} .

Two deuterated solvents were used for SANS experiments, d-ethylene glycol and d-dodecane. Due to low available volumes, the deuterated solvent densities were measured with an analytical balance and pipette, by removing via calibrated pipette a known quantity out of the bulk material and recording the weight change. Measurements were done five times each for both 100 μL and 200 μL quantities for each solvent. In addition, the method was checked for accuracy with the non-deuterated solvent and a calibration standard.

2.2.3 Atomic Force Microscopy Nano-indentation of Particles

Atomic Force Microscopy (AFM) nano-indentation experiments were performed on various particles used in this thesis. The procedure follows an established method in the literature [51, 52]. A Veeco Bioscope 2, which is an inverted Zeiss Axiovert 200 microscope with an AFM attachment, was used with Nanosensors'

PointProbe (Silicon-SPM-Sensors) tips. These tips are made of highly doped, single crystal silicon. First, an image was collected in tapping mode. Then, numerous indentation force curves at the center of various particles in the image were collected by the PicoForce module in contact mode via point-and-shoot. Finally, the sample was imaged again in tapping mode to ensure that the particles had not moved during the nano-indentation experiment.

Figure 2.1 shows representative force versus displacement data along with a typical analysis. During the indentation experiment, the tip head is moved toward the sample, the tip contacts the sample and is deflected. Once a trigger value of maximum force is reached, the tip retracts. The tip deflection is measured via a laser reflecting onto a detector. This tip deflection is converted to a force by the cantilever spring constant, which is determined from a thermal tune in air [53]. The left pane of Figure 2.1 shows identification of the contact location on the force versus tip displacement graph. The contact location, indicated by the arrow, was determined as the location where the force begins to increase on the extension curve (solid squares). The right portion of Figure 2.1 shows the indentation force, F_{indent} , which is the measured force shifted by the value of force at contact, F_{contact} , so that all values are positive,

$$F_{\text{indent}}(z) = F_{\text{tip}}(z) - F_{\text{contact}} \quad (2.3)$$

The indentation depth, z_{indent} , is the stage displacement, z , minus the tip deflection, Δh_{tip} , shifted by the stage displacement (z_{contact}) and tip deflection values ($\Delta h_{\text{tip,contact}}$) at the contact location,

$$z_{\text{indent}} = z - \Delta h_{\text{tip}} - \Delta h_{\text{tip,contact}} - z_{\text{contact}} \quad (2.4)$$

The slope (Figure 2.1, right panel) of the retraction curve was used to calculate Young's modulus (E) from equation 2.5,

$$E = \frac{\sqrt{\pi}}{2\beta} (1 - \nu^2) \frac{S}{\sqrt{A}}, \quad (2.5)$$

where ν is the Poisson ratio, assumed to be 0.5, S is the stiffness determined from the slope ($dF_{\text{indent}}/dz_{\text{indent}}$) of the retraction curve over the top 75% of the force values, A is the area of indentation and β is an adjustment parameter. A and β are determined from calibration with a known material, a spin cast film of polystyrene and a polyolefin elastomer (ethylene-octene copolymer) standard (Veeco PS-LDPE-GS) with a modulus of 2 GPa in the polystyrene regions and 0.1 GPa in the copolymer regions [52].

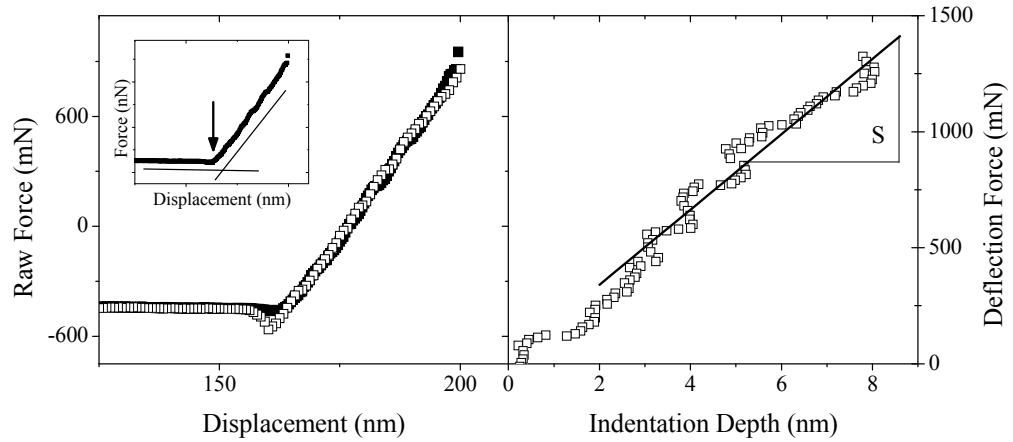


Figure 2.1 Representative force versus displacement data from atomic force microscope (AFM) nano-indentation experiments used to determine particle modulus. Filled symbols are from the extension curve, open symbols from the retraction curve.

2.3 Suspension Preparation

2.3.1 Preparation of Suspensions from Dry Particles

The silica particles used in this thesis were received dry and suspend readily in polar organic solvents, such as ethylene glycol, poly(ethylene glycol), poly(propylene glycol), and glycerol. For the hard-sphere suspensions, the particles were first dried in an oven overnight at $>100^{\circ}\text{C}$ to remove any adsorbed moisture, then weighed out into a bottle into which the solvent was then added. At high concentrations, this particle-solvent mixture would typically be a granulated powder initially, which needed additional mechanical energy to disperse. The additional mechanical energy was provided by roll-mixing overnight. Vortex mixing and sonication were also used to help disperse the particles and a stainless steel spatula was typically used to break up clumps of dry powder that stuck to the walls of the vessel. For the rheology studies, a large batch of concentrated suspension was produced and roll-mixed till homogenous, then separated into batches and diluted with additional solvent or concentrated with small quantities of additional powdered silica as needed. This procedure was followed to ensure that particle aggregates did not persist in the lower concentration samples.

The octadecyl coated silica spheres, whose preparation are discussed in section 2.3.3, were first dried over a nitrogen stream, and then dried in a vacuum oven at 60°C for one hour, before redispersing in apolar organic solvents. These suspensions form a gel at room temperature and so elevated temperatures were used to disperse them. Repeated steps of heating and vortex mixing were used to mix the sample initially, and then it dispersed while being held overnight at 60°C .

Volume fractions for these samples were determined by converting the added particle and solvent mass to volume from the measured densities.

2.3.2 Synthesis of Spherical, Monodisperse PMMA Particles

PMMA particles were produced via a dilute, surfactant-free synthesis in a methanol/water solvent mixture, the synthesis of Shim [54]. Shim's synthesis was scaled up to approximately 1.5 L total volume using 826 g of methanol, 413 g of distilled water, 41.3 g methyl methacrylate monomer, and 0.31 g potassium persulfate initiator. The reaction was carried out in a 2L round bottom flask under a stream of nitrogen, with the reaction contents held at $70\pm 2^{\circ}\text{C}$ for 3 hours after the addition of the initiator, with a condenser held at 10°C . Then the reaction was stopped by exposing the reaction mixture to oxygen in the atmosphere and cooling the temperature down by putting the flask in an ice bath.

To remove any unreacted monomer and excess methanol, the particles were dialyzed against water 3 times for at least 24 hours each. The particle mixture in water was concentrated via centrifugation both for solvent transfer into PEG-200 and for intercalation into Kevlar. The final transfer into PEG-200 for rheological experiments was done via evaporation.

2.3.3 Coating of Silica Particles with Octadecyl Chains

The nominally 60 nm silica was coated with octadecyl chains by the method of Van Helden [55]. The commercial particles (~15 g) were suspended in ethanol (60 g) with sulfuric acid added (6 drops) to protonate the surface. This silica dispersion was added to 1-octadecanol (65 g) in excess with additional ethanol (200 g). The mixture was heated slowly from 70°C to 150°C by 10° increments every 20

minutes in a rotary evaporator to melt the 1-octadecanol and remove the ethanol. Then the particles in 1-octadecanol were held at 200°C for 4 hours to react the octadecyl chains to the particle surface. The sample was cooled and suspended in a ~60/40 by volume mixture of chloroform/cyclohexane. Two centrifugation steps followed by washing with cyclohexane/chloroform removed the excess 1-octadecanol. After a final centrifugation step, the final material was resuspended in cyclohexane. These particles were dried over a nitrogen stream at room temperature and then redispersed in the solvent mixture of deuterated dodecane (Cambridge Isotopes) and mineral oil (Cannon S20 viscosity standard).

To determine the surface coverage of octadecane, TGA experiments were performed on a Mettler Toledo Multistar TGA (DTA sensor), from 25°C to 750°C, with a ramp rate of 20°C/min, in 175µL alumina crucibles, with a flow rate of 50µL/min of air. The surface coverage by weight (A_{coating}) of the 1-octadecane coating and the standard coating on the particles as received was determined from the weight percent lost by the particles, B_{coated} , minus the adsorbed water from surface humidity, determined by the weight percent lost by the base, uncoated particles, B_{base} . Before TGA experiments, the base, uncoated particles had been heated to 600°C and held for 4 hours, then allowed to equilibrate for one week – this treatment gives a measure of the adsorbed water by first removing any surface coating on the original particle and then allowing for adsorbed water to return. These results were also corrected by any weight change in an empty crucible, ΔW_{empty} , to account for temperature induced fluctuations in the measurement device. The surface coverage was determined from the data as

$$A_{\text{coating}} = (B_{\text{coated}} - B_{\text{base}}) (1 + \Delta W_{\text{empty}}). \quad (2.6)$$

2.4 Rheometry

Rheological measurements were primarily done on a TA Instruments AR-G2, although a TA Instruments AR-2000 was used to measure the viscosity of the Newtonian solvents. In all cases, a Peltier lower plate provided temperature control within 0.01°C. Tools used included aluminum 20 mm, 40 mm, and 60 mm cones of 1°, 2°, and 4°, and parallel plates of 20 mm for slip measurements. A standard pre-shear protocol was used as described here. First, a constant stress was applied for one minute at low stress (high enough to reach a shear rate above the lower measurable limit of the instrument). If the applied shear was too low to measure shear rate, then the shear stress was increased systematically until the system reached a measurable shear rate and then held there for one minute. A continuous ramp step, where the stress was continually increased over a three minute duration, was then applied as a second pre-shear and diagnostic to determine if the set stress range was appropriate. After that test, the stress was held constant at the low value again to allow the rheometer tool to slow down and dissipate residual inertia before subsequent tests. Typically, a set of steady state measurements per the protocol below were taken before any additional measurements.

2.4.1 Steady-State Rheological Measurements

The upper tool used for concentrated suspensions was a 1° aluminum cone, with 2° and 4° cones used for the lower concentration suspensions. Multiple concentration samples of each type in a concentration series were tested with multiple tools to ensure that the rheology was tool independent. Newtonian solvents were measured with a 40 mm 2° cone on the AR-2000. Steady-state measurements were done with the steady-state test on the AR rheometer. This test systematically adjusts

the applied shear stress, holds the stress at a constant value, averages the shear rate over a fixed period of time, and compares multiple shear rate averages at a constant stress to determine both if the sample reached steady state and determine the steady state shear rate. The viscosity is reported at that applied stress by dividing the stress by the measured shear rate. In particular, the measurements shown here are comprised of three sequential measurements, averaged over 10 second intervals. Steady state was achieved when the three interval measurements were within 5% and the test was aborted if steady state was not reached within 1.5 minutes. Steady-state sweeps were always done at increasing stress followed by decreasing stress. Multiple forward and backward sweeps were done to ensure the sample did not show hysteresis.

2.4.2 Stress Jump Measurements

Additionally, for some samples, stress jump measurements were performed to show the transient behavior. Specifically, the 1° aluminum cone was used on the AR-G2 with the pre-shear protocol and steady-state measurements described above. Following those measurements, the applied stress was held at a low stress, with measurements recorded every second for ten minutes. The stress was then increased in a step change to a higher stress and data was recorded every second for ten minutes. The stress was then lowered to the original stress and held for ten minutes, with measurements recorded every second. Following this general procedure, the stress was jumped from a low stress in the shear thinning regime to subsequently higher stresses in the thinning regime and thickening regime as well as a low stress near the instrument limit.

2.4.3 Normal Stress Measurements

Measurements of normal stress of concentrated suspensions with the AR-G2 rheometer can exhibit long time transients, taking much longer to reach steady state than the shear viscosity. This result is both due to the instrument compliance and long time decays in the equilibrium microstructure [24]. In addition, since the normal stress changes are very small, the signal to noise ratio is small, requiring long times to acquire adequate data (see Figure 2.2). Finally, drift in the laboratory temperature during the long experiment can cause the baseline value of normal force under zero load to drift (see Figure 2.3). To properly account for these issues, the following protocol for measuring normal stress was used. First, the 60 mm 1° cone was used for all measurements to allow for the largest signal (large cone size), with the smallest inertial correction as the small cone angle requires lower rotational velocity to achieve the same shear rate (correction seen in equation 2.5, from [56]). The preshear described above was used followed by a set of steady state sweeps forward and backward as described above. Then, to measure the normal stress at a constant shear stress, the shear stress was imposed for at least one hour (longer for the lowest shear stresses to ensure at least two full tool rotations and longer for the highest shear stresses to account for the transient behavior). To account for transducer drift caused partly by lab temperature changes, the baseline or zero force value was measured between each constant stress measurement by a creep test at zero stress. For the normal stress under shear or zero force condition, the transient at the start of the test was ignored and the normal force value was averaged over the remainder of the test. The zero-force value was subtracted from the force value measured under shear, the force was converted to a stress by the tool geometry, and the normal stress was corrected for inertia per equation 2.7:

$$N_1 = \frac{2*(F_z - F_{z,0})}{\pi R^2} - 0.15*\rho\Omega R^2 \quad (2.7)$$

where N_1 is the first normal stress difference, F_z and $F_{z,0}$ are the measured normal force under shear and static conditions, respectively, R is the cone radius, ρ is the sample density, and Ω is the cone angular velocity.

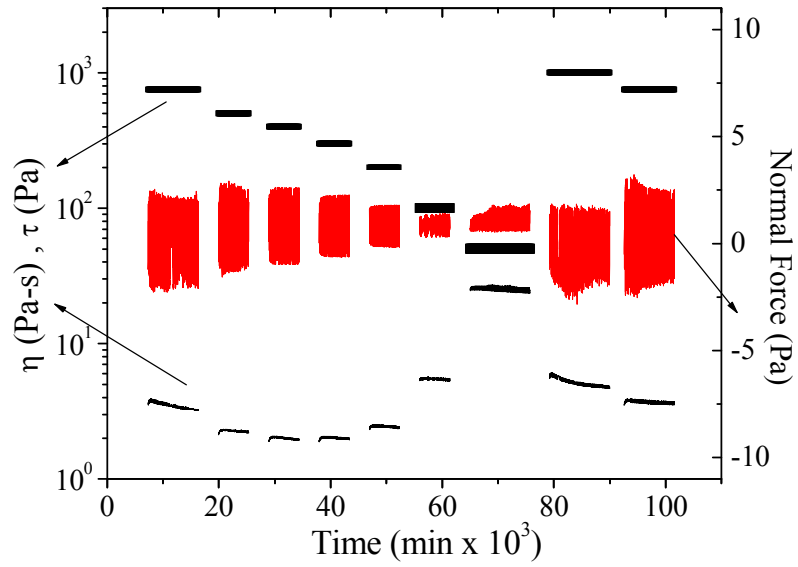


Figure 2.2 Normal stress measurements for 60 nm silica in PEG-200; the time gaps are when the creep measurements such as those shown in Figure 2.3 were performed.

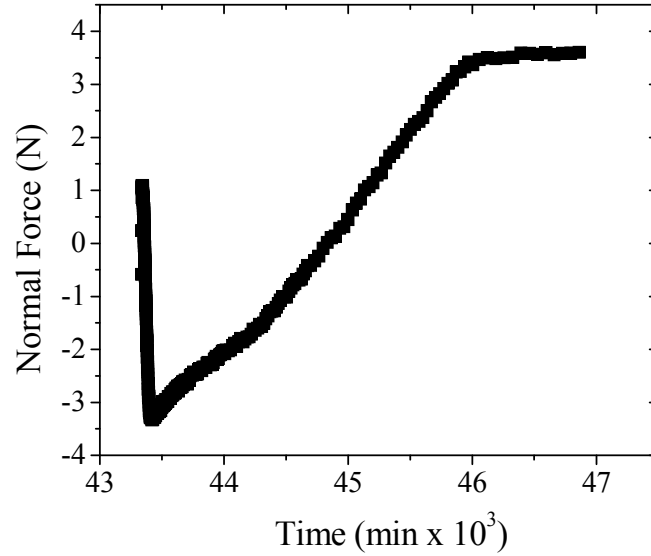


Figure 2.3 Creep measurement after a peak hold at 300 Pa and before a peak hold at 200 Pa on 60 nm silica in PEG used to determine zero normal force value.

2.4.4 Determination of Rheological Slip

Standard analysis of steady-state rheological measurements assumes the no-slip boundary condition to determine the kinematics of flow. Concentrated suspensions are known to exhibit slip as a result of particle depletion near the boundary [56, 57]. Measurements of slip were done by the standard method using parallel plates of varying gap height to measure the slip length and velocity to determine the true shear rate [58]. Figure 2.4 illustrates the slip phenomenon. The steady shear rheology was measured at several gap heights with 40 mm aluminum parallel plate geometry. The slip velocity, v_{slip} , and true shear rate, $\dot{\gamma}_{\text{true}}$, are assumed

to be a function only of the rim shear stress, τ_R . The slip velocity can be calculated using data collected at multiple gap heights (H) at the same shear stress (and therefore same true shear rate) via equation 2.8,

$$\dot{\gamma}_{\text{apparent}} = \dot{\gamma}_{\text{true}}(\tau_R, R) + \frac{2v_{\text{slip}}(\tau_R)}{H}, \quad (2.8)$$

where $\dot{\gamma}_{\text{apparent}}$ is the measured or apparent shear rate for that value of rim shear stress and slip velocity. The rim shear stress for each gap height is calculated from equation 2.9,

$$\tau_R = \frac{M}{2\pi R^3} \left[3 + \frac{d \ln M}{d \ln \dot{\gamma}_{\text{apparent}}(R)} \right], \quad (2.9)$$

where M is the torque and the bracketed portion is a function of gap height. We can also calculate the characteristic slip length as

$$l_{\text{slip}} = \frac{v_{\text{slip}}}{\dot{\gamma}_{\text{true}}}. \quad (2.10)$$

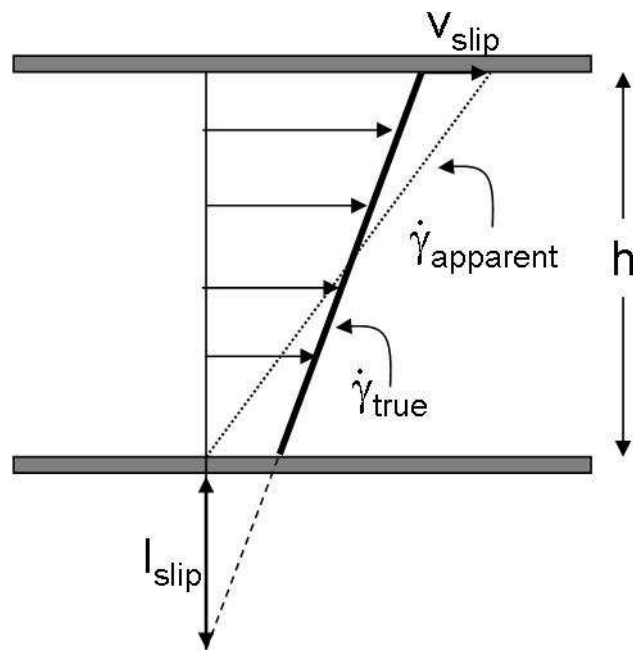


Figure 2.4 Diagram of rheological slip behavior in parallel plate rheometry. Slip contributes to a higher apparent shear rate than the true shear rate.

2.4.5 Small Amplitude Oscillatory Shear Measurements

Small amplitude oscillatory shear measurements are also performed on the AR-G2 with a 40 mm cone of 1, 2, or 4° cone angle. Once again, data are checked by the use of multiple tools for consistency. Strain sweeps are used to determine the linear viscoelastic region, frequency sweeps at either controlled stress or controlled strain are used to measure the rheological behavior.

2.4.6 Critical Stress Determination

The critical stress for shear thickening is determined directly from the steady-state rheology measurements as the point where the first increase in viscosity is observed [19, 20, 59]. The viscosity and shear rate at this point are termed the critical viscosity and critical shear rate, respectively. Due to the shear thinning and shear thickening components of the rheology being controlled by different forces, this point does not necessarily indicate the onset of clustering. Some prior work has used the minimum value of the viscosity determined from a polynomial fit to a log-log plot of the viscosity-shear rate data, which in general gives a slightly lower value of the critical stress [9, 16, 45]. Note that this method is sensitive to the test parameters; all tests used ten points per decade and the error in critical stress is shown as the stress difference between adjacent points.

2.5 Neutron Scattering Techniques

2.5.1 Flow-Ultra Small Angle Neutron Scattering (Flow-USANS)

USANS experiments were performed using the BT5 thermal neutron double-crystal instrument at the National Institute of Standards and Technology (NIST), National Center for Neutron Research (NCNR) in Gaithersburg, MD [60, 61]. The USANS instrument uses multiple reflections from perfect crystals both to tightly collimate the neutron beam before the sample and select a small wavelength range to be detected on the line detector after the sample. This geometry gives no measure of anisotropy. The data as recorded has both wavelength smearing ($\lambda=2.38 \text{ \AA}$, $\Delta\lambda/\lambda=5.9\%$ wavelength spread) and effective slit smearing (due to the low vertical resolution on the detector required to measure at ultra-small angles). The slit smearing dominates and so, only slit-smearing will be applied to models to fit to the data [50].

USANS measurements on quiescent samples were performed in 1 mm thick titanium sandwich cells with quartz windows, except for the highest concentration sample, which was measured in the shear cell due to loading issues in the sandwich cell.

Flow-USANS measurements are performed with the sample in the NIST-SANS shear cell. The cup and bob dimensions are 60 mm and 61 mm diameter, respectively, for a gap of 0.5 mm. The quartz bob fits tightly over a hollow titanium cylinder frame with water flowing through it for temperature control. The inner titanium bob has a hole through it for the neutron beam to pass. The outer cup is driven by a servomotor, allowing for control of the applied shear rate. The beam is oriented radially through the center of the Couette along the velocity gradient direction and therefore passes through the sample twice, as depicted in Figure 2.5. The beam is oriented radially through the center of the Couette along the velocity gradient direction and therefore passes through the sample twice. The scattering is a projection in the velocity-vorticity (1-3) plane, with each q value representing primarily q in the velocity direction averaged over a rectangular section of q in the vorticity direction. The data was reduced using standard procedures [50]. As noted, USANS yields slit smeared data; hence, under shear USANS yields a one-dimensional scattering profile that is a slit-smeared average over an anisotropic scattering pattern in the velocity-vorticity (1-3) plane of flow. Therefore, unlike for isotropic scattering patterns, it is not possible to desmear data acquired under flow. The analysis is further described in section 2.5.3.

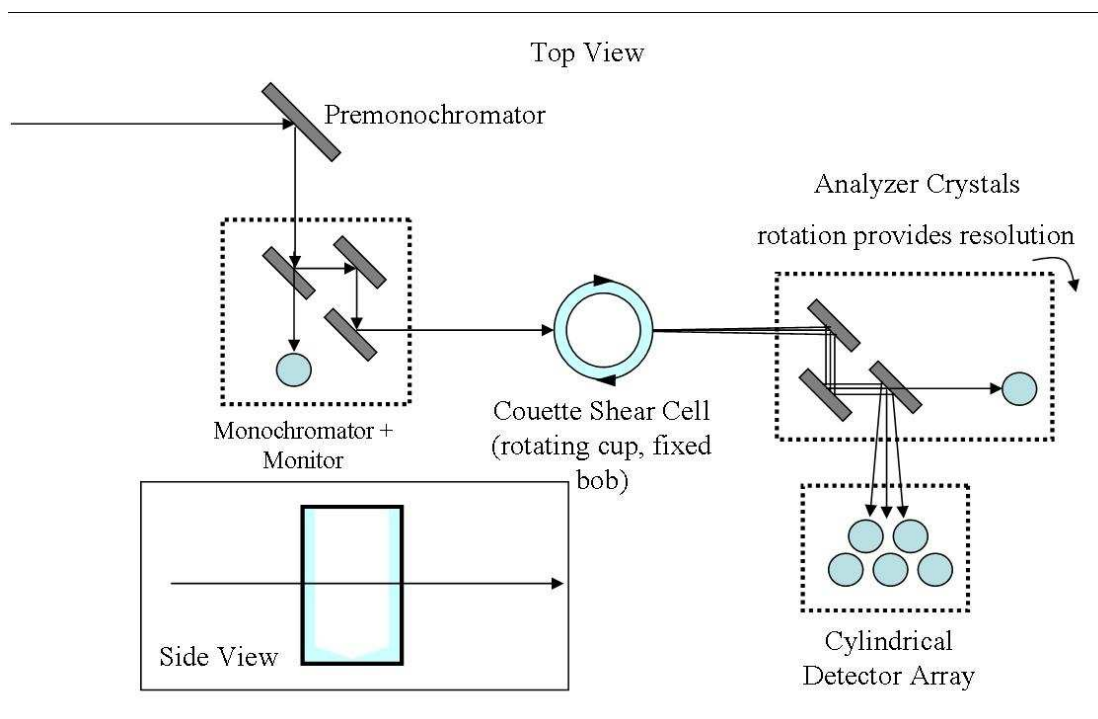


Figure 2.5 Schematic of Flow-USANS experiment, lines with arrows indicate the neutron beam.

2.5.2 Flow- and Rheo- Small Angle Neutron Scattering (Flow-SANS/Rheo-SANS)

There are three different planes of shear for which SANS measurements can give structural information, depicted in Figure 2.6. SANS measurements were performed in the velocity-vorticity (1-3) plane of flow in the NIST SANS rheometer, a Paar Physica UDS 200 which controls various Couette geometries. There were two geometries used, both made of titanium and with a 0.5 mm gap: a 30 mm inner diameter cup with a 29 mm outer diameter, 35.4 mm long bob with a 1.923° cone angle and a 50 mm inner diameter cup with a 49 mm outer diameter, 70 mm long bob. The smaller cup and bob was used to extend the measurement range beyond the maximum stress of ~ 500 Pa achievable with the larger cup and bob. Experiments were

performed on NG-3 SANS at NIST-NCNR in Gaithersburg, MD, with 8.4 Å (λ) wavelength neutrons with a wavelength spread ($\Delta\lambda/\lambda$) of 15% at 13.1 m detector distance (with both geometries), and on NG-7 SANS with 6.0 Å (λ) wavelength neutrons with a wavelength spread ($\Delta\lambda/\lambda$) of 11% at 15 m detector distance (with the larger cup and bob). A 1.0 cm diameter circular aperture was used to collimate the beam.

SANS measurements were also performed in the velocity-gradient (1-2) plane of flow in a 1-2 plane shear cell recently built by NIST and employed in various studies of surfactant solutions [62]. The cell is a sealed aluminum Couette cell with a short 5 mm cylinder height, limited due to the cylinder height also being the neutron path length. The cell had a sealed sample chamber with a radius of 26.46 mm and inner rotating cylinders of 25.11 mm or 25.46 mm radius, for a 1.35 mm or 1.00 mm gap, respectively. The rotor is driven by a servomotor controlled by a Labview® program which communicates with the SANS instrument control software to synchronize velocity control with the scattering experiment. Temperature control was provided by flowing a heat transfer fluid through channels built into the cell, controlled by an external, independently controlled bath. The cell temperature was verified by an external thermocouple. The cell was filled by injecting sample through a syringe, down a U-shaped channel and into the bottom of the cell. The beam was collimated to go through the quartz windows and through the sample chamber by slits of various width (1 mm for use with the 1.35 mm gap rotor, 0.75 mm or 0.6 mm for use with the 1.0 mm gap rotor, and 0.1 mm for gap resolved measurements) and 3 mm high.

Various SANS scattering configurations were used at 6.0, 8.0, and 8.8 Å neutron wavelengths (λ), with a spread ($\Delta\lambda/\lambda$) of 11%, and either an 11 or 13.1 m detector distance. These configurations were selected to optimize flux and scattering range for various experiments on either NG3 or NG7, the two SANS beamlines available at NCNR NIST.

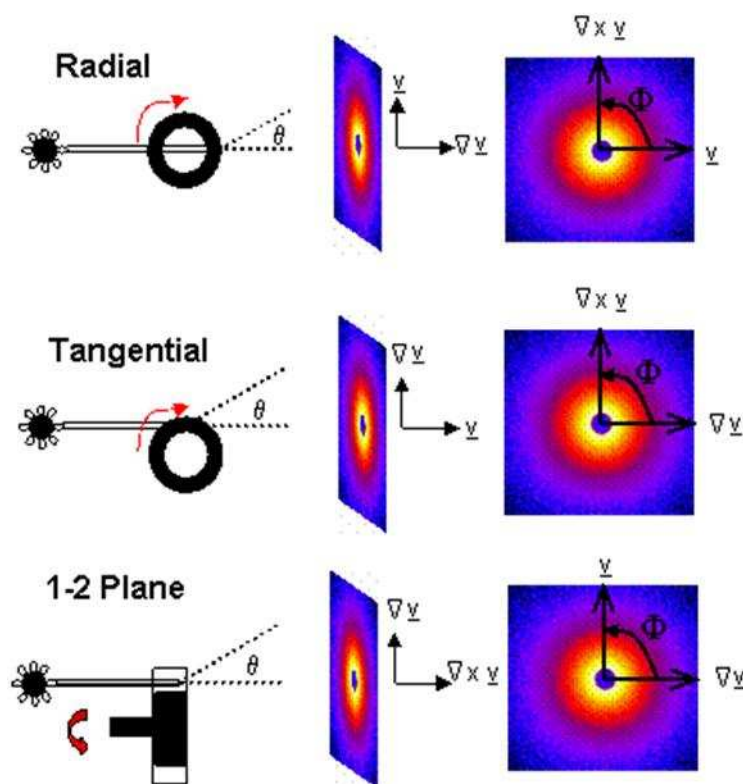


Figure 2.6 Various planes of shear available for scattering measurements. View on left is from above; directions on right are vertical and horizontal projections onto the detector.

2.5.3 Small Angle Neutron Scattering Theory and Analysis

The neutron scattering experiment gives a measure of the particle size and shape convoluted with the relative location of the particles (the microstructure). For monodisperse spheres, the scattered intensity, $I(q)$ follows equation 2.11,

$$I(q) = \phi V_p (\Delta\rho)^2 P(q) S(q) \quad (2.11)$$

where q is the scattering vector, ϕ is the volume fraction, $P(q)$ is the particle form factor, $S(q)$ is the structure factor describing the interactions between particles, and V_p is the volume of a particle determined from the particle radius a , via equation 2.12,

$$V_p = \frac{4\pi a^3}{3}. \quad (2.12)$$

Particle size polydispersity and instrument smearing affect the measured scattering, so typically a model fit to data for form factor and structure factor will include the polydispersity and the overall model will be transformed to account for instrument smearing such as the neutron wavelength spread [50].

For the particle size measurement, a dilute suspension of particles ($\phi \sim 0.01$) was measured via SANS or USANS, a sphere form factor model (polydisperse, Schultz distribution for the larger particles by USANS) was fit to the 1-dimensionally averaged intensity versus wave vector data to extract a radius and polydispersity. For the case of dilute suspensions, the structure factor contribution to the SANS or USANS approaches unity and the scattering can be determined from equation 2.13,

$$I(q, \phi) = \phi V_p (\Delta\rho)^2 \overline{P(q, a, \sigma)} + B, \quad (2.13)$$

where the average radius, a , and polydispersity, σ , are the fit parameters. The form factor was determined from a dilute, static measurement ($\phi \sim 0.01$) and by fitting to the

model for a sphere (equation 2.14) that is integrated over a Schulz size distribution [63]:

$$P(q) = \left[\frac{3(\sin(qa) - qa \cos(qa))}{(qa)^3} \right]^2. \quad (2.14)$$

The USANS data, due to the instrument configuration, only gives a slit-smear 1-dimensional scattered intensity (I) versus scattering vector (q) average, which can be analyzed the same as 1-d averaged SANS data as long as the smearing is accounted for in the model. For the USANS measurement, the model was also slit-smear for instrument resolution per equation 2.15,

$$I_s(q) = \frac{1}{\Delta q_v} \int_0^{\Delta q_v} I(\sqrt{q^2 + u^2}) du, \quad (2.15)$$

where I_s is the smeared intensity and Δq_v is the maximum extent of the vertical resolution in the instrument [50]. For any of the model fitting, the volume fraction is calculated from the measured densities and weights of addition, and the SLD is allowed to vary from the calculated value to fit the data.

Effective structure factors for USANS will be determined from 1-dimensional averages via equation 2.16,

$$S_{\text{eff}}(q, \phi, \dot{\gamma}) = \frac{I(q, \phi, \dot{\gamma}) - B(\phi)}{I(q, \phi_{\text{dilute}}, \dot{\gamma})_{\text{fit}} - B(\phi_{\text{dilute}})} \left(\frac{\phi_{\text{dilute}}}{\phi} \right), \quad (2.16)$$

where S_{eff} denotes the effective structure factor, I is the scattered intensity where a fit is used for the form factor at dilute conditions, B is the background incoherent scattering, and q is the average q from 1-dimensionally averaged data. Note that this effective structure factor would only be equivalent to the actual structure factor in the absence of particle polydispersity, instrument smearing, and structural anisotropy. At

dilute conditions, the structure component vanishes leaving only the particle form factor contribution to the total scattered intensity.

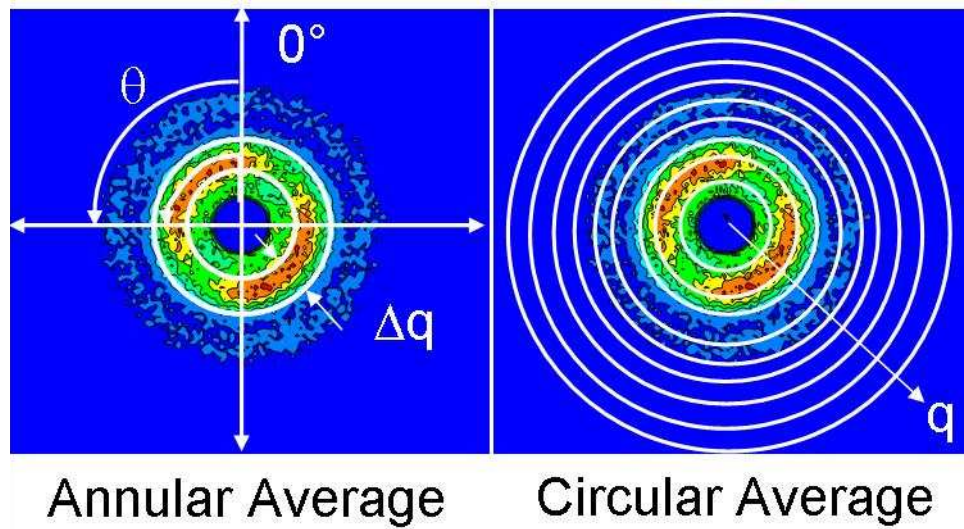


Figure 2.7 SANS data analysis averages.

In this work, SANS data will be presented in three distinct ways. Circular averages, like that seen on the right in Figure 2.7, give a 1-dimensional intensity versus wave vector data summary. This data can be fit to 1-dimensional models, interpreted as to the wave vector or size-dependent features in the scattering, or used to calculate effective structure factors per equation 2.16.

Alternatively, annular averages, seen in the left pane of Figure 2.7, will summarize the data in terms of intensity versus angle averaged over a range of q -values (a center q -value and a Δq in terms of number of pixels from the SANS analysis software [50]). The third method by which data will be presented is as the full 2-

dimensional scattering intensity. These 2-dimensional spectra can be compared qualitatively to radial distribution function data when the structure factor component dominates over the particle form factor.

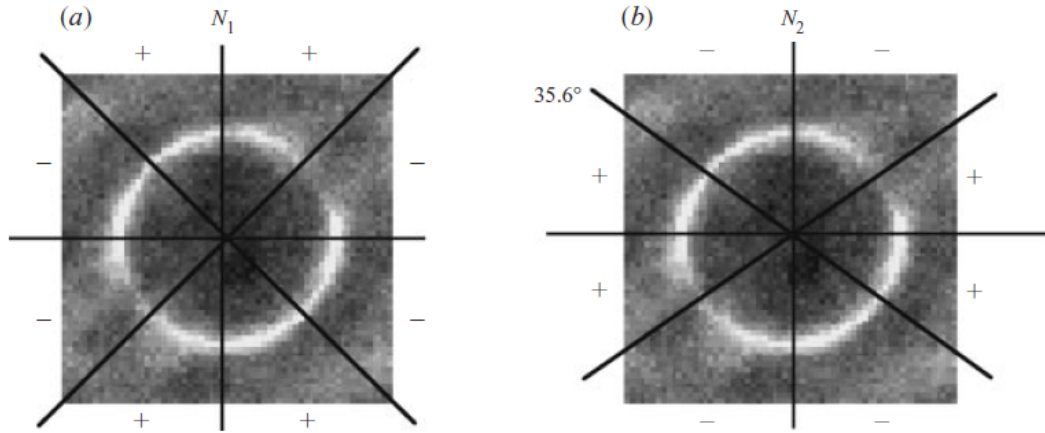


Figure 2.8 Projections of the pair distribution function, showing the sign on the contribution to the Brownian or thermodynamic component to the normal stress difference (N_1 on left, N_2 on right) from particle concentrations in that region (reproduced from [24]). These positive and negative contributions come from the same theory discussed in this section, where the contribution is the same in real space pair distribution function data as it is in the Fourier transformed pair distribution function data determined from SANS.

In addition, harmonic weighted data based on q and angle can provide additional insight into anisotropic structure measurements via SANS as described below. Spherical harmonic decomposition is used to create a stress-SANS law to correlate the microstructure measured via SANS with rheological parameters. This method has successfully been done in the past with SANS experimental data [23, 64, 65] and is analogous to the stress-optic law used in rheo-optics experiments [21, 32].

The scattering data gives a measure of the radial distribution function, as its Fourier transform, the structure factor. As the two-dimensional measured structure factor is the scattering from a particular orientation of a three-dimensional structure, a method is needed to deduce the structure from the scattering pattern. Here, the method of spherical harmonics is used to reduce the complex scattering patterns into components that can be related back to the real space microstructure [66]. For example, Figure 2.8 shows how the contributions to the radial distribution function affect the thermodynamic component of the normal stress differences [24]. In this case, particles in the area marked by a + give positive contributions to the thermodynamic normal stress and particles in the area marked by a – give negative contributions to the thermodynamic normal stress. As the SANS data gives a Fourier transformed measure of this radial distribution function, the same theory used to determine the contribution to the various rheological parameters from the simulations can be used on the SANS data.

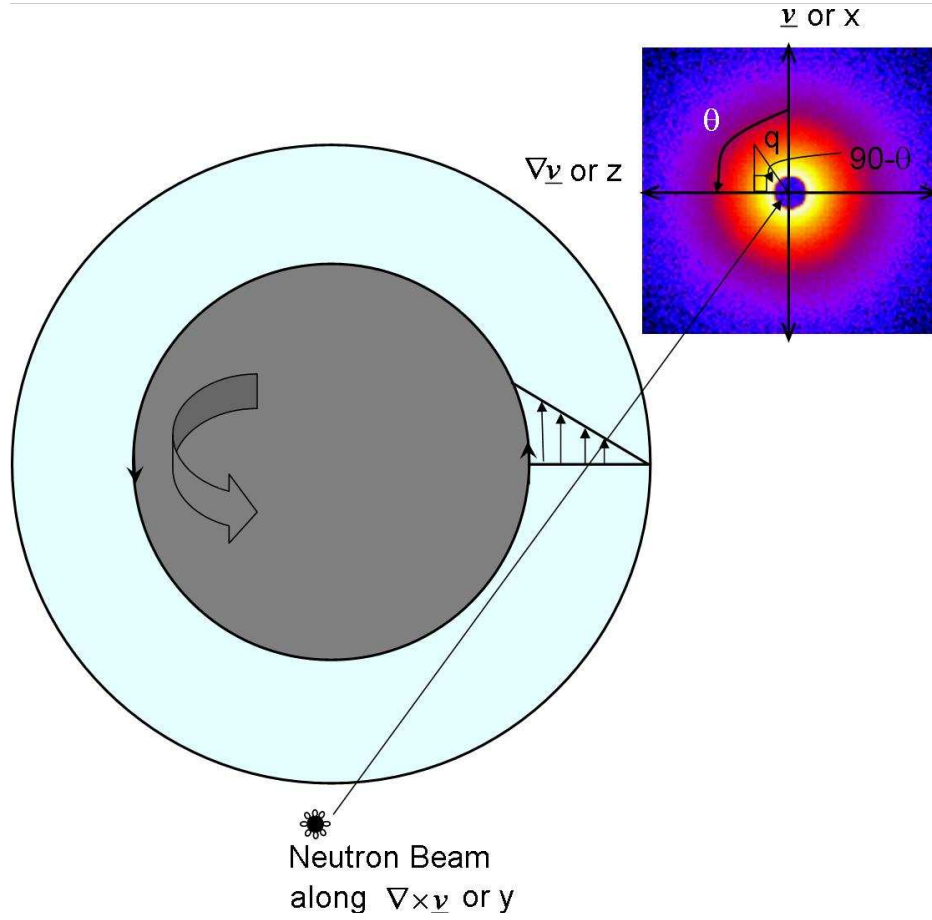


Figure 2.9 Geometry for 1-2 plane flow-SANS analysis. The angle ϕ is between the neutron beam ($\nabla \times \underline{v}$) and the vertical direction (\underline{v}) and hence is zero due to the small angle assumption.

As noted in prior work [23, 65, 66], the shear-imposed suspension microstructure deformations are quantified through spherical harmonic expansions. The expansion yields irreducible tensor components (Y) with scalar coefficients (A) that quantify the microstructure changes, including the dependence on both shear rate and scattering vector as seen in equation 2.17,

$$\hat{h}(q) = S(q) - 1 = \sum_{l,m} A_{l,m}(q, C_N, Pe) Y_{l,m}(\Omega_q), \quad (2.17)$$

$$l \geq m, \Omega = \frac{q}{|q|},$$

where l and m refer to the indices of the spherical harmonics. In terms of the Cartesian coordinate frame shown in Figure 2.9 for the 1-2 plane flow-SANS experiment, the scalar coefficients are denoted as $B_{l,m}^+(q)$ and the scattering becomes [66],

$$\begin{aligned} \tilde{h}(q) = & \frac{1}{\sqrt{\pi}} B_{0,0}^+(q) + \sqrt{\frac{5}{4\pi}} B_{2,0}^+(q) \left(3 \frac{q_z^2}{q^2} - 1 \right) \\ & + \sqrt{\frac{15}{2\pi}} B_{2,1}^+(q) \left(\frac{q_x q_z}{q^2} \right) \\ & + \sqrt{\frac{15}{8\pi}} B_{2,2}^+(q) \left(\frac{q_x^2 - q_y^2}{q^2} \right) \end{aligned} \quad (2.18)$$

where the vectors q_x , q_y , and q_z are (with $\phi=0$ due to the small angle assumption):

$$\begin{aligned} q_x &= |q| \sin(90^\circ - \theta) = |q| \cos\theta \\ q_y &= 0 \\ q_z &= |q| \cos(90^\circ - \theta) = |q| \sin\theta \end{aligned} \quad (2.19)$$

and in terms of angles for this geometry the scattering from equation 2.18 becomes

$$\begin{aligned} \tilde{h}(q) = & S(q) - 1 = \frac{1}{\sqrt{\pi}} B_{0,0}^+(q) + \sqrt{\frac{5}{4\pi}} B_{2,0}^+(q) (3\cos^2\theta - 1) \\ & + \sqrt{\frac{15}{2\pi}} B_{2,1}^+(q) (\sin\theta \cos\theta) \\ & + \sqrt{\frac{15}{8\pi}} B_{2,2}^+(q) (\sin^2\theta) \end{aligned} \quad (2.20)$$

Note that the angles as described in Figure 2.9 and the above equations differ from the standard convention in spherical coordinates such that θ goes from x to z , ϕ goes from x to y , and both are zero at x .

For data analysis in the 1-2 plane of shear, we will take the ratio of the data under shear to the static data and calculate integral functions, $W_{n,\text{vorticity}}$, as

$$W_{n,\text{vorticity}} = \frac{1}{2\pi} \int_0^{2\pi} \cos(n\theta) \left(\frac{I_{\text{shear}}(q, \theta, \dot{\gamma})}{I_{\text{static}}(q)} \right) d\theta, \quad (2.21)$$

where, due to a lack of the relevant $B_{2,1}^+(q)$ component in any of the W_n (see below), we will also define $W_{2,1}$ as

$$W_{2,1} = \frac{1}{2\pi} \int_0^{2\pi} \cos(\theta) \sin(\theta) \left(\frac{I_{\text{shear}}(q, \theta, \dot{\gamma})}{I_{\text{static}}(q)} \right) d\theta. \quad (2.22)$$

The vorticity subscript denotes that these are from measurements with the SANS beam oriented along the vorticity direction, or in the flow-gradient plane, and separates them from the radial and tangential SANS experiments discussed below. In the actual calculations performed here, we assume I_{static} is independent of θ and bring it outside of the integral. The W 's can also be written as,

$$W_n = \frac{1}{2\pi} \int_0^{2\pi} \cos(n\theta) \left(\frac{S_{\text{shear}}(q, \theta, \dot{\gamma})}{S_{\text{eq}}} \right) d\theta = \frac{1}{2\pi} \frac{1}{S_{\text{eq}}} \int_0^{2\pi} \cos(n\theta) (S_{\text{shear}}(q, \theta, \dot{\gamma})) d\theta \quad (2.23)$$

so we take combine equation 2.20 into the variations of equation 2.23 (and 2.22) and integrate to get the coefficients of the $B_{l,m}^+(q)$ terms as follows

$$\begin{aligned}
& \frac{1}{2\pi} \int_0^{2\pi} \left\{ \begin{bmatrix} \frac{1}{\sqrt{\pi}} B_{0,0}^+(q) \\ \sqrt{\frac{5}{4\pi}} (3\cos^2\theta - 1) B_{2,0}^+(q) \\ \sqrt{\frac{15}{2\pi}} (\sin\theta \cos\theta) B_{2,1}^+(q) \\ \sqrt{\frac{15}{8\pi}} (\sin^2\theta) B_{2,2}^+(q) \end{bmatrix} \begin{bmatrix} 1 & \cos 2\theta & \cos 4\theta & \sin\theta \cos\theta \end{bmatrix} \right\} d\theta \\
&= \begin{bmatrix} \frac{1}{\sqrt{\pi}} B_{0,0}^+(q) & 0 & 0 & 0 \\ \frac{1}{2} \sqrt{\frac{5}{4\pi}} B_{2,0}^+(q) & \frac{3}{4} \sqrt{\frac{5}{4\pi}} B_{2,0}^+(q) & 0 & 0 \\ 0 & 0 & 0 & \frac{1}{8} \sqrt{\frac{15}{2\pi}} B_{2,1}^+(q) \\ \frac{1}{2} \sqrt{\frac{15}{8\pi}} B_{2,2}^+(q) & -\frac{1}{4} \sqrt{\frac{15}{8\pi}} B_{2,2}^+(q) & 0 & 0 \end{bmatrix} \quad (2.24)
\end{aligned}$$

Substituting the coefficients from 2.24 into equation 2.21 and 2.22 for the 1,2 plane flow-SANS results gives

$$\begin{aligned}
W_{0,\text{vorticity}} &= \frac{1}{S_{\text{eq}}(q)} \left(\frac{1}{\sqrt{\pi}} B_{0,0}^+(q) + \frac{1}{2} \sqrt{\frac{5}{4\pi}} B_{2,0}^+(q) + \frac{1}{2} \sqrt{\frac{15}{8\pi}} B_{2,2}^+(q) \right) - 1 \\
W_{2,\text{vorticity}} &= \frac{1}{S_{\text{eq}}(q)} \left(\frac{3}{4} \sqrt{\frac{5}{4\pi}} B_{2,0}^+(q) - \frac{1}{4} \sqrt{\frac{15}{8\pi}} B_{2,2}^+(q) \right) - 1 \\
W_{4,\text{vorticity}} &= W_{6,\text{vorticity}} = 0 \\
W_{2,1} &= \frac{1}{S_{\text{eq}}(q)} \left(\frac{1}{8} \sqrt{\frac{15}{2\pi}} B_{2,1}^+(q) \right) - 1
\end{aligned} \quad (2.25)$$

In prior work, different combinations of the W 's were used to calculate the desired $B_{l,m}^+(q)$ terms. In this work, as the samples and shear rates measured are different between the different geometries, we will treat the data from the 1-2 plane of shear separately from the radial SANS experiments. We can clearly calculate the $B_{2,1}^+(q)$ term directly from $W_{2,1}$ as

$$B_{2,1}^+ = S_{eq}(q) \left(8\sqrt{\frac{2\pi}{15}} (W_{2,1} + 1) \right). \quad (2.26)$$

In addition, we see that $W_{0,vorticity}$ has contributions from both $B_{0,0}^+(q)$ and a $B_{2,0}^+(q) + B_{2,2}^+(q)$ term, whereas $W_{2,vorticity}$ evaluates the difference, $B_{2,0}^+(q) - B_{2,2}^+(q)$. This sum and difference will become useful in calculating stresses as described below. With this method of analysis, flow-SANS in the 1-2 shear of plane can now give a generalized description of the flow induced microstructure. As will be seen in the following analysis, only the 1-2 plane measurements provide the insight necessary to measure the $B_{2,1}^+(q)$ component, which is required for calculations of the thermodynamic shear stress and hydrodynamic normal stress differences.

The thermodynamic components of the shear stress and normal stress coefficients are given in Reference [66] as:

$$\begin{aligned} \tau(\dot{\gamma})_{thermo} &= -\frac{\rho_{num}}{\pi\sqrt{30\pi}} \int \theta^*(q) B_{2,1}^+(q; Pe) q^2 dq, \\ \Psi_1(\dot{\gamma})_{thermo} &= \frac{\rho_{num}}{\pi\sqrt{30\pi}} \int \theta^*(q) \left(B_{2,2}^+(q; Pe) - \sqrt{6} B_{2,0}^+(q; Pe) \right) q^2 dq, \\ \Psi_2(\dot{\gamma})_{thermo} &= \frac{\rho_{num}}{\pi\sqrt{30\pi}} \int \theta^*(q) \left(B_{2,2}^+(q; Pe) + \sqrt{6} B_{2,0}^+(q; Pe) \right) q^2 dq. \end{aligned} \quad (2.27)$$

The hydrodynamic component of the viscosity is:

$$\tau(\dot{\gamma})_{\text{hydro}}/2\mu\dot{\gamma}=1+\frac{5}{2}\phi(1+\phi)+2.7\phi^2$$

$$+\frac{5}{2}\phi\sqrt{\pi}\int\left[\begin{array}{l} B_{0,0}^+(q;\text{Pe})\left(2\alpha(q)+\frac{4}{15}\zeta_0(q)\right) \\ +B_{2,0}^+(q;\text{Pe})\left(\frac{2}{3\sqrt{5}}\beta(q)-\frac{4\sqrt{2}}{15\sqrt{7}}\zeta_2(q)\right) \\ +B_{2,2}^+(q;\text{Pe})\left(\frac{2\sqrt{2}}{105}\zeta_2(q)+\sqrt{\frac{2}{15}}\beta(q)\right) \\ +B_{4,0}^+(q;\text{Pe})\left(\frac{-16}{105}\zeta_4(q)\right) \\ +B_{4,2}^+(q;\text{Pe})\left(\frac{4\sqrt{2}}{21\sqrt{5}}\zeta_4(q)\right) \end{array}\right]q^2dq, \quad (2.28)$$

and the hydrodynamic component of the normal stress coefficients are:

$$\Psi_1(\dot{\gamma})_{\text{hydro}}/2\mu\dot{\gamma}=-5\phi\sqrt{\pi}\int\left[\begin{array}{l} B_{2,1}^+(q;\text{Pe})\left(\frac{2\sqrt{2}}{7\sqrt{15}\beta(q)}\zeta_2(q)\right) \\ +B_{4,1}^+(q;\text{Pe})\left(\frac{5\sqrt{6}+24\sqrt{5}}{105\sqrt{30}}\zeta_4(q)\right) \\ +B_{4,3}^+(q;\text{Pe})\left(\frac{1}{3\sqrt{35}}\zeta_4(q)\right) \end{array}\right]q^2dq,$$

and

$$\Psi_2(\dot{\gamma})_{\text{hydro}}/2\mu\dot{\gamma}=-5\phi\sqrt{\pi}\int\left[\begin{array}{l} B_{2,1}^+(q;\text{Pe})\left(\frac{2\sqrt{2}}{\sqrt{15}\beta(q)}\beta(q)\right) \\ +B_{4,1}^+(q;\text{Pe})\left(\frac{5\sqrt{6}-24\sqrt{5}}{105\sqrt{30}}\zeta_4(q)\right) \\ +B_{4,3}^+(q;\text{Pe})\left(\frac{1}{3\sqrt{35}}\zeta_4(q)\right) \end{array}\right]q^2dq. \quad (2.29)$$

The Greek lettered functions which have not been previously described in the above equations are the thermodynamic stress integral, $(\theta^*(q))$ and multiple hydrodynamic functions $(\alpha, \beta, \text{ and } \zeta_n)$, all of which can only be calculated for pairwise interactions. In the pairwise case, these integrals do show a few distinct types of characteristic behavior. Most importantly, they all decay to zero at high values of qa and only significantly deviate from zero at low values of qa . Because of this behavior, in our development below, we will only perform integrations to calculate rheological parameters up to the end of the structure peak and will replace these functions with their sign in the low q limit.

A more specific description of the behavior of these functions is given here. θ^* shows a negative peak at low values of qa and shows oscillations about zero which decay to zero at high q . β and ζ_4 show peaks at low values of qa and then decay to zero at high qa . ζ_2 shows a broad minimum, which is negative, at low qa , and then decays to zero at high qa . α is negative at low qa with an asymptote to negative infinity as $qa \rightarrow 0$ and slightly positive values at $qa \sim 1.4$ before decaying to zero. ζ_0 is positive at low qa with an asymptote towards infinity as $qa \rightarrow 0$. If we look at the behavior in the low- q limit and study only the sign of these contributions, we get that β , ζ_2 , and ζ_4 are positive in the low q limit and θ^* , ζ_0 , and α are negative in the low q limit, so we will replace these coefficients with their sign and integrate up to the peak to calculate the stresses. Note that $B_{2,0}^+$ is expected to have the largest contribution to the hydrodynamic shear stress as the hydrodynamic functions in the description of τ_{hydro} are additive for $B_{2,0}^+$, but counteract each other for $B_{0,0}^+$ and $B_{2,2}^+$. In addition, we are forced to ignore the higher order $B_{l,m}^+(q)$ harmonics which were not calculated above.

We will therefore correlate the thermodynamic stresses from 1-2 plane SANS using equations 2.25 and 2.26 in equation 2.27 to get

$$\begin{aligned}\tau(\dot{\gamma})_{\text{thermo}} &\propto \int_{\text{peak}} B_{2,1}^+(q;Pe) q^2 dq + C, \\ \text{and} \\ \Psi_1(\dot{\gamma})_{\text{thermo}} &\propto \int_{\text{peak}} S_{\text{eq}} W_{2,\text{vorticity}}(q;Pe) q^2 dq + C.\end{aligned}\tag{2.30}$$

In addition, we will correlate the hydrodynamic stresses using equations 2.28 and 2.29 in conjunction with the harmonics calculated via 2.25 and 2.26:

$$\tau(\dot{\gamma})_{\text{hydro}} / 2\mu\dot{\gamma} \propto \int_{\text{peak}} [S_{\text{eq}} W_{0,\text{vorticity}}] q^2 dq + C\tag{2.31}$$

and

$$\begin{aligned}\Psi_1(\dot{\gamma})_{\text{hydro}} / 2\mu\dot{\gamma} &\propto -\int_{\text{peak}} [B_{2,1}^+(q;Pe)] q^2 dq + C \\ \Psi_2(\dot{\gamma})_{\text{hydro}} / 2\mu\dot{\gamma} &\propto -\int_{\text{peak}} [B_{2,1}^+(q;Pe)] q^2 dq + C\end{aligned}\tag{2.32}$$

where Ψ_1 and Ψ_2 are identical in these calculations due to the lack of the $B_{4,1}^+(q)$ harmonic. These numerical integrations are done via the trapezoidal method, with the wavevector q made non-dimensional by multiplying by the particle radius.

For data in the 1-3 plane of shear or radial direction, we will follow the work of Maranzano et al. [23], where the W 's are defined similarly,

$$\begin{aligned}W_{n,\text{radial}} &= \frac{1}{2\pi} \int_0^{2\pi} \cos(n\phi) \frac{S(q)}{S_{\text{eq}}(q)} d\phi \\ &= \frac{1}{2\pi} \int_0^{2\pi} \cos(n\phi) \frac{I(q)}{I_{\text{eq}}(q)} d\phi,\end{aligned}\tag{2.33}$$

which yields the W 's as a function of B 's such that

$$W_{0,\text{radial}} = \frac{1}{S_{\text{eq}}} \left(1 + B_{0,0}^+ \sqrt{\frac{1}{\pi}} - B_{2,0}^+ \sqrt{\frac{5}{4\pi}} \right)$$

and

$$W_{2,\text{radial}} = \frac{1}{S_{\text{eq}}} \left(\frac{1}{2} B_{2,2}^+ \sqrt{\frac{15}{8\pi}} \right). \quad (2.34)$$

In the prior work, through the use of combined harmonics from radial and tangential scattering, the $B_{l,m}^+(q)$ terms were separable, but without the tangential scattering or without combining the radial SANS with the 1-2 plane SANS, $B_{0,0}^+(q)$ and $B_{2,0}^+(q)$ cannot be separated. Utilizing Equation 2.28 for the hydrodynamic stress we will attempt to correlate the stresses as

$$\tau_{\text{hydro}}(\dot{\gamma})/2\dot{\gamma}\mu_s \propto \int_{\text{peak}} S_{\text{eq}} (W_{2,\text{radial}} - W_{0,\text{radial}}) q^2 dq \quad (2.35)$$

where we will ignore the fact that in this correlation we get a negative contribution from $B_{0,0}^+$ rather than the positive contribution, as the $B_{2,0}^+$ term is expected to make the largest contribution. It is important to note, however, that without the tangential scattering, we are unable to differentiate between contributions from the $B_{0,0}^+(q)$ and $B_{2,0}^+(q)$ terms in $W_{0,\text{radial}}$.

2.6 Application Testing of Shear Thickening Fluid/Fabric Composites

2.6.1 Yarn Pull-Out

Yarn pull-out testing was performed using a 20.3 cm × 20.3 cm sheet of fabric with transverse yarns removed on the top and bottom to create free lead and tail yarns, respectively (Figure 2.10). The fabric was put in a frame with two clamped edges (0.635 cm in each clamp, leaving 19.1 cm of fabric between the grips) at a transverse tension of 100 N, with 10.2 cm of lead yarn and a 5.08 cm tail. The lead yarn was clamped in a pneumatic grip mounted in an MTS Synergie load frame, and

pulled at a rate of 50 mm/min until the yarn was completely removed or completely broken. To account for slack, zero displacement was defined as the displacement at which force first reaches 0.1 N. For further details, see Kirkwood et al. [67]. Note that the fabric elastically deforms slightly upward as the yarn is being pulled (Figure 2.10), so that the crosshead displacement is slightly larger than the true yarn displacement relative to the fabric during most of the experiment [67].

Yarn pull-out testing consists of three distinct stages [67], seen in Figure 2.11. In the first stage, uncrimping, the yarn is progressively straightened from the top to the bottom of the fabric. During this stage the load on the yarn rises rapidly, reaching a peak value when the yarn straightening has progressed past the final, bottom transverse yarn. The load then typically drops slightly, as static friction is overcome and the yarn begins to translate through the fabric. During this second stage, which is referred to as the plateau region, the load exhibits oscillating behavior, typically around a constant average pull force, as the residual crimp in the yarn moves alternately over and under transverse yarns. The length of this average load plateau is approximately equal to the length of the original yarn tail. As the end of the yarn tail reaches the lowest transverse yarn and then begins to pull through the fabric, the yarn load drops monotonically as fewer and fewer transverse yarns are engaged. This third stage of pull-out continues until the yarn is fully extracted from the fabric and the pull force drops to zero. In some cases, the yarn breaks rather than completely pulling out, and only the first stage and sometimes part of the second stage are observed.

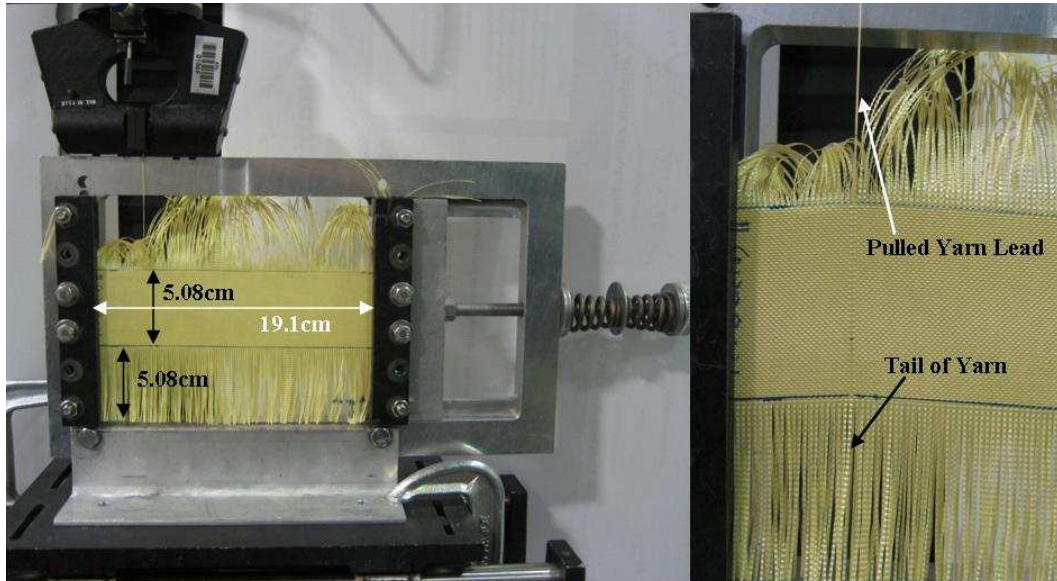


Figure 2.10 Yarn pull-out (YPO) testing apparatus.

The yarn pull-out data is summarized as loading peak force (the peak force at the end of the first, uncrimping stage), loading displacement (location of the loading peak force), and plateau force (average force during the second, constant yarn translation stage). The total, integrated energy for yarn pull-out is also tabulated, although it does not provide a consistent measure of resistance to pull-out since some materials exhibit yarn breakage rather than pull-out. Also included for completion is the crosshead displacement range of the force plateau.

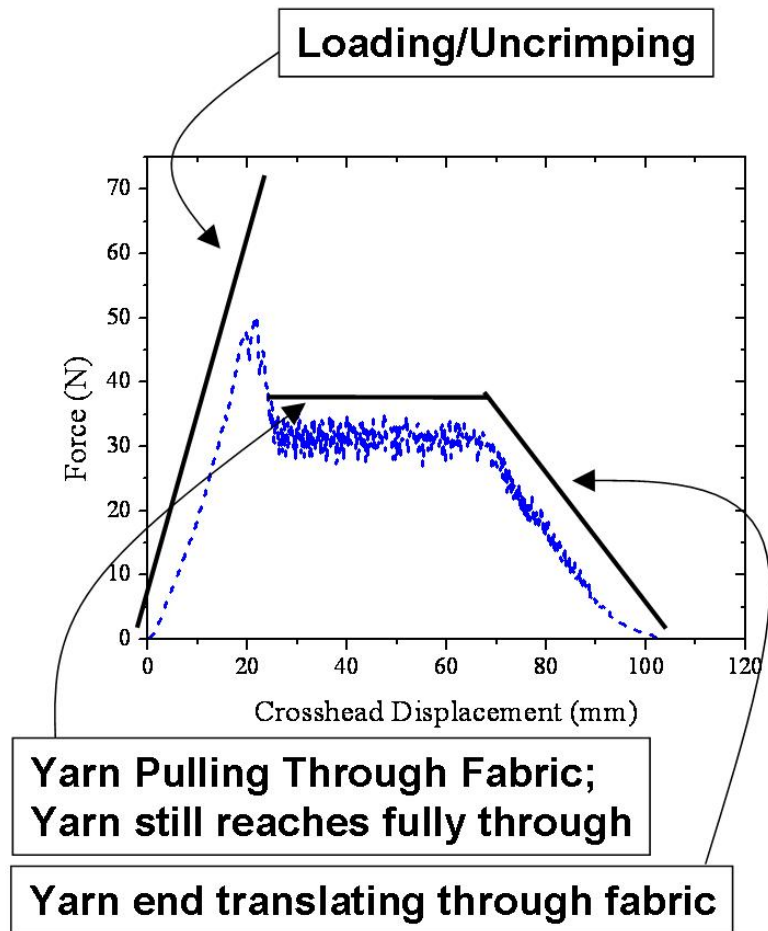


Figure 2.11 Typical yarn pull-out results.

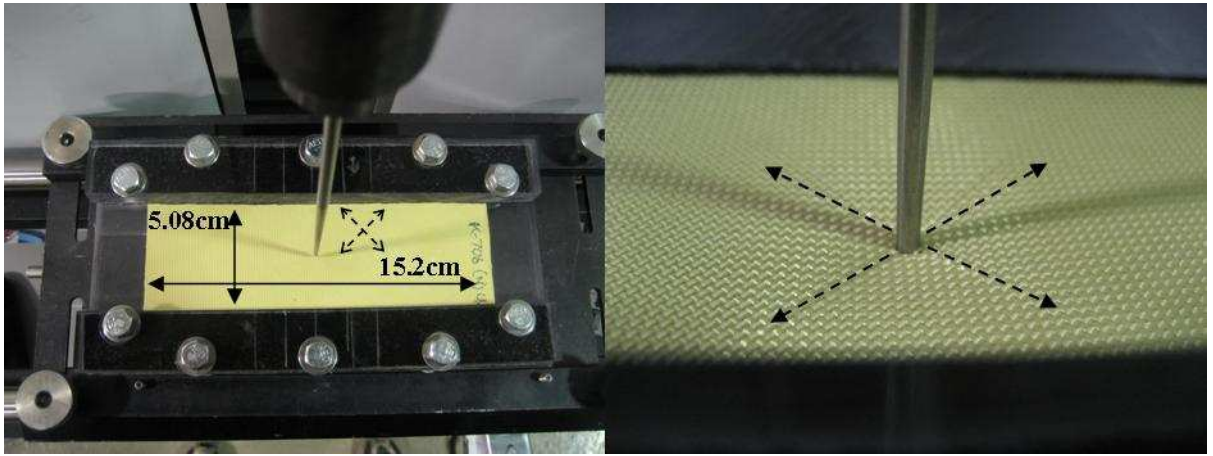


Figure 2.12 Spike puncture testing apparatus. Dashed arrows indicate fabric weave orientation.

2.6.2 Single-Layer Quasi-static Spike Puncture

The quasistatic puncture testing used a single 15.2 cm \times 7.62 cm fabric strip, cut on a bias so that the yarns are oriented at 45° relative to the edges of the strip. This bias configuration allows multiple, consistent puncture experiments to be executed on a single strip of fabric without significant interaction between puncture events, as unique principal yarns are engaged in each puncture. The fabric strip was mounted in a frame as seen in Figure 2.12 with 1.27 cm of fabric clamped along the long edges of the fabric, with the shorter edges of the fabric unclamped, such that a 15.2 cm \times 5.08 cm, unbacked fabric strip is exposed. An MTS Synergie load frame was used to push a National Institute of Justice standard spike [68] from Industrial Knife and Cutter (Simpsonville, SC) into the fabric at a rate of 5 mm/min. Zero

displacement was again defined as the displacement at which force is equal to 0.1N. The NIJ spike has an initial, relatively sharp tip angle along its first 4 mm, followed by a less acute, more gradual but increasing shaft angle over its remaining length. This spike geometry results in a loading curve that shows gradual initial loading as the spike begins to push against the fabric, including one or more dips in the curve due to partial tip breakthrough, followed by a sharp drop when the spike tip penetrates completely through the fabric, and finally a long tail of low but slightly increasing force as the fabric is pushed through the gradually increasing diameter of the main shaft. A typical loading curve with explanation is seen as Figure 2.13. The puncture data is summarized as peak force (which may not be at the final breakthrough point if a partial tip breakthrough point occurs near the final breakthrough), displacement at failure, and integrated energy to failure, which does not include the final tail region after the spike tip has broken through the fabric.

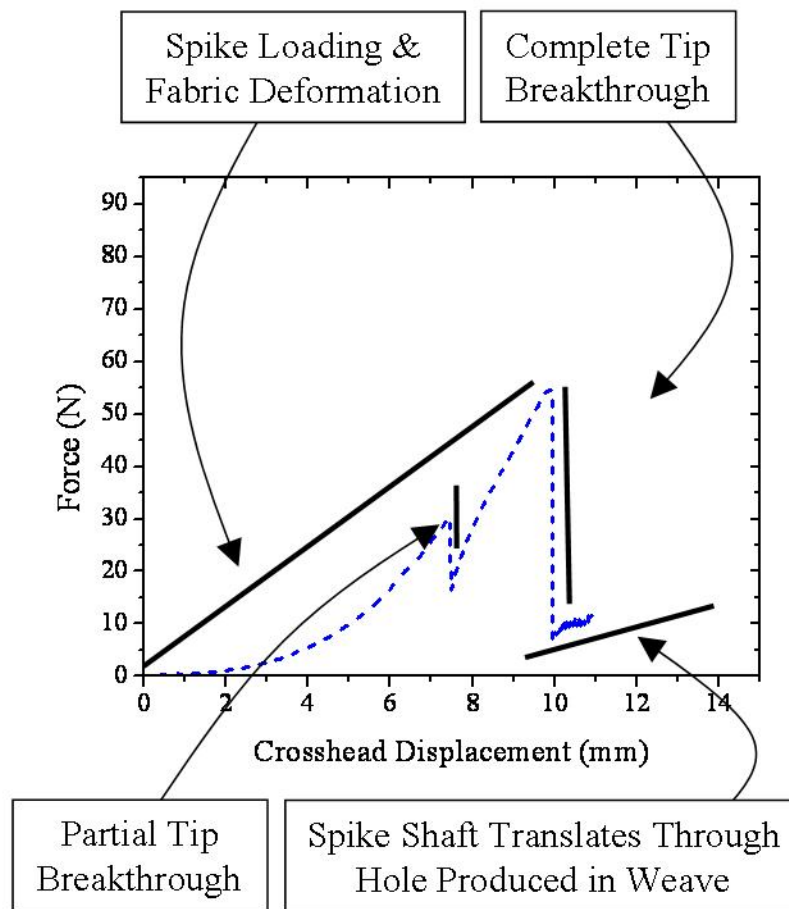


Figure 2.13 Typical spike puncture results.

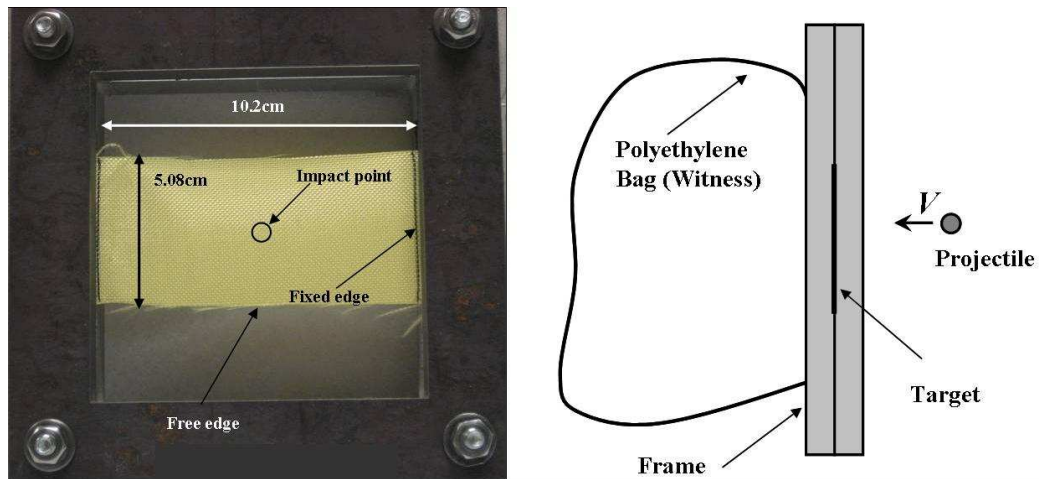


Figure 2.14 Ballistic V_{50} testing frame and witness configuration.

2.6.3 Single-Layer Ballistic V_{50} Testing

Ballistic testing is performed by firing spherical steel projectiles of 0.22 caliber (5.56 mm diameter) and 0.692 ± 0.002 g from a smooth-bore, helium gas gun at single layer fabrics. The velocity is adjusted by varying the gas pressure, and measured by a time-of-flight light chronograph in front of the target. As seen in Figure 2.14, the fabric is clamped along two edges in a steel frame with adhesive grip tape on contact surfaces to increase frictional coupling. The fabric strips used are $15.2 \text{ cm} \times 5.08 \text{ cm}$, with 2.54 cm clamped along each fixed edge leaving a $10.2 \text{ cm} \times 5.08 \text{ cm}$ exposed area. A thin plastic bag is taped on the back of the target frame to act as a witness [2]. If the projectile is in the bag or penetrates through the bag after impact, it is considered a penetrating impact. Ballistic performance was characterized by impacting the targets at a range of velocities, until a data set was achieved with five penetrating impacts and five non-penetrating impacts in which all impact velocities

were within 7.62 m/s (25 fps) of the average of those ten impact velocities. The average velocity of these five penetrating and five non-penetrating impacts is reported as the V_{50} , the velocity at which the projectile is expected to exhibit a 50% probability of penetration [2, 69].

Chapter 3

RHEOLOGY OF SPHERICAL, NEAR HARD-SPHERE, COLLOIDAL SILICA PARTICLE SUSPENSIONS

3.1 Introduction

The rheology of colloidal suspensions is controlled by the interparticle potential, particle size, and solvent viscosity, as well as the relative arrangement of the particles under flow, termed the microstructure. The development of structure-property relations for colloidal suspension rheology therefore requires fully characterizing the suspending fluid, suspension particles, their interactions, and rheology, as well as the suspension microstructure under flow. The focus of this chapter is to show a full rheological characterization of model suspensions, which will be further interrogated in later chapters via novel microstructure measurements.

Much information about the particles and particle interactions can be gained directly from the measured shear rheology and existing models for suspension rheology. Steady-shear rheology will show that these suspensions are nearly Newtonian at low concentrations and can be characterized as effective hard-spheres. Shear thinning is also evident at moderate concentrations, again in both qualitative and quantitative agreement with hard-sphere suspension rheology. Especially important here, these suspensions exhibit continuous shear thickening at moderate concentrations and discontinuous shear thickening above a critical volume fraction. This rich rheological behavior can be interpreted within an emerging framework for the

rheology of hard-sphere suspensions based on the formation of hydroclusters driving shear thickening. As will be shown, a critical stress for shear thickening is found to follow the expected scaling as a function of particle size, temperature, and volume fraction based on the hydrocluster theory of shear thickening. The first normal stress difference is also measured as it is particularly sensitive to the shear-induced microstructure. Stress jump measurements will be used to both explore the short-time transitions in the rheology and confirm the use of SANS and USANS to measure the average microstructure over a time period of minutes to hours. Linear viscoelastic measurements will also be used to characterize the properties of these suspensions.

3.2 Background

There are a number of useful correlations in suspension rheology to compare the behavior of suspensions of different particle size and interactions. Often, to compare suspensions with particles of different size, a dimensionless shear rate known as the Péclet number, Pe , is used,

$$Pe = \frac{\dot{\gamma} a^2}{D_0} = \frac{6\pi\mu\dot{\gamma}a^3}{k_b T}, \quad (3.1)$$

where $\dot{\gamma}$ is the shear rate, μ is the solvent viscosity, a is the particle radius, D_0 is the particle translational self-diffusivity, k_b is the Boltzmann constant, and T is the temperature. Typically, calculations in suspension rheology and simulations, such as the Stokesian dynamics simulations, are performed in a dimensionless manner by using the Péclet number as the dimensionless shear rate.

An empirical model, known as the Cross model [70] can be fit to the shear thinning portion of the data to systematically evaluate the changes in various features

of the steady shear rheology. Parameterizing the data in this manner allows a simple comparison to the behavior expected for hard-spheres. The Cross model is:

$$\eta_r = \frac{\eta}{\mu} = \eta_{r\infty} + \left(\frac{\eta_{r,0} - \eta_{r\infty}}{1 + \left(\frac{\tau_r}{\tau_{\text{Cross}}} \right)^m} \right) \quad (3.2)$$

where η_r is the reduced viscosity, μ is the solvent viscosity, $\eta_{r\infty}$ is the infinite shear viscosity, η_{r0} is the zero shear viscosity, τ_{Cross} is the Cross model critical stress for shear thinning, or the stress where the viscosity is at the midpoint between the zero and infinite shear viscosity, m is the shear thinning power law exponent, expected to have a value of one for hard-spheres [49], and τ_r is the reduced shear stress,

$$\tau_r = \tau a^3 / kT. \quad (3.3)$$

In addition, for samples that appear to have a yield stress, the yield stress component can be added in directly [71]:

$$\eta_r = \frac{\eta}{\mu} = \frac{\tau_{r,\text{yield}}}{\dot{\gamma}} + \eta_{r\infty} + \left(\frac{\eta_{r,0} - \eta_{r\infty}}{1 + \left(\frac{\tau_r}{\tau_{\text{Cross}}} \right)^m} \right), \quad (3.4)$$

where $\tau_{r,\text{yield}}$ is the yield stress. Since the model is fit to the data as a function of stress, the shear rate is calculated iteratively from the model reduced viscosity at each value of the applied reduced stress. The model viscosity will be infinite at applied stresses below the yield stress. In addition, a yield stress material will not have a zero-shear viscosity; therefore, the zero-shear viscosity will be a model fit parameter.

The infinite and zero shear relative viscosities can be compared to that expected from the empirical Quemada relation [49],

$$\eta_r = \left(1 - \frac{\phi}{\phi_m}\right)^{-2}, \quad (3.5)$$

where the expected volume fraction at maximum packing, ϕ_m , is 0.63 at low shear and 0.71 at high shear [72]. Alternatively, the infinite shear relative viscosity has been shown empirically to follow equation 3.6 for volume fractions up to 0.56 [73]:

$$\eta_{r,\infty} = \frac{1 + \frac{3}{2}\phi \left[1 + \phi(1 + \phi - 2.3\phi^2)\right]}{1 - \phi \left[1 + \phi(1 + \phi - 2.3\phi^2)\right]}. \quad (3.6)$$

In addition, we will compare the fit zero-shear and high-shear viscosity to that expected from equations 3.5 and 3.6 with an increase in the effective concentration from additional non hard-sphere interactions as measured by SANS or USANS (section 3.5.1).

Prior work has examined the effect of short-range attractions on the zero-shear viscosity of suspensions through the use of the Baxter potential [74-76], where the strength of the attraction is characterized by the Baxter sticky parameter, τ_b . At low concentrations, the zero-shear viscosity for the sticky hard-sphere fluid was derived fundamentally and shown to follow equation 3.7 [75],

$$\eta_{r,0} = 1 + 2.5\phi + \left(5.9 + \frac{1.9}{\tau_b}\right)\phi^2, \quad (3.7)$$

and at higher concentrations, the viscosity is expected to follow the fundamental relation given by equation 3.8 [76],

$$\eta_{r,0} = \eta_{r,0}^{\text{HS}}(\phi) \left(1 + \frac{1.9}{\tau_b}\right)^2, \quad (3.8)$$

Where $\eta_{r,0}^{\text{HS}}$ is the value of the zero-shear viscosity for the hard-sphere suspension at the relevant volume fraction, given by correlations of the type of equation 3.5.

When investigating shear thickening, the primary focus of theoretical work is in predicting the critical shear rate or shear stress for the onset of thickening. Prior work has attempted to use a simple force balance model to predict the critical shear rate or shear stress for thickening. Initially, Boersma et al. predicted a critical shear rate for thickening from a simple model balancing repulsive electrostatic forces with compressive hydrodynamic forces [77]. Bender et al. extended this force balance model by considering the balance for Brownian repulsion and considering interactions between two particles in an effective medium that contains the averaged effects of all other particles [15]. This balance yielded a dimensionless critical shear stress:

$$\frac{\tau_{\text{crit}} a^3}{k_b T} = \frac{-h}{3\pi} \frac{\eta}{\mu_0} \left(\frac{d \ln(g(r))}{dr} \right), \quad (3.9)$$

where τ_{crit} is the critical stress for shear thickening, η/μ_0 is the reduced suspension viscosity predicted by equation 3.5, which effects a mean field correction for the other particles in the suspension, $g(r)$ is the radial distribution function, and h is the separation distance between the particles, determined from equation 3.10,

$$h/2a = (\phi/0.71)^{1/3} - 1. \quad (3.10)$$

Maranzano extended this relation for electrostatically stabilized particle suspensions [19] as

$$\tau_{\text{crit}} = 0.024 \frac{k_b T (\kappa a) \Psi_s^2}{a^2 l_b}, \quad (3.11)$$

where κ^{-1} is the Debye-Hückel screening length, l_b is the Bjerrum length and Ψ_s is the dimensionless surface potential. Note that for Brownian spheres as in equation 3.10 and the additional scaling rules to come, the critical stress is inversely proportional to the cube of particle size, whereas equation 3.11 shows the critical stress to be a

function of the inverse of the square of particle size, assuming $\kappa a \Psi_s^2$ is constant. Based on this and other prior work [15, 19, 20], Krishnamurthy and Wagner [18] predicted the critical shear stress for thickening in the Brownian case to follow the simplified expression given in equation 3.12:

$$\frac{\tau_{\text{crit}} a^3}{kT} = 0.1 e^{\phi/0.153} . \quad (3.12)$$

3.3 Suspension Preparation and Characterization

Silica dispersions studied in this chapter are made from a series of commercial particles of three nominal sizes, 60 nm, 130 nm, and 260 nm in radius. In this chapter, these particles will be referred to by these sizes in radius – later chapters will not regularly compare the different sized particle suspensions and so radius and diameter will both be used as appropriate. Figure 3.1 shows SEM micrographs of the three particle sets. These particles are commercial particles, received dry, and come with an unspecified surface coating on the particles to prevent aggregation and promote dispersion in the suspending medium.

TGA results of the 60 nm particles shown in Table 3.1. TGA data from the following samples are listed: the 60 nm silica particles with no additional processing, two separate batches of the octadecane coated particles produced as described in section 2.3.3, and a batch described as the previously cooked particles, which have been heated to 600°C for ~6 hours, then allowed to cool and equilibrate with the atmosphere. These results indicate that the particles retain about 4.0 % water by weight and have a coating that is removed by heating to high temperature of an additional 6.0 %. In addition, the octadecane coating is a ~9.4 % weight addition.

Suspensions are prepared by weight, by adding solvent to the commercial silica particles, which have been dried either overnight in an oven at $\sim 100^{\circ}\text{C}$ or dried under vacuum at $\sim 100^{\circ}\text{C}$ for at least 3 hours. For the dilution series shown here in PEG-200 or a PEG-600/ethylene glycol mixture, a high concentration sample of 64% silica by weight or about 52% by volume was produced by roll-mixing for at least two days, periodically breaking solid chunks up with a spatula to homogenize, and then that sample was separated into samples to be diluted with additional solvent or enriched with additional powder to the desired concentration. The samples were produced by weight, with the weight fraction for each sample converted into a volume fraction via the measured densities of the particles and solvent (particle densities are seen in Table 3.2 and solvent densities are seen in Table 3.3).

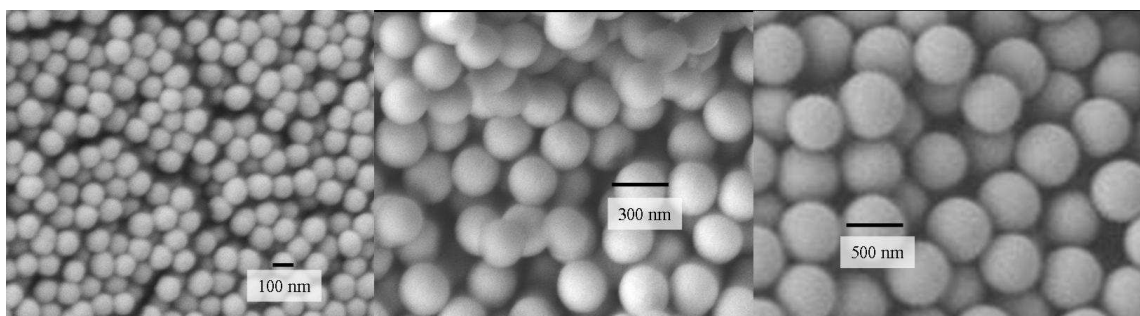


Figure 3.1 SEM micrographs of three sizes of silica particles (increasing size from left to right, nominally 60 nm, 130 nm, and 260 nm radius).

Table 3.1 TGA results – the third column is the coating weight, determined from equation 2.6.

Sample	Weight Loss	Coating Weight
Base Silica Particles	10.01%	6.00%
Octadecane Coated - Batch 1	13.51%	9.49%
Octadecane Coated - Batch 2	13.31%	9.30%
Previously Cooked Silica Particles	4.02%	-
Empty Crucible	0.059%	-

3.4 Experimental

3.4.1 Particle Size and Particle Interactions

Particle size was determined from dynamic light scattering, SEM micrographs, SANS, and USANS. In addition, particle interactions can be determined from zeta-potential measurements and SANS or USANS measurements. These techniques are described in sections 2.2.1 and 2.5.

3.4.2 Rheology

Rheological measurements were performed as described in section 2.4, on a TA Instruments AR-G2 rheometer with the stiff bearing setting and a Peltier lower plate at 25°C, unless otherwise noted. Prior to use, the instrument was calibrated, and the instrument and tooling were also regularly checked with calibration standards. The upper tool was typically a 40 mm aluminum cone with a 1° cone angle, but a 2° and 4° cone angle tool were used for some experiments. In particular, all of the highest concentration sample rheology was measured using a 1° cone and all of the lowest concentration (Newtonian) was measured using a 4° cone. For each concentration series, at least one sample was measured with both the 1° and 4° tool to ensure the same result. In addition, slip measurements were performed using a 40 mm upper

plate. One initial sample was loaded at a large gap, and then after testing was completed at that gap, the tool was lowered to the next gap and the excess sample removed. Normal stress measurements were performed as described in section 2.4.3, with a 60 mm 1° cone. All of these experiments were performed in a stress-controlled mode, which is required to measure discontinuous shear thickening (which is the phenomenon where further increases in the applied shear stress do not cause any increases in the shear rate beyond a certain point, yielding a vertical rise in the viscosity versus shear rate curve).

Data will be fit to the Cross model and the variant with the addition of the yield stress as described here. All fitting is done via a weighted, linear least squares regression. For lower concentration data where there does not appear to be a yield stress, the data will be systematically fit to equation 3.2 as follows. First, the infinite shear viscosity will be set to the average value seen at high shear before thickening occurs. The zero-shear viscosity is then set to the average value seen in the low shear plateau. The exponent m is held constant at one following the expectations from hard-spheres and the critical stress for shear thinning, τ_{Cross} , is set as the stress where the measured viscosity is at the midpoint between the fit zero-shear and infinite-shear viscosity. In cases where there is no low-shear plateau due to the data not extending to low enough stresses, the zero-shear viscosity is adjusted to get the best fit to the data with m set as one and τ_{Cross} as described above. Finally, the value of m is fit to the data with all other fit parameters held constant. Typically adjusting m does not significantly improve the fit and therefore it is left at one.

For samples where there is an apparent yield stress, the yield stress is set to the value of stress where the viscosity appears to diverge, ignoring any apparent low

shear plateau which is a result of slip. Specifically, we set the model yield stress to the point in the apparent shear-thinning regime with the largest magnitude of the slope on the log-log viscosity versus stress curve (the slope is negative in the shear thinning portion of the curve). This definition of the yield stress likely gives a low value of the yield stress as the measured shear-thinning can still be quite extreme for many data points after this, therefore the model fit is expected to be poor at stresses only slightly higher than this value. Since there is no low-shear plateau due to the yield stress, the zero-shear viscosity is adjusted to fit the data along with the exponent m . In addition, the model critical stress for shear thinning, τ_{Cross} , is set as the stress where the measured viscosity is at the midpoint between the fit zero-shear and infinite-shear viscosity. The data below the yield stress is ignored, which allows the data to be collapsed onto the hard-sphere model along with the data without yielding.

3.5 Results and Discussion

3.5.1 Particle Size and Interactions

Table 3.2 shows a summary of the particle size and particle density measurements. The SEM micrographs seen in Figure 3.1 were used to measure the average size and asphericity, defined in this case as the relative value of the larger dimension to the smaller dimension for two perpendicular measures on each particle. SANS and USANS data on dilute suspensions were also used to measure the particle size for the 60 nm and 260 nm particles, respectively. Dynamic light scattering of the particles suspended in ethanol provided an additional measure of size. The hydrodynamic diameter from dynamic light scattering is seen to be 289 ± 58 nm for the largest particles, 137 ± 30 nm for the middle size particles, and 70.2 ± 3.1 nm for the

smallest particles; consistently the largest measure of size for each particle. These size results are consistent with the differences between the measurements caused by both polydispersity and measurement of different fundamental sizes. The DLS measurement is a z-weighted or volume-squared average based on the hydrodynamic volume. As such, even small quantities of aggregated particles as doublets can noticeably increase the measured size. The USANS and SANS measurements are volume weighted averages based on the particle physical size through a chemical disparity with the solvent, with the USANS including Schultz polydispersity. The SEM is a length-weighted average with the dimensions of the particle defined by the round shape, ignoring particle contacts. Aggregated particles in the neutron scattering or SEM measurements would not significantly change the measured size. In addition, the SEM, SANS and USANS measurements appear to be of the silica particle core (an additional excluded volume shell is needed to account for the interactions seen in the concentrated suspensions), whereas the DLS hydrodynamic size measurement would include the effect of any polymer brush coating on the particle surface. Accounting for all these differences between the various particle size measurements, one would expect the size from DLS to be the largest and the size from SEM to be the smallest, consistent with the data.

Table 3.2 Summary of particle property measurements. Error is standard deviation except for USANS, which utilizes the polydispersity in particle size used in the model to fit the data. The SANS data was fit to a monodisperse model.

a – SEM	255±10	126±8	54.4±3.9	nm
asphericity	1.03±0.02	1.06±0.04	1.07±0.06	
a - DLS	289±58	137±30	70.2±3.1	nm
a - USANS	260±26	-	-	nm
a - SANS	-	-	60.6	nm
ρ	1.96±0.03	1.88±0.02	1.89±0.02	g/mL
mobility	$<10^{-11}$	-	-	$\text{m}^2 \cdot \text{V}^{-1} \text{s}^{-1}$

Table 3.3 Solvent properties.

	η_0 (Pa-s)	ρ (g/mL)
PEG-200	0.049	1.120
Ethylene Glycol	0.01647	1.115
d-Ethylene Glycol	-	1.234
PEG-600	0.1468	1.125
PEG-600/EG (30/70)	0.03429	1.159
PEG-600/d-EG (30/70)		1.201
S20 (Mineral Oil) Standard	0.02924	0.8567
dodecane	1.34×10^{-3}	0.754
d-dodecane	-	0.873
S20/dodecane (25C) (50/50)	4.11×10^{-3}	0.806
S20/dodecane (30C) (50/50)	3.69×10^{-3}	-
S20/d-dodecane (25C) (50/50)		0.865
D ₂ O	-	1.1

Table 3.3 shows the viscosity and density of various Newtonian solvents used in this thesis. All viscosity data is measured on an AR-2000 with a 40 mm 2° cone and plate, except the mineral oil standard, where the certified calibration value is used. All densities are determined by densitometry as discussed in section 2.2.2,

except D₂O, which is the literature value, S20 standard oil where the certified standard value is used, and the deuterated solvents which are done by repeated pipetting onto a balance as discussed in section 2.2.2.

Static SANS or USANS measurements can be used to determine particle size and interparticle interactions, through the structure factor. Figure 3.2 shows static, dilute USANS measurements from the largest particles fit the form factor for a 10% polydisperse (Schultz distribution), 260 nm radius spheres, with appropriate instrument smearing. The static scattering from the more concentrated samples of these particles, shown in Figure 3.3, shows that an excluded volume shell is required in the structure factor model to account for the non-hard-sphere interactions. Table 3.4 shows the parameters used to fit the USANS data for the 260 nm spheres. The additional excluded volume shell required to fit the suspension USANS data is 14.6-18.7 nm, or about 5.6-7.2% of the particle radius. In addition, the model does not fit the data particularly well at the highest concentration, particularly at the nearest neighbor peak in the structure factor, where the peak is at lower q than the liquid structure factor model. This deviation is due to crystallization of this particular sample – the liquid structure factor model does not fit well to the crystalline order of the actual sample.

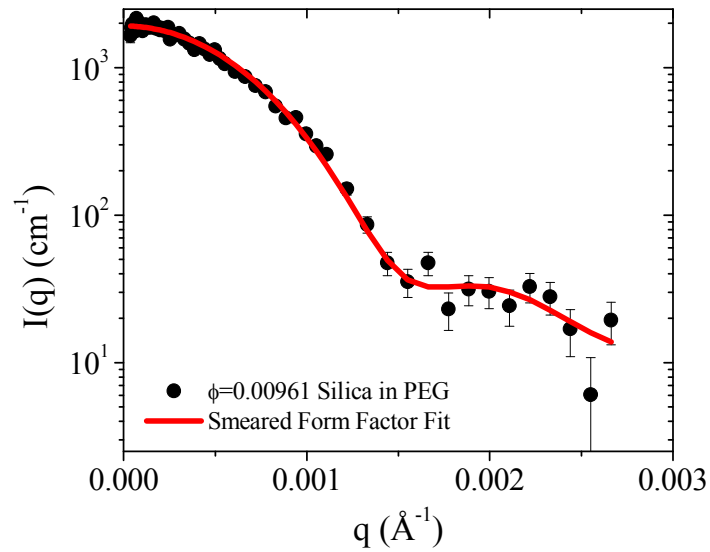


Figure 3.2 Static USANS form factor measurement of suspension of 260 nm SiO₂ in PEG with Schultz sphere model fit.

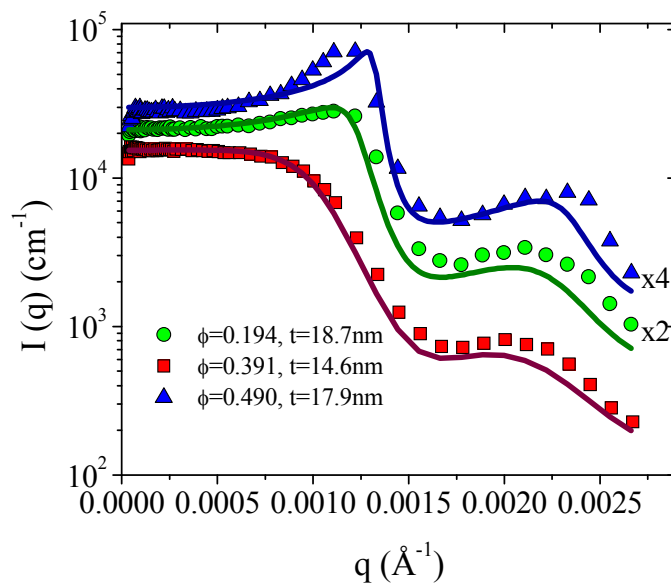


Figure 3.3 Static USANS measurements of suspensions of 260 nm SiO₂ in PEG with core-shell model fits (lines). The data are shifted as noted for clarity of presentation.

Table 3.4 Parameters from USANS fitting of 260 nm silica dispersions.

ϕ_{calc}	0.194	0.391	0.490
ϕ_{eff}	0.24	0.46	0.60
$\rho(\text{SLD, SiO}_2) \times 10^6 \text{ \AA}^{-2}$	2.88	2.76	2.86
$\rho(\text{SLD, PEG/shell}) \times 10^6 \text{ \AA}^{-2}$	0.517	0.517	0.517
Shell Thickness (nm)	18.7	14.6	17.9

Figure 3.4 shows SANS data and model fit for a dilute form factor measurement of the 60 nm particles suspended in D₂O. The volume fraction used in the model was calculated from the densities and weight fraction of silica in the sample and the size and scattering length density were fit. The radius seen from this SANS fit is 60.6 nm, which compares well with the sizes measured via SEM and DLS and seen in Table 3.2. Adding polydispersity into the model did not significantly improve the fit. The fit value of the scattering contrast ($\Delta\rho$) of $1.6 \times 10^{-6} \text{ \AA}^{-2}$ is about half of the expected value of $3.35 \times 10^{-6} \text{ \AA}^{-2}$ (determined from SiO₂ with a density of 1.89 g/mL and D₂O with a density of 1.1 g/mL). This large discrepancy is likely due to settling of the silica particles in the suspension (in D₂O) tested here; settling was observed visually. Since the concentration in the actual measured sample was lower than that used in the model to fit it (equation 2.11), the scattering length density difference in the model must be lower than the actual value to compensate.

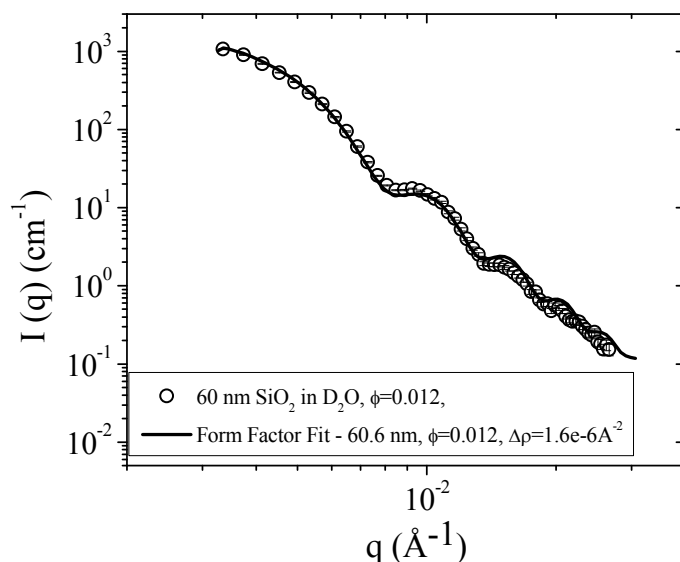


Figure 3.4 Static SANS form factor measurement of suspension of 60 nm SiO₂ in D₂O with Schultz sphere model fit.

Figure 3.5 shows the SANS data for various concentrations of suspensions of the 60 nm particles in PEG-200, along with the form factor measurement in D₂O. A core-shell, hard-sphere model, similar to the one used for USANS fitting (but assuming monodisperse particles), was fit to the highest concentration sample. Only the contrast was adjusted, and the effective volume fraction and shell thickness were assumed to be the same as that fit from the USANS of 260 nm particles at $\phi=0.391$; specifically, the 14.6 nm shell is a relative increase of 5.6% of the radius, which increases the effective volume fraction by a factor of 1.056^3 or 17.8%. The contrast was fit to the highest concentration sample and that value was used to calculate the total scattering model for the other samples. The bottom half of Figure 3.5 shows the structure factors used to fit the total scattering.

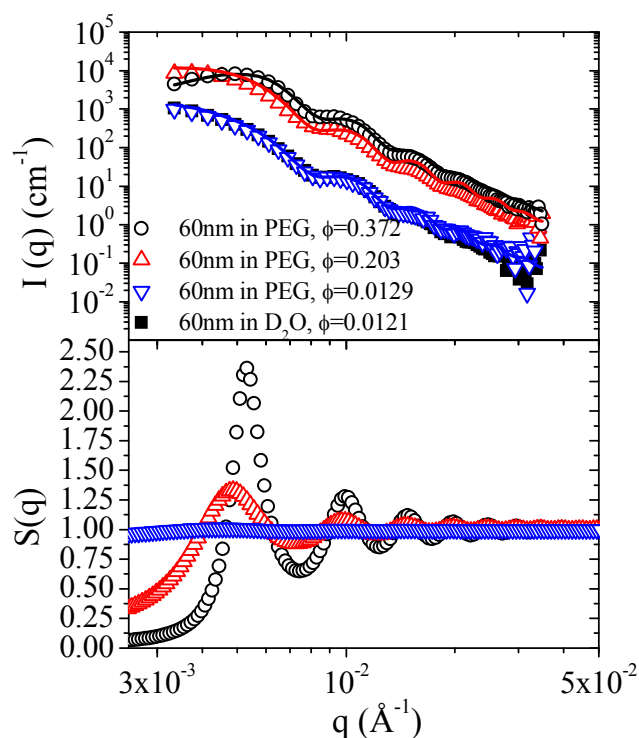


Figure 3.5 Static SANS measurements of suspensions of 60 nm SiO₂ in PEG-200. The lines indicate the instrument-smeared invisible-shell model calculated for the data. The bottom pane shows the structure factor used in the total model above.

The 60 nm particles were seen to have a coating of 6.0 % by weight from TGA experiments (Table 3.1). In addition, this coating appears to be 3.39 nm from the SANS experiments and rheology experiments that will be shown later in this chapter. Unfortunately, due to settling in the D₂O form factor sample, insufficient SANS data, and incomplete knowledge about the exact chemical makeup of the solvent, the silica particle core density cannot be determined directly from the SANS measurements via the scattering length density difference. The density measured from solution densitometry is the particle skeletal density – the mass of the particle core and any

shell divided by the skeletal volume of the particle which does not include the volume inside any pores occupied by fluid or any fluid dispersed in a polymer brush coating. If we assume that the particle core and shell are solid with no solvent penetration, that the core is 60.6 nm radius with a 3.4 nm thick shell, and that the shell is 6.0 % of the weight of the total particle, we find that the relative density of the shell to the core is 0.36. If, for example, the core density was the measured value from densitometry, 1.89 g/mL, the shell density would be 0.68 g/mL, a value much lower than a bulk polymer or the relevant solvents. Therefore, there is likely significant solvent penetration into a sparse coating, as indicated on the left of Figure 3.6, leading to this low estimate of the shell density. Since the solvent is already accounted for, any solvent penetration would lower the calculated shell density. Alternatively, the actual polymer coating is smaller than the measured excluded volume shell, and additional excluded volume shell is needed to account for other non-hard-sphere interactions.

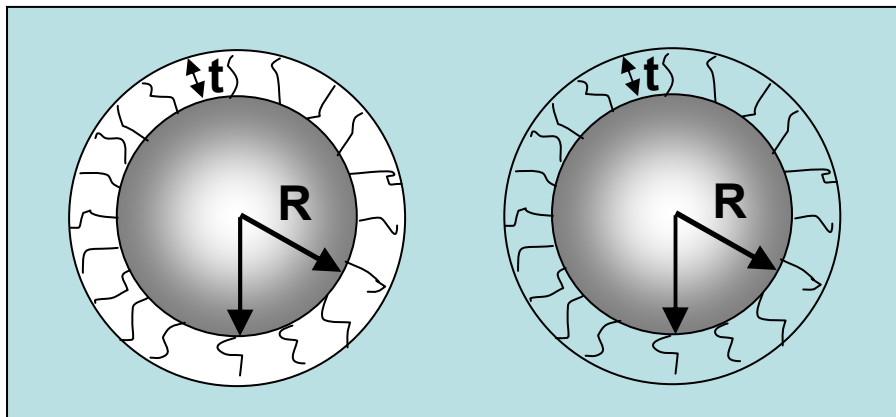


Figure 3.6 Depiction of a particle with surface coating (not to scale). The particle on the left has no solvent penetration and so the polymer density measured would be similar to a bulk polymer. The particle on the right has significant solvent penetration and so the measured particle coating would have a lower density than the bulk polymer.

3.5.2 Dilute Suspension Rheology

For the dilute suspensions up to a volume fraction of about 0.20, the steady-shear rheology is nearly Newtonian; the viscosity is constant with changes in the applied shear stress. The data for the 60 nm and 130 nm particle suspensions in the Newtonian concentration regime are summarized in Figure 3.7 as the reduced viscosity versus concentration, c (grams per milliliter). The data in dilute conditions is expected to follow equation 3.13,

$$\eta_r = 1 + [\eta]c + [\eta]^2 K_H c^2 \quad (3.13)$$

where $[\eta]$ is the intrinsic viscosity, expected to be the Einstein coefficient, 2.5, divided by the particle density, and K_H is the Huggins coefficient (0.94 for hard-spheres) [78], a measure of the interparticle interactions. Often, the $O(c^2)$ term is ignored and the intrinsic viscosity fit to data is compared to the Einstein equation to calculate a hydrodynamic density, ρ_{HD} , from the hydrodynamic volume of the particle, as described by equations 3.14 and 3.15,

$$\eta_r - 1 = [\eta]c, \quad (3.14)$$

and

$$[\eta] = \frac{2.5}{\rho_{HD}}. \quad (3.15)$$

Fits of this type to this data are seen in Figure 3.7, with parameters in Table 3.5. The calculated hydrodynamic density of the 60 nm particles in the mixture of PEG-600 and ethylene glycol is consistent with the prior densitometry measurements, but these particles and the 130 nm particles in PEG-200 show much lower hydrodynamic densities of 1.13 and 1.29 g/mL, respectively. These lower hydrodynamic densities are consistent with an additional excluded volume shell affecting the rheology, consistent with the prior SANS and USANS measurements of the structure.

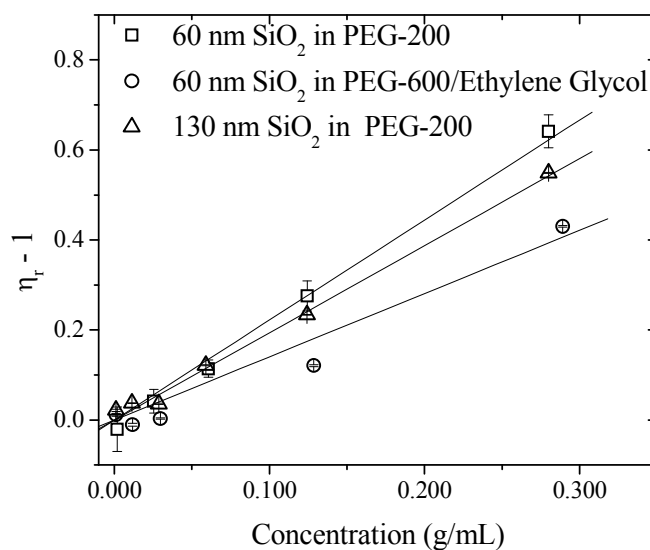


Figure 3.7 Newtonian viscosity measurements of various suspensions.

Table 3.5 Dilute viscosity measurements and fit to Einstein equation.

a (nm)	Solvent	[η] mL/g	ρ_{HD} (g/mL)
60	PEG200	2.2±0.11	1.13±0.06
60	PEG/EG	1.41±0.01	1.78±0.01
130	PEG200	1.94±0.01	1.29±0.01

3.5.3 Steady Shear Viscosity

Shear viscosity measurements were performed on all three particle sizes of silica in multiple solvents. In this section, the steady-shear data are presented as apparent viscosity versus applied stress and apparent viscosity versus apparent shear rate. The data are from cone-and-plate measurement geometries – the effects of wall

slip are investigated further in Appendix B. The Péclet number, included on a second axis, is a dimensionless shear rate, as discussed previously in section 3.2, which requires normalization by particle size; the particle size used in these calculations is the SANS measurement of 60 nm for the smallest particles, the average SEM/DLS size of 130 nm for the middle particle size, and the USANS measurement of 260 nm for the largest particles. These sizes were chosen as the SANS and USANS measures are in the actual solvents, and the goal of the rheological characterization is to provide background characterization for the microstructural measurements shown in Chapters 4 and 5. The SEM and DLS measurements for the middle particle size are consistent, and so that value of 130 nm is used due to a lack of any neutron scattering size measurement. In addition, only the rheology of the particles suspended in PEG-200 is shown here. The effects of suspending medium viscosity will be discussed in more detail in section 3.5.4. In addition, the critical stresses for shear thickening will be summarized in 3.5.5.

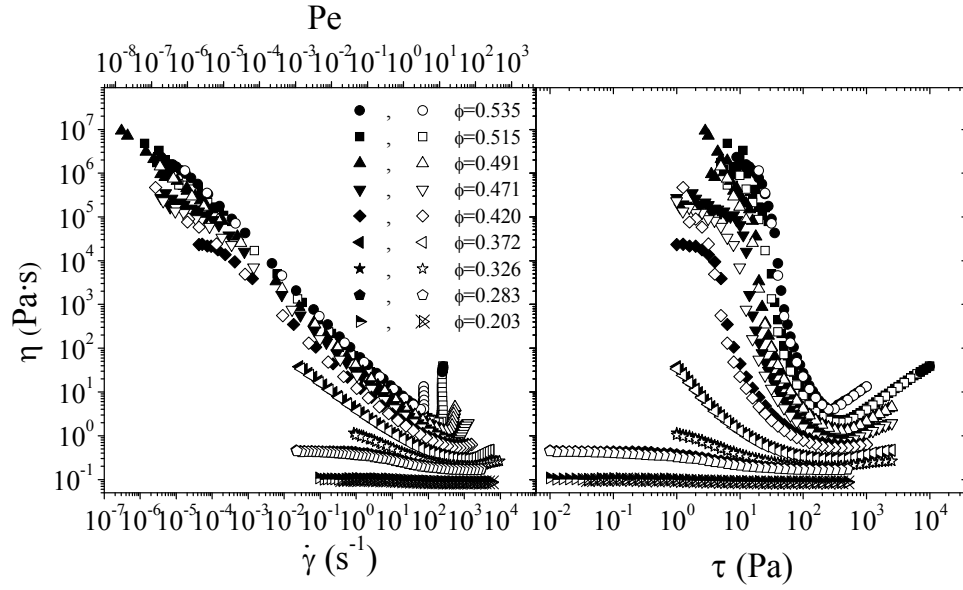


Figure 3.8 Steady-shear rheology of 60 nm silica dispersions in PEG-200 as viscosity versus shear rate and Péclet number on left and viscosity versus shear stress on the right. The microstructure of these suspensions is studied in depth in Chapter 4. Filled symbols are forward sweeps and open symbols are backward sweeps.

Figure 3.8 shows the steady shear rheology data for 60 nm silica dispersions in PEG-200. Non-Newtonian behavior is observed for volume fractions of 0.203 and above, with increasing severity of shear-thinning with increasing volume fraction. Shear-thickening is first observed experimentally at $\phi=0.326$, with increasing severity with increasing volume fraction, leading to discontinuous shear thickening at $\phi=0.515$.

A zero-shear viscosity is measured for volume fractions of 0.283 and below. The $\phi=0.326$ sample shows low-shear behavior indicative of a zero-shear viscosity, but the measurement range did not achieve low enough stresses to measure the zero-shear viscosity. Above this volume fraction, the samples show an apparent

yield stress, which manifests itself as an increased viscosity at low stresses and can be large enough to give multiple orders of magnitude drop in the measured viscosity with only a doubling in shear stress. More exactly, shear thinning will have a power law decrease in viscosity as a function of shear rate with a slope no greater than negative one; slopes with larger magnitude are due to the presence of the yield stress. The negative slope having a magnitude greater than one indicates this low shear rheology is likely yielding with slip at the lowest stresses, studied further later in this section [71]. From the location on the viscosity versus stress plot of the vertical drop in viscosity, the yield stress values appear to be on the order of 3-40 Pa. The presence of the yield stress indicates some additional interactions beyond simple hard-sphere excluded volume interactions.

Experiments with systematically increasing applied shear stress are shown, as are experiments directly following with systematically decreasing shear stress. Little hysteresis is seen between these measurements, with the exception of some higher concentration samples at low shear stresses where it is likely slip is being measured rather than the assumed linear velocity profile. This effect is discussed further in Appendix B. The microstructure of similar suspensions is studied in detail in Chapter 4.

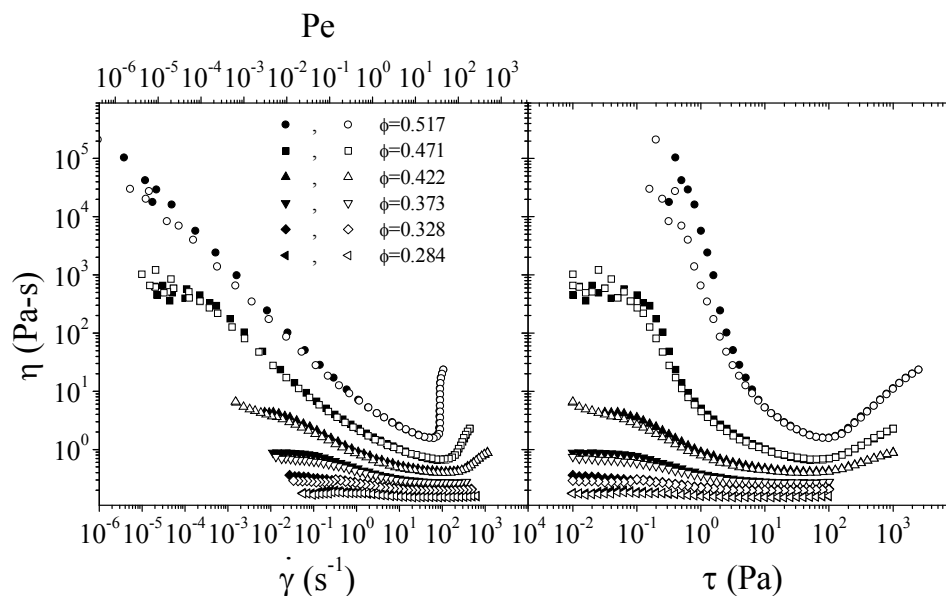


Figure 3.9 Steady-shear rheology of 130 nm silica dispersions in PEG-200 as viscosity versus shear rate and Péclet number on left and viscosity versus shear stress on the right. Filled symbols are forward sweeps and open symbols are backward sweeps.

Figure 3.9 shows the steady shear rheology data for suspensions of the 130 nm particles in PEG-200. Once again, there is relatively little hysteresis at all volume fractions, with the exception of a difference in the low shear behavior between forward and backward sweeps at volume fractions of 0.422 and above caused by the presence of a yield stress. From the low-shear behavior seen in the left pane of Figure 3.9, specifically the nearly vertical drop in viscosity with a slope less than negative one, the yield stress appears to be about 0.1 Pa for the $\phi=0.471$ sample and about 1.0 Pa for the $\phi=0.517$ sample. Once again, these suspensions show discontinuous shear thickening at $\phi=0.517$.

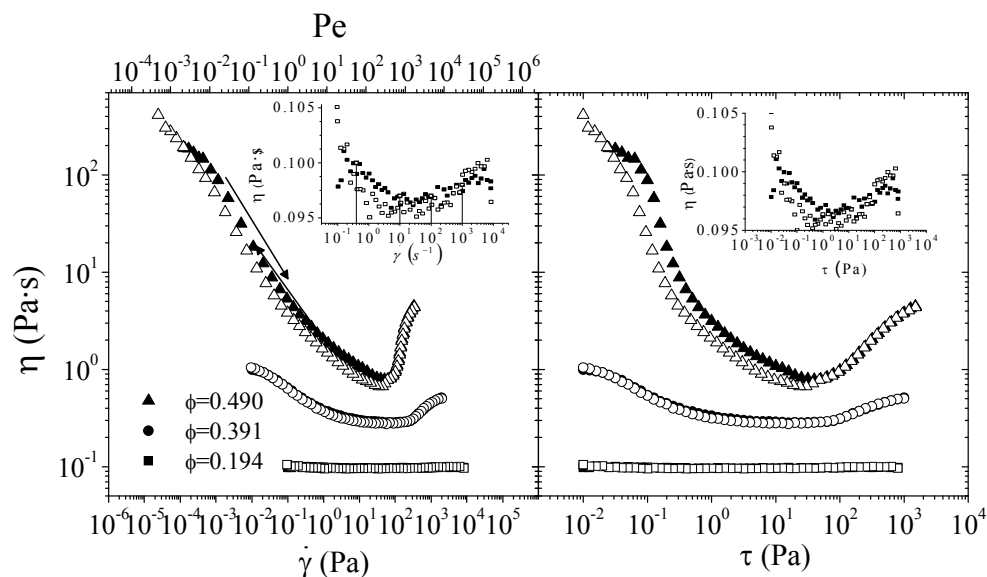


Figure 3.10 Steady-shear rheology of 260 nm silica dispersions in PEG-200 as viscosity versus shear rate and Péclet number on left and viscosity versus shear stress on the right. These samples were used for USANS measurements seen in Chapter 5. Filled symbols are forward sweeps and open symbols are backward sweeps.

Figure 3.10 shows the steady shear rheology data for suspensions of the 260 nm silica in PEG-200. It can be seen that these three concentrations show very little hysteresis in the forward and backward sweeps. The highest concentration sample has a volume fraction of 0.490 and shows two orders of magnitude decrease in viscosity from a shear rate of 10^{-5} s^{-1} to the shear rate of 10 s^{-1} , followed by an order of magnitude increase in the viscosity over a change in the shear rate from 100 to 400 s^{-1} . The middle concentration sample at $\phi=0.391$ shows a decrease in viscosity by a factor of five followed by a similar increase in the viscosity. The lowest concentration sample at $\phi=0.194$ appears Newtonian on this logarithmic scale in viscosity, but does exhibit both thinning and thickening of about 5%, as seen in the inset plot. The

microstructural changes of these specific samples under shear are studied in more detail in Chapter 5. In addition, the use of these suspensions in woven fabric armor composites is discussed in Chapter 7. A more complete volume fraction series of these suspensions was studied by Egres [16].

Figure 3.11 shows a fit of the data to the Cross model (equations 3.2 or 3.4) for the 60 nm particle dispersions. The presence of the yield stress at high concentration manifests as a vertical line on this plot of reduced viscosity versus reduced stress; the model viscosity is assumed to be infinite below the yield stress and the measured apparent viscosity comes from slip or other deviations from the expected kinematics.

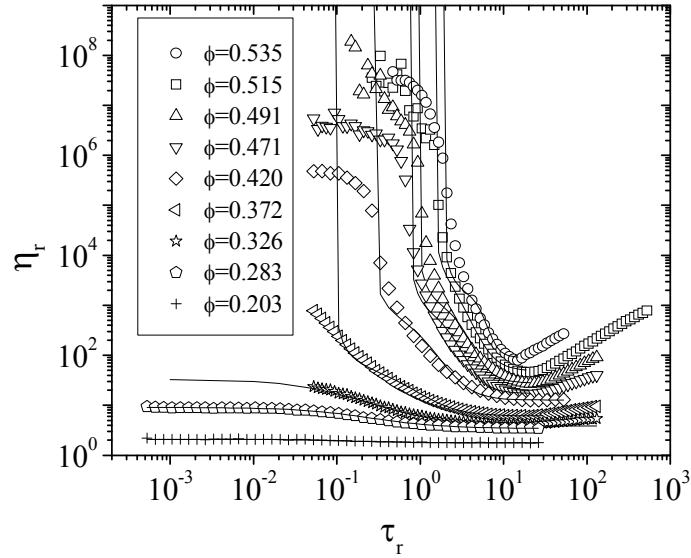


Figure 3.11 Steady shear data and fits to Cross model for 60 nm particle suspensions.

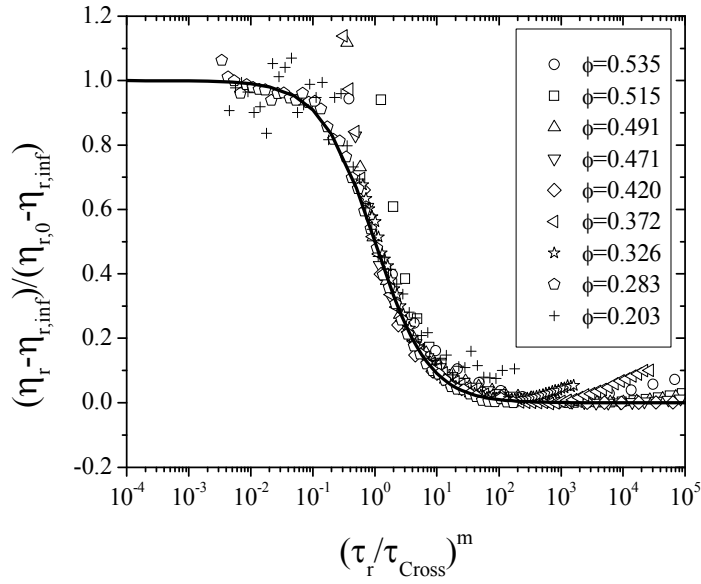


Figure 3.12 Reduction of data using Cross model for 60 nm particle suspensions.

Figure 3.12 shows the data reduced onto the Cross model using the fit parameters. Overall, the data collapses onto the model well, with deviations primarily for high concentration samples both at low stresses due to the yield stress and at high stresses due to the shear thickening.

Table 3.6 shows a summary of the fitting parameters for the 60 nm particle suspensions. The parameters in Table 3.6, $\eta_{r,\infty}$, $\eta_{r,0}$, τ_{Cross} , and m , come from the fitting described in section 3.4.2. The $\eta_{r,\infty}$ -prediction and $\eta_{r,0}$ -prediction are calculated from the Quemada relation, equation 3.5, where ϕ_m is 0.71 in the infinite shear case and 0.63 in the zero shear case. The values for the effective volume fraction, ϕ_{eff} , are calculated using the fit values of η_r with equation 3.5, working backwards to find the effective volume fraction that corresponds to that reduced viscosity. The effective volume fractions are all above the calculated volume fraction from the relative weight fractions and particle and solvent densities, except for the lowest concentration sample. Also

calculated is the shell thickness required to account for that volume fraction difference, t , based either on the zero shear or infinite shear viscosity. The effect of volume fraction and particle size on these parameters will be discussed in more detail below, after the fits of 130 and 260 nm particle suspensions are presented.

Table 3.6 Fitting parameters and results from Cross model fits to rheology of 60 nm silica spheres in PEG-200.

a (nm)	60	60	60	60	60	60	60	60	60
ϕ	0.203	0.283	0.326	0.372	0.42	0.471	0.491	0.515	0.535
$\eta_{r,0}$	2.10	9.05	33	40.	370	370	540	1430	890
$\eta_{r,\infty}$	1.8	3.4	3.8	6.1	13	17	27	46	79
τ_{Cross}	0.147	0.154	0.082	0.611	0.966	2.24	2.99	2.78	5.37
m	1	1	1	1.9	2.8	3.9	4.2	3.9	7
$\tau_{r, \text{yield}}$	0	0	0	0.09	0.26	0.74	0.93	1.48	1.86
τ_{yield} (Pa)	0	0	0	1.78	5.01	14.1	17.8	28.2	35.5
$\eta_{r,0}$ -prediction	2.18	3.30	4.29	5.96	9.00	15.7	20.5	30.0	44.0
$\eta_{r,\infty}$ -prediction	1.96	2.76	3.42	4.41	5.99	8.83	10.5	13.3	16.5
$\phi_{\text{eff},0}$	0.195	0.421	0.520	0.53	0.60	0.60	0.60	0.61	0.61
$\phi_{\text{eff},\infty}$	0.17	0.33	0.35	0.42	0.51	0.54	0.57	0.61	0.63
$\phi_{\text{eff},0}/\phi$	0.960	1.49	1.60	1.4	1.4	1.3	1.2	1.2	1.1
$\phi_{\text{eff},\infty}/\phi$	0.85	1.2	1.1	1.1	1.2	1.1	1.2	1.2	1.2
t_0 (nm)	-0.77	8.47	10.1	7.5	7.5	4.9	4.3	3.6	2.7
t_∞ (nm)	-3.1	3.0	1.2	2.6	4.0	6.6	8.0	8.3	8.4

Table 3.7 includes parameters from fitting of the 130 and 260 nm silica, fits of which are shown in Figures 3.13 and 3.15, with reduction onto the master curve in Figures 3.16 and 3.18. The yield stress, seen for volume fractions of 0.372 and above in the 60 nm particle suspensions, are only seen for volume fractions of 0.471 and above with the 130 nm suspensions and only at the highest volume fraction, 0.490 for the 260 nm suspensions. Overall, the model fitting collapses the data well, with the exception of the samples with a yield stress at stresses below the yield stress and

samples that shear thicken above the onset of shear thickening. It is also important to note that the critical stress used to collapse the data from the shear thinning portion of the rheology does not determine the onset of shear thickening – thickening is clearly seen for all three particle sizes to begin at different locations on the high stress portion of the master curve seen in Figures 3.13, 3.15, and 3.17.

As a limited measure of the error on the parameters in these fits, the parameters were systematically adjusted to determine the effect on the goodness of fit (chi-squared or χ^2). For the dilute suspensions, adjusting the infinite shear viscosity by merely 5% caused a 30% change in chi-squared. Adjusting the zero-shear viscosity by 5% caused an even larger change in chi-squared of about 500%. In addition, adjusting the exponent, m , by 5-10% does not significantly decrease the quality of fit for non-yielding samples. For samples with a yield stress, m is quite insensitive and the fit quality remains the same in some cases for variations in m up to about 30%. In addition, the yield stress as estimated here certainly appears to provide a lower bound for the actual yield stress. Increasing the model yield stress parameter by a factor of two or three could certainly improve the fit, albeit over a smaller portion of the curve. In addition, the fits can be improved slightly if the cross model shear thinning critical stress is fit to the data rather than being calculated based on the infinite and zero-shear viscosities and the data.

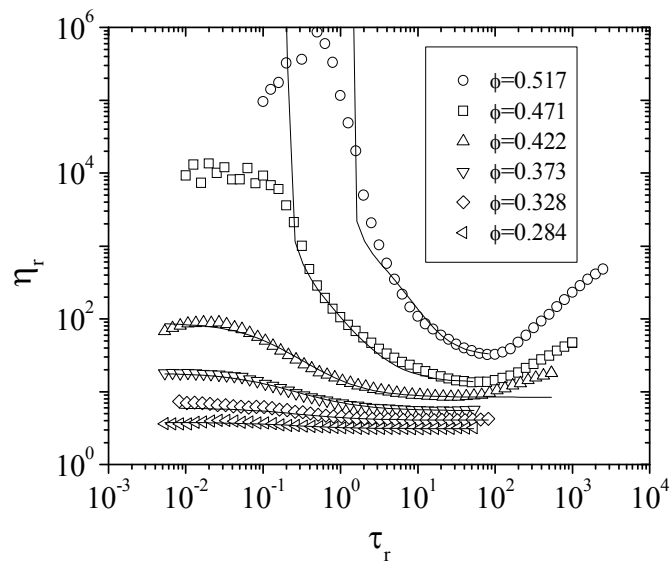


Figure 3.13 Steady shear data and fits to Cross model for 130 nm particle suspensions.

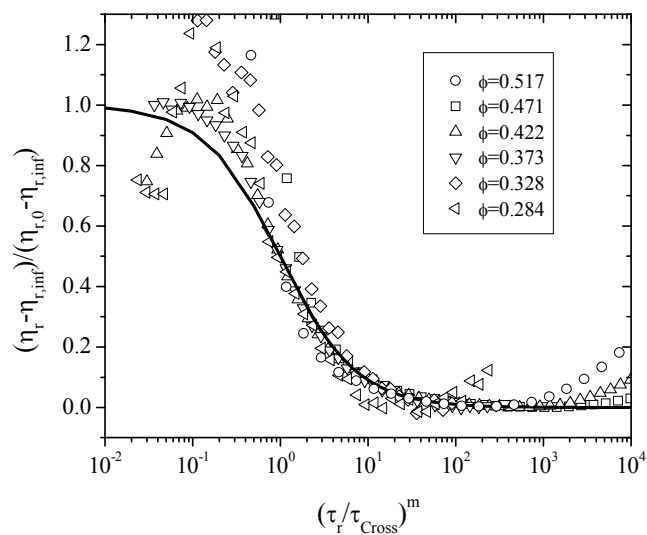


Figure 3.14 Reduction of data using Cross model for 130 nm particle suspensions.

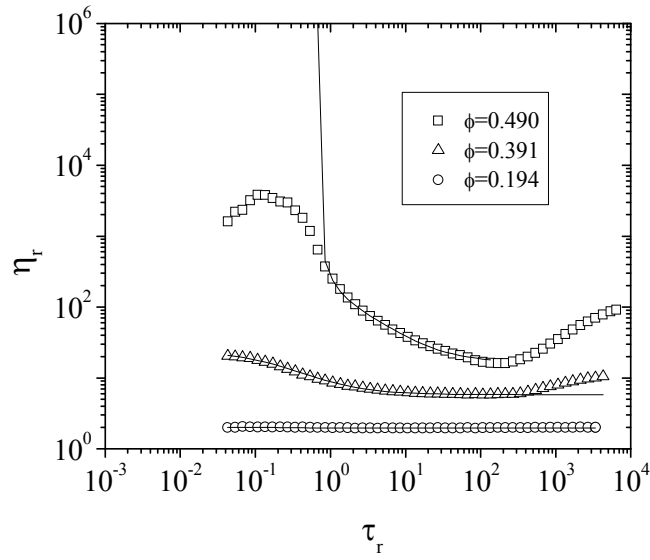


Figure 3.15 Steady shear data and fits to Cross model for 260 nm particle suspensions.

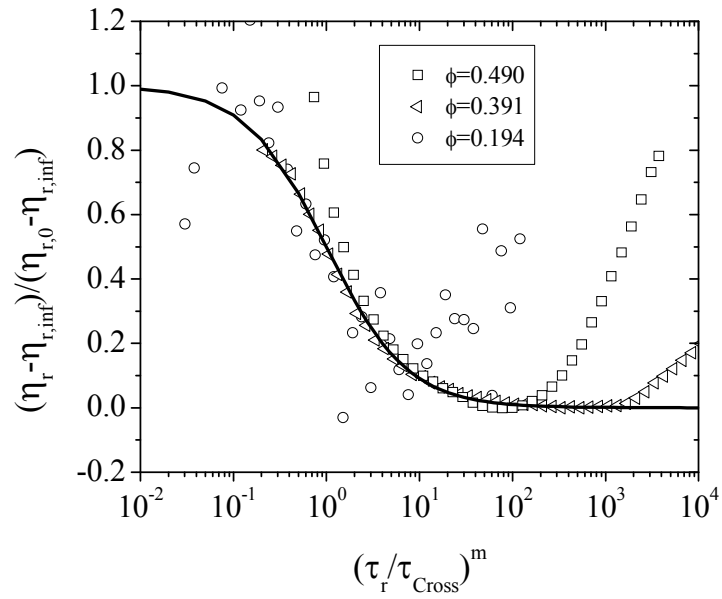


Figure 3.16 Reduction of data onto Cross model for 260 nm particle suspensions.

Table 3.7 Fitting parameters and results from Cross model fits to rheology of 130 nm and 260 nm silica spheres in PEG-200.

a (nm)	130	130	130	130	130	130	260	260	260
ϕ	0.283	0.326	0.372	0.422	0.471	0.517	0.194	0.391	0.490
$\eta_{r,0}$	3.81	6.00	18.1	88	380	500	2.03	24	110
$\eta_{r,\infty}$	3.1	4.1	5.5	8.4	13	31	2.0	5.8	16
τ_{Cross}	0.224	0.227	0.146	0.113	0.364	4.79	1.41	0.201	2.86
m	1	1	1	1.15	1.4	2.0	1	1	1.07
$\tau_{r, \text{yield}}$	0	0	0	0	0.21	1.30	0	0	0.677
τ_{yield} (Pa)	0	0	0	0	0.39	2.43	0	0	0.158
η_{r0} -prediction	3.30	4.29	5.96	9.00	15.7	31.1	2.09	6.95	20.3
$\eta_{r\infty}$ -prediction	2.76	3.42	4.41	5.99	8.83	13.5	1.89	4.95	10.4
$\phi_{\text{eff},0}$	0.307	0.373	0.482	0.563	0.60	0.60	0.187	0.50	0.57
$\phi_{\text{eff},\infty}$	0.31	0.36	0.41	0.47	0.52	0.58	0.20	0.42	0.53
$\phi_{\text{eff},0}/\phi$	1.09	1.14	1.30	1.3	1.3	1.2	0.97	1.3	1.2
$\phi_{\text{eff},\infty}/\phi$	1.1	1.1	1.1	1.1	1.1	1.1	1.1	1.1	1.1
t_0 (nm)	3.63	5.95	11.7	13	11	6.8	-3.00	22	13
t_{∞} (nm)	4.2	4.8	4.6	5.2	4.6	6.1	2.3	3.0	4.4

Figure 3.17 summarizes the zero shear and infinite shear viscosities obtained from the fitting of all three particle size suspensions in PEG-200. These viscosity values are relative viscosities – the fitting was done on relative viscosity curves normalized by the measured viscosity of PEG-200 of 0.049 Pa-s. Open symbols are the zero-shear viscosity from samples that did not exhibit a yield stress (fit to equation 3.2). Half-filled symbols are the zero-shear viscosity determined from fitting on samples in the presence of a yield stress (fit to equation 3.4), and so are not directly measured. The filled symbols are the infinite shear viscosity (from fitting to either equation 3.2 or 3.4). Also included are predictions from equation 3.5 and equation 3.6; equation 3.5 with ϕ_m set to 0.63 and 0.71 are expected to predict the hard-sphere zero-shear and infinite-shear viscosity, respectively [49]. The lines clearly under predict the low shear viscosity as a function of the volume fraction from the density

measurements, but the Quemada equation accurately predicts the infinite shear viscosity.

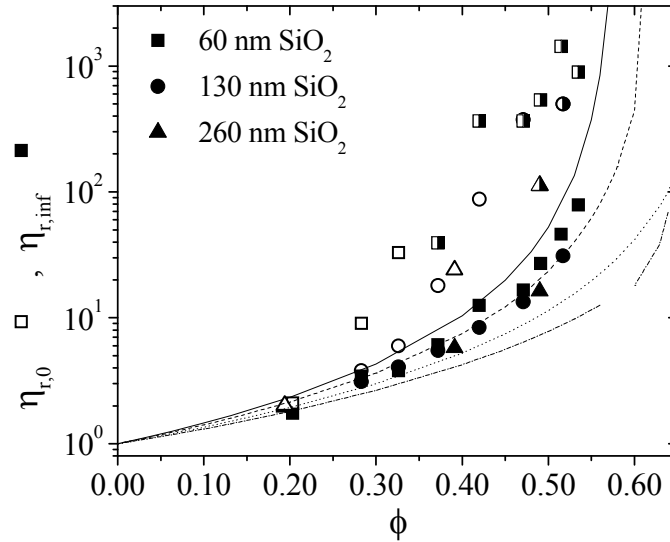


Figure 3.17 Summary of zero and infinite shear viscosities from Cross model fitting compared based on calculated volume fraction. The top three lines are equation 3.5 with ϕ_m of 0.58, 0.63, and 0.71, respectively; the bottom line is equation 3.6. Half-filled symbols are the estimated zero-shear viscosity obscured by the presence of a yield stress.

Figure 3.18 shows the same data as a function of the effective volume fraction determined from USANS and SANS as discussed in section 3.5.1. The fits of the USANS data (Figure 3.3) for the 260 nm particles and the SANS data (Figure 3.5) on the 60 nm particles yield an excluded volume corresponding to a surface layer thickness equal to 5.6% of the particle radius. No such measurements were performed on the 130 nm particles, but based on these results and the homologous similarity of the different particle sizes, we assume a proportional surface layer. The volume

fraction calculated under the assumption of this surface layer (which increases the effective volume fraction by 17.8%) will be referred to as ϕ_{eff} . Improved correlation between the fit data and the model for the zero-shear viscosity is observed. These measurements are consistent with the idea of short range repulsive interactions in these near hard-sphere suspensions. In the case of short range repulsive interactions, the low shear data is expected to follow the effective volume fraction scaling, but the additional excluded volume does not contribute to the high shear viscosity [29].

These deviations between the data and expected values indicate that while this correction improves the fit generally, the rheological excluded volume at low shear appears higher than that seen in USANS or at high shear. Alternatively, presence of a weak, immeasurable yield stress due to increased interparticle attractions in the smallest size particles could lead to an overestimation of the zero-shear viscosity. A third option is that the effect of the polymer layer is greater at low shear, which makes sense as a polymer layer would likely be compressed under high stresses, at least along the compression axis and in the direction of greatest stress transmission. Since the measurement of the excluded volume layer in SANS is at equilibrium, it would measure the uncompressed zero-shear layer. At higher volume fractions, where the yield stress is seen, a shift from the curve with maximum packing set at 0.58 towards the curve with maximum packing set at 0.63 is seen. This result is similar to the way other hard-sphere properties transition in their divergence at high concentration due to the structural change from disordered fluid to ordered solid (see, for example, the divergence of the osmotic compressibility in Figure 10.5 in Russel [49]).

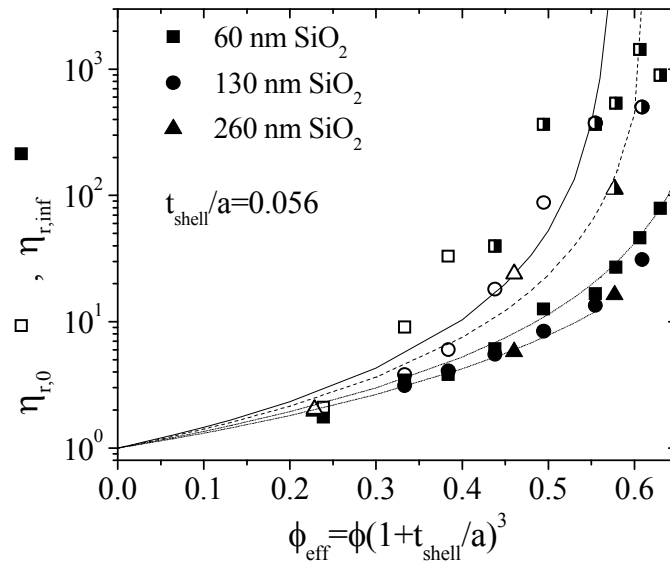


Figure 3.18 Summary of zero and infinite shear viscosities from Cross model fitting compared based on volume fraction with an additional excluded volume shell scaled for the particle radius. The top three lines are equation 3.5 with ϕ_m of 0.58, 0.63, and 0.71, respectively; the bottom line is equation 3.6.

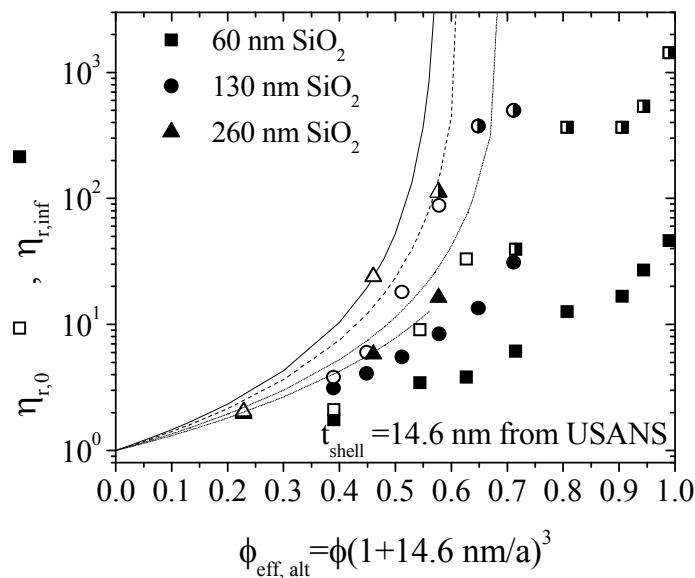


Figure 3.19 Summary of zero and infinite shear viscosities from Cross model fitting compared based on an alternate effective volume fraction with the assumption of an excluded volume shell of constant thickness for all three particle sizes. Shell thickness value used as 14.6 nm from USANS measurements on 260 nm particles at $\phi=0.396$. The top three lines are equation 3.5 with ϕ_m of 0.58, 0.63, and 0.71, respectively; the bottom line is equation 3.6.

If the additional excluded volume seen in SANS and USANS was completely caused by an adsorbed polymer layer, one might expect that the polymer coating would be the same thickness for each case. Figure 3.19 shows the infinite and zero-shear viscosity data from the fitting compared to the effective volume fraction determined from this assumption that all particle sizes have the same excluded volume layer of 14.6 nm, as seen in the USANS measurements of 260 nm spheres at $\phi=0.391$. We will refer to this alternative effective volume fraction as $\phi_{\text{eff,alt}}$. This type of

correlation clearly is unrealistic for the 60 or 130 nm particles as the effective volume fractions calculated far exceed maximum packing for hard spheres. The neutron scattering data and the rheology data are consistent with the hypothesis that the thickness is a function of the particle size and is approximately a constant fraction of the radius for all three particle sizes. This result implies that either the polymer layer used is designed to be a variable thickness and constant as a function of radius, or that the additional excluded volume accounts for both a polymer layer, which is less than the total shell thickness, and additional interactions such as electrostatics and Van der Waals dispersion forces.

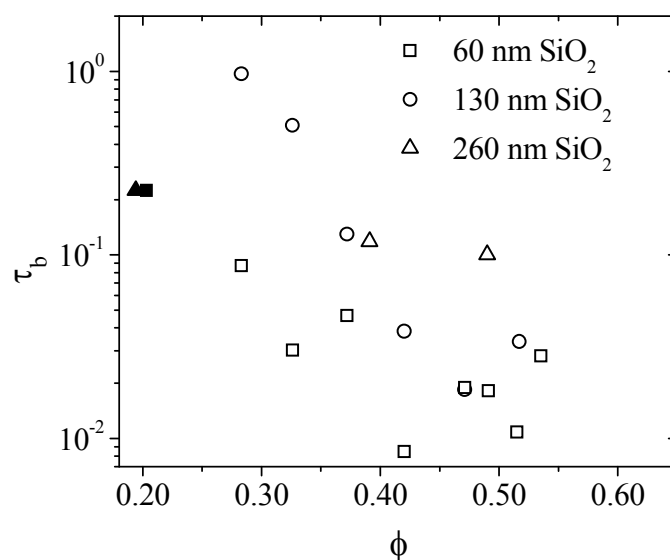


Figure 3.20 Values of the Baxter sticky parameter, τ_b , determined from fitting to the zero shear rheology.

An alternate assumption for the interparticle interactions would be a short range attraction, which could be characterized by the Baxter sticky potential. Figure 3.20 shows the Baxter sticky parameters (τ_b) determined from the zero-shear viscosity data under the assumption of the sticky hard-sphere potential, where the open symbols are calculated using equation 3.8 and the closed symbols are calculated using equation 3.7 as equation 3.8 gave unrealistic negative values of τ_b . In general, equation 3.8 gives values of τ_b 1-2 orders of magnitude lower than equation 3.7. Regardless, the large variations in the values of τ_b indicate that the sticky hard-sphere potential is unlikely to compensate for the deviations from hard-spheres.

An alternative method of evaluating the infinite and zero shear viscosity data relative to that from hard spheres is to use these viscosity data in equation 3.5 to calculate an effective volume fraction directly. Figure 3.21 shows the effective volume fraction (from equation 3.5) consistent with the fit value of either the infinite or zero shear viscosity (as shown in Figures 3.18 and 3.19 and Tables 3.6 and 3.7), normalized by the volume fraction, as a function of volume fraction (ϕ_{eff}/ϕ as a function of ϕ). At the lowest volume fractions, there are some values less than one based on the zero shear viscosity, as the zero shear viscosity for these samples was slightly less than the hard-sphere expected value. At the higher volume fractions, all the values are greater than 1.05, with a slight trend towards positive values with increasing volume fraction. With the presence of the yield stress (half filled symbols), the deviation decreases with increasing volume fraction.

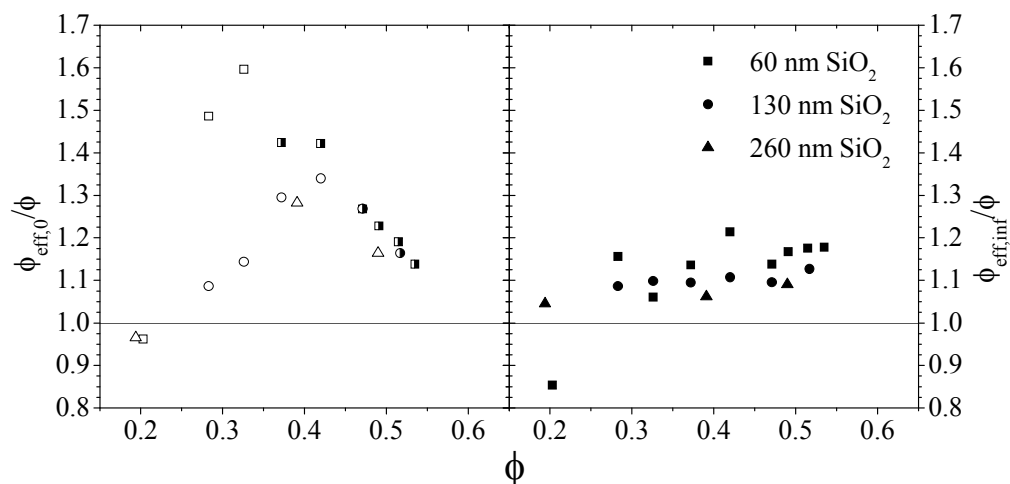


Figure 3.21 Deviation in effective volume fraction calculated from zero or infinite shear viscosity, relative to volume fraction. Half-filled symbols are from the zero shear viscosity in the presence of a yield stress. The line set at one is included to guide the eye.

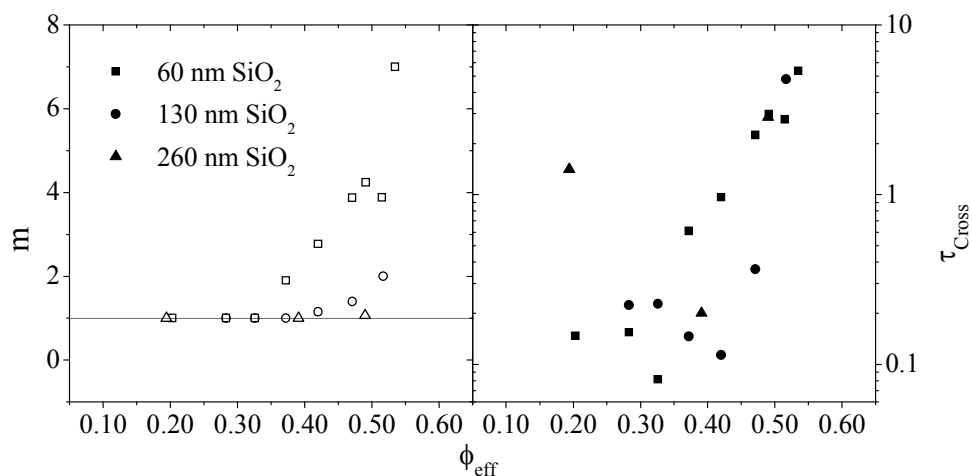


Figure 3.22 Cross model exponent m and critical stress τ_{Cross} plotted against the effective volume fraction using the 5.6% layer thickness excluded volume shell. The line set at one is included to guide the eye.

Figure 3.22 shows the Cross model exponent m and the Cross model critical stress for shear thinning, τ_{Cross} , plotted against the effective volume fraction as discussed above using the 5.6% shell thickness seen in SANS and USANS experiments. The exponent m is not changed from the hard-sphere value of one for values of the effective volume fraction below 0.35, as adjusting m does not improve the fit. At volume fractions above 0.35, m begins to rise monotonically with increasing volume fraction.

The Cross model critical stress for shear thinning generally is between 0.8 and 0.5 for effective volume fractions below about 0.35 as well, and also systematically rises at high volume fraction. In fact, on the semi-log plot in τ_{Cross} , there is a linear increase in $\log(\tau_{\text{Cross}})$ with increases in ϕ_{eff} . This result is also consistent with that seen for hard-sphere and near hard-sphere suspensions [49, 72], although no simple correlation exists to predict either m or τ_{Cross} .

The yield stress values are plotted in Figure 3.23 and also follow similar behavior as τ_{Cross} and m , having low values at low volume fractions and increasing at high volume fractions. Specifically, there is no yield stress for suspensions at an effective volume fraction below 0.40, and then the yield stress grows regularly as the concentration approaches maximum packing. The yield stress data for the 60 nm suspensions was fit to a power-law model,

$$\tau_{\text{yield}} = Y (\phi_{\text{eff}} - \phi_{y,\text{min}})^p, \quad (3.16)$$

where Y is the yield stress correlation prefactor, p is the yield stress correlation exponent, and $\phi_{y,\text{min}}$ is the minimum effective volume fraction required for yielding. This fit gave a value of $\phi_{y,\text{min}}$ of 0.283, an exponent p of 3.94, and a value of Y of 122.

The 130 and 260 nm suspensions are seen to exhibit similar behavior with a slightly larger value of $\phi_{y,min}$.

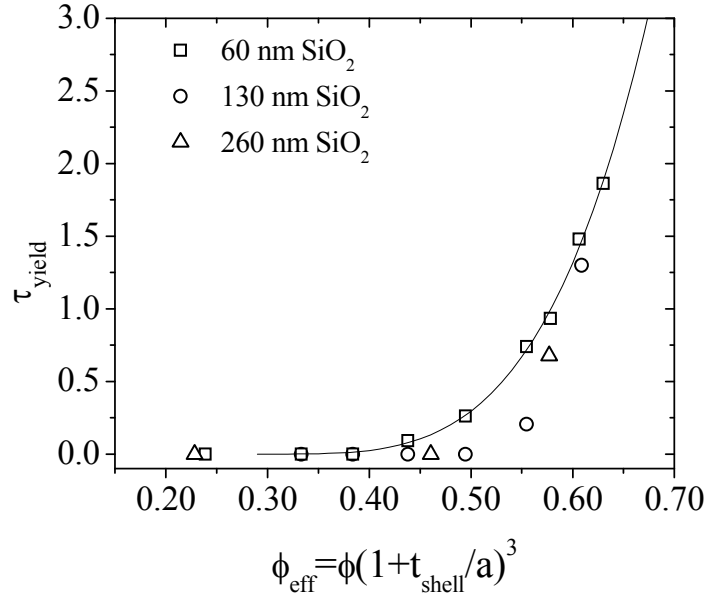


Figure 3.23 Values of the yield stress (dimensionless) plotted against the effective volume fraction using the 5.6% layer thickness excluded volume shell, for three sizes of silica sphere dispersions. The line is a fit to power-law increase in yield stress with changes in volume fraction above a minimum value.

Finally, we will look at the simplest analysis of the effect of particle size on the rheology for the three chemically analogous suspensions, which will include the shear thickening component unlike the hard-sphere mapping discussed above. In the above work, we attempted to compare the rheology of dispersions of different particle size and volume fraction based on fitting of a critical stress for shear thinning. Here, we will compare the rheology directly on scales of shear stress, shear rate, and Péclet

number. For simplicity, we will only look at the steady state sweeps at decreasing stress as the difference between ascending and descending sweeps has already been discussed.

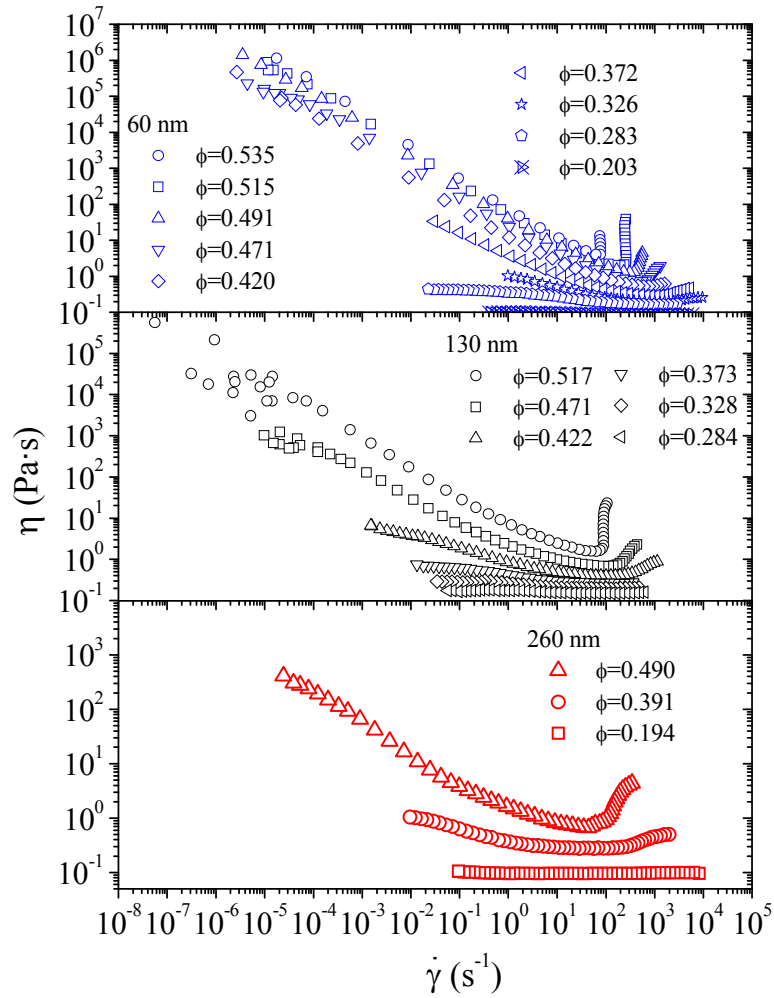


Figure 3.24 Steady-shear rheology data for suspensions of three sizes of spherical silica particles on a common shear rate axis.

Figure 3.24 shows the steady shear rheology for dispersions of all three particle sizes of silica in PEG-200 on a common x-axis of shear rate for comparison. The separate panes show the different particle sizes as indicated, with the smallest particles on top and largest particles on bottom. At a constant volume fraction, the critical shear rate for thickening increases with decreases in particle size. In addition, the critical rate decreases with increasing volume fraction at a constant particle size.

As the shear thickening is typically expected to be controlled by stress [15, 19, 20], Figure 3.25 compares the steady state rheology for the various suspensions as a function of applied stress on a common x-axis. This figure shows that the critical shear stress for thickening increases with decreasing particle size. In addition, there is no systematic change on this graph in the critical shear stress with respect to volume fraction at a particular particle size. Additional work on the critical stress and shear rate for shear thickening is shown as section 3.5.5.

Figure 3.26 shows the same data on the common Péclet axis and Figure 3.27 shows selected data from all three particle sizes overlaid on one graph of viscosity versus Péclet number. The Péclet number has been determined using the nominal size, but the results will not change qualitatively if the size is increased by including the effect of the particle shell proportional to the radius discussed previously – all the Péclet values will shift by a factor of the relative shell thickness cubed, or 17.8 %. It is clear from this figure that a single critical Péclet number does not describe the onset of shear thickening, and in fact overcompensates for the effect of particle size on the onset of thickening. The latter point is clearly shown by Figure 3.27, which shows the smallest particles, which thickened at the highest shear rate, now thicken at the lowest Péclet number. From this graph, it is also apparent that the severity of the

measured shear thinning (magnitude of the drop in viscosity) increases with a decrease in the particle size. That result is consistent with the increase in the yield stress values with decreasing particle size shown in Figure 3.23, and also manifests as larger values of the shear thinning exponent for smaller particle sizes shown in Figure 3.22, as well as Tables 3.6 and 3.7.

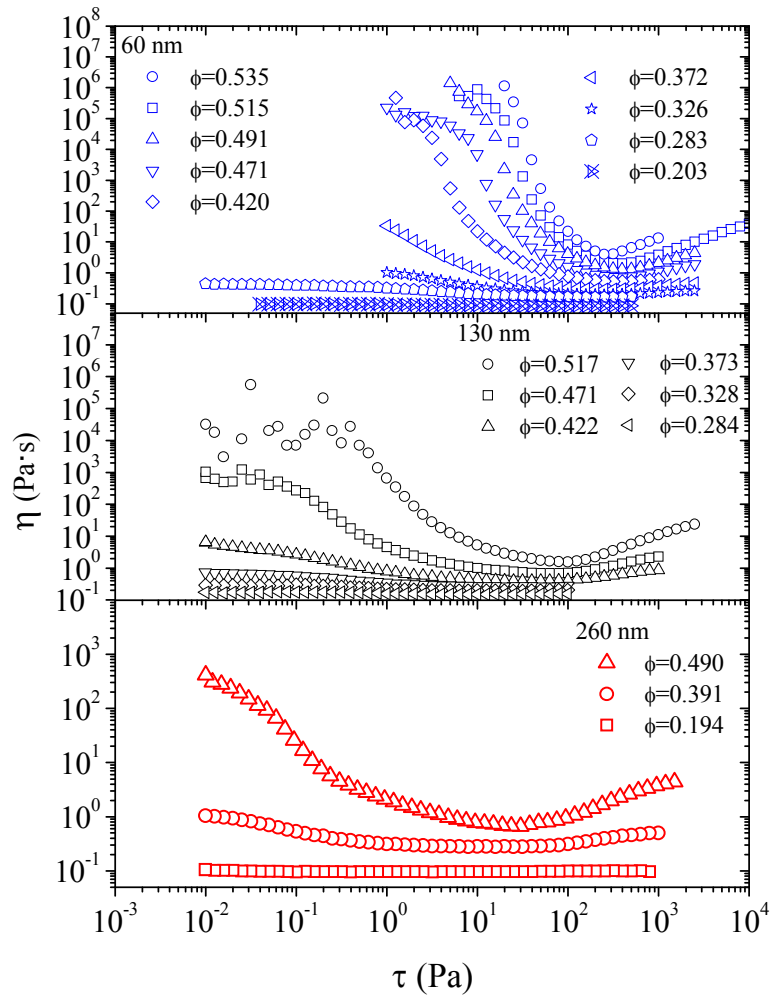


Figure 3.25 Steady-shear rheology data for suspensions of three sizes of spherical silica particles on a common shear stress axis.

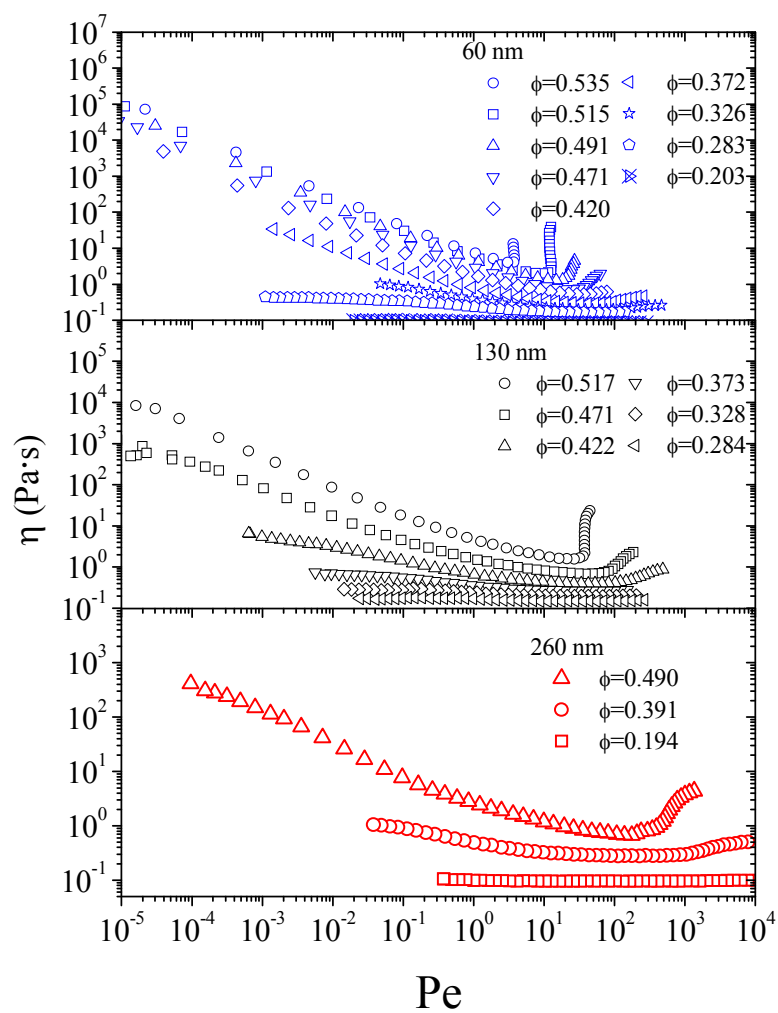


Figure 3.26 Steady-shear rheology data for suspensions of three sizes of spherical silica particles on a common axis of Péclet number.

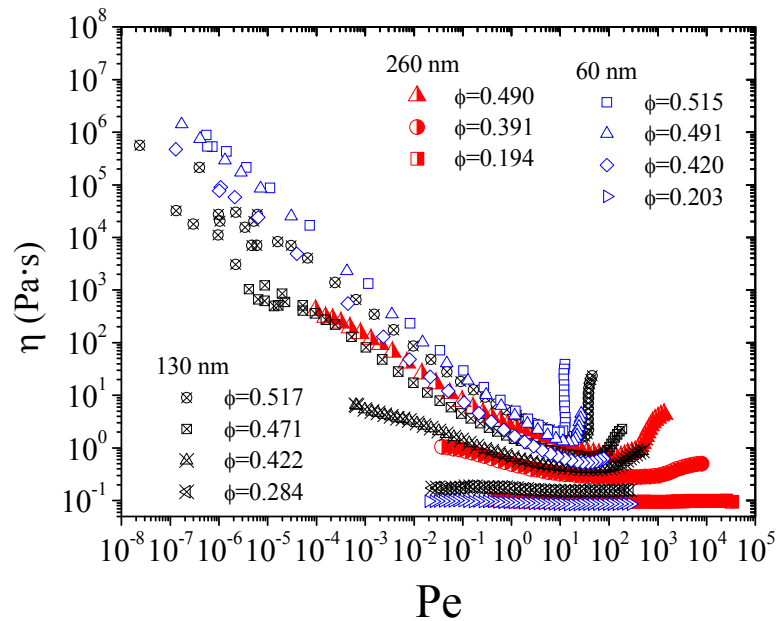


Figure 3.27 Steady-shear rheology data for selected volume fractions of suspensions of three sizes as a function of Péclet number.

3.5.4 The Effects of Suspending Medium Viscosity

If changes in the suspending medium only change the solvent viscosity without significant changes in the interparticle interactions (due to different solvents being chemically similar or the interparticle interactions being athermal), then the rheology is known to scale with the solvent viscosity [45]. The SANS experiments require changing the solvent to a partly deuterated solvent mixture of deuterated ethylene glycol and PEG-600 to reduce multiple scattering while keeping solvent viscosity high enough to measure the desired rheological effects.

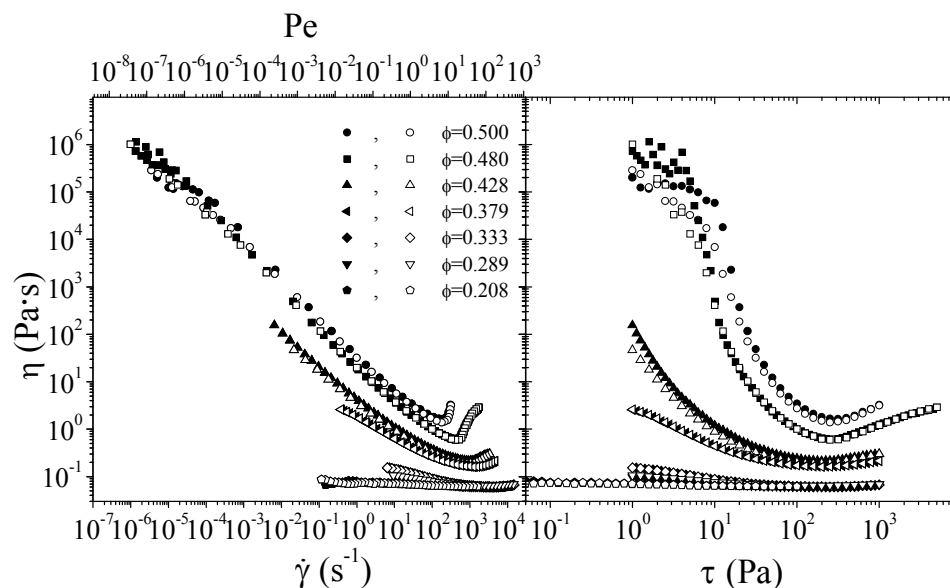


Figure 3.28 Steady-shear rheology of 60 nm silica spheres dispersed in a 70/30 mixture by volume of PEG-600 and ethylene glycol. Filled symbols are forward sweeps and open symbols are backward sweeps.

Figure 3.28 shows the steady shear rheology of suspensions of the 60 nm particles in a mixture of 70% ethylene glycol, 30% PEG-600. Qualitatively similar behavior is seen as in suspensions of the same particles in PEG-200 earlier in this chapter. A few differences are seen between the suspensions in the two different solvents, shown directly as Figure 3.29. First, the highest concentration samples, at about $\phi=0.50$, have one noteworthy difference at the highest applied stresses: the PEG-200 sample shows nearly discontinuous shear thickening whereas the sample in the PEG-600 and ethylene glycol solvent mix appears to bend over and show more mild thickening. This difference, which has been previously reported for a similar system [45], is thought to be due to the larger polymer chains suppressing the extreme lubrication forces required for discontinuous shear thickening caused by small gaps

between clustering particles. Regardless, the samples of high concentration do shear thicken at the same critical Péclet number. However, while these high concentration samples do show similar behavior at low shear stresses, the rheology for the PEG-600/ethylene glycol samples show values of the viscosity that are systematically lower than the PEG-200 samples.

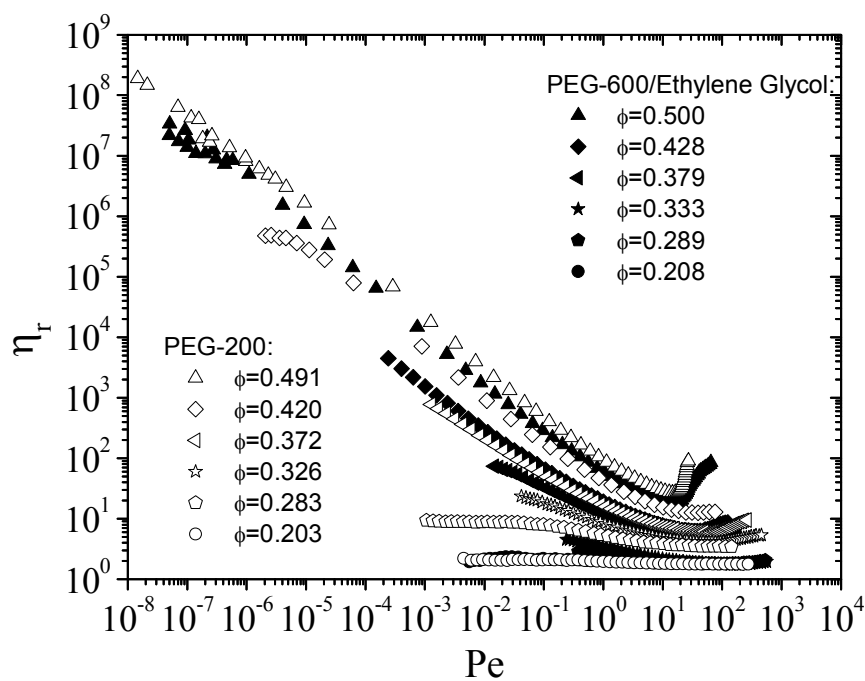


Figure 3.29 Comparison of the steady shear rheology of dispersions of 60 nm silica spheres in PEG-200 and a mixture of PEG-600 and ethylene glycol.

Further differences in the rheology become more apparent when the Cross model fitting is performed as before. Figure 3.30 shows fitting of the 60 nm silica dispersed in the 70/30 mixture of ethylene glycol and PEG-600 to the Cross model,

with reduction onto the master curve in Figure 3.31 and fit parameters shown in Table 3.8.

Similar trends as before are seen, although many of the infinite shear viscosities are less than the hard-sphere value. In addition, the zero-shear viscosities are not significantly greater than the hard-sphere expectation at volume fractions where there is no measured yield stress. The yield stress, measured for volume fractions of 0.372 and above in the PEG suspensions, is not measured at $\phi=0.379$, but appears for volume fractions of 0.428 and above. In addition, the values of m and τ_{Cross} are consistent with those seen before. Overall, the model fitting collapses the data well, with the exception of the samples with a yield stress at stresses below the yield stress. In addition, the model does not apply to samples that shear thicken above the onset of shear thickening.

At all concentrations, the PEG-200 samples show higher values of the apparent viscosity at low Péclet number, although much of this data is in the regime where there is a yield stress, so this apparent viscosity change is due to a difference in the yield stress. In general, in terms of reduced viscosity versus Péclet number, this change in solvent does cause some changes in the rheology – it does change the interparticle interactions in addition to the changes in solvent viscosity.

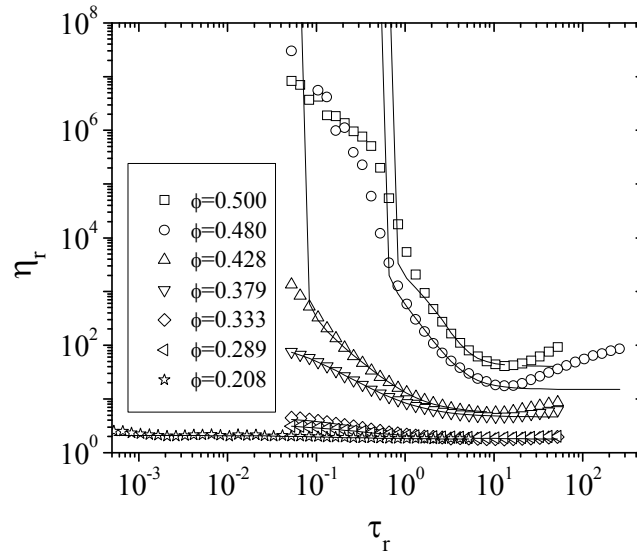


Figure 3.30 Steady shear data and fits to Cross model for 60 nm particle suspensions in solvent mixture of PEG-600 and ethylene glycol.

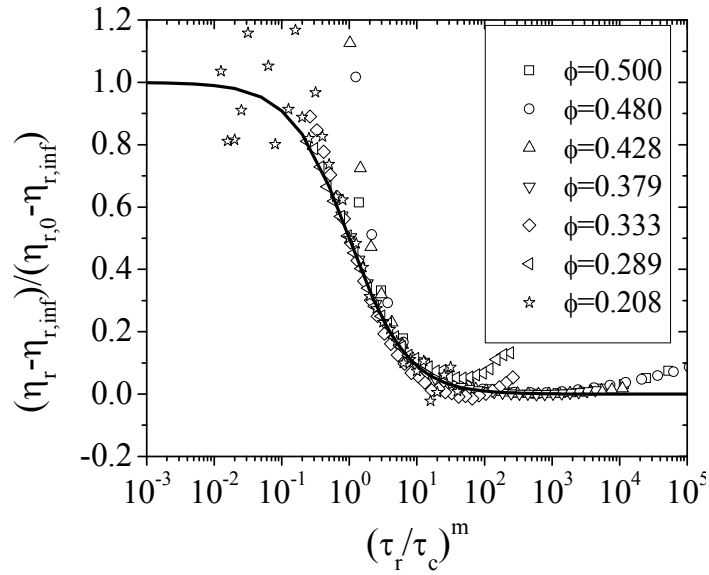


Figure 3.31 Reduction of data onto Cross model for 60 nm particle suspensions in solvent mixture of PEG-600 and ethylene glycol.

Table 3.8 Fitting parameters and results from Cross model fits to rheology of 60 nm silica spheres in solvent mixture of PEG-600 and ethylene glycol.

a (nm)	60	60	60	60	60	60	60
ϕ	0.208	0.289	0.333	0.379	0.428	0.480	0.500
$\eta_{r,0}$	2.09	3.40	4.80	130	180	580	740
$\eta_{r,\infty}$	1.8	1.8	1.8	4.6	5.5	15	40.
τ_{Cross}	0.13	0.22	0.20	0.064	0.13	0.95	1.89
m	1	1	1	1.25	1.55	2.39	3.27
$\tau_{r, \text{yield}}$	0	0	0	0	0.066	0.52	0.66
τ_{yield} (Pa)	0	0	0	0.00	1.3	10.	13
η_{r0} -prediction	2.23	3.41	4.50	6.32	9.68	17.6	23.5
$\eta_{r\infty}$ -prediction	2.00	2.84	3.55	4.61	6.32	33.4	52.7
$\phi_{\text{eff},0}$	0.194	0.288	0.342	0.58	0.58	0.60	0.61
$\phi_{\text{eff},\infty}$	0.18	0.18	0.18	0.38	0.41	0.53	0.60
$\phi_{\text{eff},0}/\phi$	0.934	1.00	1.03	1.5	1.4	1.3	1.2
$\phi_{\text{eff},\infty}/\phi$	0.87	0.63	0.53	1.0	0.95	1.1	1.2
t_0 (nm)	-1.4	-0.038	0.56	8.9	6.6	4.8	4.0
t_{∞} (nm)	-2.7	-8.7	-11	-0.023	-0.96	4.8	9.2

Figure 3.32 shows a comparison of the suspensions of 60 nm particles in the PEG-600 and ethylene glycol mix to suspensions of the same type where deuterated ethylene glycol is used. This change to deuterated ethylene glycol is necessary for suppression of multiple scattering in the SANS experiments discussed in Chapter 4. It can be clearly seen that the deuteration of the solvent does not significantly alter the rheology. The slight differences in the high concentration samples between the deuterated and non-deuterated samples are consistent with the difference in volume fraction. In addition, there is negligible difference at the lower volume fractions between deuterated and non-deuterated samples. It is important to note that deuteration does increase the density of the solvent, as seen in Table 3.3, and so the suspensions are made at the same volume fraction and relative volumes of the

two solvents, requiring a larger relative weight percent of deuterated solvent. These results imply that, as expected, the rheological characterization shown in this chapter for the samples in the non-deuterated ethylene glycol and PEG-600 solvent mixture can be assumed to apply to the partly deuterated samples whose microstructure are characterized in Chapter 4.

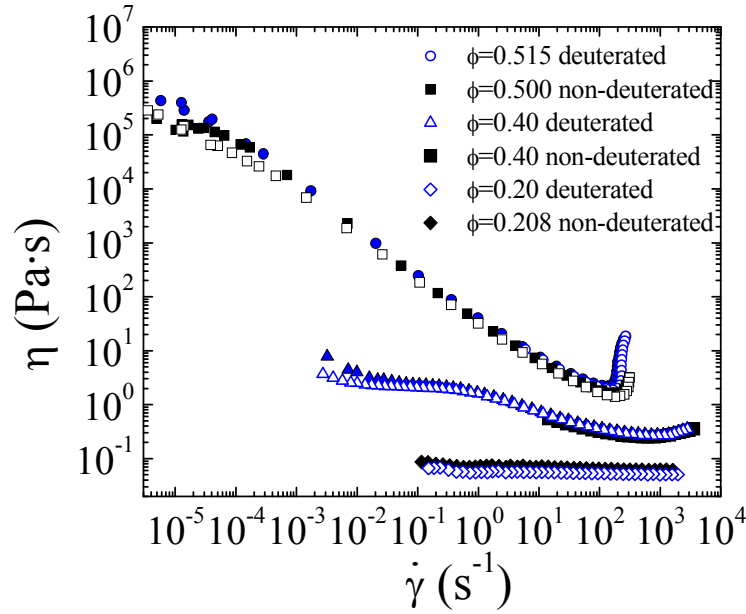


Figure 3.32 Comparison of the steady shear rheology of dispersions of 60 nm silica spheres in a mixture of PEG-600 and ethylene glycol to those in a mixture of PEG-600 and deuterated ethylene glycol. Filled symbols are forward sweeps and open symbols are backward sweeps.

3.5.5 Critical Stress for Onset of Shear Thickening

The critical shear stress or critical shear rate required for shear thickening (τ_{crit} or $\dot{\gamma}_{crit}$) is the simplest characteristic of shear-thickening suspensions and the

primary focus of typical simplified scaling theories. Figure 3.33 shows the critical stress for shear thickening for the various suspensions seen here as a function of volume fraction, determined as described in section 2.4.6. Much scatter is seen due to the varying particle sizes, but there is a general trend in each data set to increasing critical stress with increases in volume fraction. In addition, the trend is towards increasing critical stress with decreases in the particle size – the smallest particles show the largest values of the critical stress. The error bar in stress is one value of applied stress above or below the value of stress where viscosity first increased (based on a test with 10 logarithmically spaced points per decade).

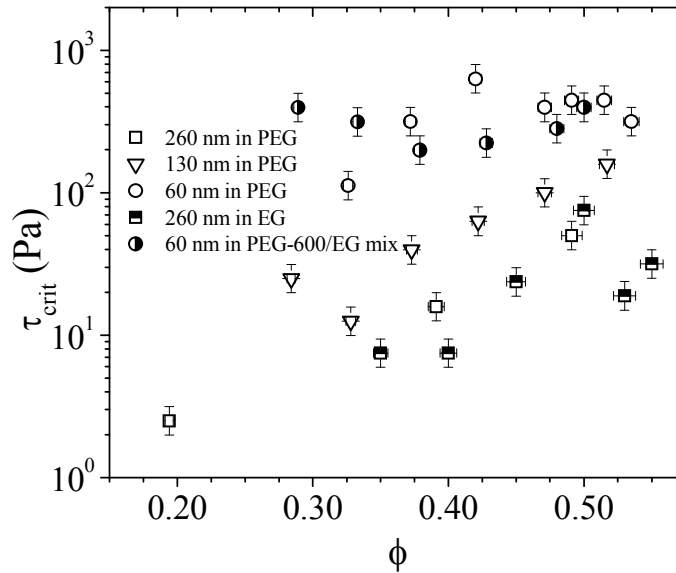


Figure 3.33 Values of the critical stress for shear thickening for various silica suspensions as a function of volume fraction.

Figure 3.34 shows the dimensionless critical shear stress for these suspensions, along with the correlation provided by equation 3.12. As this equation

clearly under predicts the critical shear stresses due to the non-hard-sphere interactions, a line of the form of equation 3.12, with the constants fit, is also included. Rather than the coefficients of 0.1 for the pre-exponential and activation energy of 0.153, the fitting gives values for the pre-exponential of 2.00 ± 1.55 and the activation energy of 0.156 ± 0.044 , with a generally poor fit R^2 of 0.327. The prediction and data show similar volume fraction dependence, but the measured stresses are an order of magnitude higher than the prediction and do not accurately follow the predicted size scaling for Brownian spheres. This fit is done using the volume fraction and not the effective volume fraction determined from the SANS and steady shear rheology data. As seen before, the effective volume fraction is 17.8% larger than the volume fraction, and so the fit activation energy would increase by 17.8% to 0.184.

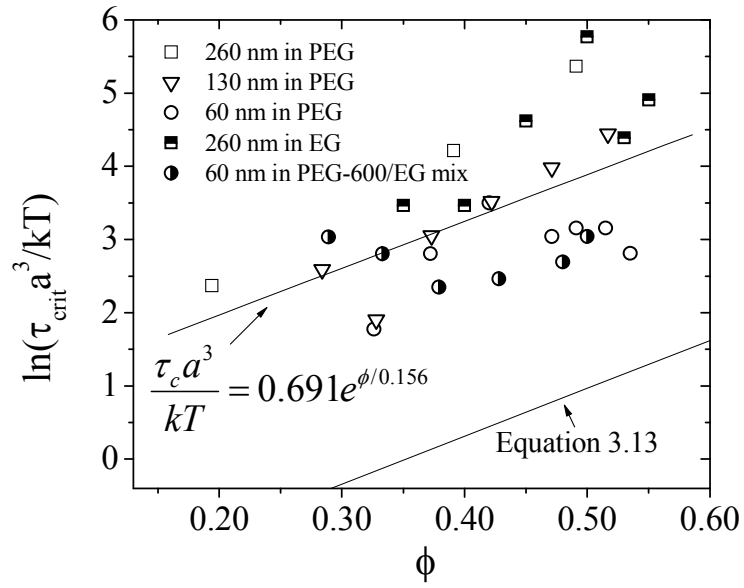


Figure 3.34 Log of the dimensionless critical stress versus volume fraction for various suspensions, used in fitting. As the values for suspensions of the largest particles fall above the fit line and those for smallest particles fall below the line, the correlation appears to overcorrect for particle size.

Inspired by the functional form of equation 3.11 with the critical stress as a function of particle size squared for suspensions with non-hard-sphere interactions, a simple empirical fit was also done to equation 3.17, as shown in Figure 3.35:

$$\ln\left(\frac{\tau_{\text{crit}} a^2 \cdot 1 \text{ m}}{kT}\right) = A_1 + \phi/A_2 \quad (3.17)$$

where A_1 and A_2 are fit constants and the arbitrary length scale 1 m is included to make the term inside the logarithm dimensionless. This fitting gives values for A_1 and A_2 of 16.67 ± 0.48 and 0.156 ± 0.027 , respectively, with an improved, but still poor R^2 value of 0.555. Considering the significantly improved fit of the critical stress to a radius-squared relation over the radius-cubed expectation, non-hard-sphere effects appear to

control the critical stress. Alternatively, Hoffman's order-disorder transition theory for thickening [37, 38, 79] does predict a radius-squared relationship for the critical stress, although the yield-stress and additional excluded volume do show these suspensions have deviations from hard-spheres, which would also cause this radius-squared relationship as seen previously by Maranzano [19, 59]. Once again, performing this fit with the effective volume fraction would increase A_2 by 17.8% to a value of 0.184.

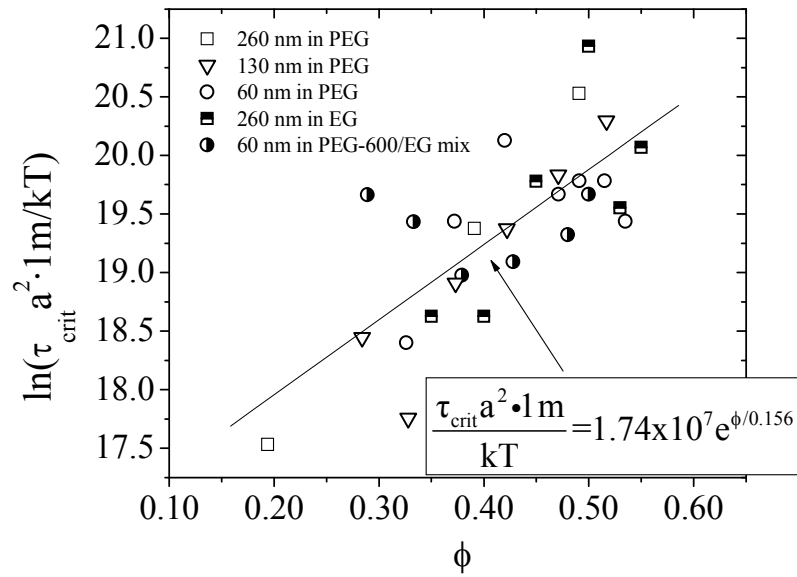


Figure 3.35 Correlation of the critical stress with volume fraction with a radius squared dependence for various suspensions, used in fitting.

3.5.6 Normal Stress Measurements

In addition to the nonlinear shear-stress versus shear-rate behavior, concentrated suspensions show unique normal stress behavior. Specifically, theoretical work [80] supported by Stokesian dynamics simulations [24] show positive values of

the first normal stress difference under shear in the shear thinning regime which transitions to negative first normal stress differences near the transition to shear thickening and into the shear thickened state. Prior experimental measurements on the normal stresses are extremely limited, partly due to the low magnitude of the normal stress difference and the large fluctuations inherent in the measurement. It is important to note that the large fluctuations in the normal stresses are not caused simply by instrument noise – there are fluctuations in the value itself, seen in simulations, which require long times to measure an average value [24]. An example of the raw data used to calculate the normal stress, which shows these fluctuations, is shown as Figure 2.2. These fluctuations are caused by the actual particle interactions under shear flow – the magnitude of the fluctuations are large relative to the normal stress values and therefore are measureable, unlike the fluctuations in the shear stress which are small relative to the magnitude of the shear stress and therefore are not noticeable in rheometric experiments. Normal stress measurements shown here are per the protocol described in section 2.4.3.

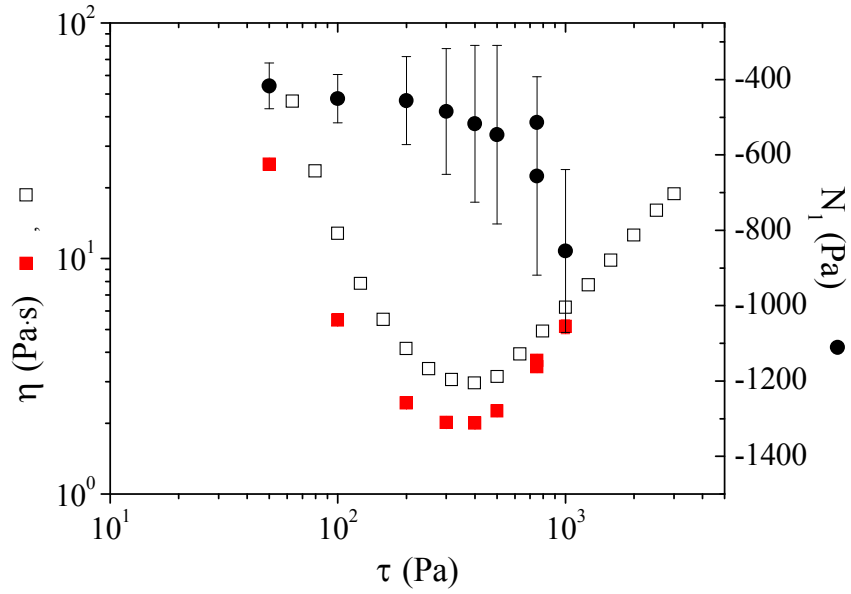


Figure 3.36 First normal stress difference rheological measurements for 60 nm silica dispersion at $\phi=0.515$ in solvent mixture of PEG-600 and ethylene glycol (70% ethylene glycol by weight). Filled circles are N_1 , filled squares are the steady-state viscosity measured during long N_1 peak hold steps, open squares are steady-state viscosity measured in cone and plate geometry shown earlier. The microstructure of these suspensions is studied in depth in Chapter 4.

Figure 3.36 shows the first normal stress difference data for the $\phi=0.515$ suspension of 60 nm spheres in the PEG-600 and ethylene glycol solvent mixture. Figure 3.37 shows the first normal stress difference data for the $\phi=0.517$ suspension of 130 nm spheres in PEG-200. In both figures, the open squares are the steady-state rheology shown previously in the cone and plate geometry, the filled squares are the average viscosity at that applied stress from the long-time experiment used to generate the normal stress in the parallel plate geometry, and the circles are the first normal stress difference. As seen in section 3.5.3, both of these suspensions have a yield stress and exhibit both shear thinning and shear thickening. The 60 nm suspensions data

includes measurements in both the shear thinning regime and the shear thickening regime. The first normal stress difference is seen to be roughly constant in the shear thinning regime at around -400 Pa, becoming more negative as the stress increases towards the shear thickening regime to a value of about -800 Pa. The first normal stress difference for hard-sphere suspensions is expected to be slightly positive; these measurements showing negative values of the normal stress at low shear stresses for the 60 nm suspensions are likely due to error arising from difficulty setting the value of zero normal stress on the fluid in the rheometer gap due to this fluid having a large yield stress. The yield stress contributes an additional normal stress under static conditions.

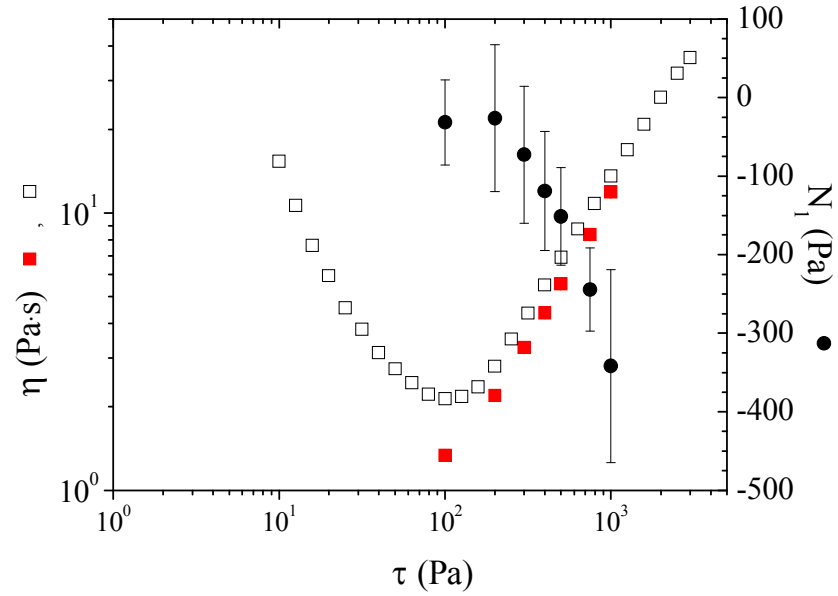


Figure 3.37 First normal stress difference rheological measurements for 130 nm silica dispersion at $\phi=0.517$ in PEG-200. Filled circles are N_1 , filled squares are the steady-state viscosity measured during long N_1 peak hold steps, open squares are steady-state viscosity measured in cone and plate geometry shown earlier.

The 130 nm suspension data, seen in Figure 3.37, does not include results in the shear thinning regime, due to the long times required for these samples at the low shear rates corresponding to these low applied stresses. Regardless, these suspensions show negative values of the first normal stress difference which are near zero at the onset of shear thickening, appear to increase slightly before decreasing to about -350 Pa at an applied stress of 1000 Pa, well into the shear thickened state. Unlike the 60 nm suspensions, the 130 nm suspensions show values that are near zero at low shear stresses and are more consistent with the expectations of a small positive value of the normal stress. In this case, the deviations from the expected slightly positive values at low stress are lower than for the smaller particle suspensions,

consistent with the deviation arising from difficulty in setting the zero-stress value of normal force. As the yield stress is an order of magnitude lower for the larger particles than for the smaller particles, the error in the zero measure of normal force is eliminated or lowered.

3.5.7 Step Rate/Stress Measurements

Rheological measurements consisting of step changes in the applied shear stress or shear rate can be useful for multiple reasons. In the past, they have been used with high speed data acquisition to separate the elastic and viscous components of the stress for concentrated suspensions [26, 27]. Presented here are some step-stress measurements for the purpose of showing that the thickening and thinning behavior have fast transitions relative to the time scales of rheometric and neutron scattering experiments, and are not caused by permanent changes in the suspension. In addition, these measurements verify the methodology of holding the stress or rate constant while using SANS or USANS to measure structure as discussed in Chapter 4 and 5 – if the rheology was not constant over long periods of time then these scattering measurements would not give a meaningful average structure. These measurements were not done under fast data acquisition which would allow for measurements of the transitions at low time; the resolution in these measurements is one second.

Figures 3.38 and 3.39 show stress jump measurements of the $\phi=0.500$ suspension of 60 nm silica in PEG-200, studied further in Chapter 4. For this sample, the yield stress is 13 Pa and the critical stress for shear thickening is 250 Pa; the steady-shear rheology is seen in Figure 3.28. At each jump, into either the shear thinning or shear thickening state, the steady-state viscosity value seems to be

achieved in a very short time on this viscosity scale. In addition, there appears to be little change with time over the 10 minutes that each stress is held.

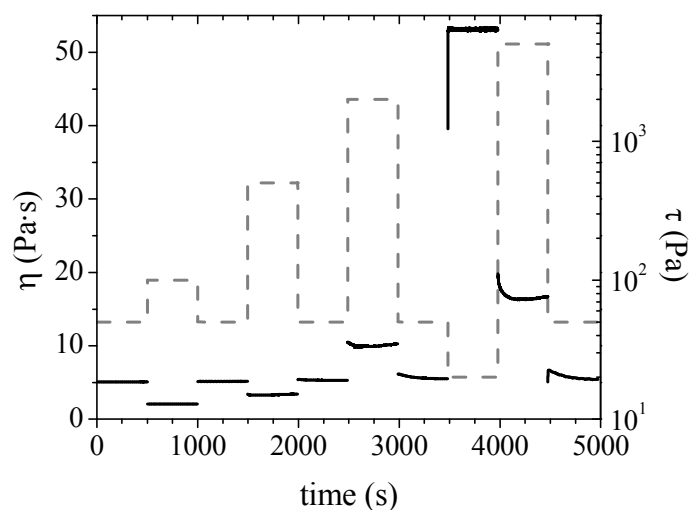


Figure 3.38 Stress jump measurements on the $\phi=0.500$ suspension of 60 nm SiO_2 in PEG-600 and ethylene glycol solvent mixture. The dashed line indicates the applied stress and the solid lines indicate the measured viscosity.

Figure 3.39 shows some of the data on a log-time axis with the first data point after each jump set to one second. In addition, the viscosity axes are over much shorter ranges than the prior figure to allow for greater clarity in the small viscosity deviations with time. The top pane shows jumps from high stresses to a low stress. As these are all jumps to the same final stress value of 50 Pa, they decay to the same steady-state stress value, but from different initial viscosities. The initial viscosity increases with the increasing stress before the jump. In addition, the initial viscosity is constant for the first 10 seconds, with a slow decay beyond that time. A jump from a

low stress (50 Pa) to a lower stress (20 Pa) shows little change with time, as does a jump from low stress (50 Pa) to a high stress just within the thickened state (500 Pa). Data taken at stresses well beyond the critical stress for thickening do show a long time relaxation on the order of 100 seconds, with the viscosity decreasing with time.

Figure 3.40 shows similar results in the case of the $\phi=0.391$ sample of 260 nm SiO₂ suspensions studied further in Chapter 5. These suspensions also appear to show little change with time after an induction period and so the microstructure changes which drive rheological changes can be appropriately measured over the ~6 hour USANS experiment time.

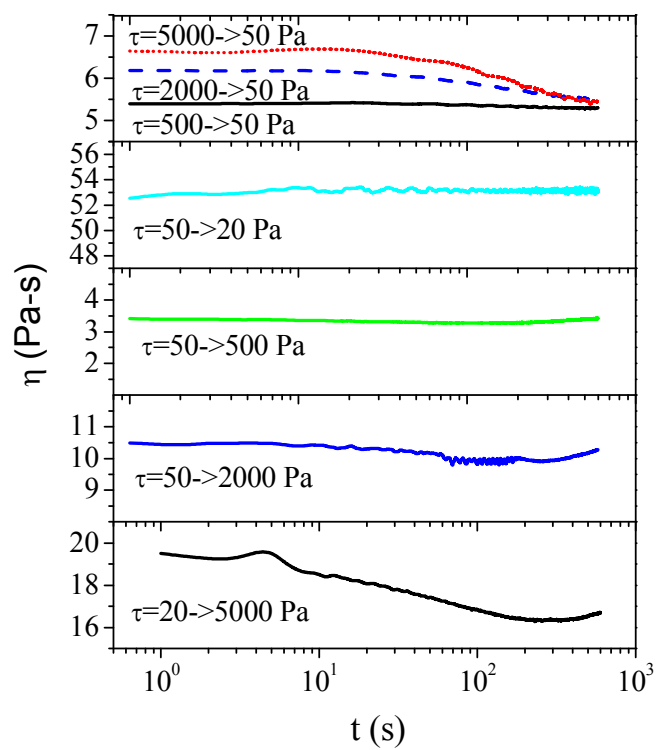


Figure 3.39 Stress jump measurements on a log-time axis, from the $\phi=0.500$ suspension of 60 nm SiO₂ in PEG-600 and ethylene glycol solvent mixture.

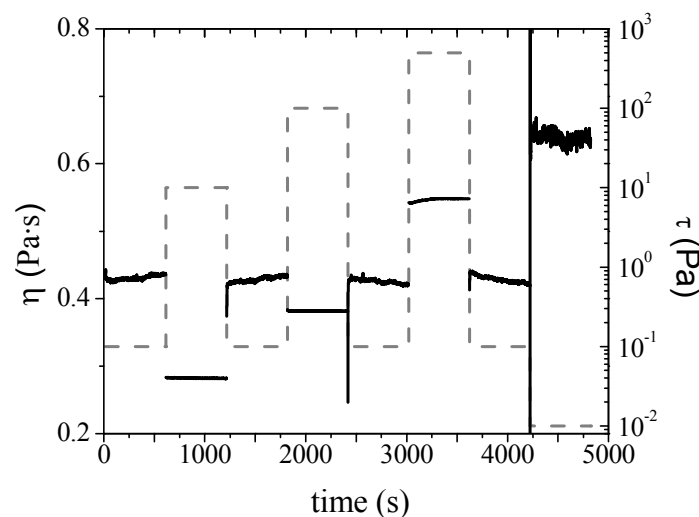


Figure 3.40 Stress jump measurements on the $\phi=0.391$ suspension of 260 nm SiO_2 in PEG-200. The dashed line indicates the applied stress and the solid lines indicate the measured viscosity.

3.5.8 Dynamic Rheology Measurements

Small-amplitude oscillatory shear (SAOS) measurements were done to evaluate the linear viscoelastic behavior of these suspensions. Frequency sweeps in the linear viscoelastic regime (for these samples, at a maximum strain of 0.01) can provide additional insight into the behavior of these suspensions. Figure 3.41 shows linear viscoelastic SAOS data for a volume fraction series of the 60 nm silica suspensions in PEG-200, while Figure 3.42 shows similar data for the 130 nm suspensions. Both moduli generally increase with increasing frequency in the measured range. Samples at volume fractions of 0.422 and below for both particle sizes show primarily viscous behavior, with a loss modulus (G'') higher than the storage modulus (G'), over much of the frequency range. High concentration samples show relatively unchanging values of G' , which are higher than the values of G'' indicating primarily elastic behavior. This

result of primarily elastic behavior at high concentrations is consistent with these suspensions storing stress rather than flowing at low stresses, as seen previously with the measurement of a yield stress in steady state data.

These highest concentration samples, at $\phi=0.372$ and above for the 60 nm suspensions and $\phi=0.471$ and above for the 130 nm suspensions, show behavior that could be indicative of a colloidal glass [81, 82], where there is a minimum in G'' at a plateau of slightly increasing G' . The model behavior expected for colloidal hard-sphere glasses is typically understood to be controlled by a nearest neighbor "cage" of particles which hinder the motion of a particle within the cage. Figure 3.43 shows a summary of the data for both suspensions in terms of the plateau modulus, G'_{plateau} , the elastic modulus at the plateau modulus, defined as the value of G' in a relative plateau where G'' is a minimum, G''_{min} , and the frequency at which these moduli are measured. The frequency location of this G'' minimum is the reciprocal of the β relaxation time, indicative of the relaxation time for local diffusive motion within a nearest neighbor cage. The frequency at the minimum is seen to be lower for the larger particles, hence the larger particle suspensions have a longer relaxation time for in-cage motion.

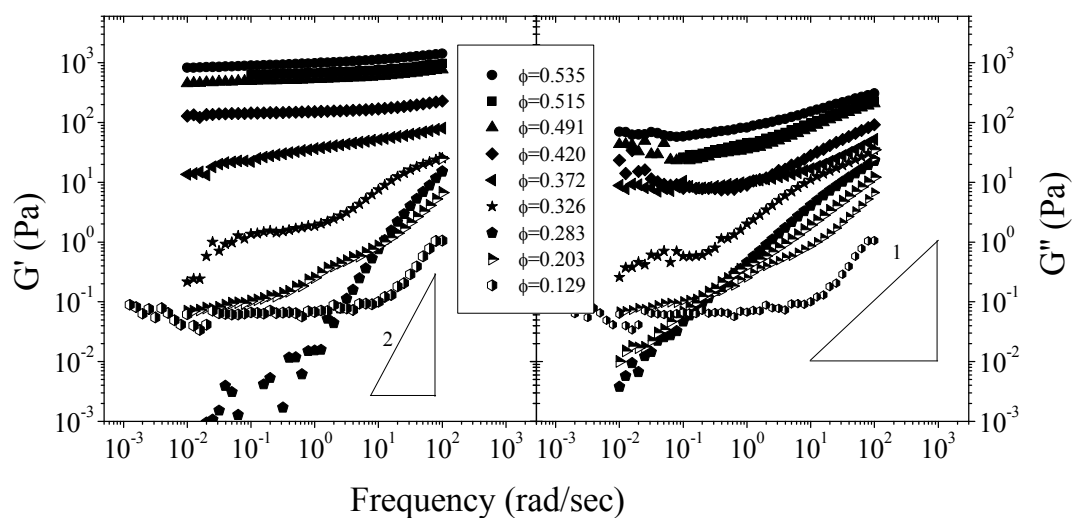


Figure 3.41 Small amplitude oscillatory shear data for suspensions of 60 nm silica in PEG-200.

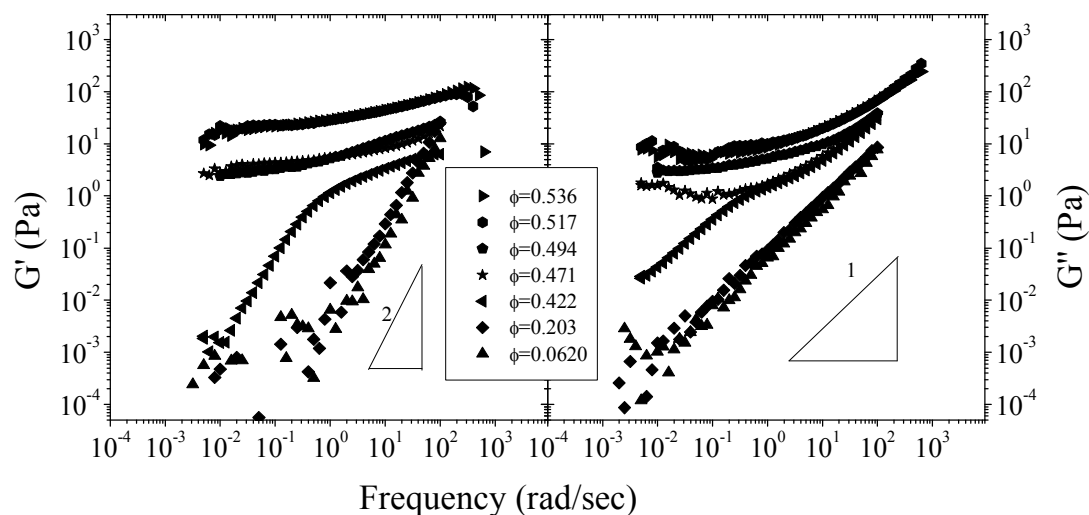


Figure 3.42 Small amplitude oscillatory shear data for suspensions of 130 nm silica in PEG-200.

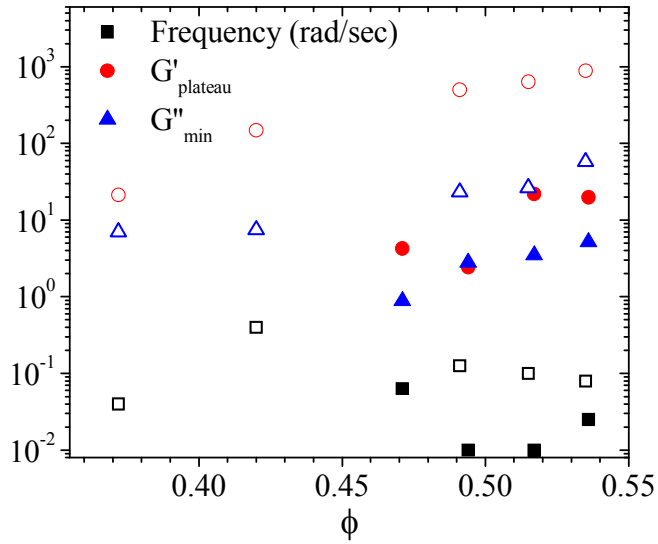


Figure 3.43 Plateau elastic modulus, loss modulus minimum, and frequency at the loss modulus minimum. Open symbols are 60 nm silica suspensions seen in Figure 3.41, closed symbols are 130 nm suspensions seen in Figure 3.42.

3.5 Conclusions

A rheological and structural study is performed to characterize a homologous series of stabilized silica particles in near index matching solvent, as a model near hard-sphere system. Analysis of the 260 nm suspensions via USANS shows the existence of an excluded volume shell in addition to the hard-sphere interactions, which is also confirmed for the 60 nm suspensions via SANS. This excluded volume shell also is confirmed for 60, 130, and 260 nm radius suspensions via mapping of the steady-shear rheology onto the expectations for hard-spheres, with the addition of a yield stress. The critical stresses for shear thickening are also seen to

follow a radius-squared relationship rather than radius-cubed, indicating the non-hard-sphere interactions control the transition to shear-thickening. In addition, the Péclet number alone is insufficient to collapse the data in the shear thinning regime, shear thickening regime, or the location of the shear thickening transition. Normal stresses are seen to follow the trends predicated for hard-spheres, although the presence of the yield stress at high concentrations makes accurately zeroing the normal force difficult and leads to deviations in the absolute values of the normal stress from expectations and between different particle sizes. Step-rate experiments verify the rheological behavior is constant over long periods of time and therefore the average microstructure is constant and can be measured via SANS or USANS. Small-amplitude oscillatory shear data are also included and show that the suspensions are dominated by elastic forces at high concentrations and show behavior consistent with hard-sphere colloidal glasses. These shear thickening colloidal suspensions will be used in further studies to elucidate the structural features and structure-property relations in the following chapters.

Chapter 4

RHEO-SANS EXPERIMENTS ON NEAR HARD-SPHERE COLLOIDAL SUSPENSIONS

4.1 Introduction

There has been significant previous work measuring the structure of concentrated, colloidal suspensions under shear flow via small angle neutron scattering (SANS) [15, 23, 33, 44, 64, 83-89]. Prior scattering experiments have been limited to microstructure measured either perpendicular to the velocity gradient direction (neutron beam oriented along the radius of the Couette and hence also known as the *radial* direction, flow-vorticity plane, or 1-3 plane) or perpendicular to the flow direction (neutron beam oriented *tangential* to the Couette, measuring the gradient-vorticity or 2-3 plane). These measurements, which are not directly in the 1-2 plane of shear (flow-gradient, measured along the vorticity direction) cannot fully elucidate the structure, particularly the structural anisotropy that dominates the thermodynamic or shear-thinning portion of the stress [23].

Due to these limitations, the structure of concentrated Brownian sphere suspensions under shear is primarily known from Stokesian dynamics simulations [24, 25, 30, 31, 40, 42, 77, 90, 91]. In particular, these suspensions are known to exhibit growing anisotropy in the structure in the flow-gradient plane with increasing shear rate. Clustering, driven by hydrodynamic interactions, is seen to drive shear thickening under high Péclet flows.

In addition, the shear thinning and shear thickening components of the viscosity have been measured experimentally in prior work. Stress-jump experiments have been used to measure the elastic component of the stress which drives shear thinning separately from the viscous component of the stress which drives shear thickening [26, 27]. In addition, rheo-optical experiments have successfully measured the thermodynamic component of the stress and separated it from the hydrodynamic contributions which drive shear thickening [21]. These optical experiments require the development of a stress-optical law from micromechanics.

Similar micromechanics theory has been developed to translate SANS experiments under shear into thermodynamic and hydrodynamic components of the viscosity [23, 65, 66]. Maranzano developed this procedure and utilized it to translate SANS measurements under shear in the radial and tangential directions into the hydrodynamic component of the shear stress and the thermodynamic component of the normal stresses [23], but was unable to measure the thermodynamic component of the shear stress that drives shear thinning due to a lack of the relevant structural harmonics from SANS along the flow (1) and gradient (2) directions.

Recent work has developed a novel shear cell for neutron scattering experiments of complex fluids under shear along the vorticity axis to measure directly in the plane of shear, the flow-gradient or 1-2 plane [62]. Previously, this experimental setup has been used to investigate surfactant solutions, especially wormlike micellar networks, including those that exhibit shear banding [62, 92, 93]. This experimental work proves that significant structural insight that can be learned from SANS measurements directly in the plane of shear.

Clearly, scattering measurements in the 1-2 plane of shear are optimal for measuring the structural anisotropy, particularly the thermodynamic component of the shear stress which drives shear thinning. With that aim, this chapter attempts to show the first structural measurements on concentrated particle suspensions via SANS in the 1-2 plane. These suspensions are some of the near hard-sphere suspensions characterized fully in Chapter 3. In addition, SANS measurements on these suspensions in radial Rheo-SANS are also presented to give a complete depiction of the structure. Micromechanics theory is used to calculate the thermodynamic and hydrodynamic components of the shear stress and normal stress differences, which are compared to the measured rheology. In addition, structural measurements are compared qualitatively and quantitatively directly with those from simulations via Stokesian dynamics.

4.2 Experimental

Neutron scattering measurements were performed in multiple separate trips at NIST in Gaithersburg, MD, primarily on the NG3 SANS beamline, with some experiments on NG7 SANS beamline (where noted). Experiments in the 1-2 plane of shear were performed in the specially built 1-2 plane shear cell, with a 5 mm neutron path length and either a 1 mm or 1.35 mm gap. The cell with the rotor for a 1.35 mm gap has approximately 8.5 mL sample volume. In one set of experiments, this sample volume was used to dilute the sample directly in the shear cell.

Additional complimentary experiments in the radial direction or 1-3 plane were performed using the SANS rheometer with one of two titanium Couette cells. The large Couette had an outer cup with a 50 mm inner radius and an inner bob with a 49.5 mm radius (0.5 mm gap) and a 2° conical bottom, set at a gap of 2 mm. The small

Couette had an outer cup with a 15 mm inner radius and an inner bob with a 14.5 mm radius (0.5 mm gap) and a 2° conical bottom, set at a gap of 2 mm. These cells had approximate sample volumes of 8 and 4 mL, respectively. For both cells, the neutron beam passed along the radius of the Couette, near the middle of the cell vertically. Therefore, the scattering volume includes only the fluid in the long gap between the two cylinders, shearing perpendicular to the beam.

The shear cell motor and rheometer are both connected to the SANS measurement control software to allow for automated control. The samples were periodically checked for air bubbles introduced into the 1-2 plane shear cell, and careful scrutiny of the transmission measurements also allows identification of changes in the sample composition due to contamination or air bubbles.

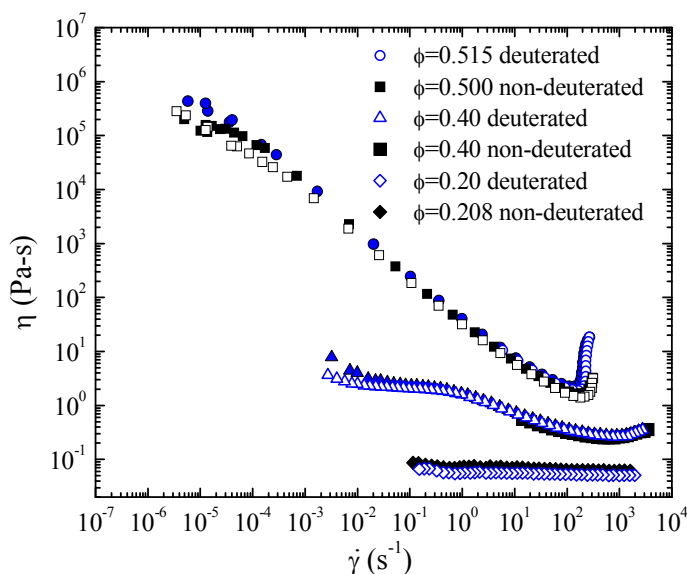


Figure 4.1 Steady-state rheology of partly-deuterated samples used in SANS experiments, compared to non-deuterated samples. Filled symbols are forward sweeps and open symbols are backward sweeps.

Figure 4.1 shows the rheology of the most common samples tested and a comparison between samples using deuterated ethylene glycol in the solvent (used in 1-2 plane SANS experiments) and non-deuterated ethylene glycol (used in radial Rheo-SANS experiments). Clearly, when the density difference of deuterated versus undeuterated solvent is accounted for to keep the volume fractions of the components consistent, as in these suspensions, the difference in the rheology is negligible.

Table 4.1 Details of samples tested in SANS experiments. The * denotes suspensions tested in the 1-2 plane which utilized deuterated ethylene glycol in the solvent – other suspensions used regular ethylene glycol.

ϕ	wt% SiO ₂	wt% EG	wt% PEG	λ (Å ⁻¹)	Detector Distance	Geometry
0.515	62.6	25.9*	11.4	6	13 m	1-2 plane, 1.35 mm gap
0.40	51	34*	15	6	13 m	1-2 plane, 1.35 mm gap
0.522	63.3	26.2*	10.5	8	13.1 m	1-2 plane, 1.0 mm gap
Coated - 0.50	68	N/A	N/A	8	13.1 m	1-2 plane, 1.0 mm gap $\phi_{\text{core}} \sim 0.5$
0.20	29	51*	21	8	13.1 m	1-2 plane, 1.0 mm gap
0.495	60.7	27.2*	12.1	8	13.1 m	1-2 plane, 1.35 mm gap (gap resolved)
0.531	65.7	23.1	11.2	6	15 m	Radial, large Couette
0.436	56.6	29.2	14.2	6	15 m	Radial, large Couette
0.53	66	23	11	8.4	13.2 m	Radial, small Couette
0.44	57	29	14	8.4	13.2 m	Radial, small Couette

Table 4.1 shows a list of the separate experiments performed and the sample compositions, which are also described in the following text. Initial experiments in the 1-2 shear plane were performed with a rotor of 25.46 mm radius,

for a 1.35 mm gap. The sample composition by weight was 62.6 % silica (60 nm, characterized in Chapter 3), 25.9 % deuterated ethylene glycol (Cambridge Isotopes DLM-132 69.4% of solvent), and 11.4 % PEG-600 (30.6%), for a sample of $\phi=0.515$. The sample composition by volume was 51.5 % silica, 32.7 % d-ethylene glycol (67.4 % of solvent), and 15.8% PEG. The instrument configuration on NG3 was 6 Å, 13 m detector distance. In addition, after completion of testing on the above described sample, additional solvent mixture of the same composition was added to the suspension in the cell, mixed by shearing and pumping the suspension between the syringes attached to the two fill ports. The additional sample added was 3.11 g of a sample with the composition 1.0 % silica, 69.5 % d-ethylene glycol (70.2% of solvent), 29.5 % PEG-600 by weight, yielding an in-cell sample at $\phi=0.40$ silica (when combined with the 8.5 mL of above sample already in the cell), confirmed by rheology as seen in Figure 4.1. Scattering measurements for these samples were done for 20 minutes, with 2 minute transmissions at every order of magnitude in shear rate in the shear thinning regime and every shear rate in the shear thickening regime. These measurements are shown as the first data set in section 4.3.1.1 at the high concentration and in section 4.3.1.2 at the lower concentration.

Subsequently, the prior sample at $\phi\sim 0.40$ was diluted with further solvent to produce a sample of composition 29 % silica, 51 % d-ethylene glycol, 21 % PEG by weight (20. % silica, 55 % d-ethylene glycol, 25 % PEG by weight.) This sample was measured on NG3 at 8 Å and 13.1 m detector distance, in the 1-2 shear cell with the smaller 1.0 mm gap. These experiments are presented in section 4.3.1.3.

An additional sample was tested in the 1-2 plane at $\phi=0.522$. The sample composition and instrument setup is seen in Table 4.1. In addition, these experiments

were done with clockwise rotation of the 1-2 plane shear cell rotor relative to the neutron beam, the opposite of the prior experiments. The data has been corrected so that the shear direction is the same in all of the figures, as indicated (except where showing the differences between opposing shear directions). These experiments are presented as the second data set in section 4.3.1.1.

The sample with shear thickening suppressed utilized octadecane-coated silica (the full procedure is described in section 2.3.3), dispersed in a solvent mixture of 50/50 mineral oil (Cannon S20 viscosity standard) and deuterated dodecane (Cambridge Isotopes DLM-338). The sample was made to have a volume fraction of $\phi=0.50$ under the assumption that the coating (amount determined by weight via TGA) would act as solvent at the same density as the solvent, and that the silica core had the same density as the original particles, as measured via densitometry. In addition, the density for the mineral oil used was 0.8567 g/mL (the density at 25°C) and the density of the d-dodecane was measured to be 0.873 g/mL at $21\pm1^\circ\text{C}$, as seen in Table 3.3 and described in section 2.2.2. Specifically, the suspension was 24.96 g particles (22.6 grams of silica using the 9.40% weight coating), 4.17 g d-dodecane, and 4.05 g S20. Note: These experiments were performed with the rotor turning clockwise as in the last experiments described above (at $\phi=0.522$). These experiments are presented in Section 4.3.1.4.

Initial experiments in radial Rheo-SANS were performed with the large Couette at a 0.5 mm gap. A sample at $\phi=0.531$ and a second sample at $\phi=0.436$ were tested on NG7 SANS at 15 m detector distance with 6 Å neutrons. As the rheometer maximum stress was insufficient to achieve shear thickening in these samples, a smaller volume (and smaller bob surface area) Couette cell was designed for

subsequent testing to reach higher stresses. Later testing was done on a sample at $\phi=0.53$ and a second sample at $\phi=0.44$ using this geometry, on NG3 with a 13.2 m detector distance and 8 Å neutrons. The compositions of these samples, which used ethylene glycol rather than the deuterated ethylene glycol in the 1-2 plane SANS experiments, are shown in Table 4.1.

4.3 Results

Microstructure measurements via small angle neutron scattering were collected in the 1-2 plane of shear and the 1-3 plane (radial direction). The 1-2 plane measurements are the first measurements directly in the plane of shear and so are most novel. The 1-3 plane or radial SANS measurements are similar to those done before [23], but complement the 1-2 plane measurements to provide a three dimensional structure measurement of a near hard-sphere suspension.

Samples at multiple volume fractions were measured in 1-2 plane flow-SANS and radial Rheo-SANS. In addition, due to experimental difficulties and limitations in the geometries used, multiple experiments at similar volume fraction were performed. In the sections below, experiments will be grouped first by the plane of shear (4.3.1 and 4.3.2 show 1-2 plane and 1-3 plane experiments, respectively). Within each plane of shear grouping, data will be divided into different sections based on different concentrations which yield different rheological behavior – strong thickening, moderate thickening, and weak thinning. Within a section, there will either be experiments only on a single sample or experiments on multiple samples at similar volume fractions and with the same behavior. Where multiple samples are shown, a complete analysis will be shown on the first sample followed by a complete analysis

on a second sample. In addition, measurements of a suspension of coated, sticky hard-sphere particles that does not shear thicken will be shown for reference in section 4.3.1.4.

The organization of each analysis will show the rheology of the particular sample tested, measured in cone and plate geometry, along with rheology measured during the experiment for radial Rheo-SANS experiments. As the 1-2 plane shear cell does not have any measure of torque, there is no in situ rheology measurement associated with these experiments. After the rheology data for each particular sample, we will present the SANS data – first the 2-dimensional SANS spectra, then the annular average of the SANS spectra in the nearest neighbor ring, and finally the circular averaged data. In addition, the 2-dimensional data under shear have subtracted from it the static data and, for shear rates in the thickening regime, the data at high shear before the thickening regime; these measurement gives a more clear indication of the structural *changes* under shear and going into the thickened state. The circular averaged data will also be presented both as the reduced data and as the data with the static intensity subtracted off. This analysis of circular averaged data can be directly compared to results of microstructure measurements on suspensions of larger particles via USANS in Chapter 5.

In addition, in section 4.3.3, the neutron scattering data will be used with spherical harmonic decomposition to calculate relevant rheological parameters. First, data weighted by relevant harmonics will be shown as difference spectra from the static case to show the relevant harmonics. Then, the data normalized by the static data for the relevant harmonics will be shown. After that, this normalized, weighted data will also be weighted by the model structure factor; this description yields a

generalized description of the wavevector-dependent microstructure. Finally, integrations up to the peak in the structure factor of this last description of the microstructure will be calculated and used to calculate relevant rheological parameters.

These measurements will be compared qualitatively to the structures expected from Stokesian dynamics simulations and other experiments. In addition, gap-resolved SANS measurements from the 1-2 plane are included as Appendix C; these measurements show no significant change in the structure or concentration across the gap.

4.3.1 Flow-SANS in the Shear Plane (Flow-Gradient or 1-2 Plane)

4.3.1.1 Microstructure Measurements of Strongly Shear-Thickening ($\phi \sim 0.5$) Suspensions

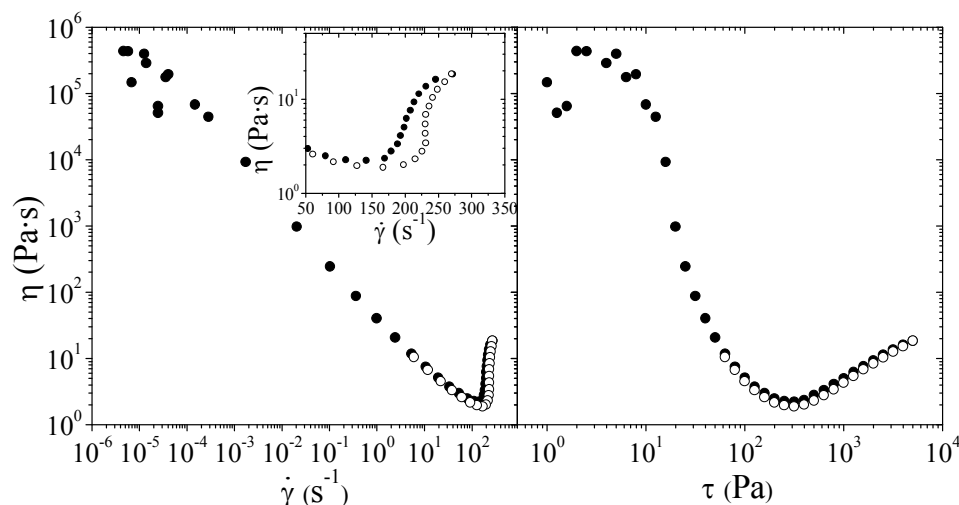


Figure 4.2 Steady shear rheological behavior for $\phi=0.515$ sample in partly deuterated solvent mixture used in following SANS experiments. (The data is measured on the exact sample tested in SANS experiments, but in a cone and plate geometry rather than the shear cell.) Filled symbols are forward sweeps and open symbols are backward sweeps.

Figure 4.2 shows the steady shear rheological data for the high concentration sample of silica in mixed PEG-600 and deuterated ethylene glycol (PEG/d-EG). The sample is seen to exhibit a yield stress, shear thinning, and nearly discontinuous shear thickening, as discussed in Chapter 3. The critical shear rate for shear thickening is approximately 200 s^{-1} or 300 Pa .

Figure 4.3 shows neutron scattering spectra from the 1-2 shear plane for this suspension. The arrows indicate the direction of shear in the sample relative to the

SANS detector. The top half of the figure is the 2-d scattering pattern measured under shear at various shear rates; the bottom half of the figure is that same 2-d scattering pattern with the pattern at rest subtracted from it to show the structural changes that are measured under shear. For further clarity of the geometry, see Figure 2.9. The SANS spectra seen in Figure 4.3 have a nearest neighbor ring and a second nearest neighbor ring. As the sample is sheared, increased peak intensity is observed in the nearest neighbor ring. With further increases in shear rate, the nearest neighbor ring scattering grows anisotropic, with low scattering along a 45° angle relative to the shear direction and high scattering on the particle leading and trailing edge (horizontal along the gradient direction on the figure). The nearest neighbor ring grows into a structure that is the shape of two comets rotating in the same direction. The data has a two-fold axis of symmetry rather than line symmetry.

A different representation of the data is shown as Figure 4.4. In this figure, the SANS data is shown as a 3-d depiction of the data under shear minus the static data combined with the relevant rheology, which accentuates the structural changes with increasing shear including the growth in anisotropy and the increased scattering in the nearest neighbor ring.

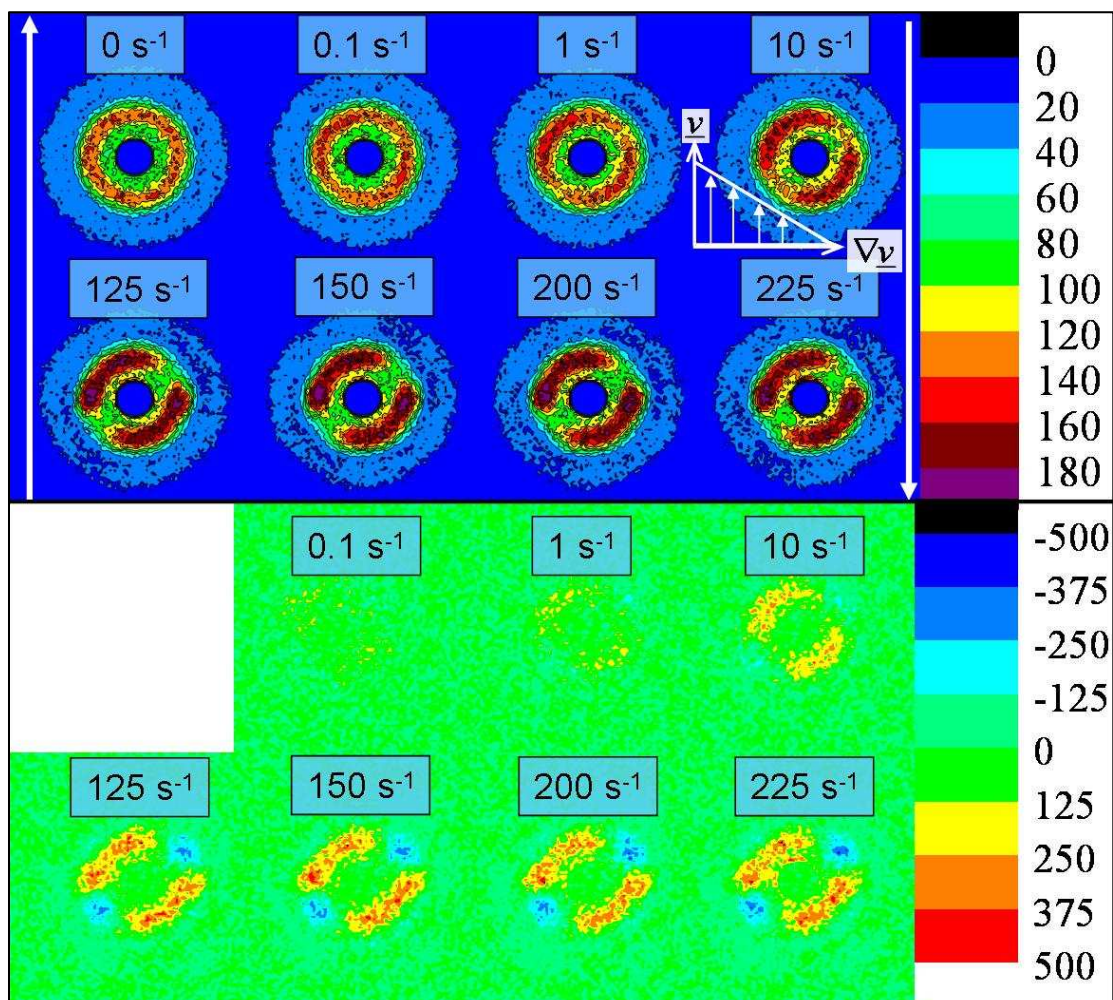


Figure 4.3 Small angle neutron scattering spectra from experiments on $\phi=0.515$ silica in partly deuterated solvent mixture sample in 1-2 plane flow-SANS. Top) SANS scattered intensity spectra. Bottom) SANS scattered intensity under shear minus static intensity.

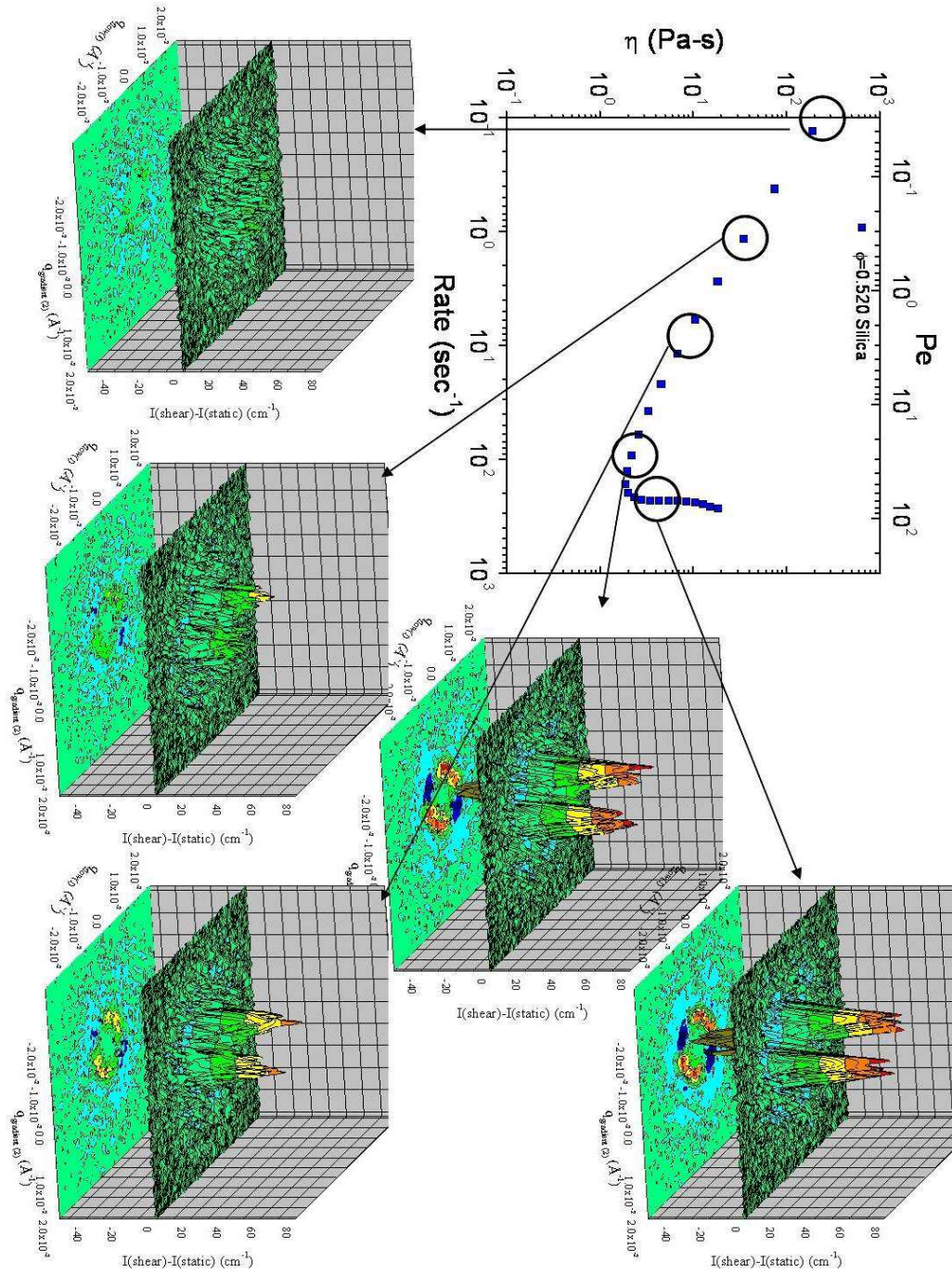


Figure 4.4 Evolution of microstructure in 1-2 Plane Flow-SANS for $\phi=0.515$ sample. Scattering data is data under shear at indicated shear rate minus static data.

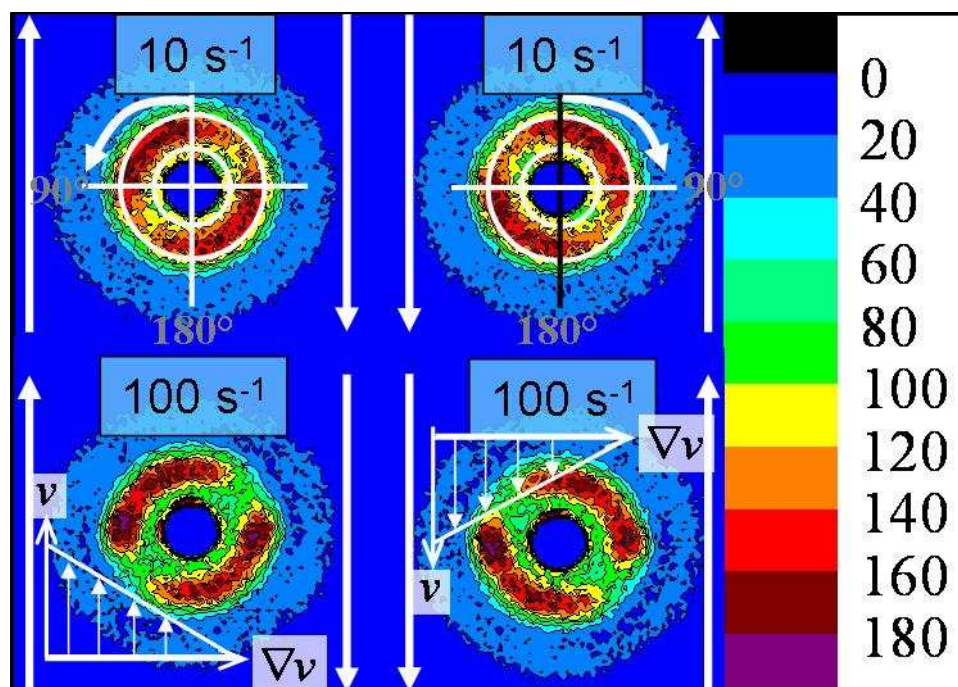


Figure 4.5 1-2 plane flow-SANS measurements exhibit varied scattering from changing the rotation direction. The arrows indicate the direction of shear.

Figure 4.5 shows how the direction of shear affects the structure measured by neutron scattering. It is important to note that in the other planes of shear, no change in the scattering pattern is measured if the shear direction is flipped. In this case, since we are measuring directly in the shear plane, we see the microstructure flip and show the mirror image (see [35] for similar results from simulations). Also indicated in this figure is the angle, θ , which starts at a vertical line through the center of the 2-d pattern and rotates for increasing angle either clockwise or counter-clockwise depending on the direction of shear. This value of theta is as defined from

the development of the spherical harmonics calculations in section 2.5.3 and Figure 2.9.

The anisotropy is summarized in Figure 4.6 as the scattered intensity averaged over the nearest neighbor ring as a function of angle. This average is performed over the nearest neighbor ring (graphically indicated in Figure 4.5), which for these samples and instrument configuration is a ring with center q value of 0.005 \AA^{-1} and a width of 5 detector pixels (i.e., from 0.0040 to 0.0060 \AA^{-1}). At rest, the sample is isotropic and little change is seen in the scattered intensity as a function of angle. As shear is applied, the scattered intensity as a function of angle has many features which are consistent amongst the different shear rates, with intensity increasing as the shear rate is increased. From 0° to 90° , there is little change in the annular averaged scattered intensity with angle, but it does have a local minimum at 45° then another maximum at $80-90^\circ$. The intensity over this angle range does increase with shear at lower shear rates, with little change with increasing shear above 125 s^{-1} . The scattered intensity is seen to decrease sharply as it goes from 90° to $120-130^\circ$, where it has a minimum. The intensity then increases strongly up to $170-180^\circ$. The slope of the decrease from $\sim 90-120^\circ$ is much steeper than the increase from $\sim 120-180^\circ$. The data beyond 180° has the same behavior as the first 180° and show the data to clearly be periodic with the two-fold axis of symmetry as discussed earlier, not symmetric about a line. The peaks at $80-90^\circ$ and $260-270^\circ$ are slightly larger than those at $0-10^\circ$ and $180-190^\circ$.

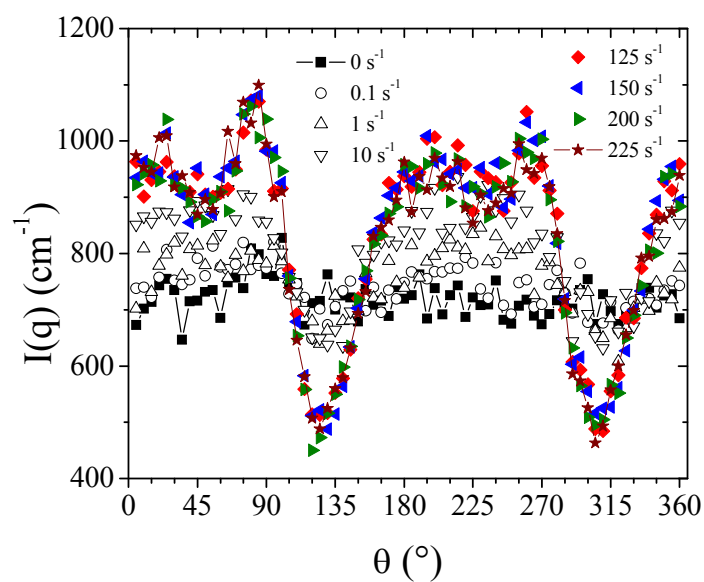


Figure 4.6 Annular averaged SANS spectra from 1-2 plane flow-SANS on $\phi=0.515$ sample. The line is included on the static data and highest rate data to guide the eye.

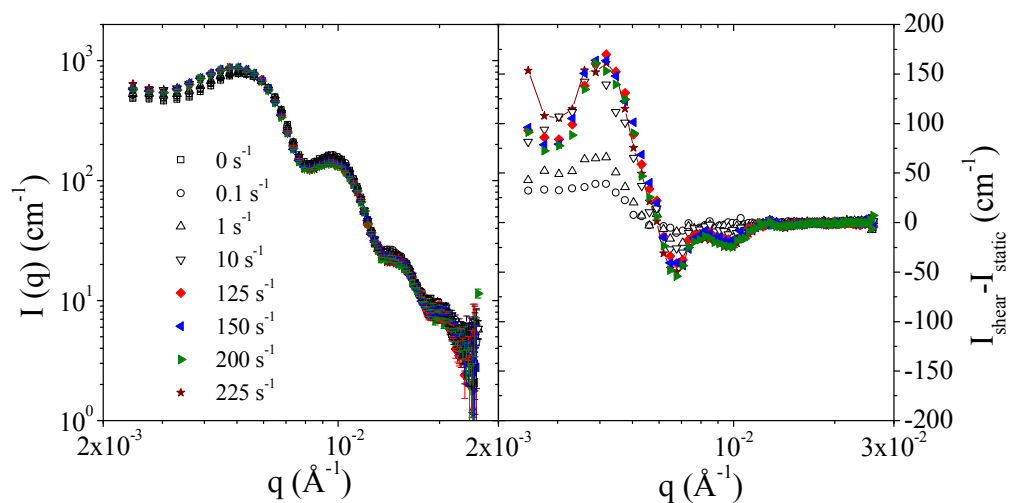


Figure 4.7 Circular averaged 1-2 plane flow-SANS data on $\phi=0.515$ sample. The line is included on the highest rate data to guide the eye.

Figure 4.7 summarizes the circular averaged neutron scattering data or the intensity (I) as a function of scattering vector magnitude (q). Increases in the measured intensity are evident at low q , within and below the nearest neighbor peak. The difference spectra, shown on the right in the picture, has a peak at about $4 \times 10^{-3} \text{ \AA}^{-1}$. In addition, a minimum in the subtracted intensity develops at higher shear rates at about $7 \times 10^{-3} \text{ \AA}^{-1}$. This peak and minimum is indicative of compression and clustering in the structure caused by changes in the structure factor [94].

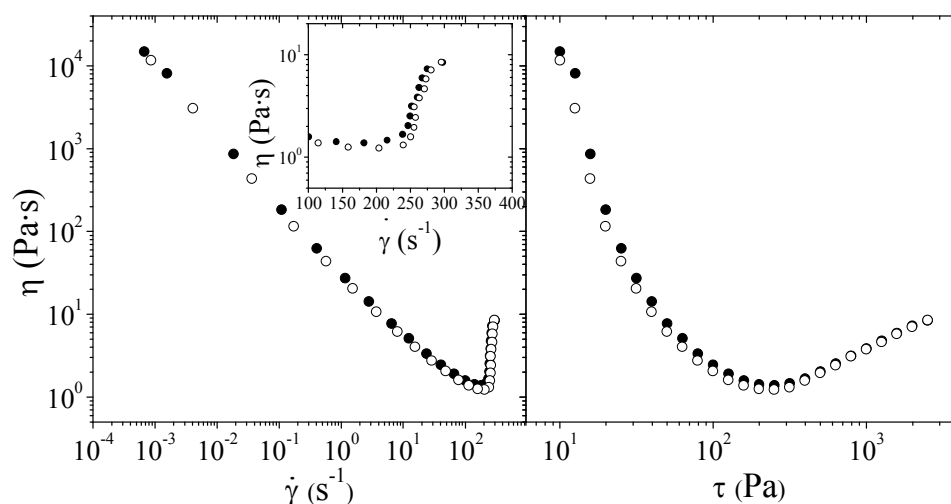


Figure 4.8 Steady shear rheological behavior for $\phi=0.522$ sample in partly deuterated solvent mixture tested in following SANS experiments. Filled symbols are forward sweeps and open symbols are backward sweeps.

Due to a lack of significant data measured in the shear thickened state on the prior sample, subsequent measurements were performed on a similar sample with a smaller gap. Figure 4.8 shows the steady shear rheology data for a sample at $\phi=0.522$,

tested using 1-2 plane flow-SANS in experiments detailed below. This data has similar behavior to that seen from the sample in Figure 4.2, but the critical shear rate for thickening is slightly higher at 250 s^{-1} . This sample was tested with the smaller, 1.0 mm gap in the 1-2 plane shear cell and so data was collected in the shear-thickened state while maintaining sample integrity.

Figure 4.9 shows the SANS intensity from this sample at numerous shear rates. Once again, the top half of the figure is the scattered intensity and the bottom half is the subtraction of data under static conditions from that under shear. It is important to note that these experiments were done with the shear in the opposite direction compared to the prior experiments, but the SANS spectra has been flipped vertically to correct and the arrows indicate the same shear direction. These results show similar behavior as the prior sample. Limited anisotropy is seen even at the lowest shown shear rate of 1 s^{-1} , which is already well into the shear thinning regime of the rheology. The degree of anisotropy and magnitude of the scattered intensity in the nearest neighbor ring both increase with increasing shear rate. The same pattern as before is seen – increased scattering in the nearest neighbor ring in the shape of a pair of comets following each other and terminating along the velocity gradient direction.

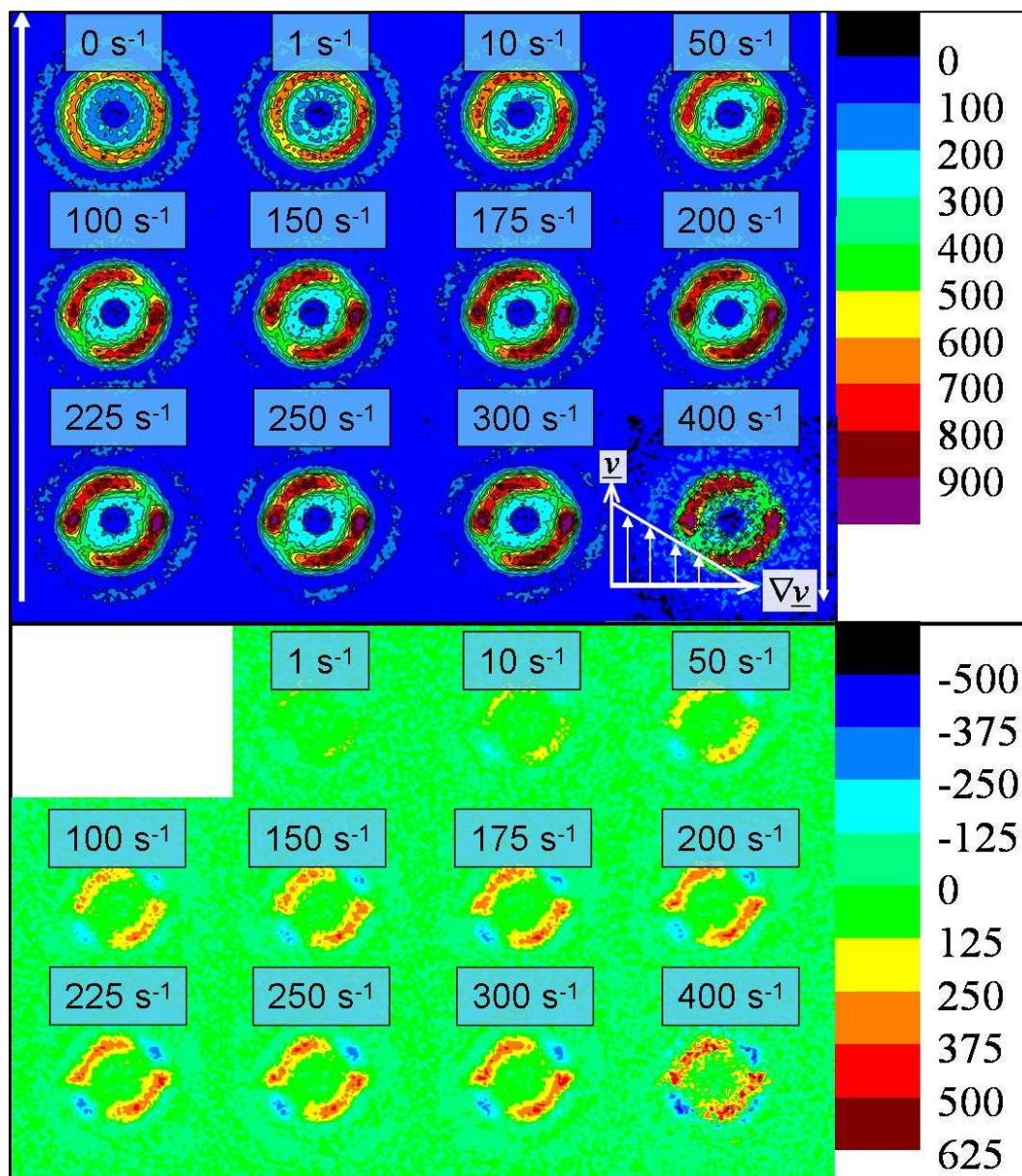


Figure 4.9 SANS scattering spectra from $\phi=0.522$ sample in 1-2 plane flow-SANS with additional high shear rate data. A larger rotor (smaller gap) was used to achieve higher shear rates stably. The measurement at 400 s^{-1} is noisy due to shortened counting time. Top) SANS scattered intensity spectra. Bottom) SANS scattered intensity under shear minus static intensity.

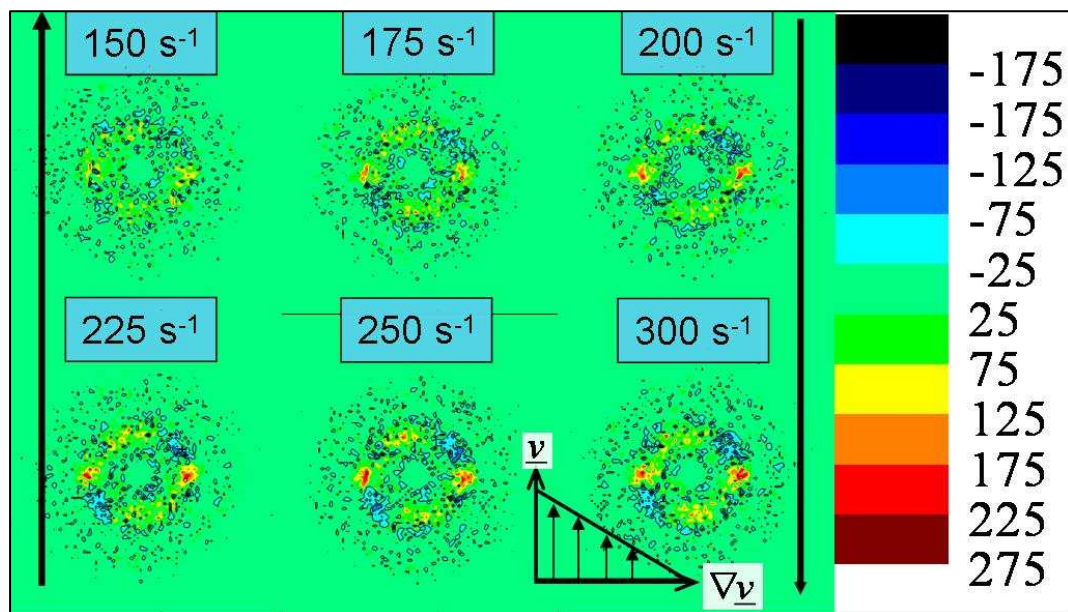


Figure 4.10 SANS subtraction pattern – shear thickened state minus pre-thickened state (100 s^{-1}) from $\phi=0.522$ sample in 1-2 plane flow-SANS.

Figure 4.10 shows the data at high shear rates, in the thickened state, with the pattern at high shear rate just before shear thickening (100 s^{-1}) subtracted. This transformation of the data accentuates the structural changes that the sample undergoes in the transition from the shear thinning regime to the shear thickened state. The outer ring has decreased scattering, indicative of less particle concentration in this secondary structure peak. The inner, nearest neighbor ring has a net increase in scattering, with a pattern that has similar peak locations and relative values as the non-subtracted scattering data. The highest scattered intensity is seen along the velocity and velocity gradient axes (vertical and horizontal), with a thin band of increased scattering

between them at 135° and 315° . The peaks in the velocity gradient directions are larger and higher intensity than those in the velocity directions.

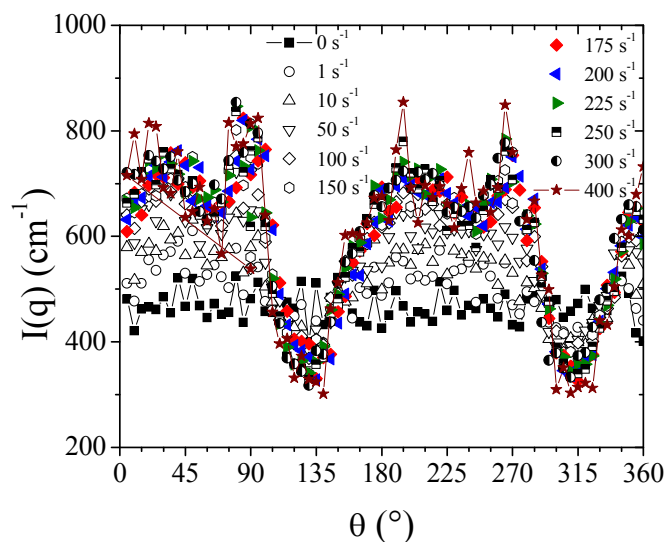


Figure 4.11 Annular averaged SANS spectra from 1-2 plane flow-SANS on $\phi=0.522$ sample. The line is included on the static data and highest rate data to guide the eye.

Figure 4.11 shows the annular averaged results which are also consistent with the prior results (the angle has been defined consistently regardless of the shear direction). This average is also over the q -range of 0.0040 to 0.0060, but due to the difference in instrument configuration from the prior experiments, that is a center q of 0.005 \AA^{-1} and a width of 7 pixels. Once again, there are peaks at $\sim 15^\circ$ and 90° with a plateau in between and the latter being a slightly higher peak. In addition, there is a minimum at $\sim 135^\circ$.

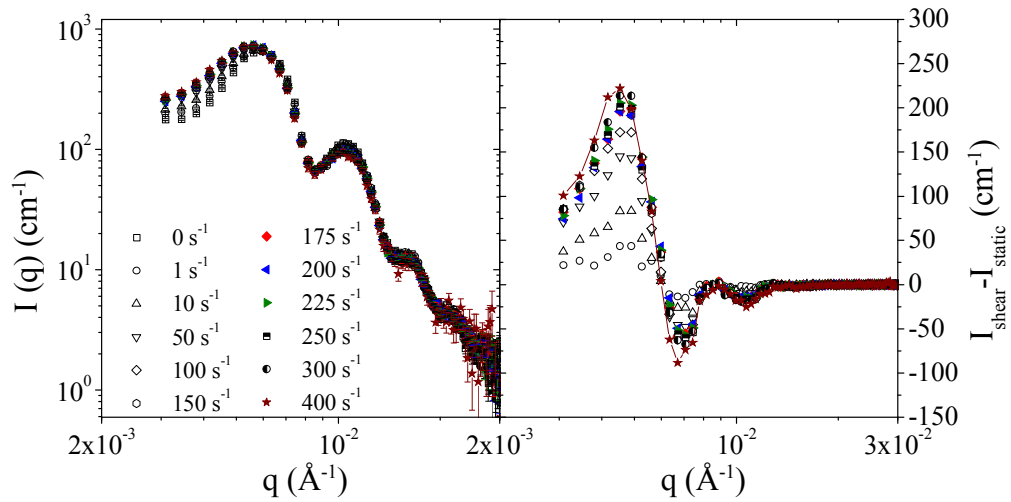


Figure 4.12 Circular averaged SANS data from $\phi=0.522$ sample in 1-2 plane flow SANS at various shear rates. The line is included on the highest rate data to guide the eye.

Figure 4.12 shows circular averaged results which are generally consistent with the prior results. One important change in the circular averaged results is that this set of experiments has a larger increase in the low- q scattering at the highest shear rates measured compared to the prior sample. A peak in the scattering difference curve (I_{shear} minus I_{static}) develops, centered around 0.0045 \AA^{-1} , along with a minimum at 0.0067 \AA^{-1} . Note that the relative scattering ($I_{\text{shear}}/I_{\text{static}}$) for many of these samples are shown in section 4.3.3 as W_0 .

Table 4.2 shows transmission measurements for both samples described in this section. The transmission values fluctuate slightly ($\sim 1.3\%$) at different shear rates for each sample. The difference in the average transmission value between the two samples is caused by both the sample differences and the instrument configuration (neutron wavelength).

Table 4.2 Transmission values from $\phi \sim 0.5$ samples in 1-2 plane flow SANS.

Oct 2006 - 1-2 plane, $\phi=0.515$			Aug 2009 - 1-2 plane, $\phi=0.522$		
Run #	Shear Rate (s^{-1})	Transmission	Run #	Shear Rate (s^{-1})	Transmission
230	10	0.250	45	0	0.217
232	-10	0.250	48	1	0.215
234	0	0.253	49	10	0.219
237	0.1	0.251	52	50	0.220
238	0.2		53	100	0.220
239	0.5		56	150	0.220
240	1	0.252	57	175	0.218
242	2		60	200	0.216
243	5		61	0	0.217
244	10	0.250	64	225	0.215
246	20		65	250	0.217
247	50		68	300	0.217
248	100	0.253	69	0	0.219
251	125	0.253	72	400	0.220
252	150	0.253			
257	200	0.254			
260	225	0.254			
261	175	0.249			
264	100	0.253			
265	1	0.255			
268	0	0.253			
269	100	0.253			
271	-100				

4.3.1.2 Microstructure Measurements of Moderately Shear-Thickening ($\phi \sim 0.4$) Suspensions

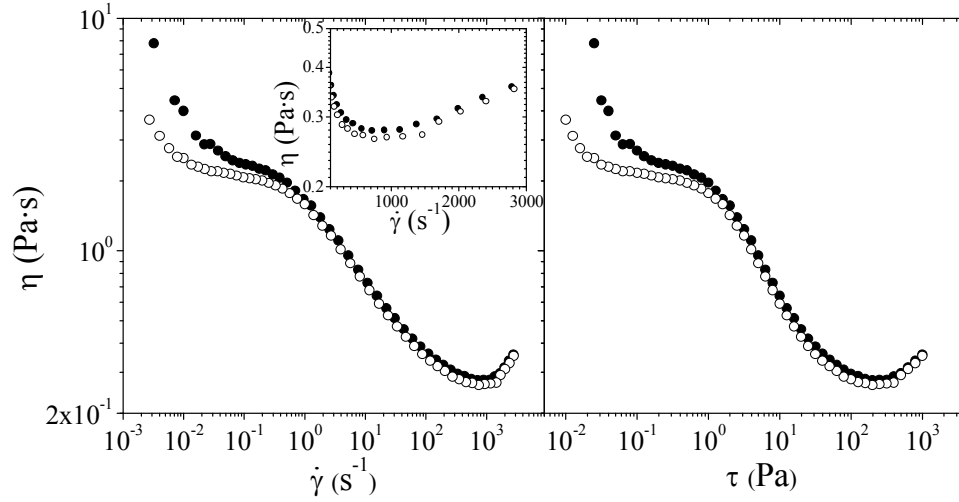


Figure 4.13 Steady shear rheological behavior for $\phi=0.40$ sample in partly deuterated solvent mixture tested in following SANS experiments. Filled symbols are forward sweeps and open symbols are backward sweeps.

The microstructure of a lower concentration sample at $\phi=0.40$ was also measured via 1-2 plane flow-SANS. The rheology of that suspension is seen in Figure 4.13. This sample has some yielding at low stresses, followed by an apparent low shear plateau, strong shear thinning, and shear thickening. The shear rates measured in the experiment are in the plateau and shear thinning regions of the curve; the shear thickened structure was not measured.

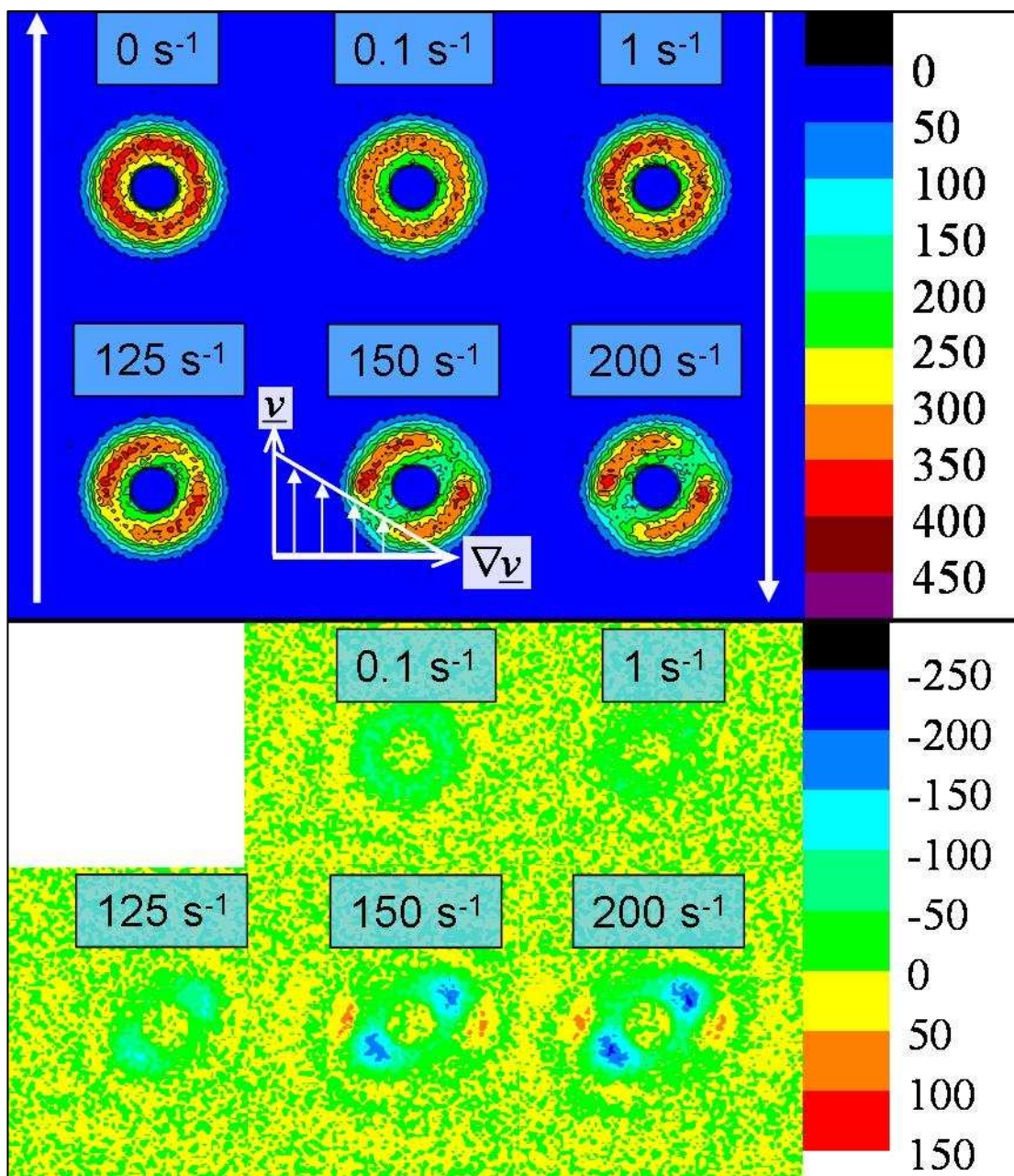


Figure 4.14 Small angle neutron scattering spectra from experiments on $\phi=0.40$ silica in partly deuterated solvent mixture sample in 1-2 plane flow-SANS. Top) SANS scattered intensity spectra. Bottom) SANS scattered intensity under shear minus static intensity.

Figure 4.14 shows SANS spectra from these measurements. As seen before for the higher concentration samples, the pattern is relatively isotropic at low shear rates. In fact, the pattern has little anisotropy at 1 s^{-1} , whereas the higher concentration samples already had significant anisotropy at that shear rate. The significant anisotropy is apparent at 125 s^{-1} and above, with similar characteristics as that seen in the most concentrated samples in the prior section. The difference pattern clearly shows spots of decreased intensity under shear growing at 45° angles between the flow and gradient directions, with increased intensity primarily noticeable along the gradient direction.

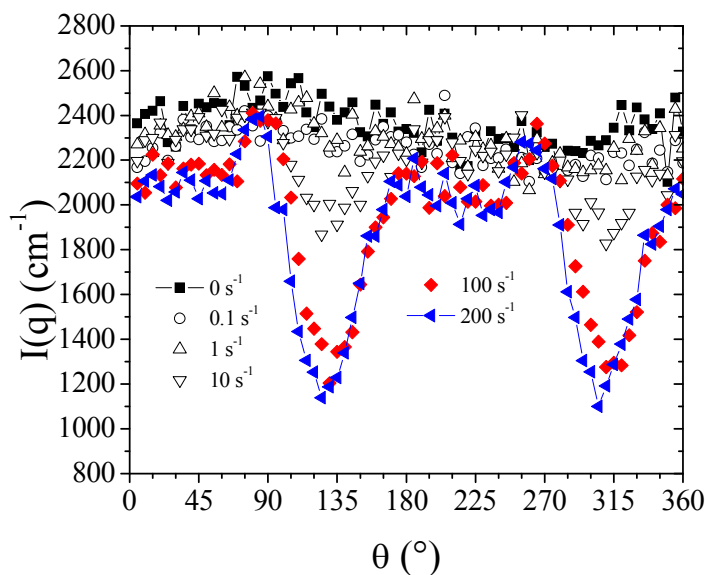


Figure 4.15 Annular averaged SANS spectra from 1-2 plane flow-SANS on $\phi=0.40$ sample. The line is included on the static data and highest rate data to guide the eye.

Figure 4.15 shows the annular averages of this data. For this instrument configuration, the annular average is calculated from 0.0040 to 0.0060 Å⁻¹ (q-center of 0.005Å⁻¹, Δq of 5 pixels). It is important to note that the sample transmission increased when the sample was measured at the highest shear rates of 100 and 200 s⁻¹ as seen in the transmission measurements in Table 4.3. This increase in transmission is indicative of air bubbles being introduced into the system. It also causes the decrease in overall scattering at the highest shear rates seen in Figures 4.15 and 4.16. With consideration for this sample transmission issue, the anisotropy in these results is consistent with that seen for the more concentrated suspensions, with peaks in the same locations in the annular average.

Table 4.3 Transmission data from $\phi=0.40$ sample in 1-2 plane flow SANS.

Oct 2006 - 1-2 plane, 40pc		
Run #	Shear Rate (s ⁻¹)	Transmission
273	0	0.199
276	0.1	0.199
277	0.2	
278	0.5	
279	1	0.199
281	2	
282	5	
283	10	0.203
285	20	
286	50	
287	100	0.214
290	200	0.214
291	0	0.221

Figure 4.16 shows the circular average SANS data for the $\phi=0.40$ suspension. As discussed previously, due to experimental error introducing air bubbles into the sample, the transmission causes the overall scattered intensity to decrease at the highest shear rates. Therefore, the same result as before of increased low-q scattering with a slight decrease outside the nearest neighbor peak is not clearly seen. This decrease in scattering at high shear rates is indicative of this sample scattering volume lost by introduction of air bubbles and not in contradiction to the clustering seen via increased low-q scattering.

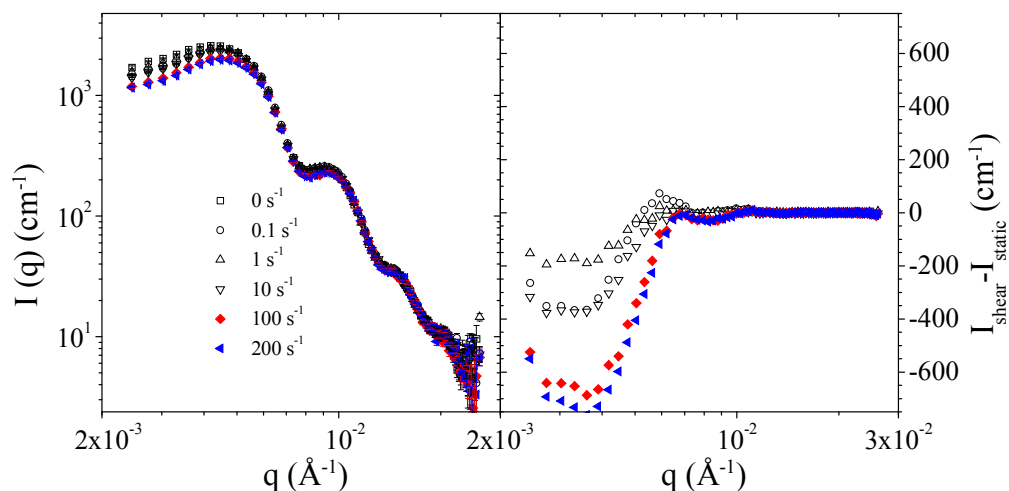


Figure 4.16 Circular averaged SANS data from $\phi=0.40$ sample in 1-2 plane flow SANS at various shear rates. The line is included on the highest rate data to guide the eye.

4.3.1.3 Microstructure Measurements of Low Concentration ($\phi \sim 0.2$), Shear-Thinning Suspension

Additional experiments were performed in the 1-2 plane shear cell on a weakly shear thinning sample at $\phi=0.20$, with rheology seen in Figure 4.17. This sample has a steep initial drop in the viscosity at the lowest shear rates, below 1 s^{-1} , which is likely yielding as seen in the more concentrated samples. The viscosity then has little change from $1\text{-}10 \text{ s}^{-1}$, with fluctuations within the error of this measurement. From $10\text{-}2000 \text{ s}^{-1}$ there is a drop of about 12% in the viscosity. This drop in viscosity is markedly different from the orders of magnitude changes seen in the more concentrated samples. Neither a plateau nor thickening was measured for this system at high shear stresses.

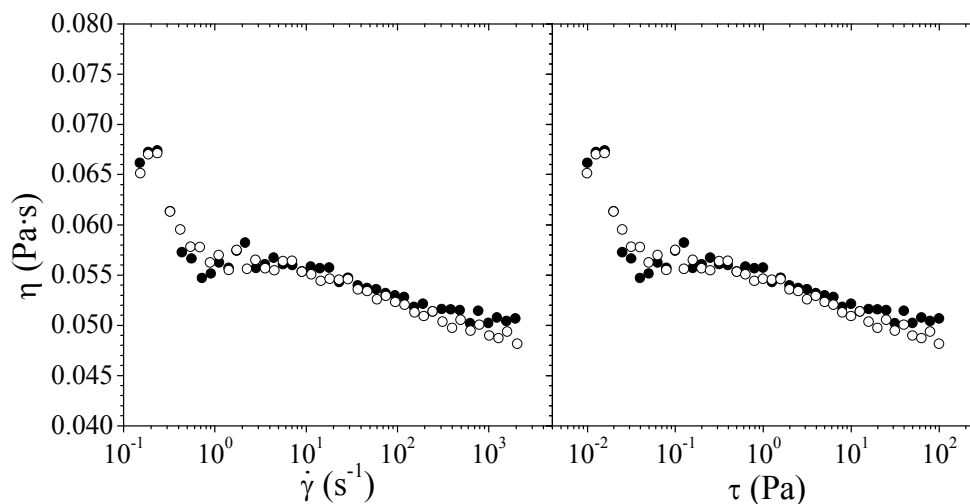


Figure 4.17 Steady shear rheological behavior for $\phi=0.20$ sample in partly deuterated solvent mixture tested in following SANS experiments. Filled symbols are forward sweeps and open symbols are backward sweeps.

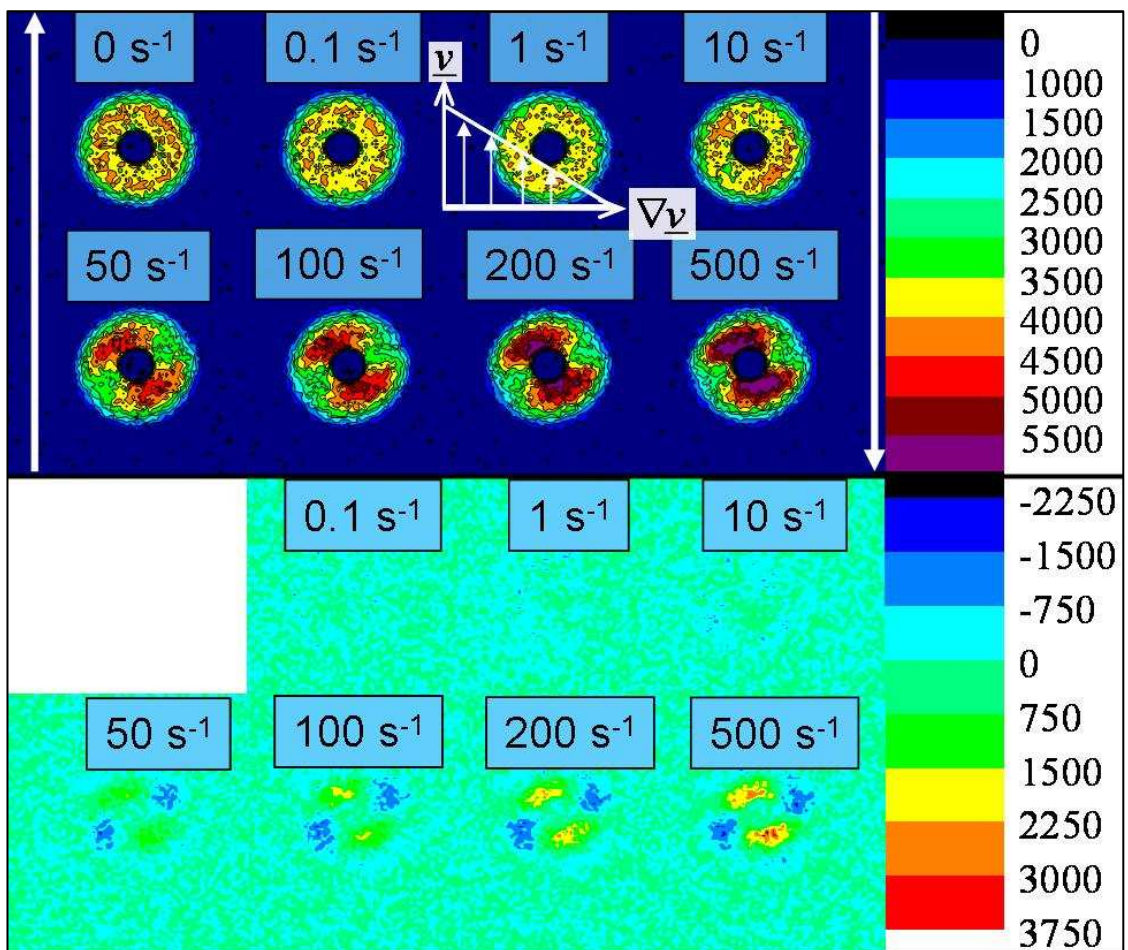


Figure 4.18 Small angle neutron scattering spectra from experiments on $\phi=0.20$ silica in partly deuterated solvent mixture sample in 1-2 plane flow-SANS. Top) SANS scattered intensity spectra. Bottom) SANS scattered intensity under shear minus static intensity.

Figure 4.18 shows the SANS scattering spectra of this sample at various shear rates. This sample is seen to begin having anisotropy at 10 s^{-1} , approximately the same location where shear thinning was identified in the rheology (rather than the apparent viscosity drop from yielding). Further inspection of the annular averaged data

in Figure 4.19 shows this anisotropy at 10 s^{-1} has a peak at ~ 50 and 230° , with a minimum at ~ 110 and 290° . The data at higher shear rates have similar structure to that seen at higher concentrations, except the angle ranges of high scattering are sharper, shaped more like peaks than the plateaus seen for higher concentration samples. In fact, the intensity grows monotonically from 0° to 45° , and then decreases consistently until $\sim 100^\circ$, before increasing again to the peak at 225° . It is important to note, the anisotropy in the structure is seen at a lower q -value – this average is done at a center q of 0.003 \AA^{-1} , with a Δq of 7 pixels (0.0020 \AA^{-1} width for an averaging range of $0.0020\text{-}0.0040 \text{ \AA}^{-1}$).

The circular averaged data is shown as Figure 4.20. This data has similar behavior as before with slight increases in the low q scattering with increasing applied shear rate. Unlike the prior experiments, a peak in the scattering difference at low q is not measured – the intensity difference between the sheared and static suspensions has an increase at low q with no measured peak. The intensity difference does increase with increasing shear rate. Like the experiments at higher concentration, a minimum is seen at $0.0043\text{-}0.0045 \text{ \AA}^{-1}$.

Table 4.4 shows the transmission values. Once again, little change is seen in the transmission indicative of maintaining sample integrity throughout these experiments. The lower overall sample transmission compared to the prior samples is due both to the instrument configuration (neutron wavelength) and the sample composition (increased quantity of hydrogen due to lower silica concentration).

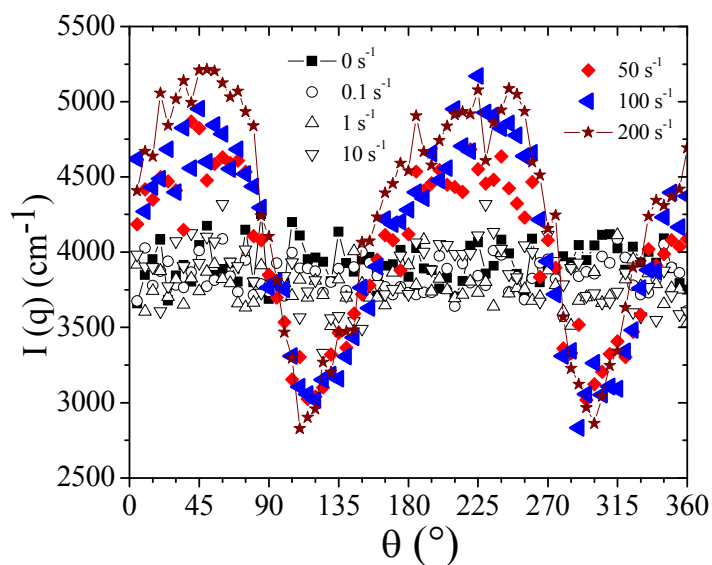


Figure 4.19 Annular averaged SANS spectra from 1-2 plane flow-SANS on $\phi=0.20$ sample. The line is included on the static data and highest rate data to guide the eye.

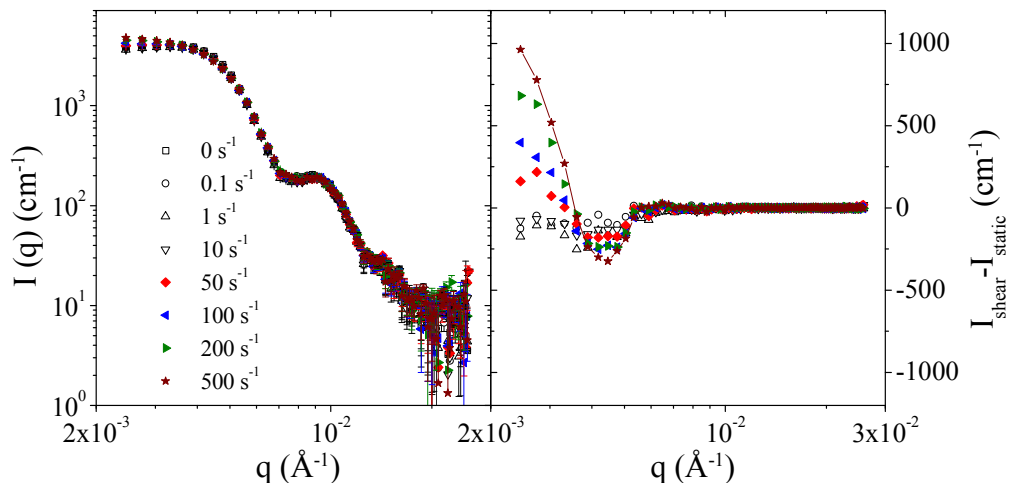


Figure 4.20 Circular averaged SANS data from $\phi=0.20$ sample in 1-2 plane flow SANS at various shear rates. The line is included on the highest rate data to guide the eye.

Table 4.4 Transmission measurements from $\phi=0.20$ sample in 1-2 plane flow SANS.

Sep 2007 - 1-2 plane $\phi=0.20$		
Run #	Shear Rate (s^{-1})	Transmission
220	0	0.00862
223	0.1	0.00848
224	0.2	
225	0.5	
229	1	0.00869
231	2	
232	5	
233	10	0.00853
235	20	
236	50	
237	100	0.00868
240	200	0.00859
241	500	0.00860
245	1000	0.00855

4.3.1.4 Microstructure Measurements of Non-Thickening, High Concentration ($\phi_{\text{core}} \sim 0.5$), Polymer Coated Sticky Hard-Sphere Particle Suspension

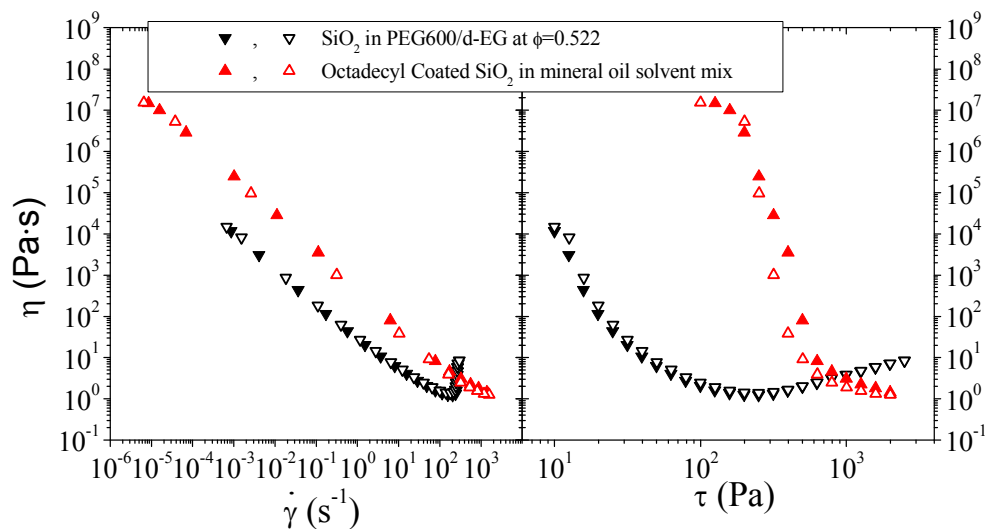


Figure 4.21 Steady-shear rheology comparison of octadecyl-coated 60 nm silica in mineral oil solvent mix to standard 60 nm silica in PEG-600 and ethylene glycol solvent mix. Filled symbols are forward sweeps and open symbols are backward sweeps.

Figure 4.21 shows a comparison of the 60 nm octadecyl coated silica in mineral oil and deuterated dodecane mix to the suspension rheology shown in Figure 4.8, the $\phi=0.522$ 60 nm silica suspension in the mixture of PEG-600 and deuterated ethylene glycol. Specifically, the suspension is formulated to have a similar volume fraction of particle cores (with the same density as the original particles) when the polymer coating shell is assumed to act as additional solvent (at the same density as the solvent). The coating is seen to suppress the shear thickening as seen previously [18, 45]. Higher shear rates were not achieved as the sample comes out of the gap, in a manner similar to that seen in a rod-climbing non-Newtonian polymer solution. The

coating has previously been measured in the fluid state (this and similar suspensions gel at lower temperatures) to be 1.85 nm, consistent with expectations from the carbon chain length [95]. Note that, this coating suppresses the thickening, but the excluded volume shell seen in the original suspensions in prior sections and Chapter 3 allows for thickening even with a larger shell thickness. Therefore, the physical polymer chain coating in the original suspensions must either be significantly shorter than the measured excluded volume meaning that the excluded volume is not primarily steric stabilization, or the coating in the original suspensions is sparse enough to still allow for lubrication hydrodynamics in close gaps between particles driving thickening.

Figure 4.22 shows this rheology data on a reduced viscosity versus Péclet number plot. The suspension is seen to reach similar Péclet numbers as the original suspension. Rather than shear thickening, the suspension ejects from the gap in the cone and plate experiments. Additional experiments in a non-sealed lab Couette on similar suspensions also had the sample come out of the gap at these high shear rates. Note that, in both Figure 4.21 and 4.22, the octadecyl coated silica suspension rheology was measured at 30°C. The SANS measurements for this sample were also done at 30°C by elevating the ethylene glycol bath which provides temperature control to the shear cell.

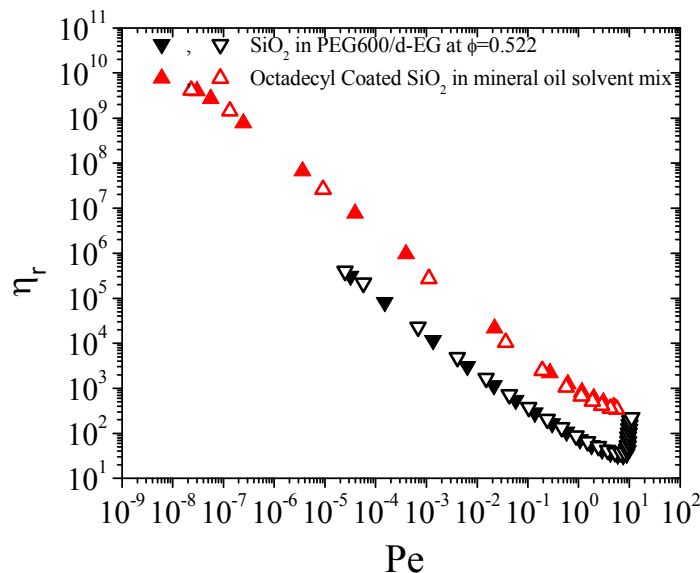


Figure 4.22 Rheology comparison of reduced viscosity versus Péclet number for coated, thickening-suppressed suspensions compared to uncoated suspension. Filled symbols are forward sweeps and open symbols are backward sweeps.

Figure 4.23 shows the 2-dimensional SANS spectra for these coated silica suspensions at various shear rates. These suspensions have qualitatively similar behavior to the high concentration suspensions that were not coated in this manner. The scattered intensity in the nearest neighbor ring increases under shear and begins to have some anisotropy even at the lowest measured shear rate (10 s^{-1}). The anisotropy grows with increasing shear rate and appears to saturate or become unchanging with increasing shear rate above 1000 s^{-1} .

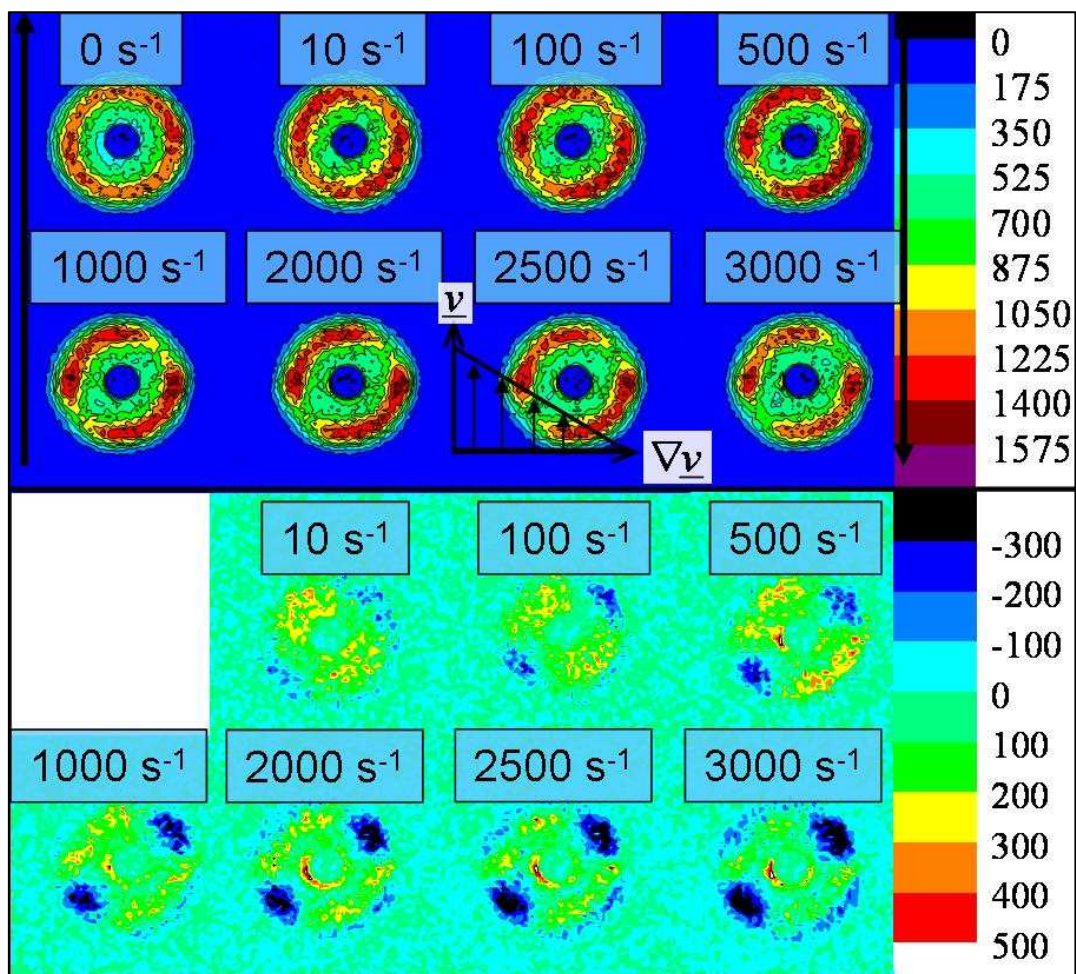


Figure 4.23 Small angle neutron scattering spectra from experiments on octadecyl-coated silica in partly deuterated solvent mixture sample in 1-2 plane flow-SANS. Top half) Scattering data. Bottom half) Scattering data under shear with static data subtracted.

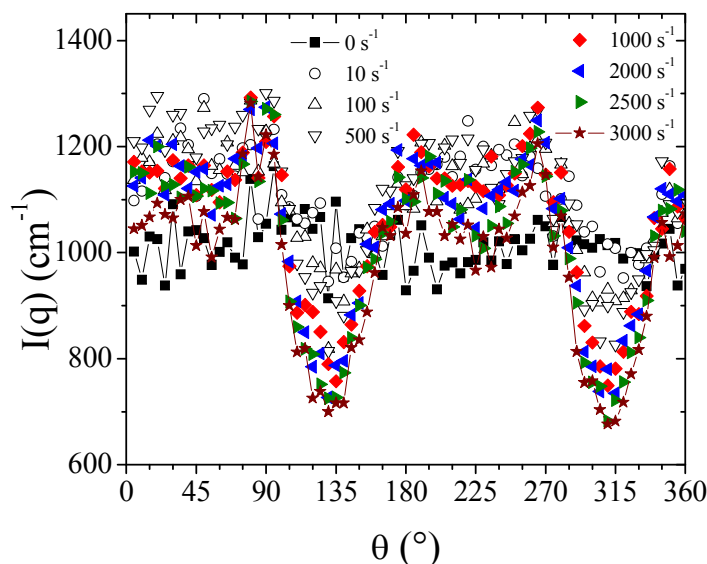


Figure 4.24 Annular averaged SANS spectra from 1-2 plane flow-SANS on octadecyl-coated silica sample. The line is included on the static data and highest rate data to guide the eye.

Figure 4.24 shows the annular averaged data for these suspensions. This average is performed over the q -range of 0.0040 to 0.0060, (center q of 0.005 \AA^{-1} , Δq of 7 pixels). These annular averages have generally similar behavior as the high concentration uncoated suspensions, although there is very little net increase in scattering in the nearest neighbor ring. The pattern does grow anisotropic with a peak at 90° and 270° , minima at 135° and 315° , and plateaus from 0 - 90° and 180 - 270° . At the highest shear rates (greater than 1000 s^{-1}), the plateaus decrease in intensity with increasing shear rate. In addition, local minima within the plateau at ~ 60 and 240° are seen, which have decreasing values of the intensity with increases in shear rate at the high shear rates. Unlike the uncoated suspensions, the anisotropy in these suspensions comes from increased scattering at the peaks and decreased scattering at the minima and plateaus compared to the static case. In the uncoated suspensions, only small

decreases in the intensity were seen between the peaks at 0° and 90° or 180° and 270° and the increase in scattering at the peak came from an overall increase in scattering within the nearest neighbor ring.

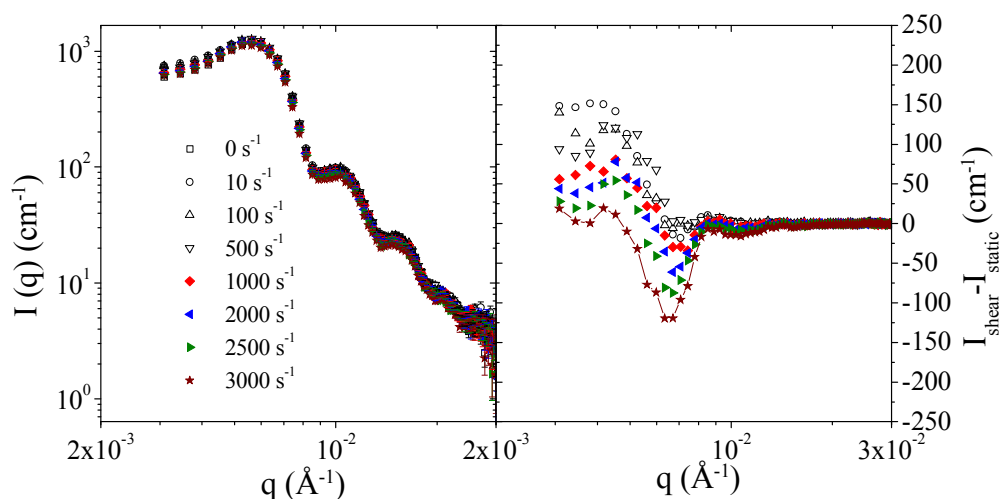


Figure 4.25 Circular averaged SANS data from octadecyl-coated silica sample in 1-2 plane flow SANS at various shear rates. The line is included on the highest rate data to guide the eye.

Figure 4.25 shows the circular averaged SANS data for this suspension. At the lower shear rates measured, an increase in the scattered intensity is seen with increasing shear rates at low values of q . With increasing shear rate beyond 1000 s^{-1} , the scattered intensity decreases at low q , in stark contrast to the experiments with uncoated suspensions. Overall, relative to the magnitude of the scattering, these changes in the intensity are small. The maximum change in intensity under shear from the static case ($I_{\text{shear}} - I_{\text{static}}$) is 150 cm^{-1} , which relative to the scattered intensity value of ~ 700 at the peak in the difference curve at $4 \times 10^{-3} \text{ \AA}^{-1}$ is about 20%, whereas the

difference for uncoated particles seen in Figure 4.12 is 250 cm^{-1} relative to scattering values of around 500 cm^{-1} , for a change of 50%.

Table 4.5 shows the transmission values measured during shear for these suspensions. The average value is 0.121 with a standard deviation of 0.002 and there is no systematic trend with shear rate, suggesting the sample integrity is maintained at all shear rates.

Table 4.5 Transmission values for low concentration samples in 1-2 plane flow-SANS.

Aug - 2009 - 1-2 Plane – Coated, $\phi_{\text{core}} \sim 0.5$		
Run #	Shear Rate (s^{-1})	Transmission
84	0	0.120
86	1	0.118
87	1	0.118
90	10	0.117
91	100	0.117
94	500	0.119
95	0	0.121
99	0.1	0.122
100	50	0.121
103	200	0.123
105	1000	0.122
106	0	0.123
109	2000	0.119
110	0	0.122
111	0	0.122
114	2500	0.120
115	2750	0.122
118	3000	0.122
119	0	0.122

4.3.2 Radial (1-3 Plane) Rheo-SANS Microstructure Measurements

4.3.2.1 Microstructure Measurements of Strongly Shear-Thickening ($\phi \sim 0.5$) Suspensions

Measurements on similar samples were also done in radial Rheo-SANS. These samples did not use deuterated solvent as the lower path length in this experiment helps to reduce the multiple scattering as an issue. In addition, as the shear cell in these experiments is attached to a rheometer, rheological measurements are performed simultaneously with the neutron scattering experiments.

Figure 4.26 shows the steady-shear rheology for a high concentration sample. The half-filled points connected by a line are those measured during the SANS experiment in the SANS Couette. The sample has a yield stress of about 1 Pa, shear thins at moderate stresses, and shear thickens with a critical stress of 200 Pa and critical rate of 100-200 s⁻¹. The rheology measured in the sample cell follows that from the cone and plate geometry experiments, albeit with a slightly larger viscosity at all shear rates.

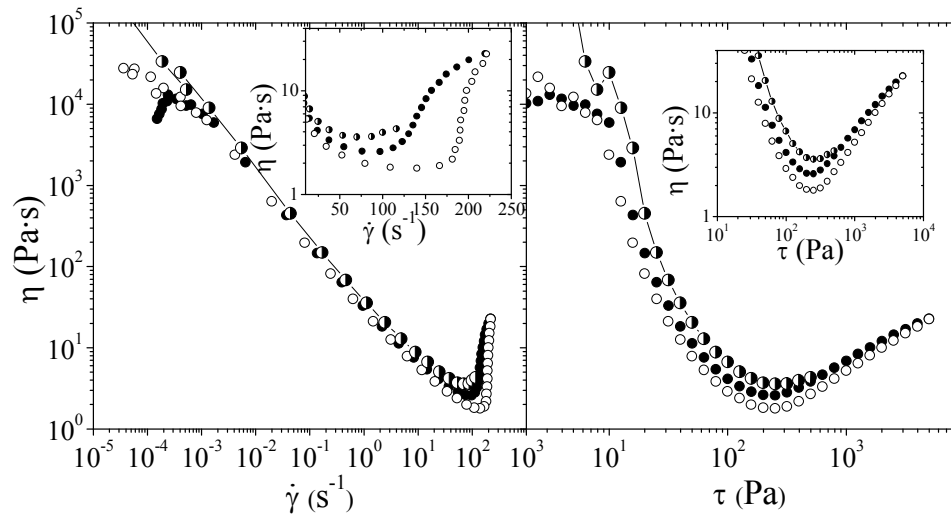


Figure 4.26 Steady shear rheological behavior for $\phi=0.531$ sample tested in following SANS experiments. Filled symbols are forward sweeps and open symbols are backward sweeps. The half filled circles connected by a line are the data directly from the SANS rheometer during scattering measurements.

Figure 4.27 shows SANS scattering spectra at various shear stresses for this high concentration sample in radial Rheo-SANS. Once again, the top half of the figure shows the SANS scattering spectra and the bottom half shows the difference pattern between that under shear and that under static conditions. Anisotropy in the pattern is first seen at 63 Pa (shown much better by the subtraction pattern in the bottom half of the figure). In addition, the left portion of the outer scattering ring is flattened and has a line, due to spurious noise in the neutron detection system which was not masked out in these images – there is no reason to believe the outer ring scattering would not be isotropic without this instrument issue. The anisotropy at the highest stresses appears as increased scattering in opposing crescent moon shaped bands oriented in the vorticity direction. The total scattered intensity is much larger in

these samples due to the higher particle-solvent contrast from using non-deuterated solvents. For this sample, regular measurements of the sample neutron transmission were not done – the sample transmission measured under static conditions was 0.570.

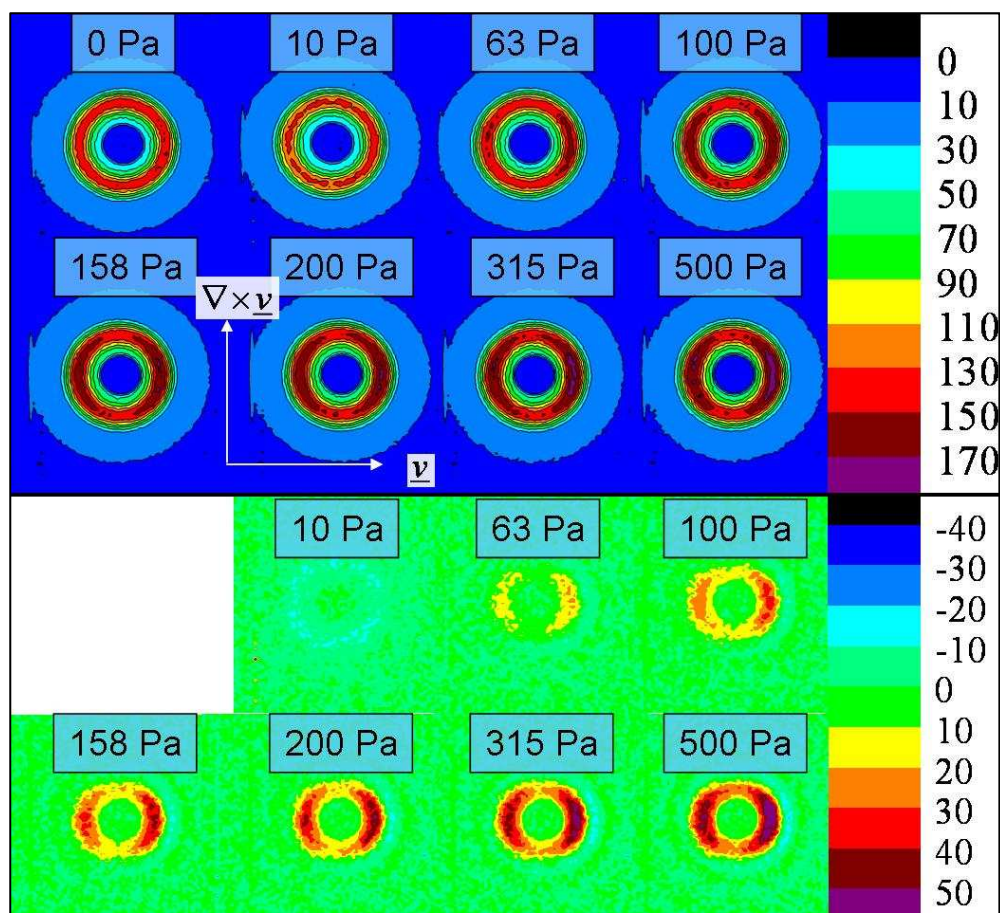


Figure 4.27 Small angle neutron scattering spectra from experiments on $\phi=0.531$ sample in radial Rheo-SANS. Intensity is $\text{cm}^{-1}/100$. Top half) Scattering data. Bottom half) Scattering data under shear with static data subtracted.

Figure 4.28 shows a diagram of the angle for the annular averaged measurements on these radial SANS patterns. For clarity, the angle from radial SANS patterns is termed θ_{rad} . This angle is defined such that 0° is the velocity direction (\underline{v} or 1) and 90° is the vorticity direction ($\nabla \times \underline{v}$ or 3).

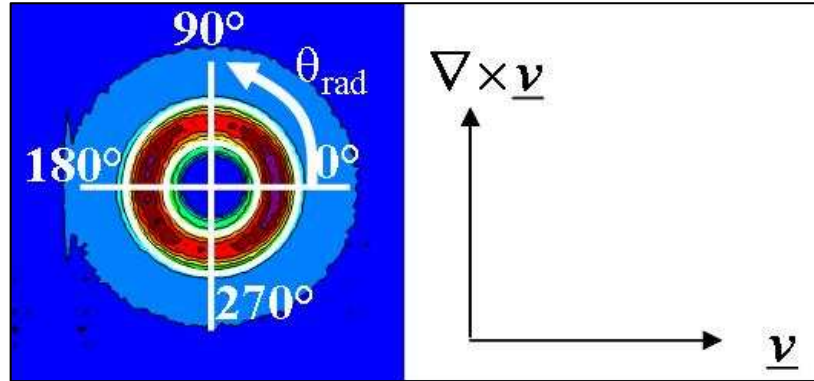


Figure 4.28 Diagram of angular averaging on radial SANS data and definition of θ_{rad} .

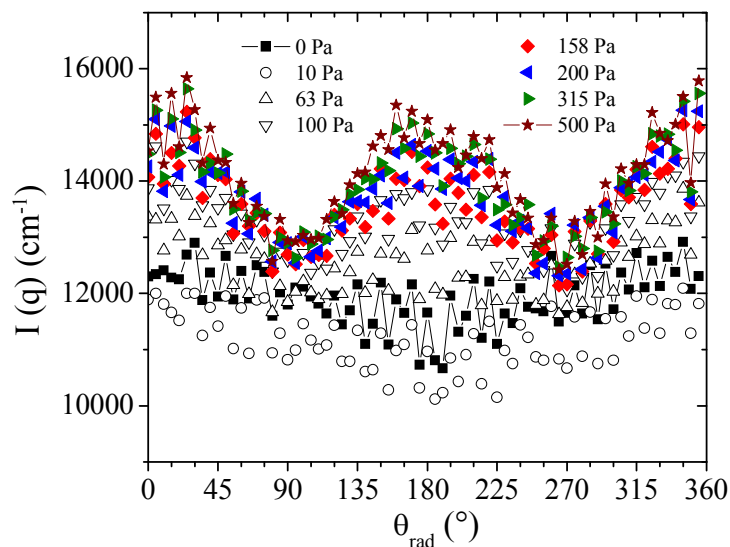


Figure 4.29 Annular averaged SANS spectra from radial Rheo-SANS on $\phi=0.531$ sample. The line is included on the static data and highest stress data to guide the eye.

Figure 4.29 shows the annular averaged SANS spectra over the nearest neighbor structure peak. This average is done over the range of $0.0038\text{--}0.0062\text{ \AA}^{-1}$ (q -center of 0.005 , Δq of 7 pixels). In radial SANS, the anisotropy is symmetric about either vertical (vorticity at 90° and 270°) or horizontal (flow at 0° and 180°) axes, as opposed to the 1-2 plane SANS structure at moderate shear rates which is not symmetric about a single plane but has a two-fold axis of rotation. The degree of the anisotropy and the average and peak values of the scattering in this nearest neighbor ring both increase with increasing shear stress. With increasing applied shear stress, the intensity grows peaks at 0° and 180° , with minima at 90° and 270° which still have increased scattered intensity with increasing shear stress. At the highest shear stresses, the intensity drops linearly as angle increases from 0° to 90° , and then increases linearly to 180° before repeating for the other 180° .

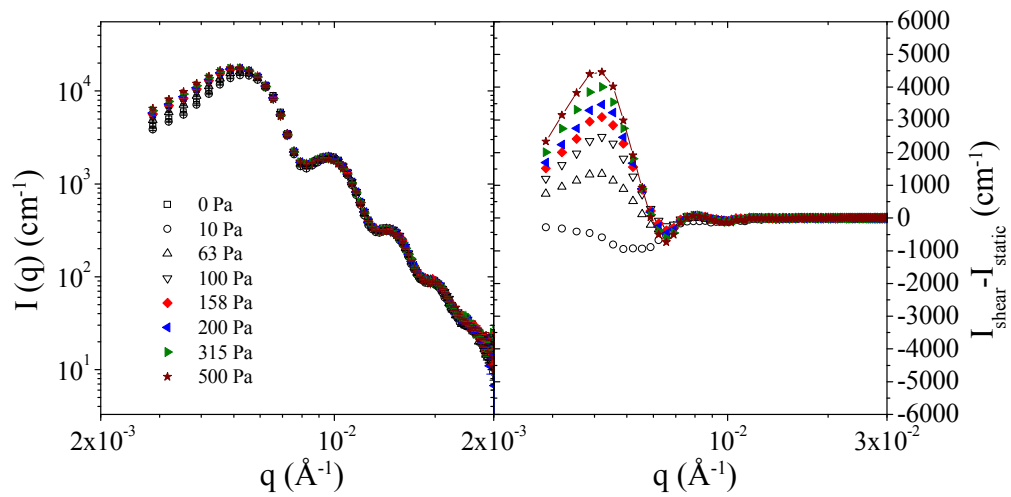


Figure 4.30 Circular averaged SANS data from $\phi=0.531$ sample in radial Rheo-SANS at various shear stresses. The line is included on the highest stress data to guide the eye.

Figure 4.30 shows the circular averaged SANS spectra as a function of shear rate. The intensity is clearly seen to increase with increasing shear rate, having a peak at $4.2 \times 10^{-3} \text{ \AA}^{-1}$ which grows in intensity with increasing applied stress. This peak is indicative of cluster formation and consistent with prior results [23].

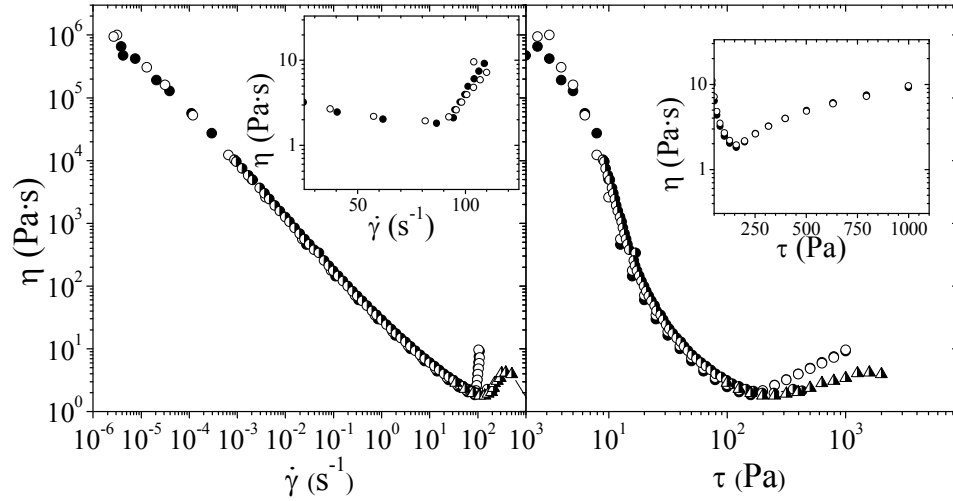


Figure 4.31 Steady shear rheological behavior for $\phi=0.53$ sample tested in following SANS experiments. Filled symbols are forward sweeps and open symbols are backward sweeps. Half filled symbols are the rheological data from the SANS rheometer taken during the scattering measurements. Two sets of measurements are included – those from the rate-sweep-SANS measurement and those from stress sweep.

A similar sample at $\phi=0.53$ was also tested in radial Rheo-SANS with a smaller Couette cell, which allowed for higher applied shear stresses. The rheology of this particular sample is shown as Figure 4.31. The rheology is strongly thinning and thickens at just below 100 s^{-1} or 150 Pa . The rheology from the SANS rheometer follows the data from the cone and plate rheometer experiment extremely well in the shear thinning region, but has less severe thickening. These experiments were tested at low and moderate shear rates in rate control mode, in order to match the shear rates measured in the 1-2 plane flow-SANS experiments of shear-thinning, but were also tested at high shear in stress control mode as the thickening was expected to be very

strong and erratic behavior is often seen in rate controlled tests on discontinuously thickening suspensions.

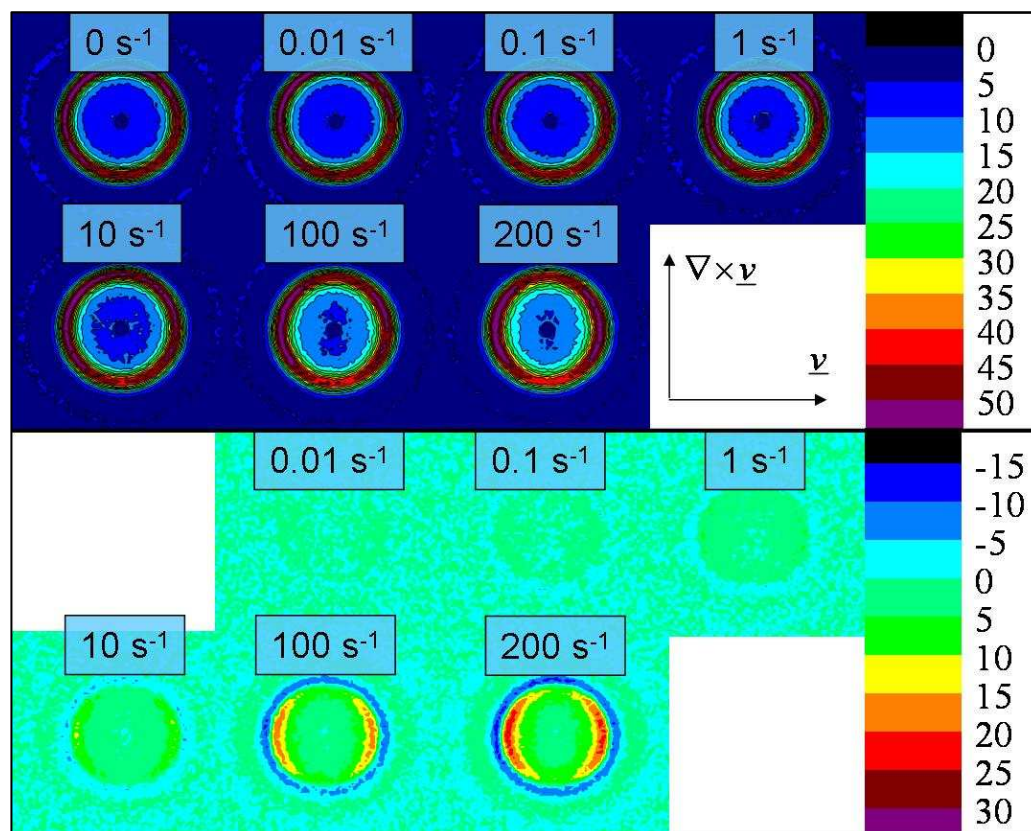


Figure 4.32 Small angle neutron scattering spectra from experiments on $\phi=0.53$ sample in radial Rheo-SANS. Test done in rate control mode. Intensity is in $\text{cm}^{-1}/100$. Top half) Scattering data. Bottom half) Scattering data under shear with static data subtracted.

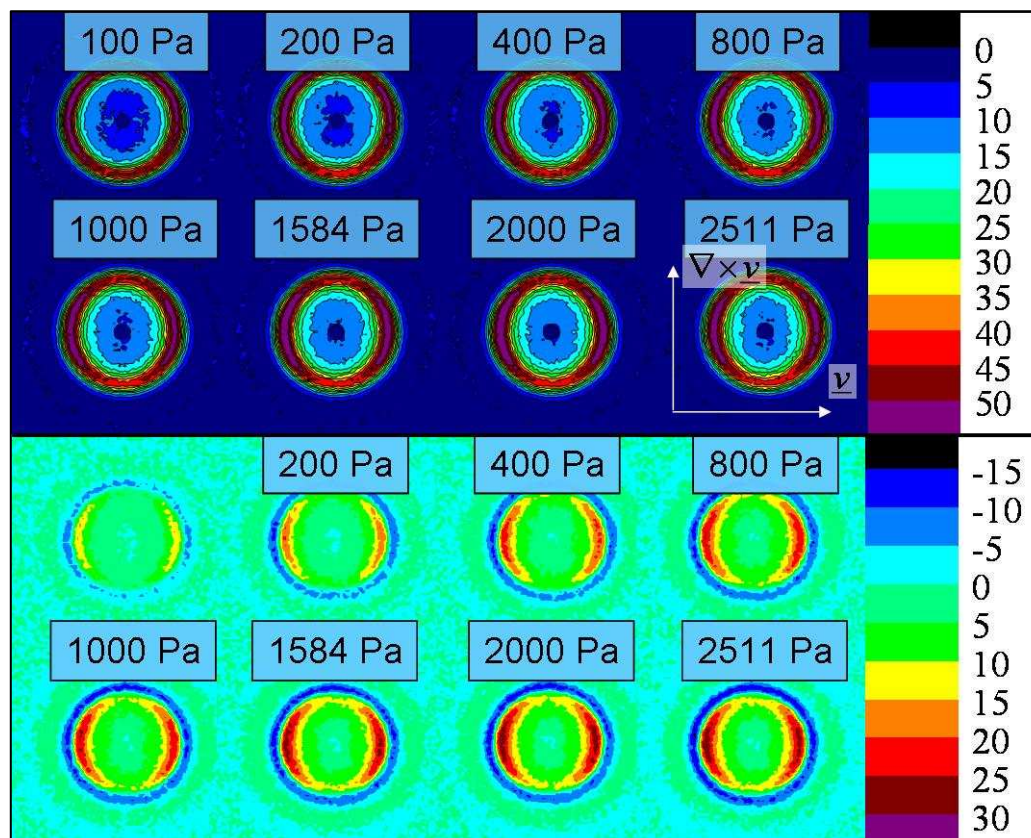


Figure 4.33 Small angle neutron scattering spectra from experiments on $\phi=0.53$ sample in radial Rheo-SANS. Test done in stress control mode. Intensity is in $\text{cm}^{-1}/100$. Top half) Scattering data. Bottom half) Scattering data under shear with static data subtracted.

Figures 4.32 and 4.33 show the 2-dimensional SANS spectra from these experiments at low-moderate shear rates and at high stresses, respectively. The scattering is isotropic at low shear rates with growing anisotropy with shear, similar to the prior sample. The anisotropy once again manifests as increased scattering in opposing crescent moon shaped bands oriented in the vorticity direction, which grow in intensity with applied shear.

Figure 4.34 shows the SANS difference spectra in the shear thickened state— the 2-d data with the data in the pre-thickened state (100 Pa) subtracted. The scattered intensity grows in the nearest neighbor ring with similar shape and characteristics as those seen at stresses in the shear thinning regime.

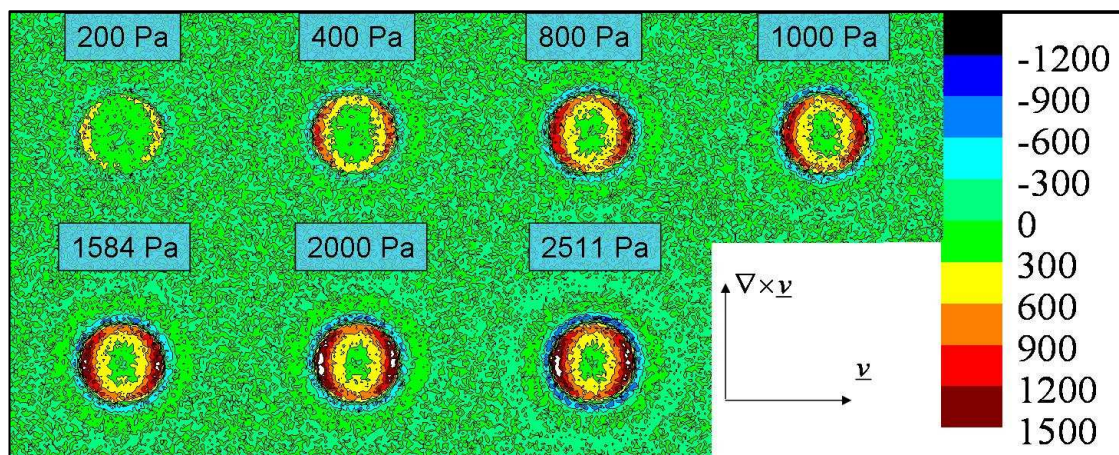


Figure 4.34 SANS subtraction pattern – shear thickened state minus pre-thickened state (100 Pa) from $\phi=0.53$ sample in radial Rheo-SANS.

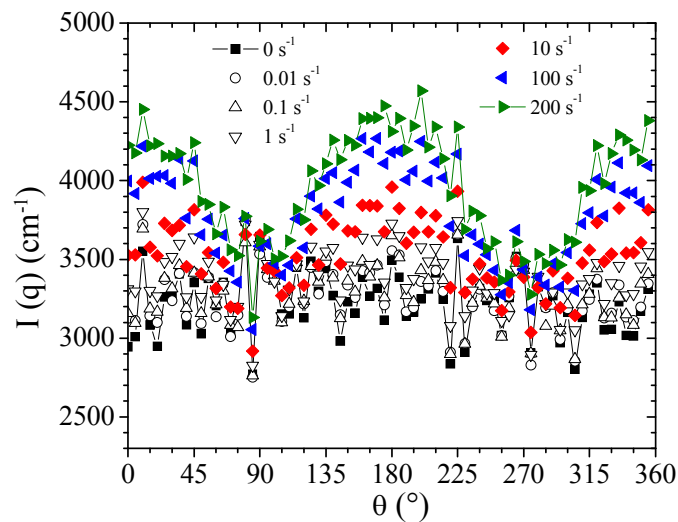


Figure 4.35 Circular averaged SANS data from $\phi=0.53$ sample in radial Rheo-SANS at various shear rates. Test done in rate control mode. The line is included on the static data and highest rate data to guide the eye.

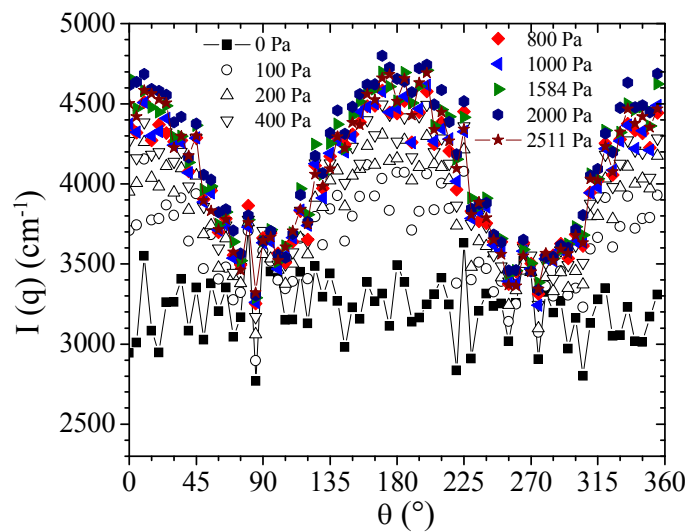


Figure 4.36 Circular averaged SANS data from $\phi=0.53$ sample in radial Rheo-SANS at various shear rates. Test done in stress control. The line is included on the static data and highest stress data to guide the eye.

Figures 4.35 and 4.36 show the annular averaged SANS data around the nearest neighbor ring for this sample, measured in both rate and stress controlled mode, respectively. This average is in the range of 0.0040-0.0060 \AA^{-1} (q-center of 0.005, Δq of 7 pixels). Once again, the intensity is isotropic at low rates, stays constant at 90° and 270° with increasing shear, but grows peaks of increasing size with increasing applied stress at 0° and 180°.

Figures 4.37 and 4.38 show the circular averaged SANS data for this sample and the SANS difference data between those under shear and under static conditions. The scattered intensity is seen to grow with increasing applied shear at low q, with a peak at 0.0048 \AA^{-1} and a minimum at 0.0059 \AA^{-1} . The height of the peak and depth of the valley both increase with increasing applied shear, but the location of the peak and minimum do not change significantly with applied shear.

Table 4.6 shows the transmission values measured concurrently with these scattering experiments. This measurement fluctuates around 0.440 for the rate controlled experiments, but has a consistent, but small drop in the transmission in the stress controlled measurements with increasing stress.

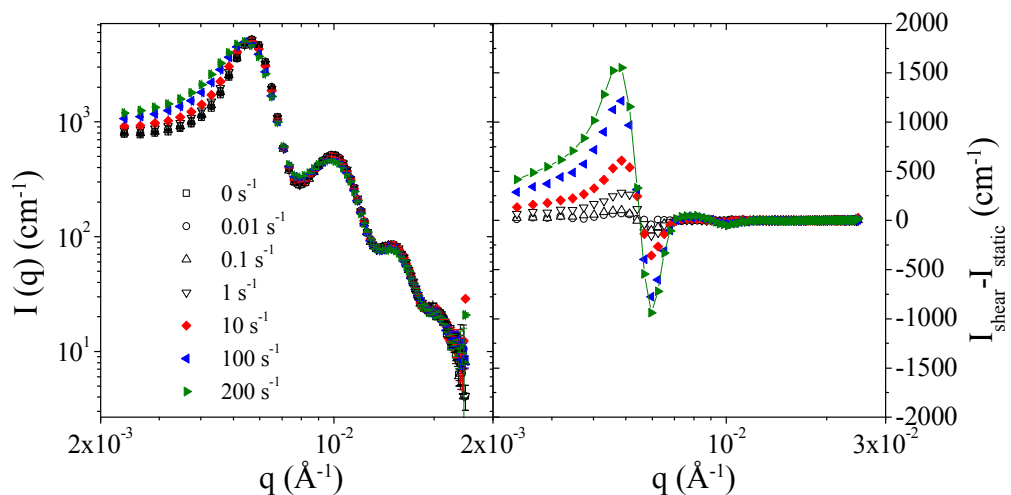


Figure 4.37 Annular averaged SANS spectra from radial Rheo-SANS on $\phi=0.53$ sample. Test done in rate control mode. The line is included on the highest rate data to guide the eye.

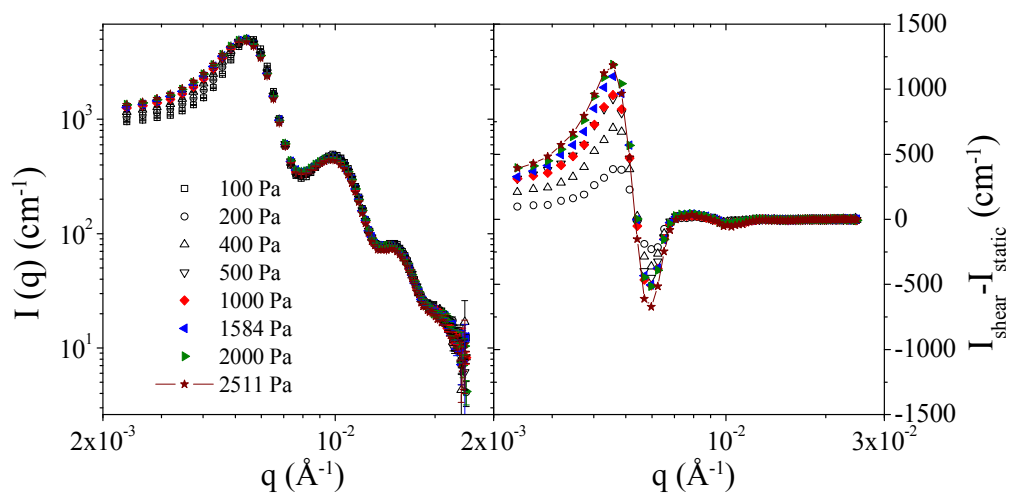


Figure 4.38 Annular averaged SANS spectra from radial Rheo-SANS on $\phi=0.53$ sample. Test done in stress control mode. The line is included on the highest stress data to guide the eye.

Table 4.6 Transmission values for strongly thickening samples in radial Rheo-SANS.

Aug - 2008 – Radial Rheo-SANS – $\phi=0.53$		
Run #	Shear Rate (s^{-1})	Transmission
110	0	0.441
114	0.01	0.441
115	0.02	
116	0.05	
117	0.1	0.445
119	0.2	
120	0.5	
121	1	0.439
123	2	
124	5	
125	10	0.438
127	20	
128	50	
129	100	0.438
132	200	0.433
135	0	0.447
Run #	Shear Stress (Pa)	Transmission
136	100	0.439
139	200	0.439
140	400	0.434
143	800	0.433
144	1000	0.436
147	1584	0.431
148	2000	0.430
151	2511	0.430
153	0	

4.3.2.2 Microstructure Measurements of Moderately Shear-Thickening ($\phi \sim 0.45$) Suspensions

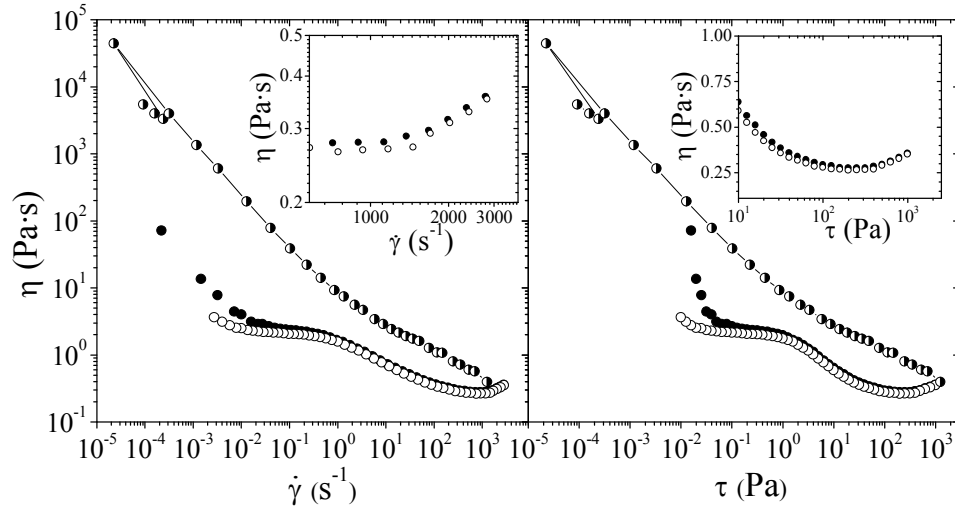


Figure 4.39 Steady shear rheological behavior for $\phi=0.436$ sample tested in following SANS experiments. Filled symbols are forward sweeps and open symbols are backward sweeps. Half filled symbols are the rheological data from the SANS rheometer taken during the scattering measurements.

Figure 4.39 shows the rheology for a sample at $\phi=0.436$, also tested in radial Rheo-SANS using the larger Couette. The cone and plate rheology shows yielding at low stresses with a zero shear viscosity of about 2.1 Pa-s for stresses below 1 Pa or rates below 0.5. In addition, this sample shear thickens for shear rates above 1000 s^{-1} or stresses above 400 Pa. The rheology measured in the SANS Couette shows very different behavior, with very strong thinning. Although this data was collected during the scattering experiments, this data was consistent with other measurements on this sample in the Couette. No thickening was measured, only shear thinning was

measured. For this sample, regular measurements of the sample neutron transmission were not done – the sample transmission was 0.513.

Figure 4.40 shows the SANS spectra for this sample at various applied shear stresses, as well as the difference pattern (shear minus static spectra). Like the prior sample in radial SANS, the scattered intensity in the nearest neighbor ring increases with increasing applied stress, as does the anisotropy. The anisotropy grows as seen before with two opposing crescent moon shapes.

This result is also seen in the annular averages seen as Figure 4.41. This average is in the range of 0.0038-0.0062 \AA^{-1} (q-center of 0.005, Δq of 7 pixels). Unlike the prior experiments, these measurements do show a decrease in the scattered intensity at higher shear stresses at the minima seen at 90° and 270°.

The circular averaged SANS data is seen as Figure 4.42. These data have an increase in the low q scattering with shear, growing a peak with increasing intensity as the applied shear increases. In addition, the location of the peak shifts to lower q as the applied shear is increased.

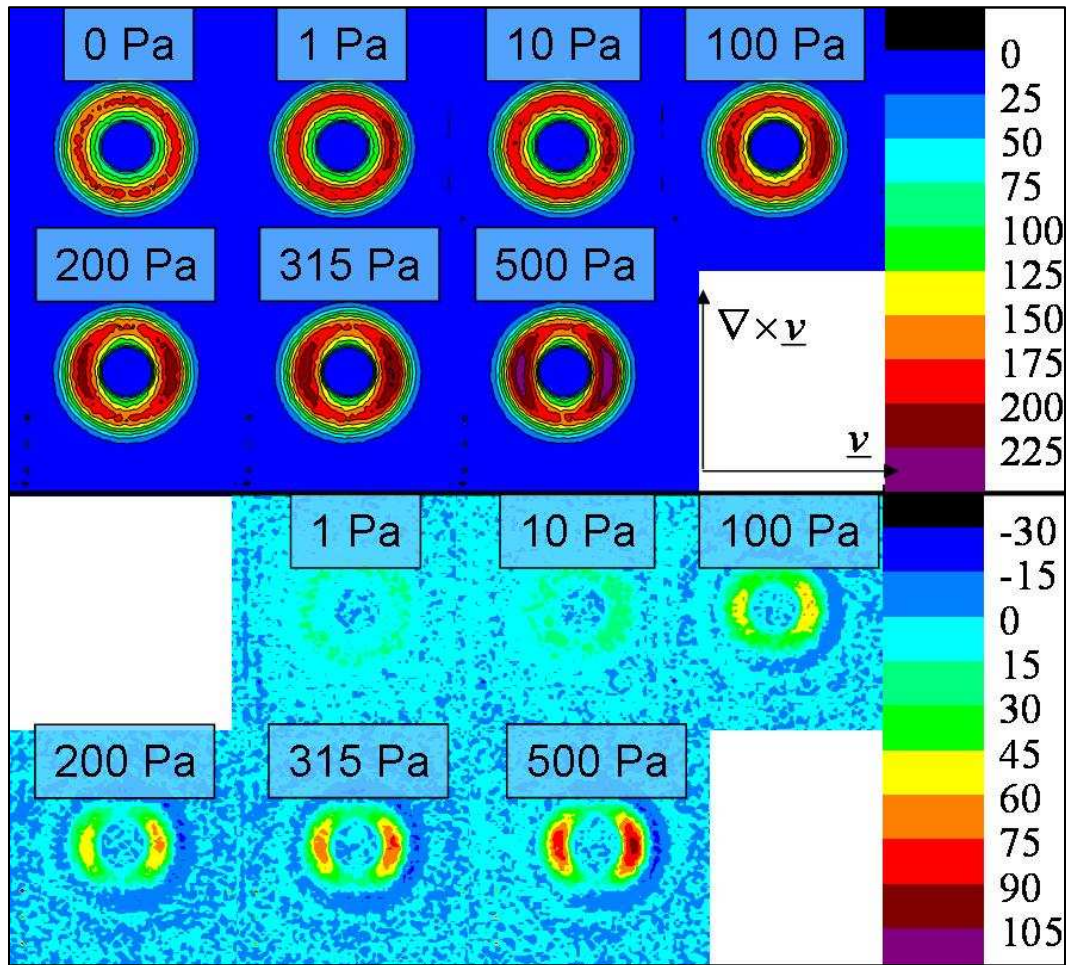


Figure 4.40 Small angle neutron scattering spectra from initial experiments on $\phi=0.436$ sample in radial Rheo-SANS. Top half) Scattering data. Bottom half) Scattering data under shear with static data subtracted. Intensity is in $\text{cm}^{-1}/100$.

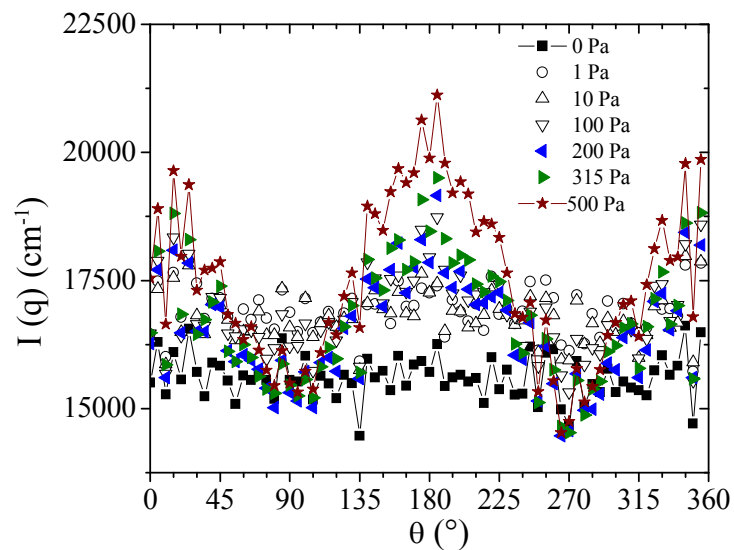


Figure 4.41 Annular averaged SANS spectra from radial Rheo-SANS on $\phi=0.436$ sample. The line is included on the static data and highest stress data to guide the eye.

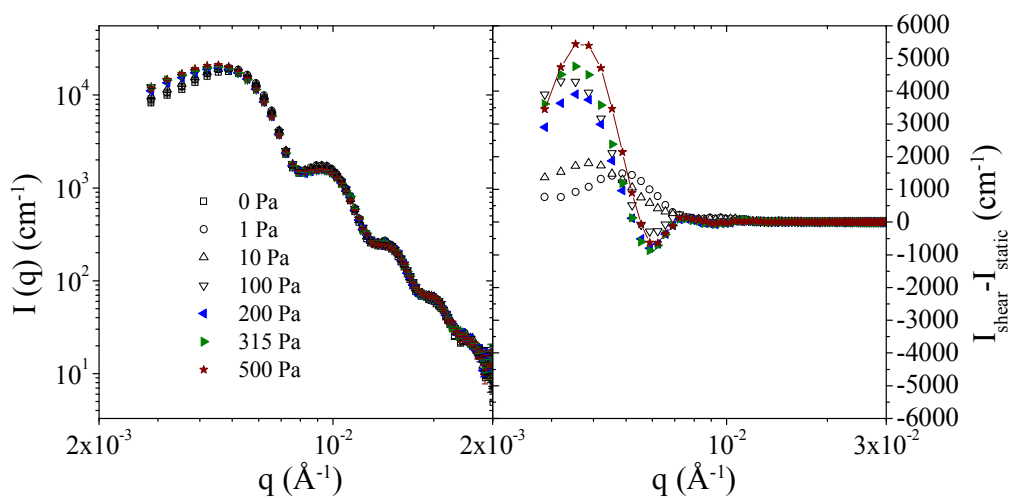


Figure 4.42 Circular averaged SANS data from $\phi=0.436$ sample in radial Rheo-SANS at various shear rates. The line is included on the highest stress data to guide the eye.

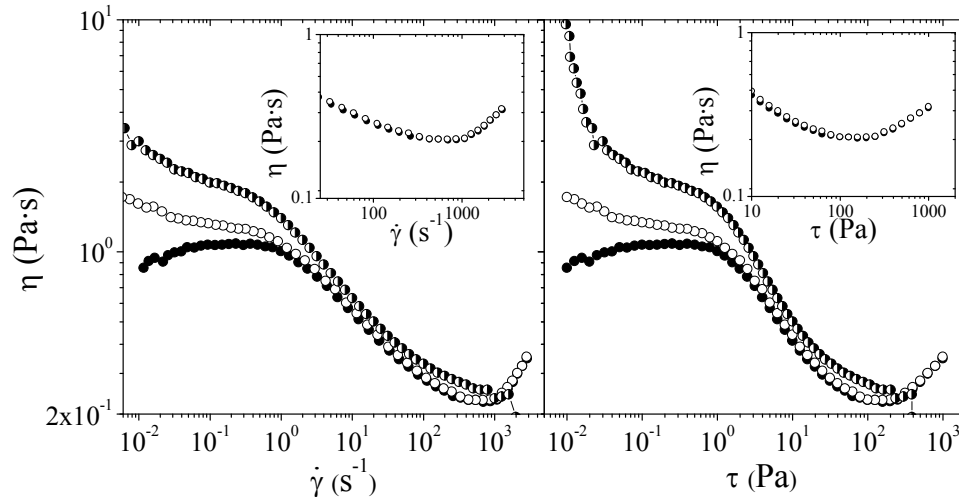


Figure 4.43 Steady shear rheological behavior for $\phi=0.44$ sample tested in following SANS experiments. Filled symbols are forward sweeps and open symbols are backward sweeps. Half filled symbols are the rheological data from the SANS rheometer taken during the scattering measurements.

Figure 4.43 shows the rheology of an additional sample at $\phi=0.44$ which was tested in the smaller SANS Couette geometry. The cone and plate rheology shown in the figure shows shear thinning at shear rates above 1 s^{-1} or stresses above 1 Pa . The rheology shear thickens at about 900 s^{-1} or 200 Pa . In addition, there is some hysteresis in the rheology at stresses below 1 Pa , where the forward sweep has slight increases in the viscosity with increasing shear rate and the backward sweep has a decrease in viscosity with increases in the shear rate. The SANS Couette rheology data has a decrease in the viscosity at high shear rates where the cone and plate rheology has shear thickening. This result is likely due to slip rather than loss of sample quality as similar rheological tests in the Couette on this sample, both directly before and after

these experiments, had the same results along the entire curve, albeit with slightly less pronounced thinning at the highest shear rates.

Figure 4.44 shows the two dimensional SANS spectra for this sample at various shear rates. At applied shear rates of 1 s^{-1} and below, the scattering is isotropic. With increasing shear, anisotropy grows both in the nearest neighbor ring, and at even lower q inside the nearest neighbor ring. As seen with prior samples in this plane, the shape of the scattering pattern is that of opposing crescent moons oriented in the vorticity direction, which grown in intensity and thickness with increasing shear rate.

Figure 4.45 shows the annular averaged data around the nearest neighbor peak. This average is in the range of $0.0040\text{-}0.0060 \text{ \AA}^{-1}$ (q -center of 0.005 , Δq of 7 pixels). The anisotropy clearly starts at 10 s^{-1} and increases with increasing shear rate. In addition, whereas prior samples have what appears to be a sharp peak at 0° and 180° , this sample has a sharp rise from 90° to 135° , with a much smaller increase from 135° to the peak at 180° .

Figure 4.46 shows the circular averaged SANS data for this sample. With increasing shear rate, there is strong increase in the scattering at low q with a commensurate decrease in the scattering near the nearest neighbor peak. The peak in the scattering is seen at slightly below $4 \times 10^{-3} \text{ \AA}^{-1}$ and the minimum is seen at slightly above $5 \times 10^{-3} \text{ \AA}^{-1}$.

Table 4.7 shows the transmission measurements for this suspension under shear. The transmission starts at about 0.40 and decreases systematically with increasing shear by a total of 5% to 0.38, but recovers when shear is removed. This is indicative of some reversible change in the sample during experiments, such as a few air bubbles, but does not seem to affect the results.

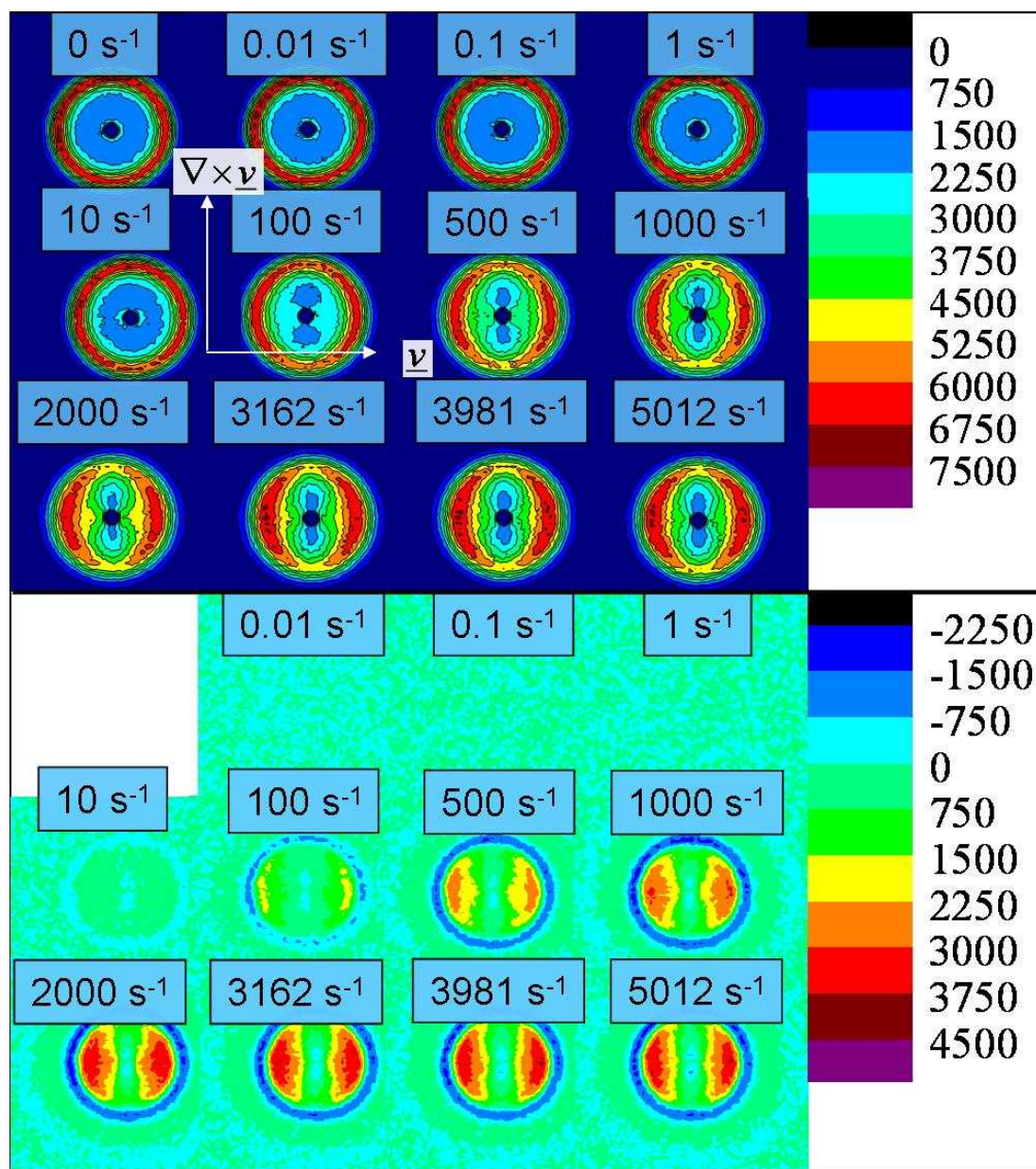


Figure 4.44 Small angle neutron scattering spectra from initial experiments on $\phi=0.44$ sample in radial Rheo-SANS. Top half) Scattering data. Bottom half) Scattering data under shear with static data subtracted.

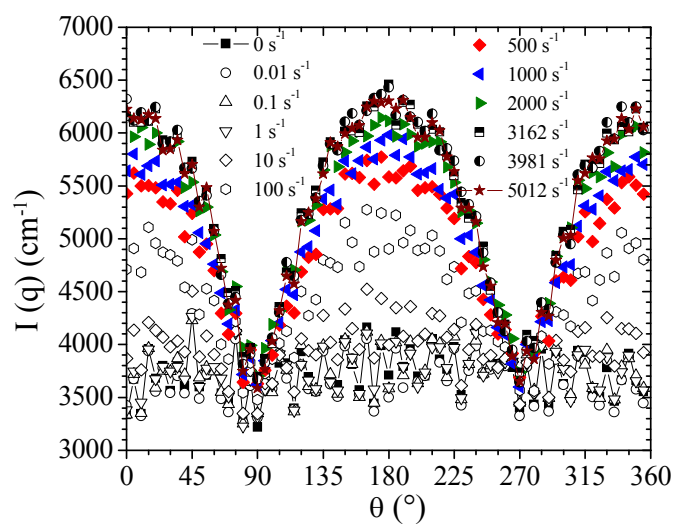


Figure 4.45 Annular averaged SANS spectra from radial Rheo-SANS on $\phi=0.44$ sample. The line is included on the static data and highest rate data to guide the eye.

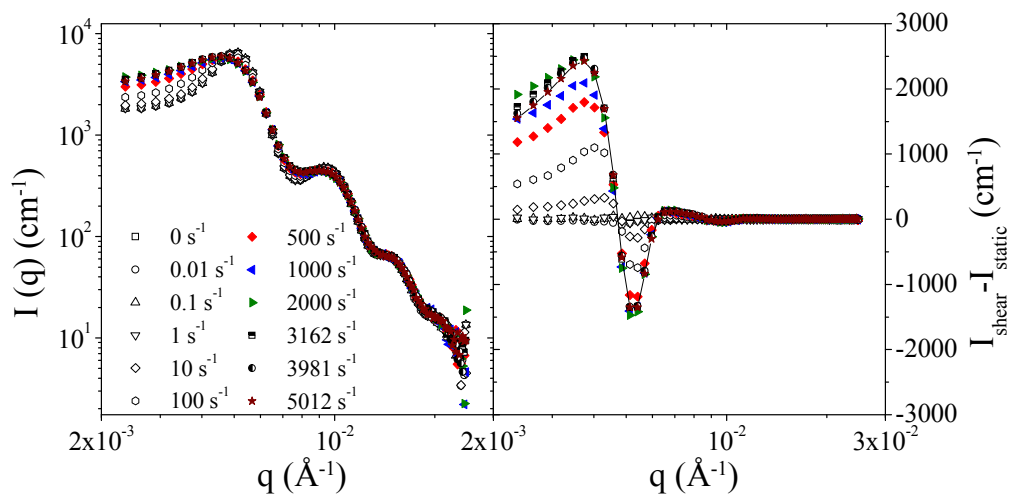


Figure 4.46 Circular averaged SANS data from $\phi=0.44$ sample in radial Rheo-SANS at various shear rates. The line is included on the highest rate data to guide the eye.

Table 4.7 Transmission values for mildly thickening samples in radial Rheo-SANS.

Aug - 2008 – Radial Rheo-SANS – $\phi=0.44$		
Run #	Shear Rate (s^{-1})	Transmission
68	0	0.400
69	0.001	0.401
72	0.01	0.404
73	0.02	
74	0.05	
75	0.1	0.398
77	0.2	
78	0.5	
79	1	0.400
81	2	
82	5	
83	10	0.398
85	20	
86	50	
87	100	0.390
90	200	0.390
91	500	0.386
94	1000	0.390
95	2000	0.382
98	2512	0.384
99	3162	0.380
102	3981	0.380
103	5012	0.381
107	0	0.402

4.3.3 Micromechanics Calculations via the Stress-SANS Law

In this section, a micromechanics analysis of the SANS data measured via 1-2 plane flow-SANS and radial Rheo-SANS will be presented. Considering the available data already presented, we will present a micromechanics analysis of the $\phi=0.522$ (section 4.3.1.1), $\phi=0.40$ (section 4.3.1.2) and $\phi=0.20$ (section 4.3.1.3) suspensions in 1-2 plane flow-SANS, and the $\phi=0.53$ (section 4.3.2.1) and $\phi=0.44$ (section 4.3.2.2) suspensions in radial SANS. In addition, a micromechanics analysis of the octadecane-coated silica suspensions measured via 1-2 plane flow-SANS (section 4.3.1.4) will also be presented.

To calculate the harmonics and the stresses, the model, unsmeared structure factors are required. Figure 4.47 shows the static data for the three concentrations of near hard-sphere silica in the 1-2 plane SANS experiment (top left) and the two concentrations in radial SANS (top right). Also shown are polydisperse, core-shell models for the data with the appropriate instrument smearing (bottom), similar to those used previously and described below. Note that, no single shell thickness fits the data from both geometries and all five concentrations well. For the 1-2 plane data, the same model as that used in section 3.5.1 is used; this model is an instrument smeared, core-shell hard-sphere model with a 3.4 nm layer thickness at the effective volume fraction calculated by including the shell volume as done in Chapter 3. The scattering length density is adjusted to fit the data. These models include 10% polydispersity, consistent with previously measured results via light scattering and SEM, but not used in the prior SANS modeling. For the radial SANS experiments, this model is seen to overestimate the strength of the structural peak and so the layer thickness and effective volume fraction are fit to the data (t_{shell} of 1.0 nm is used). Note

that the 1-2 plane static data has poor fits for any model due to multiple scattering caused by the high concentration and large path length.

In the bottom half of the figure, the unsmeared, polydisperse hard-sphere structure factor models used in the overall models are shown. A monodisperse hard-sphere structure factor at these high concentrations is generally near zero until the nearest neighbor peak, where it has a spike well above one, before oscillating about one while decaying with increasing q . A polydisperse structure factor has a nearest neighbor peak at a broader and lower q range, consistent with the measured data. The polydisperse structure factor model is necessary both to better represent the system and to allow scattering data over a range of wavevectors to count in the final calculations of rheological properties from the scattering via the stress-SANS law. Despite adding polydispersity, the structure factor still causes the model to have a poor fit to the low q data in most cases.

Figure 4.48 shows the circular averaged static SANS data for the octadecane coated silica, compared to the uncoated suspension. The model fit to the octadecane coated silica is the sticky hard-sphere potential, with $\phi=0.596$, sticky parameter, τ_b of 0.545, and perturbation parameter of 0.0137 [50, 96].

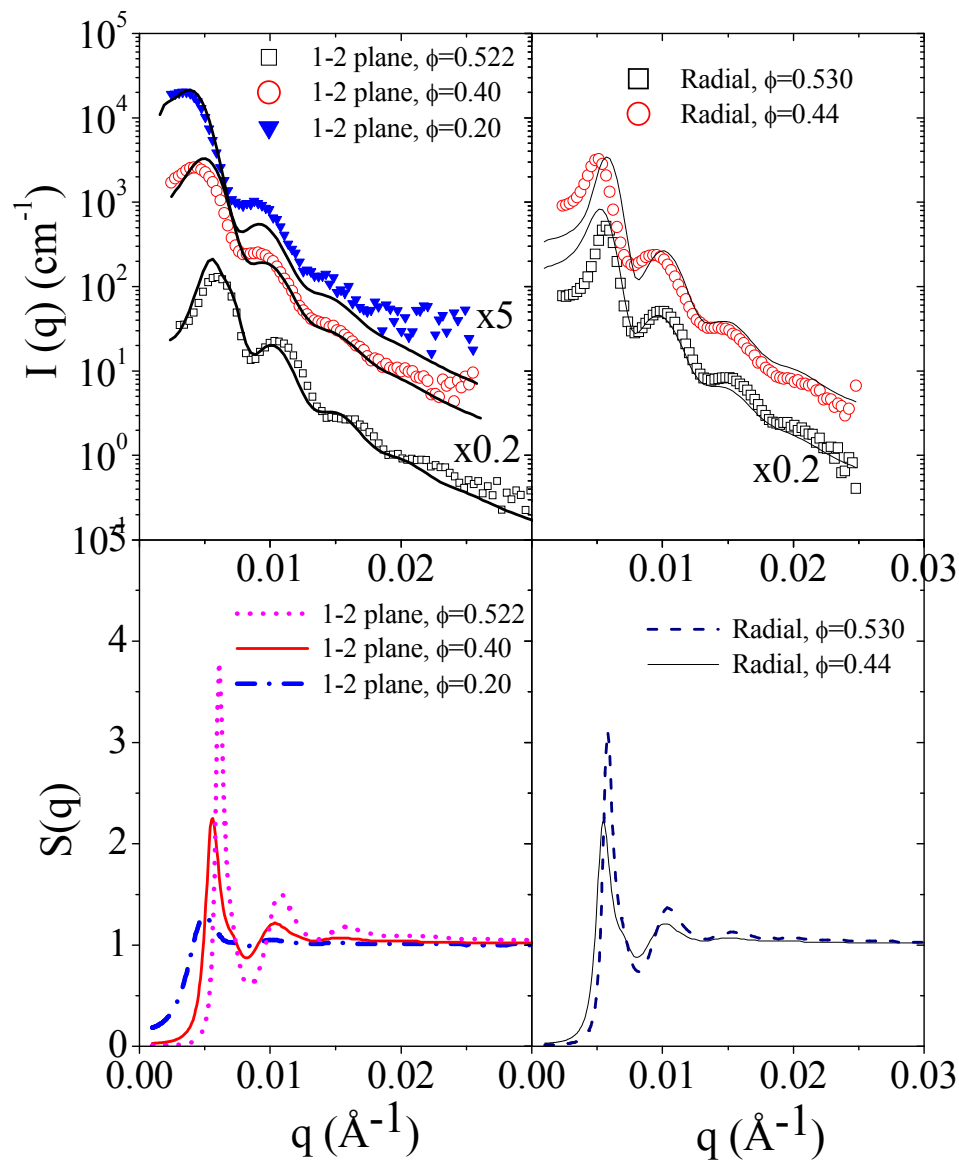


Figure 4.47 Circular averaged static SANS data in shear cells for hard-sphere suspensions. Also shown are the smeared model predictions (with scattering length density fit) and the unsmeared structure factors.

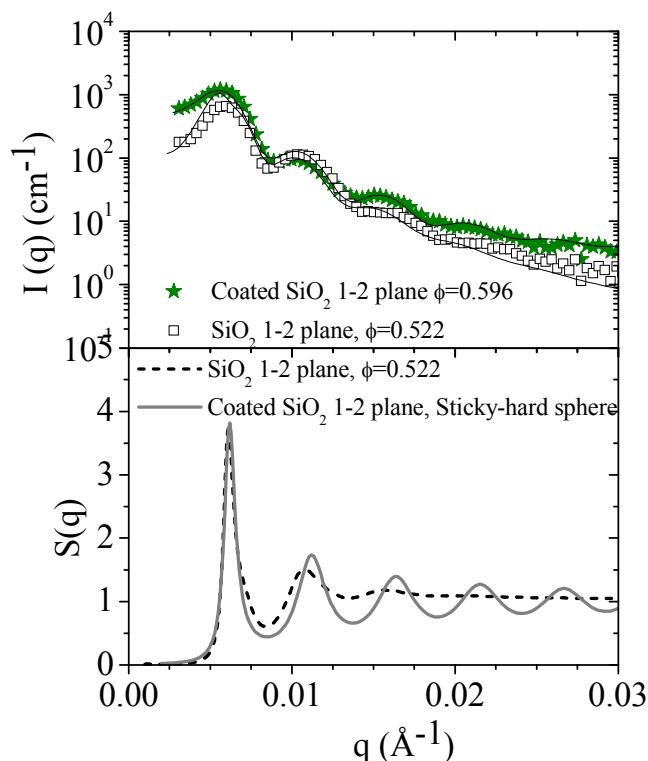


Figure 4.48 Circular averaged static SANS data in 1-2 plane shear cell for coated sticky hard-sphere suspension compared to hard-sphere suspension. Also shown are the smeared models and the unsmeared structure factors – the model is a prediction for the hard-sphere suspensions and fit to the coated particle suspensions.

Multiple transformations of each dataset will be shown. First, difference spectra ($I_{\text{shear}} - I_{\text{static}}$), weighted by appropriate harmonic weightings of the angle will be presented. The difference spectra can show the degree of two-fold, four-fold, and six-fold symmetry through systematic changes in the $\cos 2\theta$, $\cos 4\theta$, and $\cos 6\theta$ weighted data. Next, the harmonic weighted relative scattering ($I_{\text{shear}}/I_{\text{static}}$) will be shown. These transformations of the data are also the W terms described in section 2.5.3. After that,

the structure factor weighted W terms (either proportional to a single $B_{l,m}^+$ term or a linear combination of multiple $B_{l,m}^+$ terms) will be shown, where the $B_{l,m}^+$ will be shown if they can be calculated independently from other terms. Note that the $B_{l,m}^+$ terms are a generalized description of the behavior and are geometry independent, whereas the W_n terms have a particular shear plane associated with them. Finally the integrals of these $W_n \cdot S_{eq}$ or $B_{l,m}^+(q)$ terms as a function of shear rate will be presented. These integrals are expected to be proportional to various rheological functions and are also described in more detail in section 2.5.3. The thermodynamic and hydrodynamic viscosities and normal stresses will also be presented. Note that only the 1-2 plane data can be used to calculate the thermodynamic viscosity, and that normal stress rheological data is only available at the highest concentration. As discussed in section 2.5.3, in the 1-2 plane SANS, the relevant harmonics for stress-SANS law calculations are the W_0 , W_2 , and $W_{2,1}$; those integrations yield a component which contains factors of the sum of $B_{0,0}^+(q)$, $B_{2,0}^+(q)$, and $B_{2,2}^+(q)$, a component which contains the difference between $B_{2,0}^+(q)$ and $B_{2,2}^+(q)$, and a component proportional to $B_{2,1}^+(q)$, respectively. In the radial SANS, the stress-SANS law relevant harmonics are W_0 and W_2 , which can be used to calculate the difference between $B_{0,0}^+(q)$ and $B_{2,0}^+(q)$ and $B_{2,2}^+(q)$ alone, respectively. The 1-2 plane, therefore, provides the $B_{2,1}^+(q)$ harmonic not previously measured, necessary for the calculation of the thermodynamic component of the shear stress.

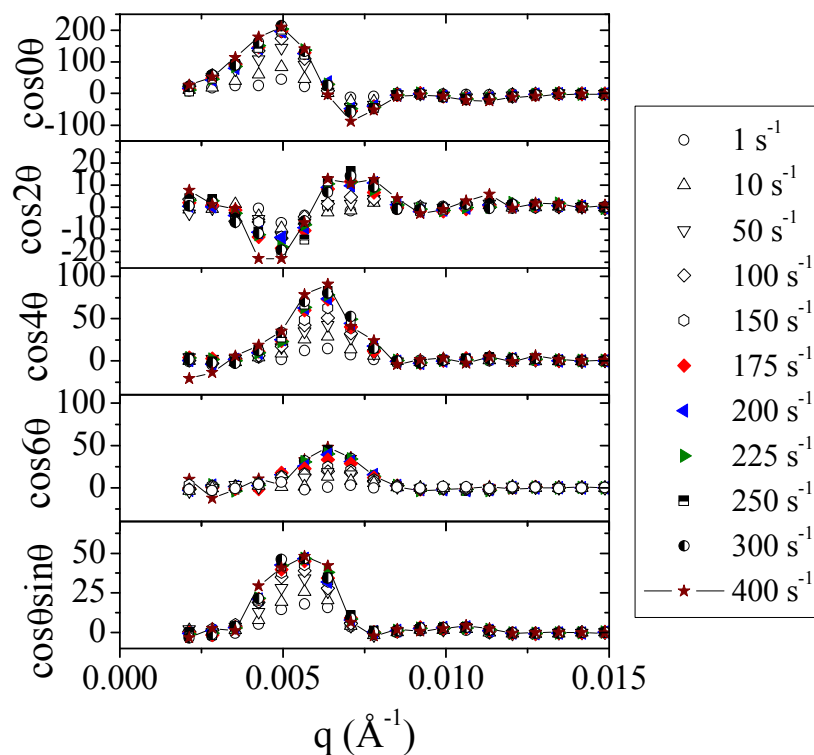


Figure 4.49 Harmonic weighted difference spectra ($I_{\text{shear}} - I_{\text{static}}$) data from $\phi=0.522$, 1-2 plane flow-SANS.

Figure 4.49 shows the harmonic weighted, annularly averaged difference spectra for the $\phi=0.522$ sample measured via 1-2 plane flow-SANS (the second dataset shown in section 4.3.1.1). This presentation gives a compact description of the microstructural changes under shear – no difference is seen where the microstructure is unchanged from the equilibrium state. Even low shear of 1 s^{-1} gives slight changes to the unweighted SANS data, as seen before. Note that the unweighted SANS data shown here is the same as the circular averaged difference spectra shown in the prior results sections. There is some weak two-fold symmetry seen in the $\cos 2\theta$ weighted spectra, having a decrease in scattering at 0.005 \AA^{-1} and an increase at 0.007 \AA^{-1} . The

location of these peaks appears to shift to slightly higher q with increasing shear rate. There is clearly four-fold and six-fold symmetry represented in the $\cos 4\theta$ and $\cos 6\theta$ weighted SANS spectra as peaks at 0.0064 \AA^{-1} , which grow systematically with increasing shear rate. The data at high q is removed due to the large error.

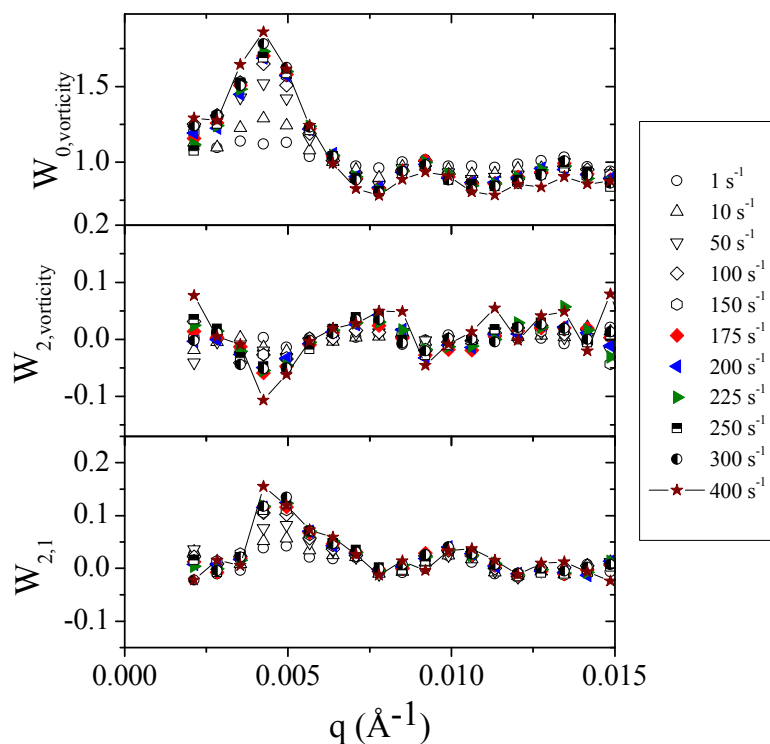


Figure 4.50 Harmonic weighted SANS data normalized by static data ($I_{\text{shear}}/I_{\text{static}}$), or W terms, from $\phi=0.522$, 1-2 plane flow-SANS.

Figure 4.50 shows the calculated W_n components for this $\phi=0.522$ sample from 1-2 plane flow-SANS. This data is similar to that seen in the top two panes and bottom pane of Figure 4.49, except this is the scattering data under shear normalized by the equilibrium data rather than the difference between the two. Once again, the

unweighted data, $W_{0,\text{vorticity}}$, has a large structural peak at 0.004 \AA^{-1} and a secondary dip at 0.0075 \AA^{-1} . The changes seen in W_2 and $W_{2,1}$ are of smaller magnitude than those seen in W_0 , but also have significant changes at 0.004 \AA^{-1} . W_2 has a decrease at this location, with an increase at low q and another increase at higher q (0.0075 \AA^{-1}); these peaks and minima grow with increasing shear rate. $W_{2,1}$ has a peak at 0.004 \AA^{-1} which grows with increasing shear rate as well and no other significant structural features.

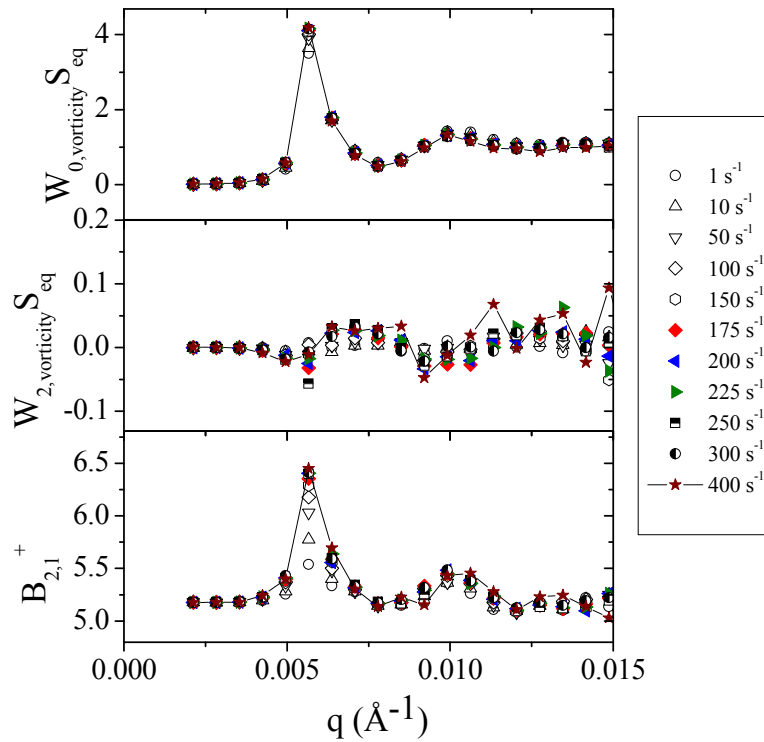


Figure 4.51 Structurally weighted harmonics calculated from $\phi=0.522$, 1-2 plane flow-SANS. Note that $B_{2,1}^+$ is proportionally to $W_{2,1}$.

Figure 4.51 shows the relevant harmonics with the equilibrium structure factor (unsmeared model) component included. This data is the same data as that seen in Figure 4.50 multiplied by S_{eq} (shown in Figure 4.47), although the bottom component is $B_{2,1}^+$ which is proportional to $W_{2,1}$ times S_{eq} (see equation 2.26). Recall that, the generalized, shear plane independent description of the structure is the set of $B_{l,m}^+$ terms, whereas the W_n are the experimental descriptions for a particular geometry. Therefore, comparing $B_{l,m}^+$ terms is preferred and so where they can be calculated individually ($B_{2,1}^+$ in 1-2 plane SANS and $B_{2,2}^+$ in radial SANS), they will be shown rather than the W term. Otherwise, W_n times S_{eq} will be shown; this representation will be a linear combination of multiple $B_{l,m}^+$ terms. The data seen in Figure 4.51 have similar behavior as that seen in Figure 4.50, although the static structure factor masks the differences seen under shear in W_0 and significantly weights the data for the other harmonics by the first structural peak seen at 0.0057 \AA^{-1} , such that the values at this point will dominate the following integrations.

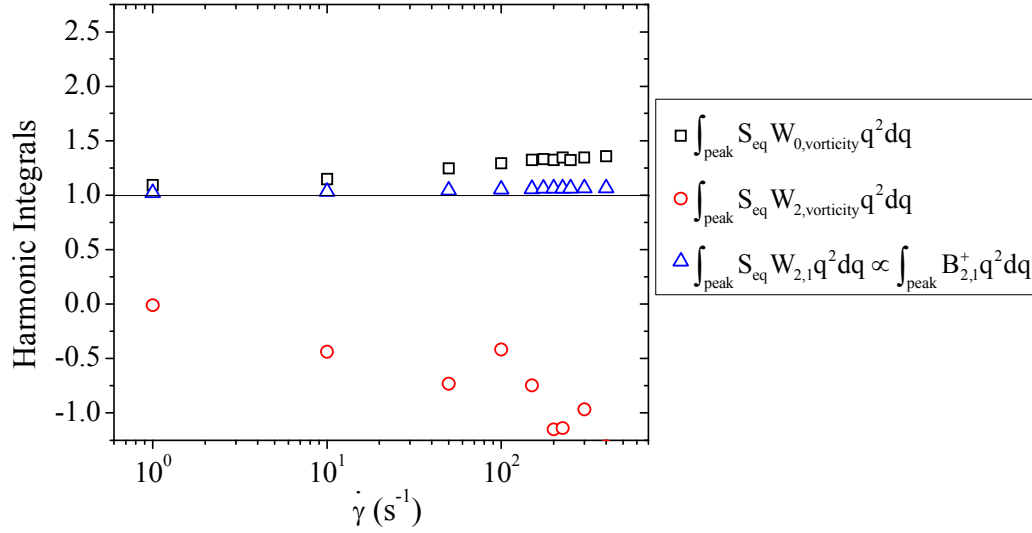


Figure 4.52 Harmonic integrals calculated from micromechanics analysis of SANS data in 1-2 plane measurements of $\phi=0.522$ hard-sphere silica. Integrals are all normalized by the value at equilibrium. The line at 1 is included to guide the eye.

Figure 4.52 shows integrations of these structural components (multiplied by $(qa)^2$, at low q , up to the first peak in S_{eq} , as described in section 2.5.3). The changes in these components are expected to be proportional to the changes seen in the rheological parameters as described in section 2.5.3. To give a direct comparison, and remove differences in the low q behavior of S_{eq} amongst different volume fractions, these integrations have also been normalized by the value at zero shear. The W_0 integral grows monotonically with increasing shear rate. The values of the W_2 integral not normalized are very small relative to the fluctuations. These W_2 integral results are effectively zero, with fluctuations due to error in the measurement. The $B_{2,1}^+$ integral grows systematically with increasing shear rate ($\sim 7\%$ greater at the highest shear rate than at equilibrium).

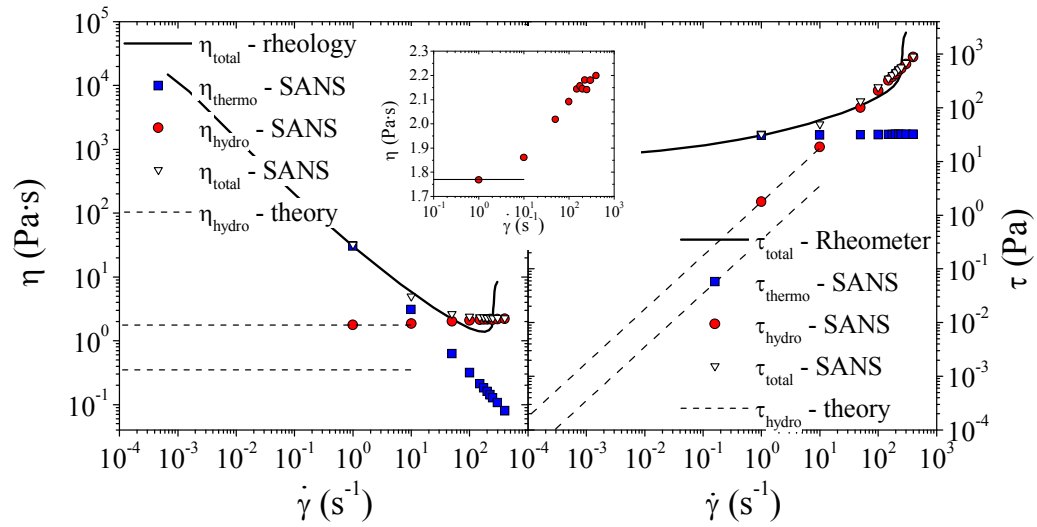


Figure 4.53 Comparison of thermodynamic and hydrodynamic components of the viscosity from SANS microstructure measurements to viscosity from rheometry for 1-2 plane measurements of $\phi=0.522$ hard-sphere silica.

Table 4.8 Parameters used to correlate viscosity from SANS using spherical harmonic decomposition to the measured rheology.

Direction	1-2 plane	1-2 plane	1-2 plane	1-2 plane	Radial	Radial
ϕ	0.522	0.40	0.20	.596 Sticky	0.53	0.44
ϕ_{eff}	0.615	0.47	0.24	.596 Sticky	0.62	0.52
η_{solvent} (Pa-s)	0.0377	0.0377	0.0377	0.00369	0.0377	0.0377
$\eta_{\text{r,hydro}} - \text{theory, effective Hard-sphere}$	47.19	6.15	2.01	26.7	75.89	8.93
$\eta_{\text{r,hydro}} - \text{theory, Sticky Hard-sphere}$				536		
η_{hydro} (Pa-s)	1.78	0.23	0.076	1.98	2.9	0.34
C_{hydro}	1.62	0.245	0.05	2.0	0.05	0.01
C_{thermo}	30	0.23	0.0065	400	-	-

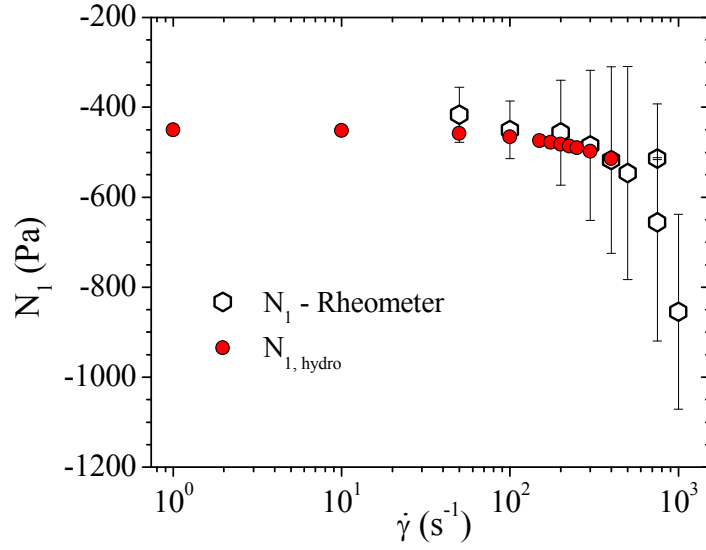


Figure 4.54 Comparison of thermodynamic and hydrodynamic components of the first normal stress difference, N_1 , from SANS microstructure measurements to N_1 from rheometry for 1-2 plane measurements of $\phi=0.522$ hard-sphere silica.

Figures 4.53 and 4.54 show a comparison of the rheological behavior from the stress-SANS law to the measured rheological behavior. In Figure 4.53, the steady-shear rheology is compared to the thermodynamic and hydrodynamic components of the rheology measured from the microstructure changes summarized in Figure 4.52 and via the procedure described in section 2.5.3 and below. The thermodynamic component of the viscosity, η_{thermo} , is fit to the data using a form of equation 2.30 shown below as equation 4.1, where there is a constant of proportionality between viscosity and normalized $B_{2,1}^+$ described as C_{thermo} ,

$$\eta(\dot{\gamma})_{\text{thermo}} \approx C_{\text{thermo}} \frac{1}{\dot{\gamma}} \frac{\int_{\text{peak}} B_{2,1}^+(\dot{\gamma}) q^2 dq}{\int_{\text{peak}} B_{2,1}^+(\text{static}) q^2 dq}. \quad (4.1)$$

Specifically, C_{thermo} is adjusted such that the η_{thermo} fits the rheology at the lowest shear rate measured via SANS and the rest of the viscosity curve is predicted from that single point. As the thermodynamic viscosity at low shear rates is typically orders of magnitude above the hydrodynamic viscosity, ignoring the hydrodynamic component in this fitting is appropriate. The values of C_{thermo} used in these correlations for all experiments are shown in Table 4.8.

In addition, the hydrodynamic viscosity, η_{hydro} , is correlated to the data via a form of equation 2.31, described as equation 4.2,

$$\eta(\dot{\gamma})_{\text{hydro}} \approx C_{\text{hydro}} \frac{\int_{\text{peak}}^{\text{peak}} [S_{\text{eq}} W_{0,\text{vorticity}}(\dot{\gamma})] q^2 dq}{\int_{\text{peak}}^{\text{peak}} [S_{\text{eq}} W_{0,\text{vorticity}}(\text{static})] q^2 dq}. \quad (4.2)$$

In this case, the low shear hydrodynamic viscosity is calculated from equation 4.3 [97],

$$\eta_{r,\text{hydro}} = \frac{1 + \frac{3}{2} \phi [1 + \phi - 0.189 \phi^2]}{1 - \phi [1 + \phi - 0.189 \phi^2]} \quad (4.3)$$

and C_{hydro} is adjusted such that η_{hydro} from SANS fits that calculated from equation 4.3 at the lowest measured shear rate. The values of C_{hydro} , η_{hydro} , and $\eta_{r,\text{hydro}}$ used in these correlations for all experiments are shown in Table 4.8. The figure includes as dashed lines η_{hydro} determined from both ϕ and ϕ_{eff} , the latter being the larger value. The total viscosity measured from SANS is the sum of η_{hydro} and η_{thermo} .

The thermodynamic component of the viscosity is seen to shear thin, consistent with the measured rheology. At high shear rates, where the measured rheology begins to plateau and shear thicken, the thermodynamic viscosity continues to decrease. The hydrodynamic component of the viscosity increases with increasing

shear rate going into the shear thickening regime, but does not have the order of magnitude change seen in the rheology.

Figure 4.54 shows the comparison of the first normal stress difference, N_1 , from experiments on a similar suspension described in section 3.5.6 to $N_{1,\text{hydro}}$ from the SANS microstructure measurements. As $N_{1,\text{thermo}}$ is expected to be related to W_2 , but W_2 is effectively zero for these measurements (as seen in Figures 4.51 and 4.52), only $N_{1,\text{hydro}}$ is compared. In this case, $N_{1,\text{hydro}}$ is compared to the measured N_1 from rheometry using a form of equation 2.32 such that:

$$N_1(\dot{\gamma})_{\text{hydro}} \propto -\dot{\gamma} \frac{\int_{\text{peak}} [B_{2,1}^+(\dot{\gamma})] q^2 dq}{\int_{\text{peak}} [B_{2,1}^+(\text{static})] q^2 dq} . \quad (4.5)$$

In addition, due to the offset in the rheological experiment from the expected low-shear value of N_1 of zero, $N_{1,\text{hydro}}$ is shifted by 450 Pa. The constant of proportionality, determined from a fit to the data as seen in Figure 4.54 is 0.15 Pa. The SANS measurement of $N_{1,\text{hydro}}$ is an extremely good fit to the data.

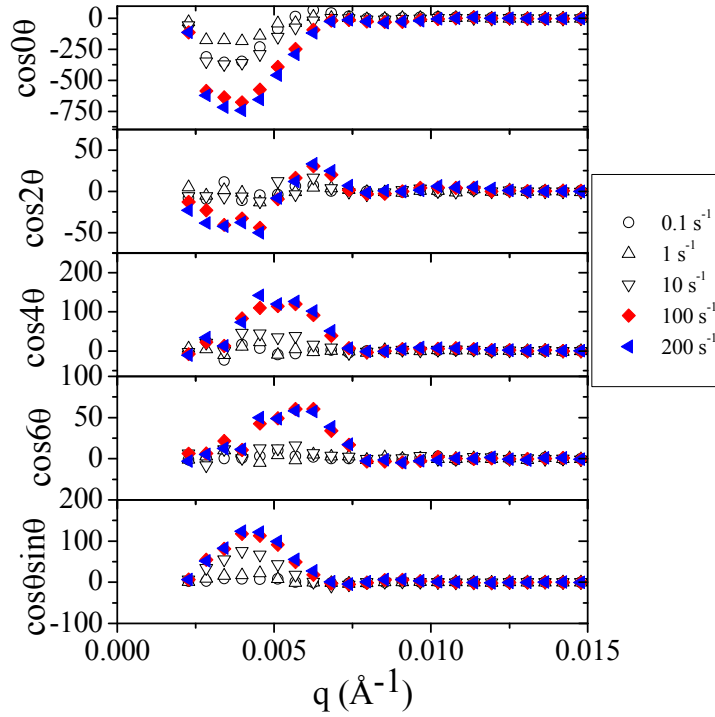


Figure 4.55 Harmonic weighted, circular averaged difference spectra ($I_{\text{shear}} - I_{\text{static}}$) from $\phi=0.40$ sample in 1-2 plane flow-SANS.

Figures 4.55-4.59 show the same analysis as above, applied to the $\phi=0.40$ sample in 1-2 plane flow-SANS (seen previously in section 4.3.1.2). Difference spectra, seen as Figure 4.55, clearly show that for these measurements, there is a decrease in scattering at low q in the unweighted data. As discussed previously, this is likely due to sample impurities such as air bubbles which developed in this sample under shear. The difference data also show a significant increase in the two-fold, four-fold, and six-fold symmetry at the highest shear rates. In addition, the $\cos\theta\sin\theta$ symmetry has a mild increase at 10 s^{-1} and a larger increase which saturates above 100 s^{-1} .

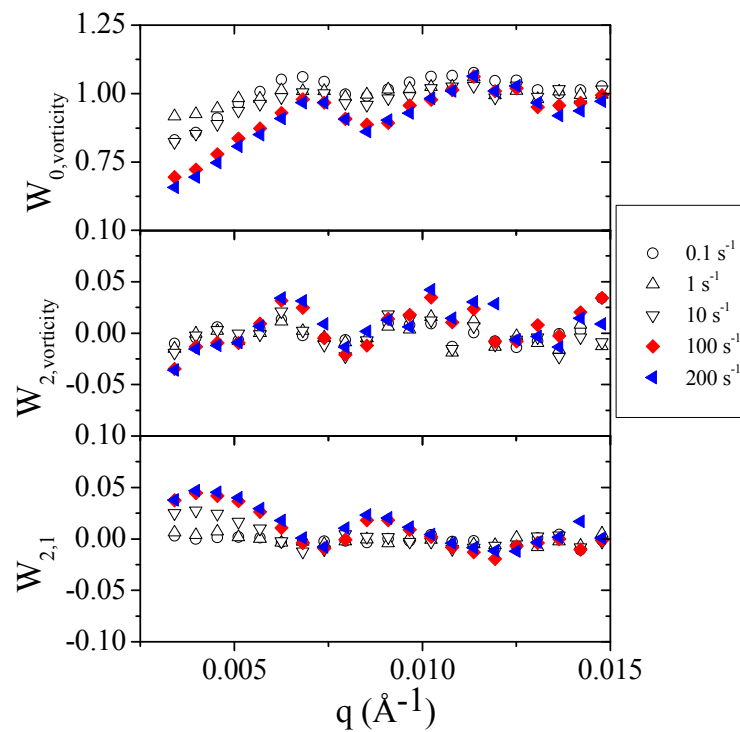


Figure 4.56 Harmonic weighted SANS data normalized by static data ($I_{\text{shear}}/I_{\text{static}}$), or W terms, from $\phi=0.40$, 1-2 plane flow-SANS.

The harmonic weighted SANS data normalized by the zero-shear data (the W_n terms) are shown in Figure 4.56. Similar trends are seen as in the difference spectra. First, W_0 has a systematic trend towards decreased scattering at all q at high shear rates. Next, W_2 has oscillations about zero with increasing amplitude with increases in shear rate. Finally, $W_{2,1}$ has two peaks with amplitude which grow with shear rate, saturating for the highest shear rates.

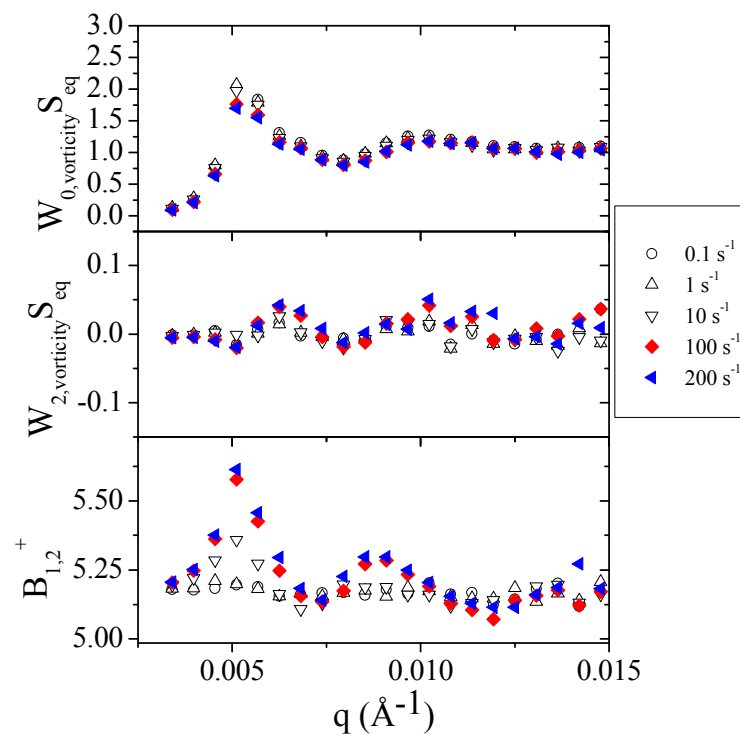


Figure 4.57 Structurally weighted harmonics calculated from $\phi=0.40$, 1-2 plane flow-SANS. Note that $B_{2,1}^+$ is proportionally to $W_{2,1}$.

Figure 4.57 shows the structure-weighted harmonics calculated from the data in Figure 4.56. The static structure factor once again masks the changes seen in W_0 , does little to change W_2 , and accentuates the data at the structure factor peak in $W_{2,1}$.

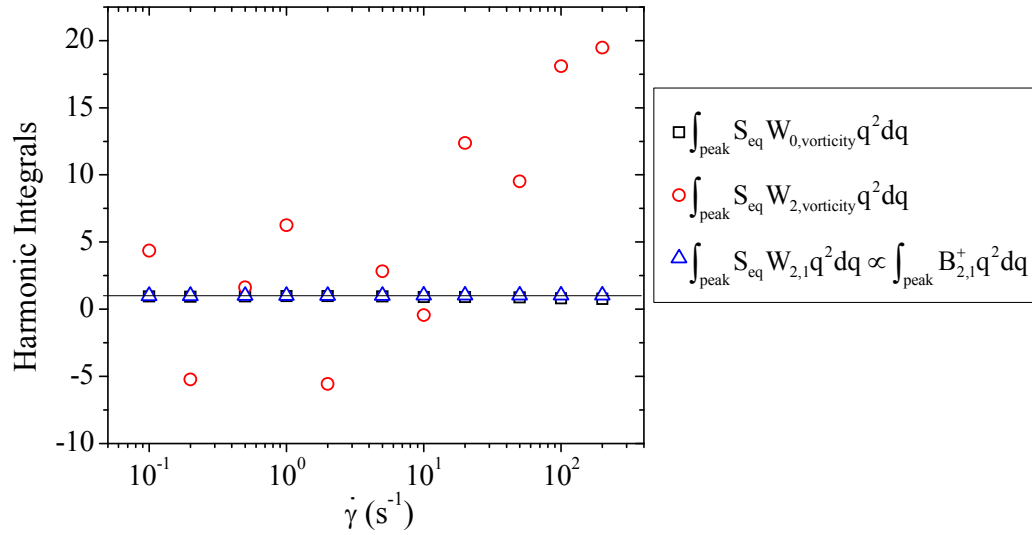


Figure 4.58 Harmonic integrals calculated from micromechanics analysis of SANS data in 1-2 plane measurements of $\phi=0.40$ hard-sphere silica. Integrals are all normalized by the value at equilibrium. The line at 1 is included to guide the eye.

Figure 4.58 shows the normalized integrations of these terms used to calculate the rheological parameters. The W_0 integral is seen to decrease slightly at the highest shear rates, consistent with the decreases in scattered intensity due to the previously described sample issues. W_2 fluctuates about zero with no systematic trend, consistent with the integrations effectively being noise about zero, normalized by a value near zero. $B_{2,1}^+$ increases slightly with increasing shear rate.

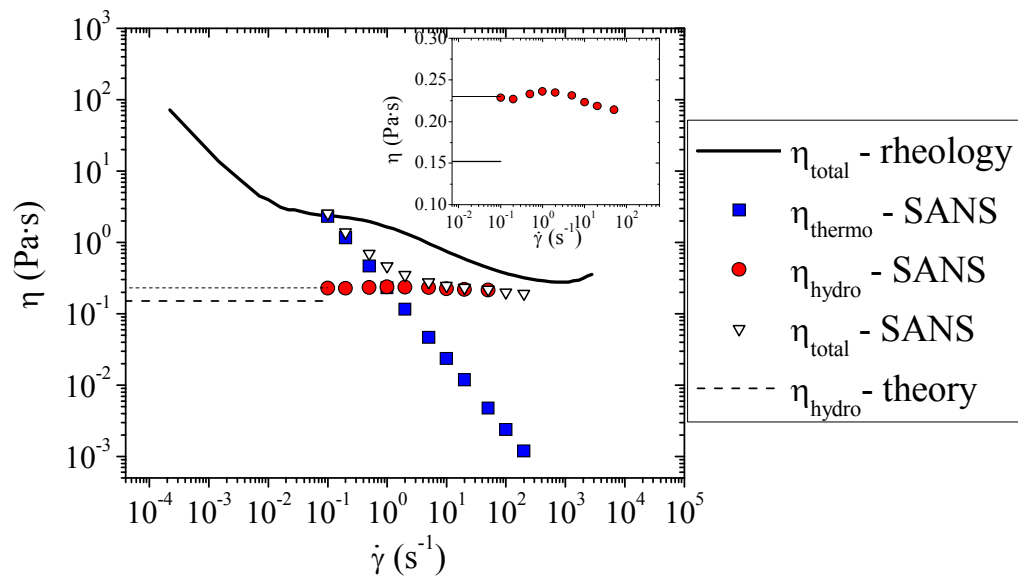


Figure 4.59 Comparison of thermodynamic and hydrodynamic components of the viscosity from SANS microstructure measurements to viscosity from rheometry for 1-2 plane measurements of $\phi=0.40$ hard-sphere silica.

Figure 4.59 shows the comparison of the rheology to the components of the rheology measured from SANS for the $\phi=0.40$ hard-sphere silica suspension. In this case, the lowest shear rate SANS data is in the plateau region of the rheology beyond the yield stress and before rheological shear thinning. As the shear thinning is not as large as that seen for the higher concentration sample, η_{thermo} has much stronger shear thinning than the measured rheology. This result is not unexpected as the hydrodynamic component of the rheology provides a high floor for the total viscosity even at low shear rates (indicated by the dashed and dotted lines on the figure). In addition, little change is seen in the hydrodynamic viscosity, although the shear thickening regime of the viscosity is not measured via SANS (the points at the two highest shear rates are removed due to the sample issues discussed previously).

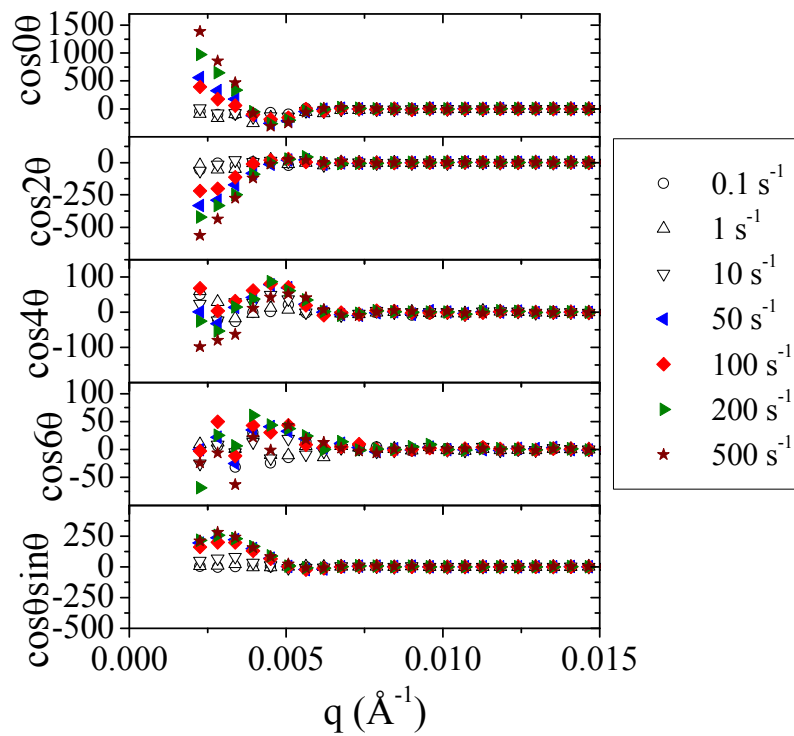


Figure 4.60 Harmonic weighted, circular averaged difference spectra ($I_{\text{shear}} - I_{\text{static}}$) from $\phi=0.20$ sample in 1-2 plane flow-SANS.

Figure 4.60-4.64 show this same analysis for the $\phi=0.20$ sample in 1-2 plane flow SANS (section 4.3.1.3). Difference spectra seen in Figure 4.60 show changes from the static scattering only at q values less than 0.006 \AA^{-1} . The unweighted data and $\cos\theta\sin\theta$ symmetry both have an increase in the low q scattering with shear. The two-fold symmetry has a decrease in scattering with increasing shear rate. The four-fold symmetry has fluctuations at the lowest q with no systematic trend with shear rate, and a peak at slightly higher q , centered around 0.0045 \AA^{-1} . This peak increases with increasing shear rate but has a slight decrease at the highest measured shear rate.

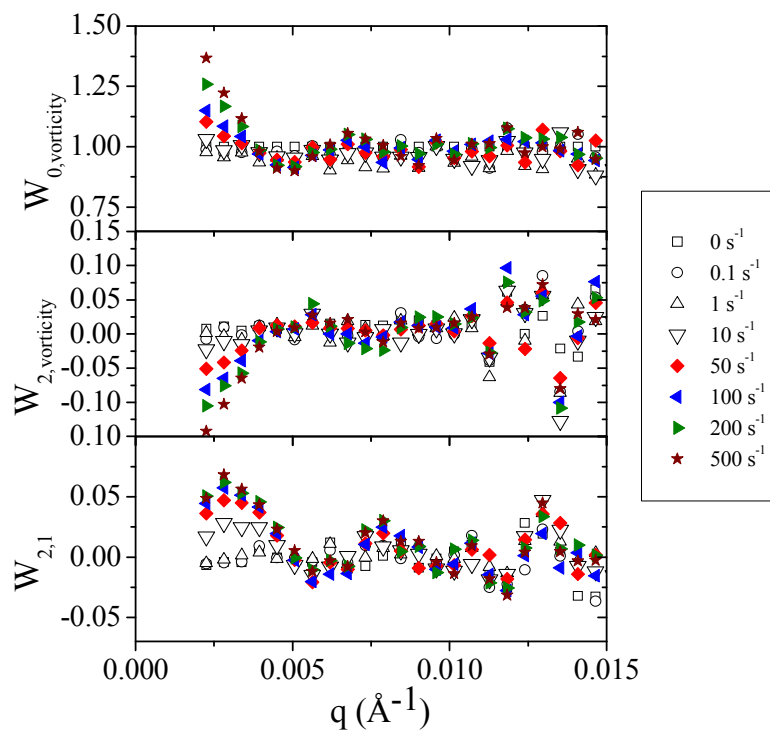


Figure 4.61 Harmonic weighted SANS data normalized by static data ($I_{\text{shear}}/I_{\text{static}}$), or W terms, from $\phi=0.20$, 1-2 plane flow-SANS.

Figure 4.61 shows the W terms, which more clearly show the systematic trends at low q with increasing shear rate in W_0 , W_2 , and $W_{2,1}$. W_0 and $W_{2,1}$ both increase with shear rate at low q , with $W_{2,1}$ having a low q peak before dropping at the data point at the lowest measured q , and W_0 continually increasing with decreasing q . W_2 decreases at low q with increasing shear rate.

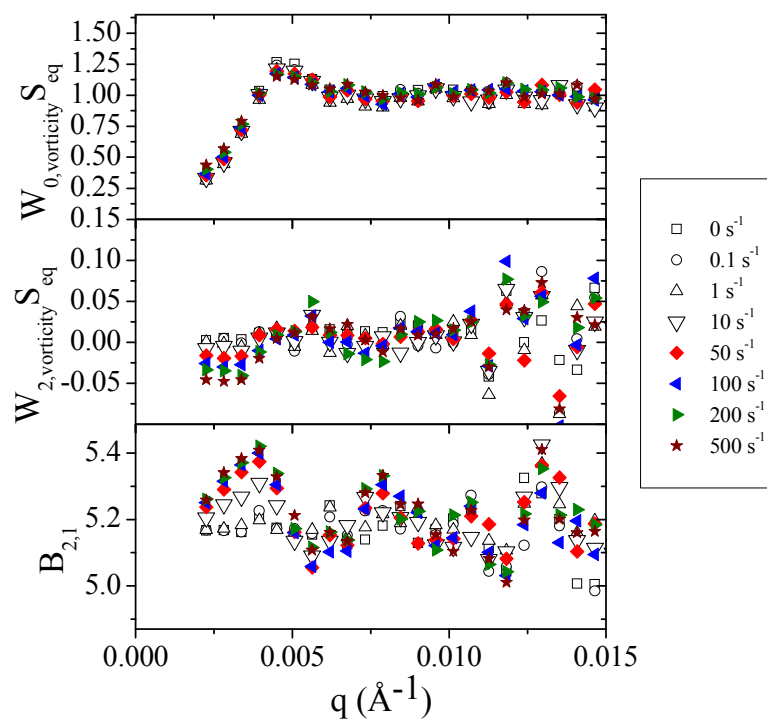


Figure 4.62 Structurally weighted harmonics calculated from $\phi=0.20$, 1-2 plane flow-SANS. Note that $B_{2,1}^+$ is proportionally to $W_{2,1}$.

Figure 4.62 shows the harmonics weighted by the equilibrium structure. Once again, the equilibrium structure washes out any significant changes with shear in W_0 , while accentuating the low q changes in W_2 and $W_{2,1}$ (seen via changes in $B_{2,1}^+$). In fact, for this sample and unlike the higher concentration samples, $W_{2,\text{vorticity}}$ actually changes significantly with shear rate.

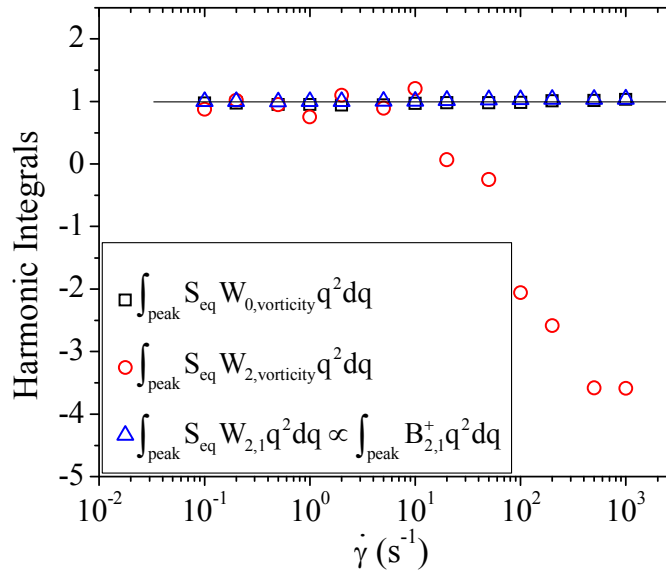


Figure 4.63 Harmonic integrals calculated from micromechanics analysis of SANS data in 1-2 plane measurements of $\phi=0.20$ hard-sphere silica. Integrals are all normalized by the value at equilibrium. The line at 1 is included to guide the eye.

Figure 4.63 shows the harmonic integrals calculated for the $\phi=0.20$ sample in 1-2 plane SANS. There are slight fluctuations and small increases in the W_0 and $B_{2,1}^+$ integrals with increasing shear rate. The W_2 integral fluctuates about one until about 100 s⁻¹, where it begins to have a large decrease with increasing shear rate. This result is unique to this sample as W_2 was effectively zero for the two samples of higher concentration.

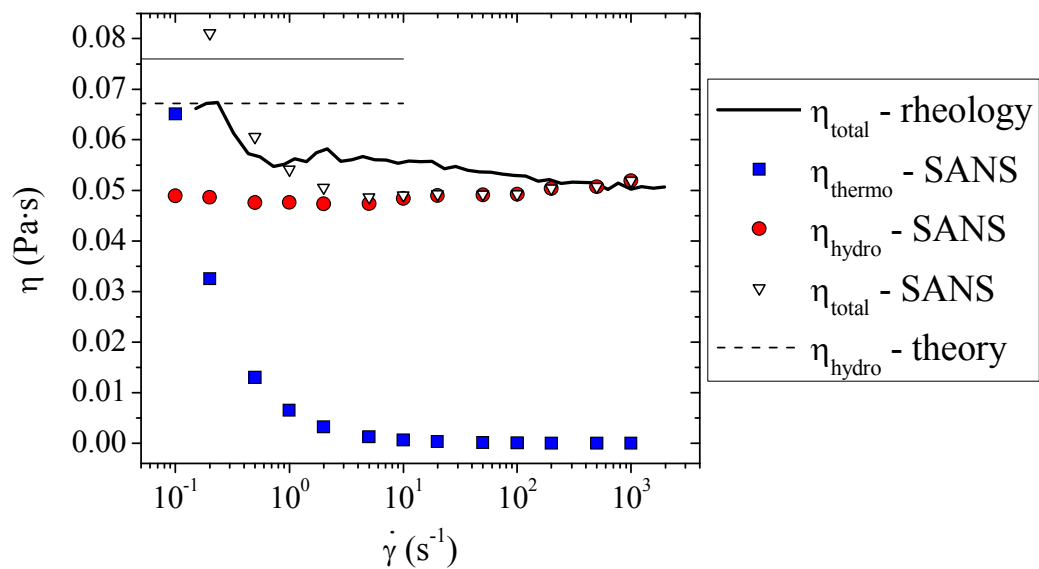


Figure 4.64 Comparison of thermodynamic and hydrodynamic components of the viscosity from SANS microstructure measurements to viscosity from rheometry for 1-2 plane measurements of $\phi=0.20$ hard-sphere silica.

Figure 4.64 shows the comparison of the rheology to the components of the rheology measured from SANS for the $\phi=0.20$ hard-sphere silica suspension. Once again, η_{thermo} decreases drastically from the lowest shear rate, whereas the suspension is only weakly shear thinning. In fact, as the rheology is only noticeably thinning on this expanded linear scale, η_{thermo} goes to practically zero by 1 s⁻¹. For this particular suspension, the prediction for the hydrodynamic viscosity from theory is above the measured viscosity, although within the error in the rheology measurement. Therefore, C_{hydro} is set such that the hydrodynamic viscosity from SANS approaches the

measured viscosity at high shear. Regardless, little change is seen in η_{hydro} as a function of shear rate and no shear thickening is measured in the rheology.

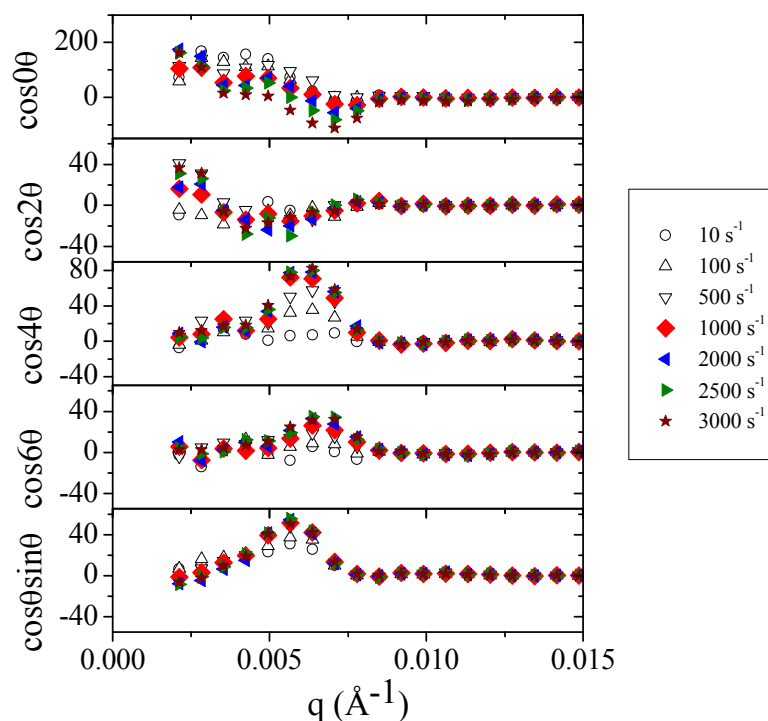


Figure 4.65 Harmonic weighted, circular averaged difference spectra ($I_{\text{shear}} - I_{\text{static}}$) from $\phi \sim 0.5$ coated sticky hard-sphere sample in 1-2 plane flow-SANS.

Figures 4.65-4.69 show the harmonics analysis for the coated sticky hard-sphere particle suspensions (section 4.3.1.4). The unweighted difference spectra (Figure 4.65, top) have an increase in scattering at low shear rates compared to equilibrium, which decreases at the higher shear rates. The highest shear rate data has an increase in scattering at the lowest q but a net decrease in scattering over a broader range of $0.003\text{-}0.007 \text{ \AA}^{-1}$. The two-fold symmetry have an increase in scattering at the

lowest q with increasing shear rate. The four-fold and six-fold symmetry have a peak centered around 0.0064 \AA^{-1} , which increases with increasing shear rate. The $\cos\theta\sin\theta$ symmetry has a peak at 0.0057 \AA^{-1} which appears at all shear rates, but has little change with increasing shear rate.

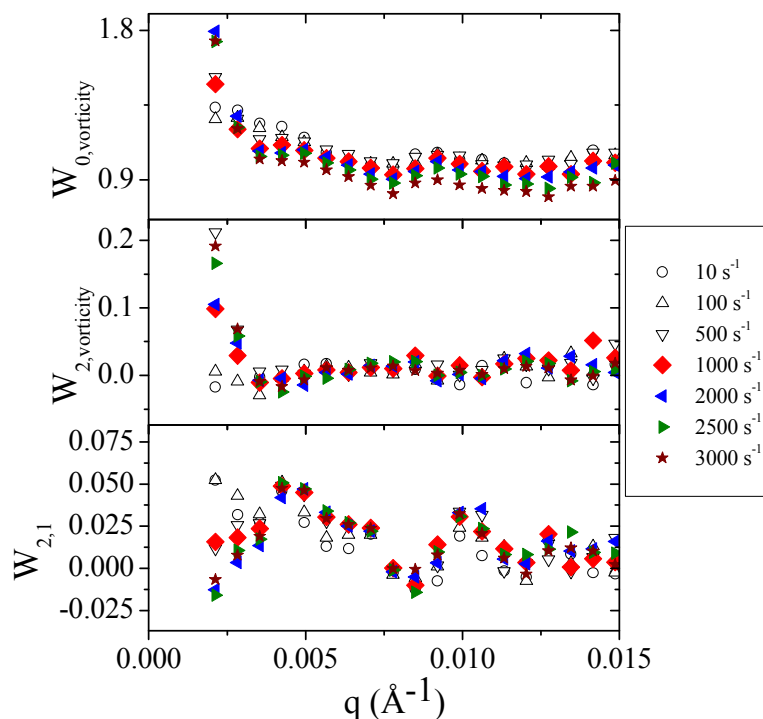


Figure 4.66 Harmonic weighted SANS data normalized by static data ($I_{\text{shear}}/I_{\text{static}}$), or W terms, from $\phi\sim 0.5$ coated sticky hard-sphere sample in 1-2 plane flow-SANS.

Figure 4.66 shows the harmonic weighed data normalized by the static data for the sticky hard-sphere suspension. Very little change is seen in W_0 or W_2 , except at the lowest q . $W_{2,1}$ has positive values at low q at low shear rates which turn negative at higher shear rates. This feature is unique to this suspension.

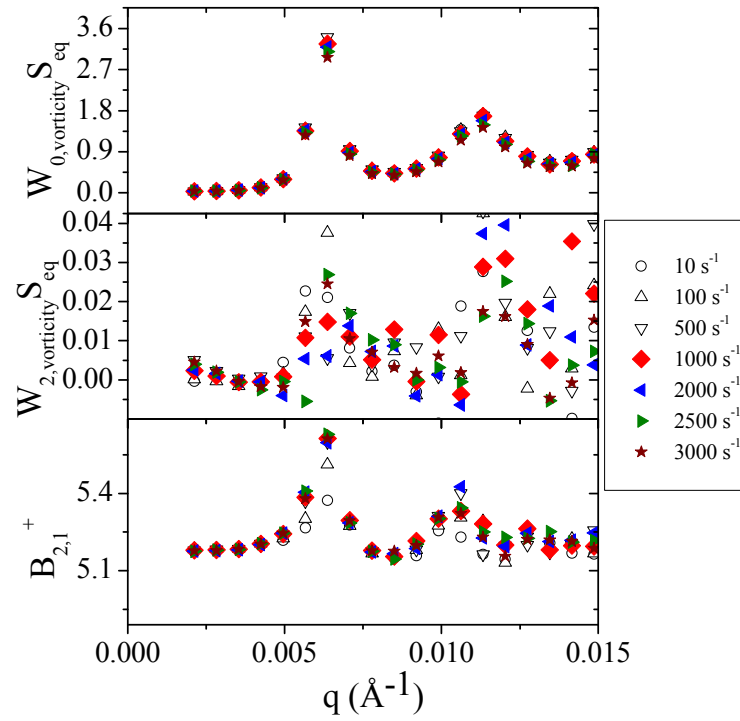


Figure 4.67 Structurally weighted harmonics calculated from $\phi \sim 0.5$ coated sticky hard-sphere sample in 1-2 plane flow-SANS. Note that $B_{2,1}^+$ is proportionally to $W_{2,1}$.

Figure 4.67 shows the prior data weighted by the equilibrium structure. The equilibrium structure washes out the majority of the changes in W_0 and W_2 at low q – oscillations are seen in W_2 which are very small in amplitude. Weighting $W_{2,1}$ by S_{eq} to get $B_{2,1}^+$ accentuates the changes seen at only a few points near the structural peaks and eliminates the changes at very low q .

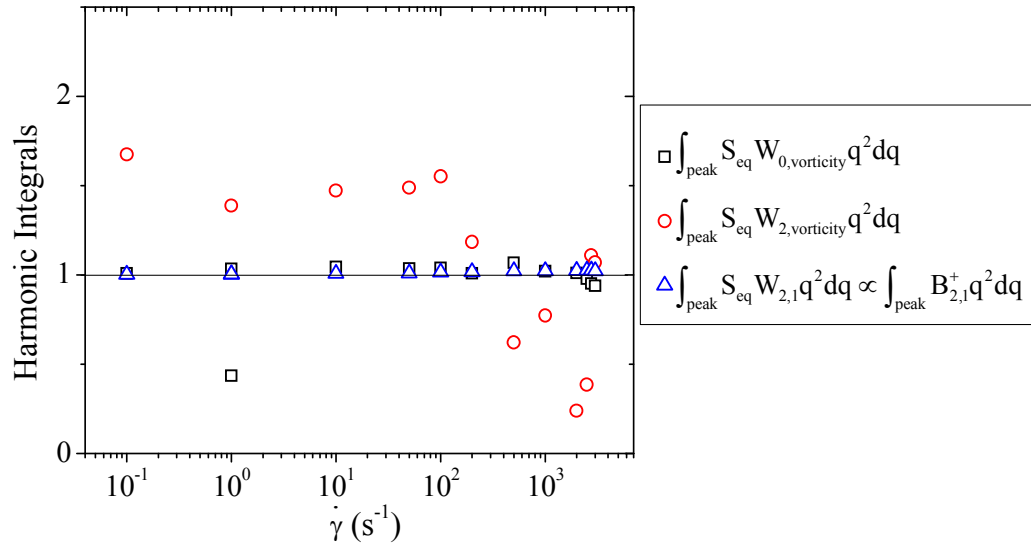


Figure 4.68 Harmonic integrals calculated from micromechanics analysis of SANS data in 1-2 plane measurements of $\phi \sim 0.5$ coated sticky hard-sphere sample. Integrals are all normalized by the value at equilibrium. The line at 1 is included to guide the eye.

Figure 4.68 shows the harmonic integrals calculated from data in Figure 4.67. The W_0 integral increases slightly over the majority of the shear rate range but then drops distinctly at the highest shear rates. The W_2 integral once again is effectively noise; it has values above 1 which sharply decrease at shear rates above 100 s^{-1} . $B_{2,1}^+$ increases slightly with increasing shear rate.

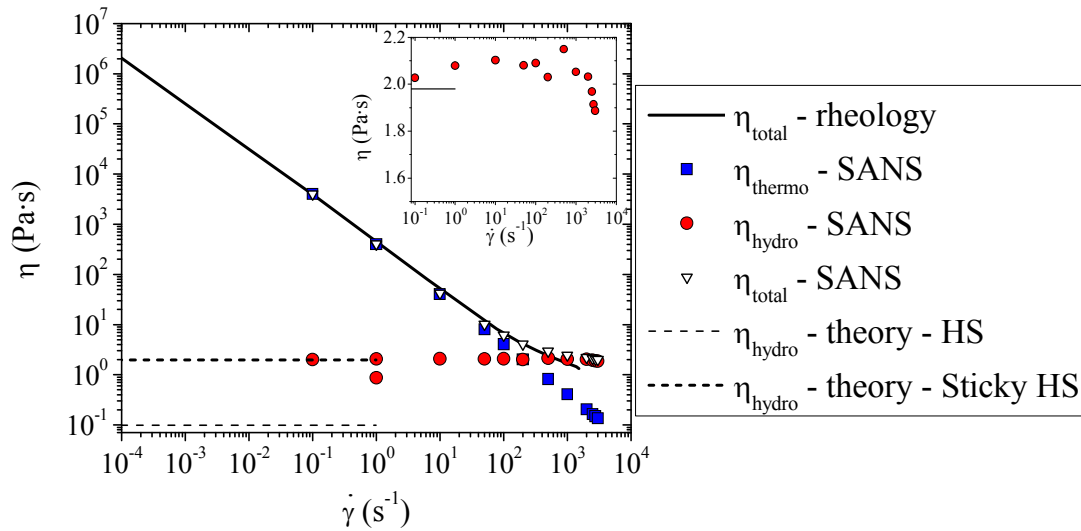


Figure 4.69 Comparison of thermodynamic and hydrodynamic components of the viscosity from SANS microstructure measurements to viscosity from rheometry for 1-2 plane measurements of $\phi \sim 0.5$ coated sticky hard-sphere sample

Figure 4.69 shows the comparison of the rheology to the components of the rheology measured from SANS for the $\phi \sim 0.5$ coated sticky hard-sphere suspension. As with the prior sample at high concentration, adjusting C_{thermo} to fit η_{thermo} at the lowest shear rate gives a good prediction of the shear thinning viscosity for about three orders of magnitude. Above a shear rate of 100 s^{-1} , η_{hydro} begins to dominate the total viscosity. In this figure, the two lines for η_{hydro} show the hard-sphere (lower) and sticky hard-sphere (upper) predictions. The hard-sphere model is calculated from equation 4.3 as before, with $\phi = 0.596$ determined from the SANS fit. The sticky hard-sphere model uses the hard-sphere model (equation 4.3) scaled using the sticky parameter of $\tau_b = 0.545$ in equation 3.8 (τ_b is fit from SANS data as seen in Figure 4.48). The hydrodynamic viscosity increases slightly with increasing shear rate at moderate shear, but decreases strongly at the highest shear rates. Note that, for the

shear thickening sample at high concentration, η_{hydro} increased continuously at high shear rates in the shear thickened state. For this sample, which does not shear thicken, η_{hydro} has a distinct and unique decrease at high shear rates, where shear thickening would be expected for the hard-sphere suspension based on the Péclet number.

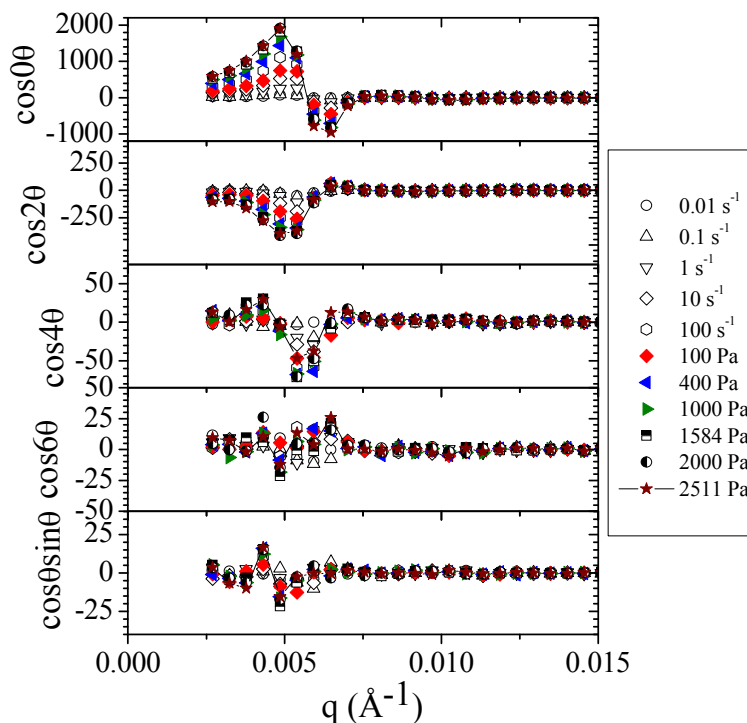


Figure 4.70 Harmonic weighted, circular averaged difference spectra ($I_{\text{shear}} - I_{\text{static}}$) from $\phi=0.53$ sample in radial Rheo-SANS.

Figures 4.70-4.73 show the micromechanics analysis for the high concentration, $\phi=0.53$ sample in radial Rheo-SANS (2nd data set in section 4.3.2.1). The weighted difference spectra are shown as Figure 4.70. As seen before, for the unweighted data there is a peak of increased scattered intensity at low q (0.005 \AA^{-1})

which increases with increasing shear rate, with a dip at slightly higher q (0.0065 \AA^{-1}) which also increases in intensity with increasing shear rate. The two-fold symmetry, shown by the $\cos 2\theta$ weighted harmonic, has a negative peak (minimum), also at 0.005 \AA^{-1} . There is little four-fold or six-fold symmetry indicated by the $\cos 4\theta$ and $\cos 6\theta$ weightings, nor is there a systematic trend in the $\cos\theta\sin\theta$ weighted data.

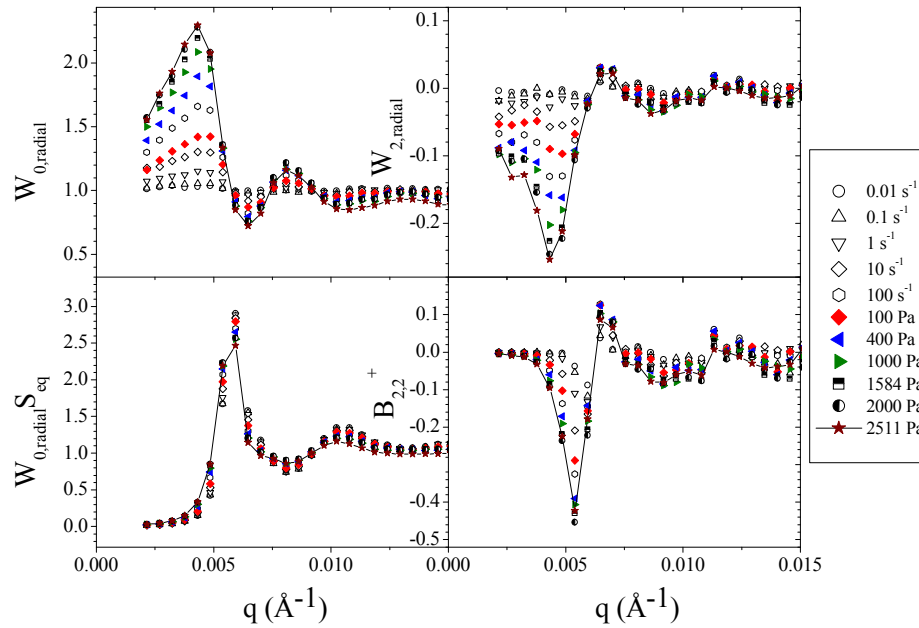


Figure 4.71 Harmonic weighted SANS data ($I_{\text{shear}}/I_{\text{static}}$), from $\phi \sim 0.53$ sample in radial Rheo-SANS. Top) Normalized harmonics or W's. Bottom) Structurally weighted harmonics.

Figure 4.71 shows both the normalized, harmonic weighted data ($W_{0,\text{radial}}$ and $W_{2,\text{radial}}$ shown on top), and the data weighted by the equilibrium structure factor ($W_{0,\text{radial}}S_{\text{eq}}$ and $B_{2,2}^+$, which is proportional to $W_{2,\text{radial}}S_{\text{eq}}$). The W_0 and W_2 have basically the same behavior as the unweighted and $\cos 2\theta$ weighted subtraction patterns

discussed in the prior paragraph. Weighting these harmonics by S_{eq} minimizes the majority of the peak in W_0 except over a few data points of q near the transition from a peak of increased scattering to a valley of decreased scattering under shear; the value of W_0 at the structure peak still increases with increasing shear rate. The structure peak is also near the higher q part of the broad minimum seen in W_2 , and so $B_{2,2}^+$ also has a broad minimum which increases in intensity with increasing shear.

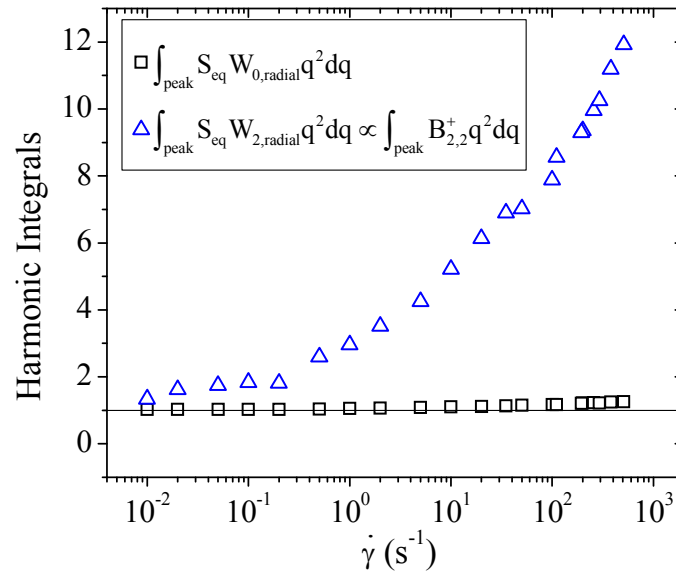


Figure 4.72 Harmonic integrals calculated from micromechanics analysis of SANS data in radial Rheo-SANS measurements of $\phi=0.53$ hard-sphere silica. Integrals are all normalized by the value at equilibrium. The line at 1 is included to guide the eye.

Figure 4.72 shows the harmonic integrals calculated up to the structure peak of the structure-factor weighted harmonics seen in Figure 4.71. The $W_{0,radial}$ integral is basically unchanged for shear rates up to 1 s⁻¹, and increases slightly at shear

rates beyond 1 s^{-1} . The $B_{2,2}^+$ integral has a slight increase with increasing shear up to 0.2 s^{-1} , and then begins to systematically increase with increasing shear rate.

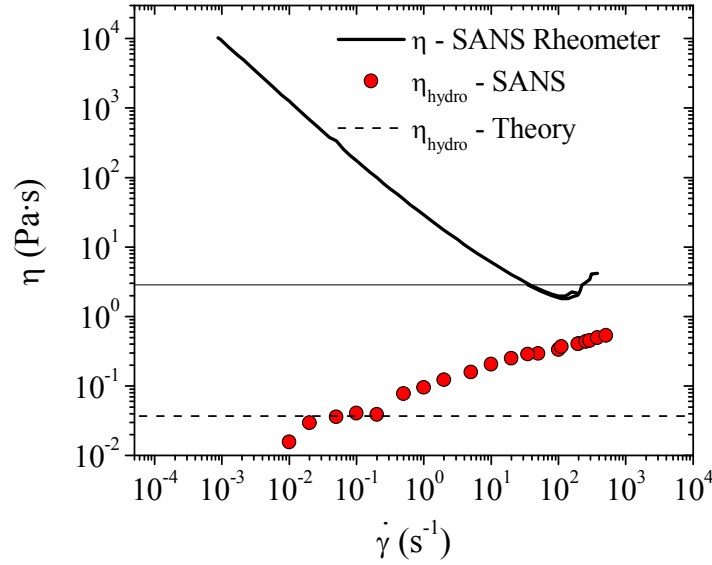


Figure 4.73 Comparison of hydrodynamic component of the viscosity from SANS microstructure measurements to viscosity from rheometry for radial Rheo-SANS measurements of $\phi=0.53$ hard-sphere silica.

Figure 4.73 shows a comparison of the hydrodynamic component of the viscosity from Radial SANS microstructure measurements on the $\phi=0.53$ hard-sphere silica sample. In this plane of shear, the thermodynamic component of the viscosity cannot be determined as discussed previously. The hydrodynamic component of the stress is determined from a form of equation 2.35 shown as equation 4.6

$$\eta_{\text{hydro}}(\dot{\gamma}) \approx C_{\text{hydro}} \left[\frac{\int_{\text{peak}} S_{\text{eq}} W_{2,\text{radial}}(\dot{\gamma}) q^2 dq}{\int_{\text{peak}} S_{\text{eq}} W_{2,\text{radial}}(\text{static}) q^2 dq} - \frac{\int_{\text{peak}} S_{\text{eq}} W_{0,\text{radial}}(\dot{\gamma}) q^2 dq}{\int_{\text{peak}} S_{\text{eq}} W_{0,\text{radial}}(\text{static}) q^2 dq} \right]. \quad (4.6)$$

Once again, C_{hydro} is adjusted such that the η_{hydro} data fits the theory value at low shear rates. For this experiment, η_{hydro} does increase with increasing shear rate as the suspension approaches the shear-thickened portion of the rheology. This increase is driven by the increase in W_2 seen in Figure 4.72.

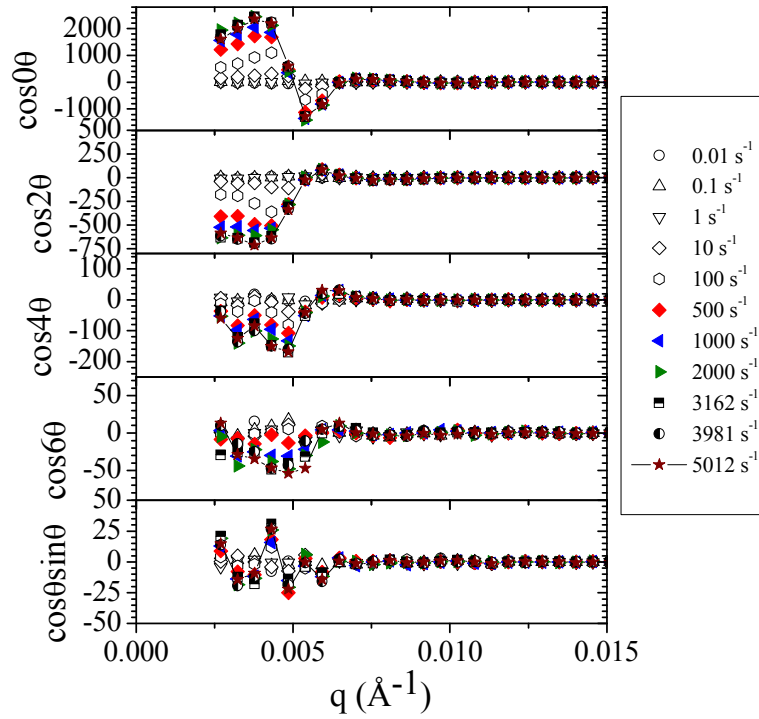


Figure 4.74 Harmonic weighted, circular averaged difference spectra ($I_{\text{shear}} - I_{\text{static}}$) from $\phi=0.44$ sample in radial Rheo-SANS.

Figures 4.74-4.77 show the micromechanics analysis for the $\phi=0.44$ sample in radial Rheo-SANS (2nd data set in section 4.3.2.2). The weighted difference

spectra are shown as Figure 4.74. As seen before, there is a peak of increased scattered intensity at low q (0.0038 \AA^{-1}) which increases in intensity with increasing shear rate, with a dip at slightly higher q (0.0054 \AA^{-1}) which also increases in strength (decreased intensity) with increasing shear rate. The two-fold symmetry, shown by the $\cos 2\theta$ weighted harmonic, has a negative peak (minimum), also at 0.0038 \AA^{-1} . There is weak four-fold and six-fold symmetry indicated by the $\cos 4\theta$ and $\cos 6\theta$ weightings; the changes in these datasets grow systematically with shear rate. As seen in the data on the higher concentration sample, there is no systematic trend in the $\cos\theta\sin\theta$ weighted data.

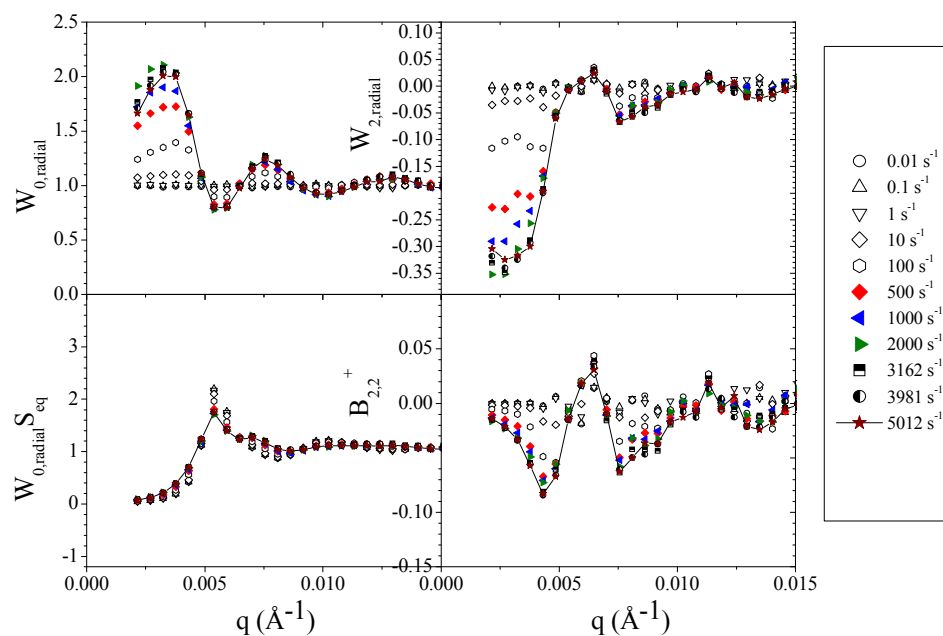


Figure 4.75 Harmonic weighted SANS data ($I_{\text{shear}}/I_{\text{static}}$), from $\phi \sim 0.44$ sample in radial Rheo-SANS. Top) Normalized harmonics or W's. Bottom) Structurally weighted harmonics.

Figure 4.75 shows both the normalized, harmonic weighted data ($W_{0,\text{radial}}$ and $W_{2,\text{radial}}$), and the normalized harmonic weighted by the equilibrium structure factor ($W_{0,\text{radial}}S_{\text{eq}}$ and $B_{2,2}^+$). Overall, the results here are similar to that seen in the higher concentration sample. W_0 and W_2 have the same behavior as the unweighted and $\cos 2\theta$ weighed subtraction patterns discussed previously. Once again, weighting these harmonics by S_{eq} accentuates the minimum in W_0 , causing the value at the structure peak to decrease with increasing shear rate. Including S_{eq} does not significantly change the trends with shear rate seen in W_2 (transforming it to $B_{2,2}^+$).

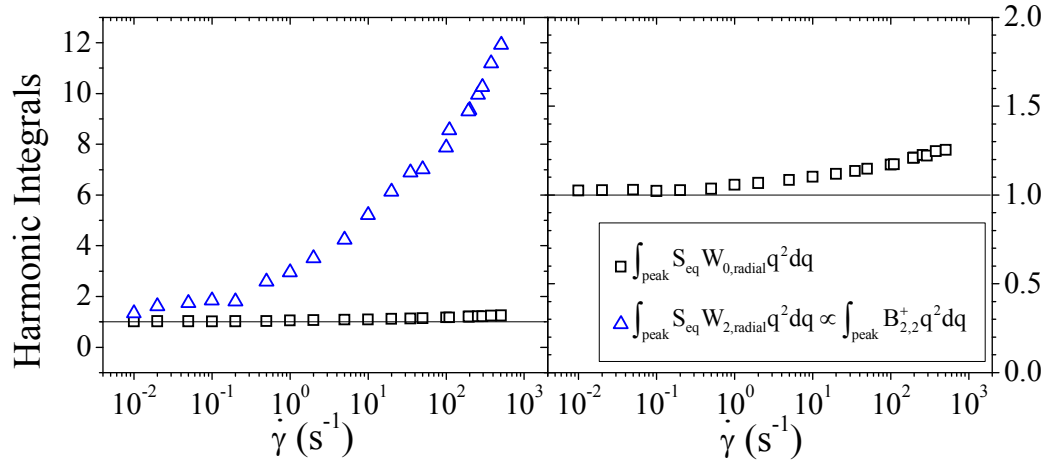


Figure 4.76 Harmonic integrals calculated from micromechanics analysis of SANS data in radial Rheo-SANS measurements of $\phi=0.44$ hard-sphere silica. Integrals are all normalized by the value at equilibrium. The line at 1 is included to guide the eye.

Figure 4.76 shows the harmonic integrals calculated up to the structure peak of the structure-factor weighted harmonics seen in Figure 4.75. The $W_{0,\text{radial}}$ integral is basically unchanged for shear rates up to 0.2 s^{-1} , and then increases

systematically with increases in shear rate. The $B_{2,2}^+$ integral fluctuates at low shear rate, dipping to a minimum at 50 s^{-1} , and then increasing monotonically with shear rate as the shear rate increases beyond 50 s^{-1} .

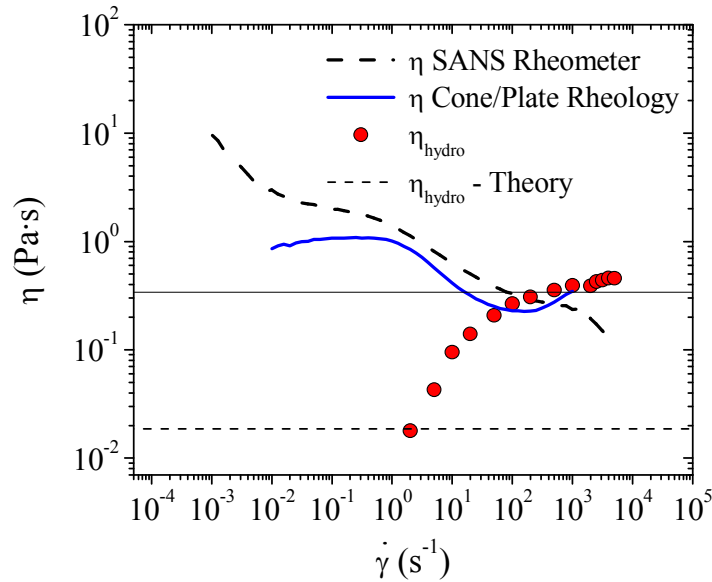


Figure 4.77 Comparison of hydrodynamic component of the viscosity from SANS microstructure measurements to viscosity from rheometry for radial Rheo-SANS measurements of $\phi=0.44$ hard-sphere silica.

Figure 4.77 shows a comparison of the hydrodynamic component of the viscosity from SANS microstructure measurements of Radial SANS experiments on the $\phi=0.44$ hard-sphere silica sample. For this experiment, η_{hydro} also increases with increasing shear rate as the suspension reaches the shear-thickened portion of the rheology. Interestingly, the change in η_{hydro} with increases in shear rate decrease near the thickened state, consistent with either slip or the instrument limitations (instrument not reaching the given stress).

4.4 Discussion

The microstructure of concentrated suspensions in 1-2 plane and radial SANS has been measured successfully. For all volume fractions, anisotropy is seen as the sample is sheared into the shear thinning regime of the steady shear rheology. There is a consistent pattern to this anisotropy for each plane of shear, regardless of the concentration. In general, the degree of this anisotropy grows with increasing applied shear, but eventually saturates at the highest shear rates. In addition, the total scattered intensity in the nearest neighbor ring grows systematically as the applied shear increases towards and into the thickened state.

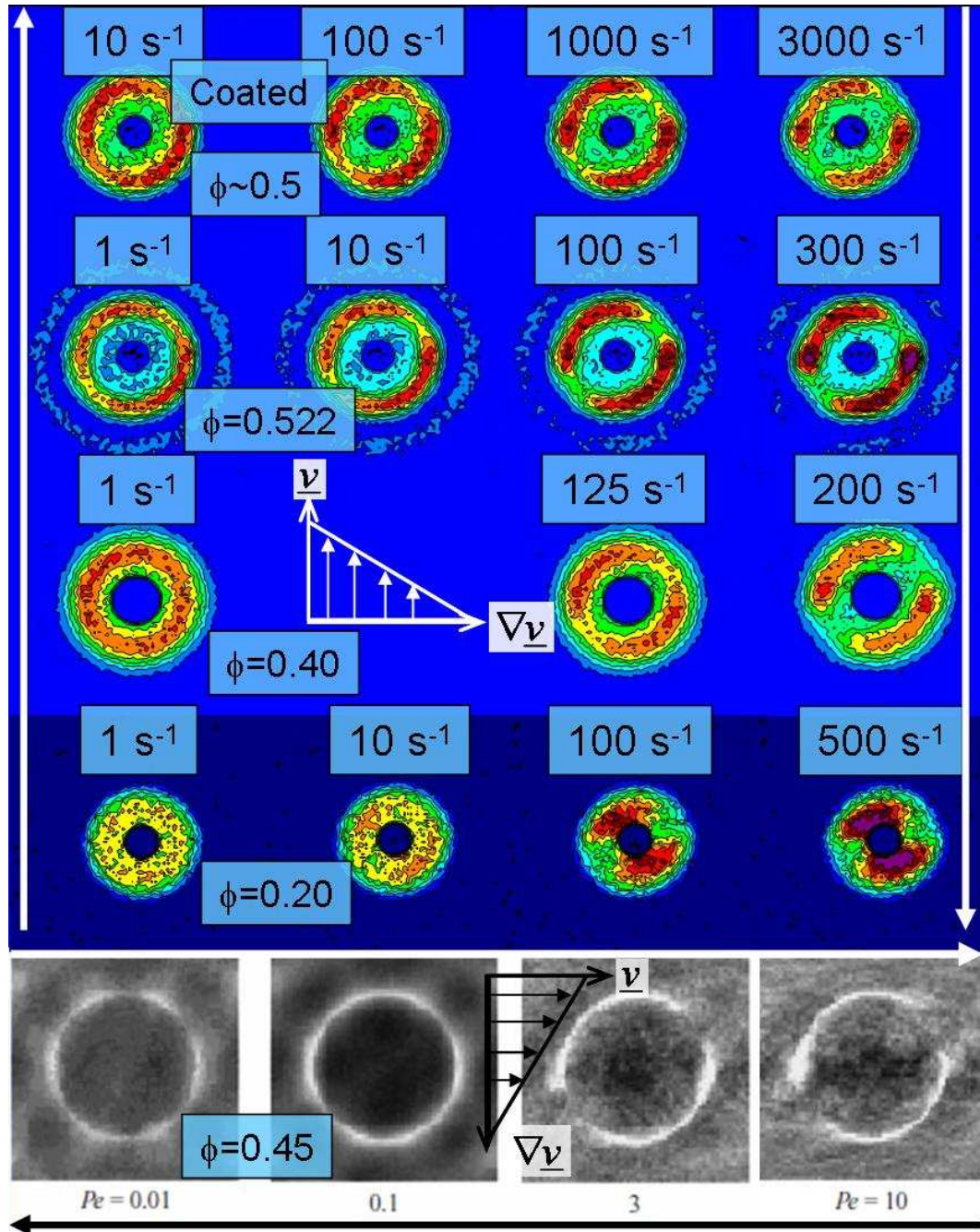


Figure 4.78 SANS spectra from 1-2 plane Flow-SANS experiment, compared to expectation radial distribution function data from Stokesian dynamics simulations ($\phi \sim 0.45$) of Foss and Brady [24]. Columns are at the same order of magnitude in Pe .

Figure 4.78 shows a comparison of representative 2-d SANS spectra from 1-2 plane flow-SANS of various volume fractions and at various shear rates to the radial distribution function from Stokesian Dynamics simulations [24]. Note that the simulation radial distribution function data shows the probability of finding a particle relative to another particle with respect to distance and angle – light areas indicate high particle probability or concentration around a center particle and dark areas indicate low probability of a particle having that location. This radial distribution function data is qualitatively similar to the SANS data, where changes in scattering come from changes in the microstructure through the structure factor, which is the Fourier transform of the radial distribution function. Also included is the SANS spectra for the particles coated with the octadecyl polymer brush. Each column is at the same order of magnitude in Péclet number. (The conversion is $Pe = 0.037 \text{ seconds} * \text{rate}$ for the hard-spheres or $Pe = 0.0035 \text{ seconds} * \text{rate}$ for the sticky hard-spheres.) It is important to note that the SANS data includes contributions from the particle size and shape (form factor) as well as the structural information. In addition, while the anisotropy in the structure should be similar between the radial distribution function and SANS data, there are some differences. Most notably, as the structure factor is the Fourier transform of the radial distribution function, the anisotropy is rotated by 90° - increased scattering vertically is caused by increased concentration horizontally. Note that, for a more direct comparison, the shear direction for SANS experiments and radial distribution data in this and the following related figures are rotated by 90° relative to each other.

The Stokesian dynamics simulations can help provide insight into the measured microstructure. These simulations see increased particle correlations on the

leading and trailing edges of a particle (along the flow direction or horizontally as pictured) at high Péclet numbers and high concentrations. These simulation radial distribution functions also have the shape of two comets circling counterclockwise, with an area of very little particle concentration beyond the comet head, as seen in the 1-2 plane SANS experiments. This shape is indicative of the high particle concentration at the leading edge of a particle in shear flow (along the shear direction) having very low particle concentration just beyond the edge towards the extension axis (see the decrease in the SANS intensity at a 45° angle above the horizontal on the right side of the pattern). The high and moderate concentration ($\phi=0.522$ and $\phi=0.40$) suspension scattering have this bright leading edge, as does the coated sticky hard-sphere suspension scattering. The sticky hard-sphere suspension does not have a net increase in scattering in the nearest neighbor ring, however, nor does it have a large increase in scattered intensity along the gradient axis. The low concentration sample does have anisotropy with increased scattering in the same areas at low q , although there is not a sharp nearest neighbor ring due to the lower concentration causing decreased nearest neighbor particle correlations.

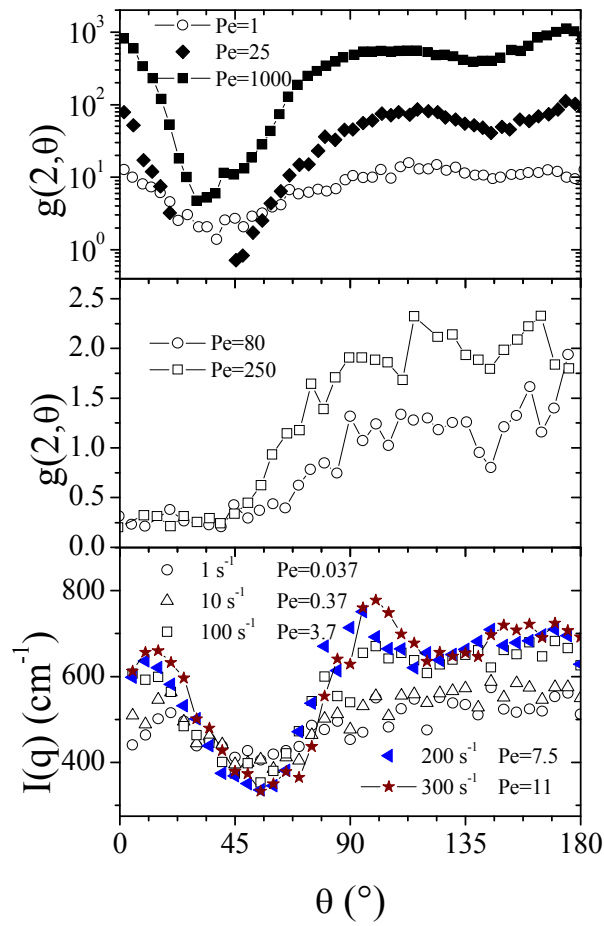


Figure 4.79 Comparisons of angular dependent SANS data to literature radial distribution at contact data. Top) Literature Stokesian Dynamics simulations [31] Middle) Literature particle tracking experiments [98]. Bottom) Annular averaged 1-2 plane flow-SANS data for $\phi=0.522$ sample (angle shifted by 90° to account for difference between SANS and real space structure).

Figure 4.79 shows some annular averaged data with comparisons to relevant literature, including Stokesian dynamics simulations [31] and particle tracking experiments [98]. As seen previously, this behavior in the 1-2 plane flow-SANS data is consistent amongst the volume fractions for highly sheared suspensions – there is a

minimum at $45\text{-}60^\circ$, a peak at 90° , a slight dip towards 135° , and back up to a plateau till 180° (note that the angle for the Fourier space structure measured by SANS has been shifted by 90° in this figure relative to the angle defined and used previously in this chapter, in order to give a direct comparison to the real-space structure).

Interestingly, the simulation data [31] have remarkably similar features, where the differences are consistent with the difference between the two different measurements; the SANS intensity changes due to the structure factor are not linearly related to the radial distribution function at contact. The particle tracking experiments also have similar behavior, with a flat region from $0\text{-}45^\circ$, followed by a sharp increase towards 90° and a plateau beyond [98].

These SANS structural measurements and Stokesian Dynamics radial distribution functions give only an average measure of the structure. The transient nature of the hydrocluster mechanism leads the data to be typically summarized in this manner. Figure 4.80 shows some snapshots of the particle configuration from Stokesian Dynamics simulations of Melrose and Ball [99]. These snapshots help give a better picture of the microstructure of a suspension at high Péclet number, in the shear thickened state. Clearly, density fluctuations lead to local clustering. In addition, the majority of these clusters are on the order of only a few particle diameters, although some clusters propagate over many particles. In addition, the structure is significantly different between the different snapshots, which are taken only one strain unit apart. Therefore the density fluctuations have short time transients.

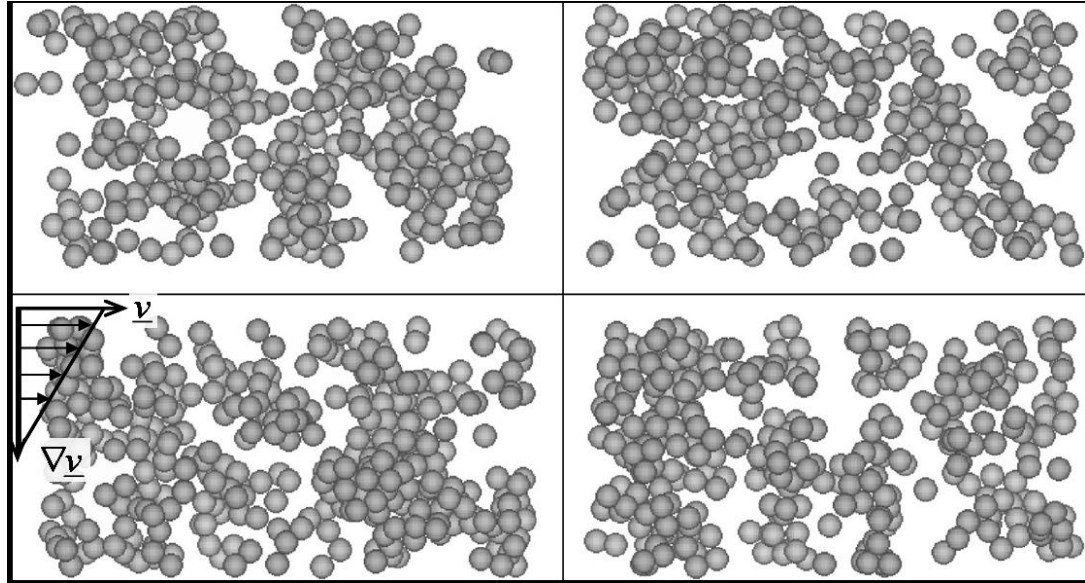


Figure 4.80 Snapshots of particle configuration from Stokesian Dynamics simulations of Melrose and Ball [99] at $Pe=3000$, in a rectangular box. Each box is separated by a unit strain.

One key factor seen in both the 1-2 plane flow-SANS experiments and radial Rheo-SANS experiments at all concentrations of hard-sphere suspensions (except the $\phi=0.40$ sample in 1-2 SANS due to sample issues) is an increase in low- q scattered intensity (circular averaged). Some representative circular averaged data in the 1-2 plane of shear is seen as Figure 4.81. In both the low and high concentration suspensions of hard-spheres, the low- q scattering is seen to increase as we go from low shear to high shear and the wavevector location of the structural peak is seen to shift to slightly lower q , indicating compression of the structure. However, the octadecane-coated sticky hard-sphere suspension has practically no change in the scattered intensity at low q between the static and high shear data. The increased low q scattering is likely due to clustering within the suspension which drives shear

thickening – this sticky hard-sphere suspension shows neither this clustering nor shear thickening.

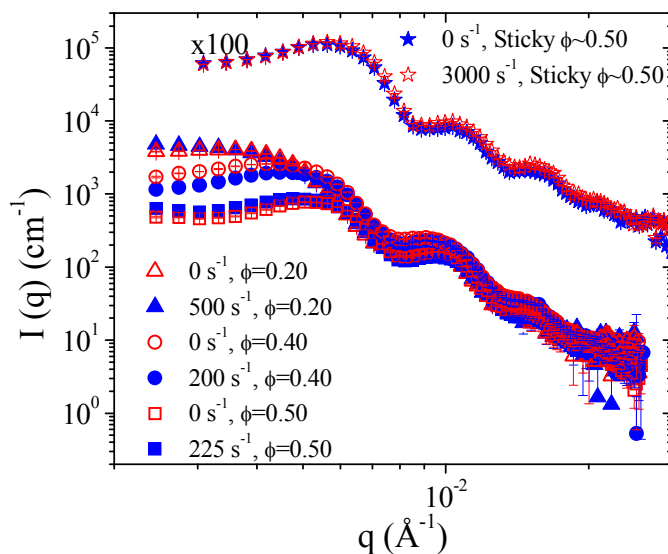


Figure 4.81 Comparison of circular averaged 1-2 plane data between static and high shear for three concentrations of near hard-sphere suspensions and a high concentration sticky hard-sphere suspensions.

The radial SANS data was also seen to have shifts in the low- q peak in the circular averaged data, consistent with prior results [23]. In radial SANS, the circular averaged data has peaks which develop at 0.0042 \AA^{-1} and 0.0048 \AA^{-1} for the high concentration samples, with minima at 0.0060 and 0.0066 \AA^{-1} , respectively (two different samples). The moderate concentration samples have peaks at either 0.0039 \AA^{-1} , shifting towards 0.0035 \AA^{-1} with increasing stress or at 0.0043 \AA^{-1} shifting to 0.0037 \AA^{-1} with increasing stress (two different samples). These samples also have minima at 0.0059 \AA^{-1} and 0.0053 \AA^{-1} , respectively. The 1-2 plane SANS

measurements have similar peaks, as expected. In 1-2 plane SANS, the high concentration sample ($\phi=0.522$) has a peak at 0.0045 \AA^{-1} , with a minimum at 0.0067 \AA^{-1} . The low concentration sample ($\phi=0.020$) has an increase in scattering at low q with no peak (peak less than 0.0025 \AA^{-1}) with a minimum at 0.0045 \AA^{-1} . The sticky hard-sphere suspension has a peak in the low q scattering at 0.0041 \AA^{-1} , with a minimum at 0.0067 \AA^{-1} , although this peak has a significantly decreased intensity at the highest shear rates.

These peaks and minima are indicative of cluster formation [94], with a characteristic length scale given by $2\pi/q_{\text{peak}} \sim 130\text{-}180 \text{ nm}$, or about 1.1-1.5 particle diameters. Note that this is not a fractal-like structure forming as it is a clear peak in the scattering (except for the $\phi=0.20$ sample) and not simply increased forward scattering. The minimum at higher q is due to a reduction in the equilibrium correlation peak in the structure factor, which is very weak at these low concentrations. Note that hydrocluster formation precedes the actual rise in the overall viscosity as the viscosity is comprised of a shear thinning component due to interparticle forces and a hydrodynamic component sensitive to the hydrocluster formation [21, 32]. The onset of shear thickening of the hydrodynamic component occurs before the measurable rise in the total viscosity [21, 34, 87].

Figure 4.82 shows a comparison of radial Rheo-SANS data from two different concentration suspensions to the Stokesian dynamics simulation results projected in this plane. These Stokesian dynamics simulations results do not show the strong anisotropy seen directly in the shear plane and the remarkable agreement in anisotropy seen between the simulations and experiments in the shear plane; however, there is similar anisotropy in the Stokesian dynamics structure and the SANS

experiments. Both concentrations' scattering data have strong anisotropy in the form of opposing crescent moon shapes oriented along the vorticity axis, as seen previously [23]. In addition, this scattering pattern is consistent with the mild anisotropy seen in the Stokesian dynamics simulations.

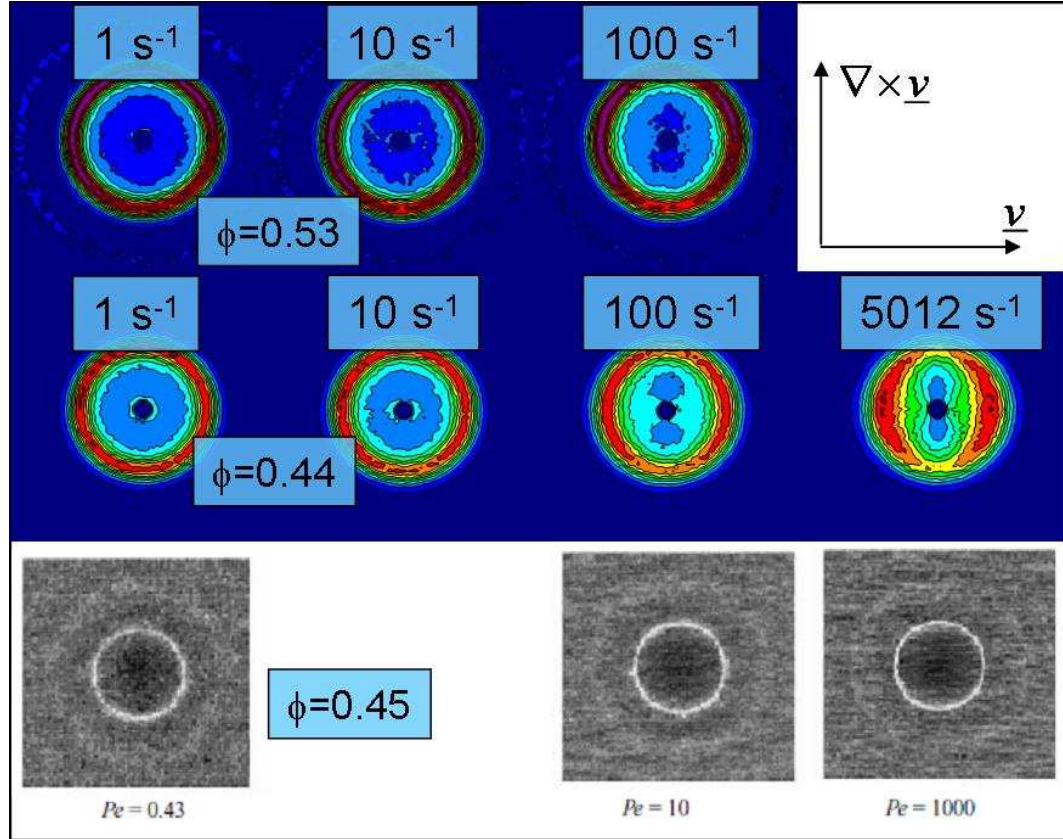


Figure 4.82 SANS spectra from radial Rheo-SANS experiment, compared to expectation radial distribution function data from Stokesian dynamics simulations ($\phi \sim 0.45$) of Foss and Brady [24]. Columns are at the same order of magnitude in Pe .

The spherical harmonic decomposition provides a summary of the shear rate dependent microstructure changes. The 1-2 plane SANS measurements are able to measure $B_{2,1}^+$ for the first time. This deformation in the microstructure is expected to drive the shear thinning or thermodynamic component of the viscosity, η_{thermo} . The thermodynamic viscosity calculated from $B_{2,1}^+$ and the micromechanics theory is consistent with the measured rheology at high concentrations. Since the theory predicts the viscosity to be proportional to $B_{2,1}^+$ divided by shear rate, this yields a strongly shear thinning η_{thermo} even for no change in $B_{2,1}^+$. In fact, the measured $B_{2,1}^+$ changes very little. Therefore, η_{thermo} does not match the measured rheology well at low and moderate concentration, where power-law shear thinning is not seen. This result is not unexpected as the hydrodynamic component of the viscosity contributes to the total viscosity to decrease the severity of shear thinning at the lower concentrations.

In addition, the hydrodynamic component of the viscosity, η_{hydro} , expected to drive shear thickening, is calculated from 1-2 plane flow-SANS and radial SANS. In both cases, a systematic rise in η_{hydro} is seen, consistent with that seen before. The SANS micromechanics analysis does not, however, show an order of magnitude rise commensurate with the order of magnitude change in the viscosity in the shear thickening regime. In fact, it is unrealistic to expect an order of magnitude increase in the scattered intensity over any small range in q with shear induced changes in the fluid microstructure. It is possible that inclusion of other harmonics in the correlation of microstructure with viscosity also caused disagreement between the rheology and the SANS calculations of viscosity. Interestingly, both η_{thermo} and η_{hydro} can be measured in the 1-2 plane flow-SANS, while radial SANS is only capable of measuring η_{hydro} .

In addition, it is possible that slip or edge effects play a role in the lack of measured increases in η_{hydro} via 1-2 plane flow-SANS. Since this instrument does not have a simultaneous measure of the stress, it is difficult to discern if slip is occurring.

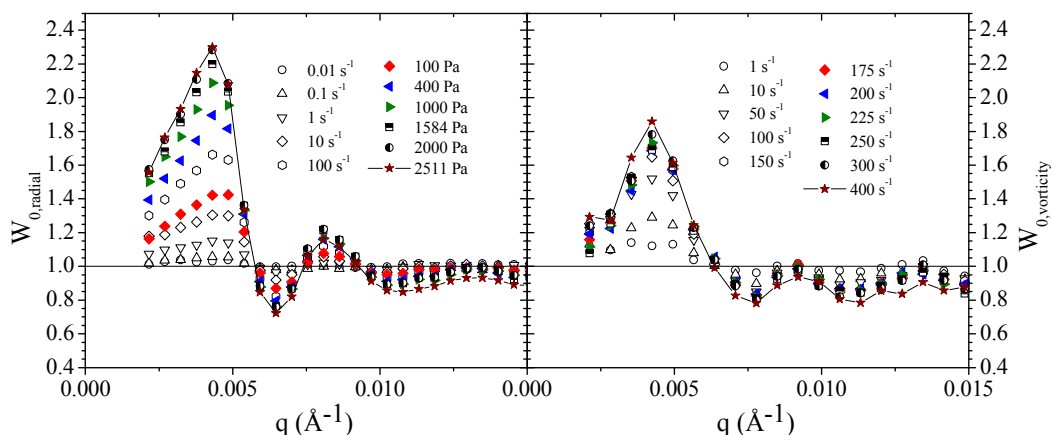


Figure 4.83 Comparison of unweighted harmonic, W_0 , between radial (left) and 1-2 plane (right) SANS experiments on comparable high concentration suspensions.

Figure 4.83 shows a comparison of the unweighted W_0 harmonic between the two planes of shear. Note that, the W_n terms are geometry dependent, unlike the $B_{l,m}^+$ terms which are a generalized description of the microstructure and are geometry independent. Regardless, since W_0 is expected to be dominated by $B_{0,0}^+$, it should have similar behavior for the two data sets. In fact, similar results are seen for the two planes of shear, although slightly higher shear rates and stresses are achieved in the radial SANS (left). The larger increases in W_0 in radial SANS over 1-2 plane SANS are more likely caused by multiple scattering in the 1-2 plane SANS decreasing the intensity changes. In addition, slip within the 1-2 plane cell could cause the lack of

significant changes in the shear thickened state, which are seen in radial SANS – a measure of stress or simultaneous velocimetry measurements during the 1-2 plane experiment would help eliminate this as a concern.

4.5 Confirmation of Scattering and Flow Field in 1-2 Plane Shear Cell

The non-standard geometry of the 1-2 plane shear cell used in these experiments is still relatively new and requires confirmation. Two distinct issues could arise in the use of a new sample geometry for use in scattering experiments under shear. First, the scattering measurement should be verified – particularly, the 1-2 plane shear cell has a 5 mm path length, which is quite long for a typical scattering experiment. Second, the rheological flow field within the shear cell requires verification – the 1-2 plane shear cell's 5 mm neutron path length is also the Couette geometry cylinder height; this value is very low relative to the desired size of the rotor for a rheological experiment. In this section, we will verify the shear cell scattering and flow field.

Figure 4.84 shows the circular averaged SANS spectra for the $\phi=0.515$ sample of the 60 nm SiO₂ particles suspended in the solvent mixture of PEG-600 and deuterated ethylene glycol taken in the shear cell under static conditions and a 1 mm static sandwich cell. This data in the shear cell was previously shown in Figure 4.7. There are some differences between the two measurements. The data in the shear cell has sharper structural peaks. In addition, these peaks are at slightly lower q in the static cell compared to the shear cell. Part of the difference between the two data sets is merely the difference in experimental setup – this is seen by comparing the model lines in the figure. The solid line indicates a hard-sphere model fit to the static cell data

with the appropriate instrument smearing for the static cell experiment. The dashed line shows the same model with the smearing appropriate for the shear cell data. The additional smoothing of these peaks and other anomalous data are likely due to multiple scattering, which has been reduced through the use of a solvent which is nearly matched to the particles in scattering length density, but is impossible to eliminate in samples of ~50% particles with the 5 mm path length. Regardless of this smearing caused by multiple scattering, the structural changes measured under shear are significant. In addition, multiple scattering is not expected to significantly change the final results which merely attempt to correlate the structural harmonics with the stresses rather than perform a complete exact calculation. In addition, the relative scattering also eliminates some of these issues as only the *changes* in the scattering due to structural changes are relevant. In different experiments with less concentrated surfactant systems, the 1-2 plane shear cell has been shown to yield identical data to that from a static cells [93].

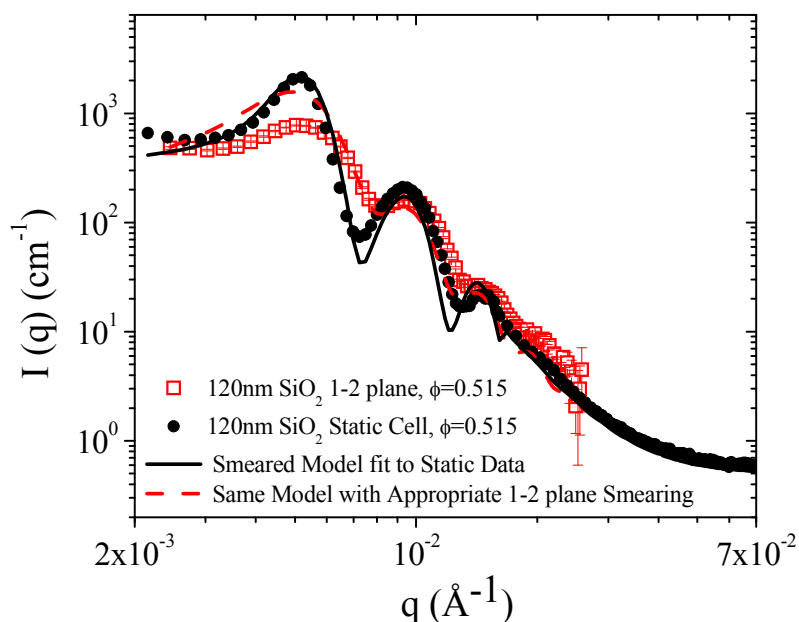


Figure 4.84 Comparison of SANS data from various path length static cells compared to 1-2 plane shear cell.

Simulations of the flow field within a similar shear cell geometry were performed using a commercial computational fluid dynamics package (Fluent). The simulated shear cell, with a 22.5 mm inner wall radius, 23.5 mm outer wall radius (for a 1 mm gap), and 7 mm height, was drawn and meshed in Gambit. This geometry was based on a prior prototype shear cell and so the dimensions differ slightly from the cell used in the SANS experiments, most notably the cylinder height being 7 mm rather than 5 mm. The total height of the simulation cell was only 3.5 mm; a symmetry plane was used to shorten computation time. The cell was meshed using a tetrahedral mesh of 0.25 mesh size, for a total of 109k tetrahedral cells and 26k nodes in a total cell half-volume of 2.02 mL. This 3-d cell was simulated in Fluent with convergence criteria of 10^{-5} on X-, Y-, and Z-velocities and 10^{-4} on continuity. The inner wall was

set as a rotational moving wall, with speeds corresponding approximately to the desired shear rates. The fluid used was Newtonian and the boundary conditions were no-slip at all four walls, which does cause a computational singularity at the corner where the moving wall meets the fixed wall.

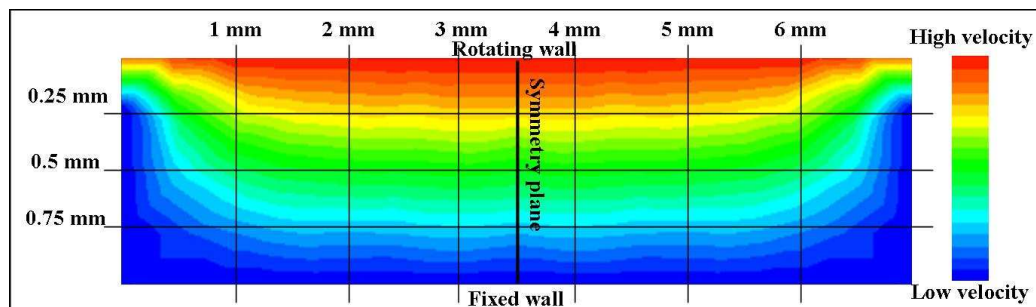


Figure 4.85 Velocity contour plot of cross-section of gap in shear cell. The top is the inner, rotating cylinder, the bottom is the fixed, outer cylinder, and the neutron beam would be oriented horizontally through the sample. Scale is 2:1 vertical:horizontal for clarity.

Figure 4.85 shows the velocity contour plot from simulations of the Newtonian fluid in the prototype shear cell discussed above. Velocity profile cross sections across the gap or along the gap are shown as Figures 4.86 and 4.87, respectively. The velocity contour plot shows that within 1 mm of the fixed cell walls (the left and right sides in Figure 4.85), the velocity profile has significant deviations from the linear velocity profile desired. Beyond 1 mm into the cell, the velocity profile is basically constant. This result is confirmed visually by Figure 4.85, which shows the velocity profile across the gap as a function of the distance from either fixed wall at the ends of the shear rotor. The most significant deviations from the desired profile are

in the outer 0.4 mm of the cell, whereas the bulk of the fluid has an acceptable velocity profile.

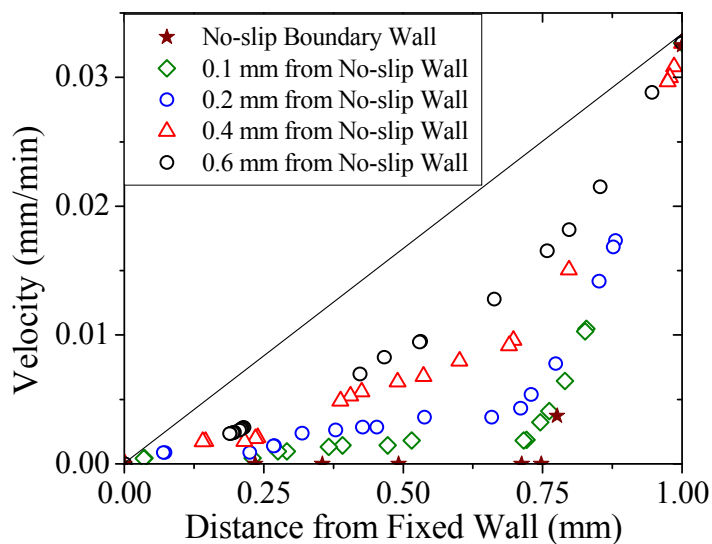


Figure 4.86 Velocity profile across the gap of the cell for a Newtonian fluid at a shear rate of 0.01 s^{-1} . The right edge is the moving wall and the left edge is the fixed wall. The data at 0.1 and 1 s^{-1} , when normalized for the wall velocity, overlay this data.

Figure 4.87 shows the alternative cross-sectional view of the velocity profile – the velocity along the gap as a function of the distance from the rotor. Clearly from this data the velocity profile is roughly constant beyond 1.5 mm from the wall, with strong deviations in the 0.5 mm closest to the no-slip wall.

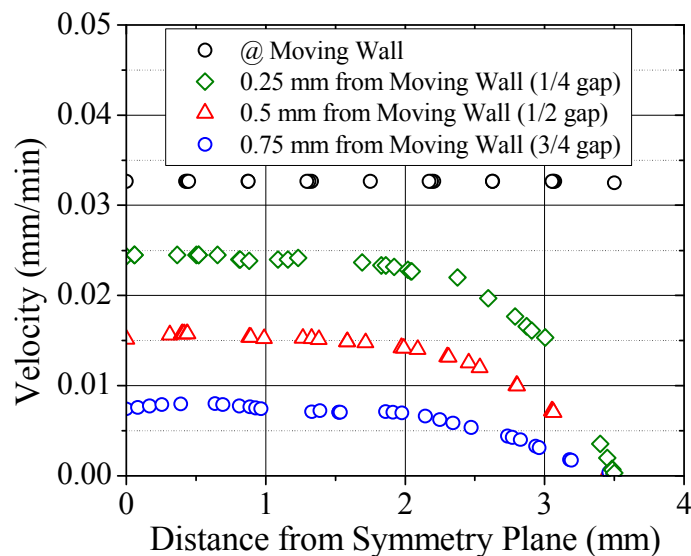


Figure 4.87 Velocity profile along the shear cell height for the Newtonian fluid at a shear rate of approximately 0.01s^{-1} . The left edge is the symmetry plane and the right edge is the fixed wall.

Near the symmetry plane, the velocity profile is both linear across the cell and unchanging along the cell. As such, ignoring the 1 mm nearest the symmetry plane gives a good estimate of the expected results for the 5 mm cylinder height cell actually used in the SANS experiments from these simulation results on the 7 mm cylinder height cell. In addition, prior work has studied shear-banding worm-like micellar systems in this geometry and seen astounding similarity between flow kinematics measured via velocimetry and the structure measured via SANS across the gap [93]. These results give additional verification of the flow field within the cell for even extremely complex rheological systems as these systems exhibit both shear-thinning and shear banding.

4.6 Conclusions

Microstructure measurements have been performed on near hard-sphere colloidal suspensions in both the 1-2 (flow-gradient) plane of shear (at three concentrations) and in the 1-3 (flow-vorticity) plane of shear (at two concentrations). The 1-2 plane measurements are novel, first of a kind, and provide unique insight into the microstructure, particularly the anisotropic structure that drives the shear thinning in the rheology. The same anisotropic microstructure seen in simulations to drive shear thinning is measured for the first time experimentally. In addition, the hydrodynamic clustering seen to drive shear-thickening is consistent with SANS measurements in both shear planes. These experiments compliment prior work [23, 59], but provide additional insight into the anisotropy in the structure through the 1-2 plane shear. In addition, comparison of the SANS data to the measurements of the normal stresses in the prior chapter also represent an improvement on prior work.

Reduction of the data by micromechanics analysis gives spherical harmonic terms that give a generalized summary of the microstructure for better comparison with potential future simulations and experiments. The component of the microstructure expected to drive shear thinning yields power law shear thinning, consistent with the data at high concentrations, but over predicting the thinning at lower concentrations. The component of the microstructure expected to drive shear-thickening via the 1-2 plane SANS experiments increases with increasing shear rate towards the shear thickened state, consistent with prior results, expectations from simulations, and the radial SANS data. In addition, the hydrodynamic component of the viscosity decrease strongly at high shear rates for the sticky hard-sphere

suspensions where a dense polymer brush suppresses shear thickening, despite increasing for all the near hard-sphere suspensions.

However, this hydrodynamic component of the viscosity measured from SANS does not show a step-change upon entering the shear-thickened state of the rheology and does not have any change large enough to account for the order of magnitude increase in the viscosity in the thickening regime. This result is consistent with the limitations on the experiment, in that the changes that drive shear-thickening can come from only a subtle change in the microstructure to increased nearest neighbor correlations which are difficult to measure via SANS. In addition, while simulations typically see only subtle changes in the structure and smaller changes in the viscosity, clearly the SANS measurements and the Stokesian dynamics simulations are missing some key structural change that drives the order of magnitude shear thickening, such as jamming of a percolated network structure. Slip, multiple scattering, and wall effects certainly affect the measured results in 1-2 plane SANS, but eliminating these issues would not change any of the conclusions presented here.

Chapter 5

FLOW-USANS EXPERIMENTS ON NEAR HARD-SPHERE SILICA DISPERSIONS

5.1 Introduction

Previous work, including that in Chapter 4, has examined the structure of concentrated, colloidal suspensions under shear flow via small angle neutron scattering (SANS) [15, 23, 33, 44, 64, 83-89]; however, SANS is limited to particle radii under 100 nm to be able to capture the structure on the nearest neighbor length scales. Substantially smaller particles are required in order to probe the longer length scale of clustering. However, the stresses, and hence shear rates required for the onset of shear thickening in hard-sphere dispersions scale inversely with particle size cubed [18, 20, 89], making it difficult to generate, as well as maintain, a stable experiment for sufficiently long durations at the required high shear rates in the SANS Couette cell (see, for example, [15, 27]). In addition, larger, $\sim 0.5 \mu\text{m}$ particles have been used in commercially relevant protective materials of recent interest in literature, also used in Chapter 7 [11, 12]; however, Rheo-SANS experiments are unable to probe the length scales required to observe hydrocluster formation in these suspensions. Finally, although suitable length scales can be probed with light scattering [64, 100-102] or direct visualization [103], few concentrated dispersions are suitably transparent.

To probe hydrocluster formation in model hard-sphere dispersions we develop a new method of flow-Ultra Small Angle Neutron Scattering (USANS) to

probe length scales up to 20 microns [104] in a suspension under steady shear flow. Here we report the first flow-USANS measurements on concentrated, colloidal dispersions and use them to examine the suspension microstructure, in particular, the possible formation of hydroclusters in the shear thickening flows at high shear rates.

Small angle x-ray scattering (SAXS) and ultra small angle x-ray scattering (USAXS) have also been used to look at dilute and concentrated, colloidal dispersions [105-110] and could potentially measure at the length scales of interest here. However, these studies for concentrated suspensions can be limited by multiple scattering due to the high contrast between particles and the solvent. This multiple scattering cannot be as easily adjusted in x-ray scattering as in neutron scattering.

5.2 Experimental

5.2.1 Flow-USANS Experiment

USANS experiments were performed using the BT5 thermal neutron double-crystal instrument at the National Institute of Standards and Technology (NIST), National Center for Neutron Research (NCNR) in Gaithersburg, MD [60, 61]. The experimental setup (Figure 2.5) required to measure high resolution in q to reach lower q gives no direct measure of structural anisotropy (the data as received is 1-dimensionally averaged in wavevector space).

USANS measurements on quiescent samples were performed in 1 mm thick titanium sandwich cells with quartz windows, except for the highest concentration sample, which was measured in the shear cell due to loading issues in the sandwich cell.

Flow-USANS measurements are performed by inserting as the sample geometry the NIST-SANS shear cell as described in section 2.5.1. The scattering is a projection in the velocity-vorticity (1-3) plane, with each q value being primarily a measure of q in the velocity direction averaged over a rectangular section of q in the vorticity direction.

The data as recorded has both wavelength smearing ($\lambda=2.38\text{\AA}$, $\Delta\lambda/\lambda=5.9\%$ wavelength spread) and effective slit smearing (due to the low vertical resolution). As the slit smearing dominates only slit-smearing will be applied to models to fit to the data [50]. The data was reduced using standard procedures [50]. As noted, USANS yields slit smeared data; therefore, under shear USANS yields a one-dimensional scattering profile that is a slit-smeared average over an anisotropic scattering pattern in the velocity-vorticity (1-3) plane of flow. Therefore, presently it is not possible to desmear data acquired under flow. The analysis is further described in section 2.5.3.

5.2.2 Suspension Properties

The suspensions used for these experiments are the nominally 260 nm radius silica spheres suspended in PEG-200, described more fully in Chapter 3. Table 5.1 shows various particle size and other particle characterization measurements including the densities of the particles and the solvent density and viscosity. Table 5.2 shows the weight and volume fraction of the various samples used here along with the critical values of shear stress, shear rate, and viscosity for shear thickening. Figure 5.1 is an SEM micrograph of these nominally 500 nm diameter particles. Figure 5.2 shows the steady shear rheology of the three suspensions measured here. The drop down lines in Figure 5.2 indicate the points at which the scattering measurements were done. Inset

in Figure 5.2 is the steady shear rheology of the lowest concentration sample on an expanded linear-scale in viscosity to show the subtle shear thinning and shear thickening. Stress-jump measurements on the middle concentration sample, shown previously in section 3.5.7 (specifically Figure 3.40), indicate that the rheology is unchanging with time over the course of our scattering experiment after a short induction time.

Table 5.1 System properties and data. Particle sizes include 95% confidence interval, except that measured via USANS which references the standard deviation.

ρ_{SiO_2}	1.96	g/mL
ρ_{PEG}	1.13	g/mL
η_{PEG}	42	mPa·s
mobility	$<10^{-11}$	$\text{m}^2 \cdot \text{V}^{-1} \text{s}^{-1}$
a - DLS	289 ± 58	nm
a - SEM	255 ± 20	nm
a - USANS	260 ± 26	nm

Table 5.2 Suspension properties.

ϕ	0.194	0.391	0.490
solids wt %	29.4	52.7	62.5
τ_{crit} (Pa)	2.50	15.8	50.1
η_{crit} (Pa·s)	0.0962	0.283	0.797
$\dot{\gamma}_{\text{crit}}$ (s^{-1})	26.0	55.9	62.9

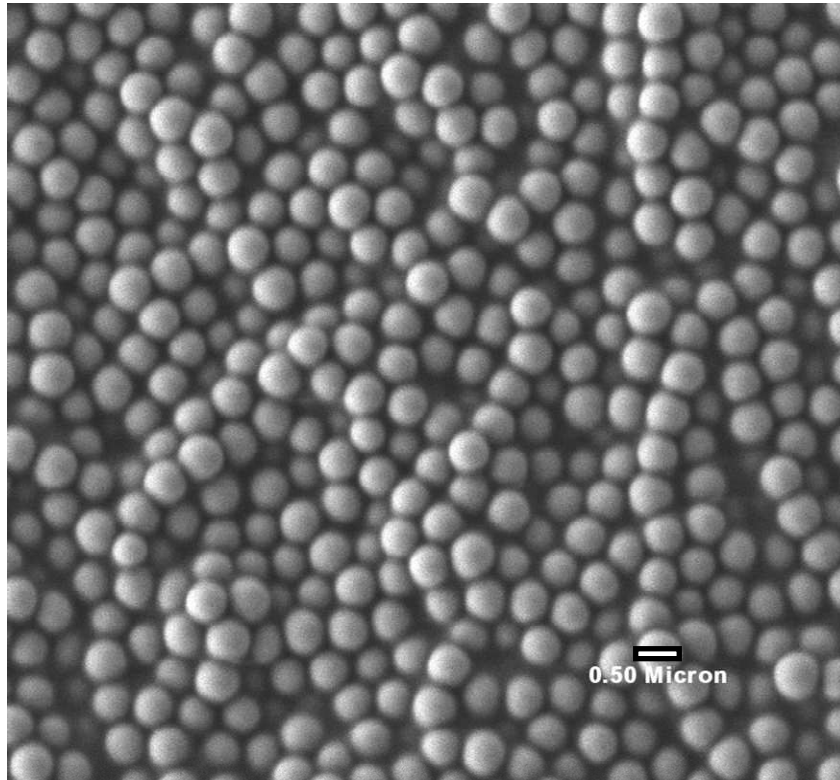


Figure 5.1 SEM micrograph of silica particles.

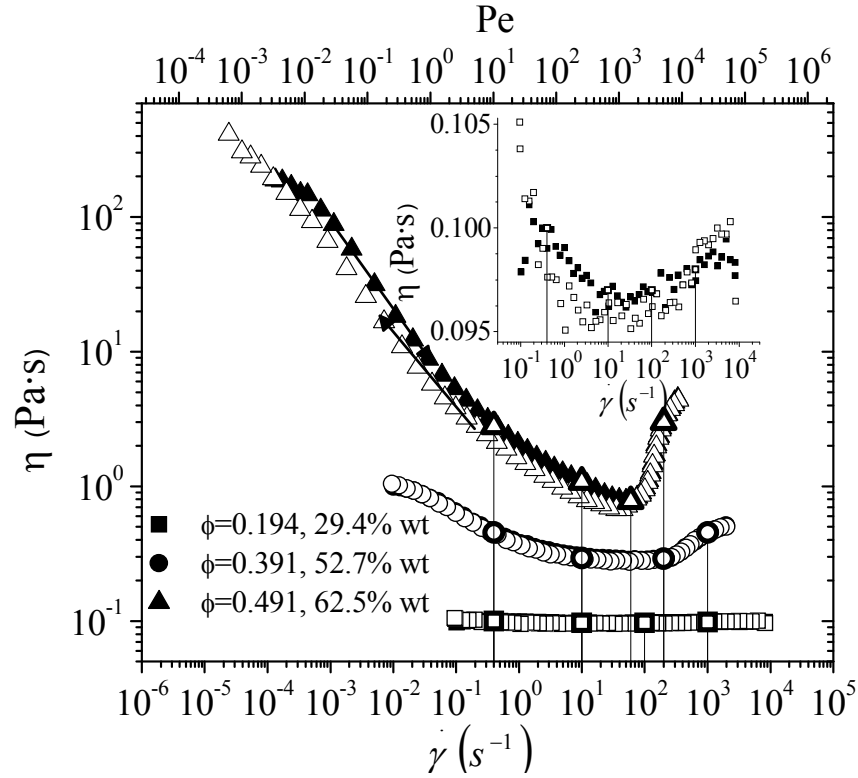


Figure 5.2 Steady-shear viscosity of a suspension of silica in PEG. The inset shows an expanded vertical scale for the low volume fraction sample to show the shear thinning and shear thickening behavior.

5.3 Flow-USANS Data

USANS measurements taken under steady shear at four shear rates for each of the three concentrated suspensions are shown in Figure 5.3, which includes the data collected under static conditions for comparison (also shown in Figure 3.3). The scattering data collected with the sample under shear is shifted vertically by progressive factors of two for clarity of presentation. The left side of the figure shows the data and the right side shows the difference between the scattered intensity under shear and that under static conditions. The predominant new feature evident in

measured intensity under shear is the shift of the scattering peak to lower scattering vector magnitudes, especially for high shear rates in the shear thickening regime. For the lowest concentration sample, the development of a very broad correlation peak at $q \sim 4 \times 10^{-4} \text{ \AA}^{-1}$ is evident with increasing shear. The moderate concentration sample exhibits a scattering peak at rest that increases in magnitude and then broadens and shifts to lower wave vector with increasing shear rate. The high concentration sample has a sharp peak indicating order or crystallinity upon shearing, which melts into a broad shoulder at low q at the highest shear rate in the shear thickening regime.

The measured effective (smeared) structure factors for the samples at rest are shown in Figure 5.4. Also included in Figure 5.4 are the calculated effective polydisperse hard-sphere structure factor; this calculated structure factor is the same structure factor used in Figure 3.3, combined with the particle form factor and instrumental smearing. Note that, as discussed in the scattering theory section (2.5.3), the measured effective structure factors will only equal the actual structure factor if there are no effects of instrument smearing, anisotropy, size polydispersity, or multiple scattering - hence the quantitative differences with the true structure factors shown for reference in Figure 5.4. Nonetheless, this comparison shows the features of these effective structure factors qualitatively represent those of the true, underlying structure. Also shown is the form factor, where the first form factor minima is observed to fall just beyond the first peak in the scattering and therefore, does not interfere with the observations of how that peak shifts under shear flow.

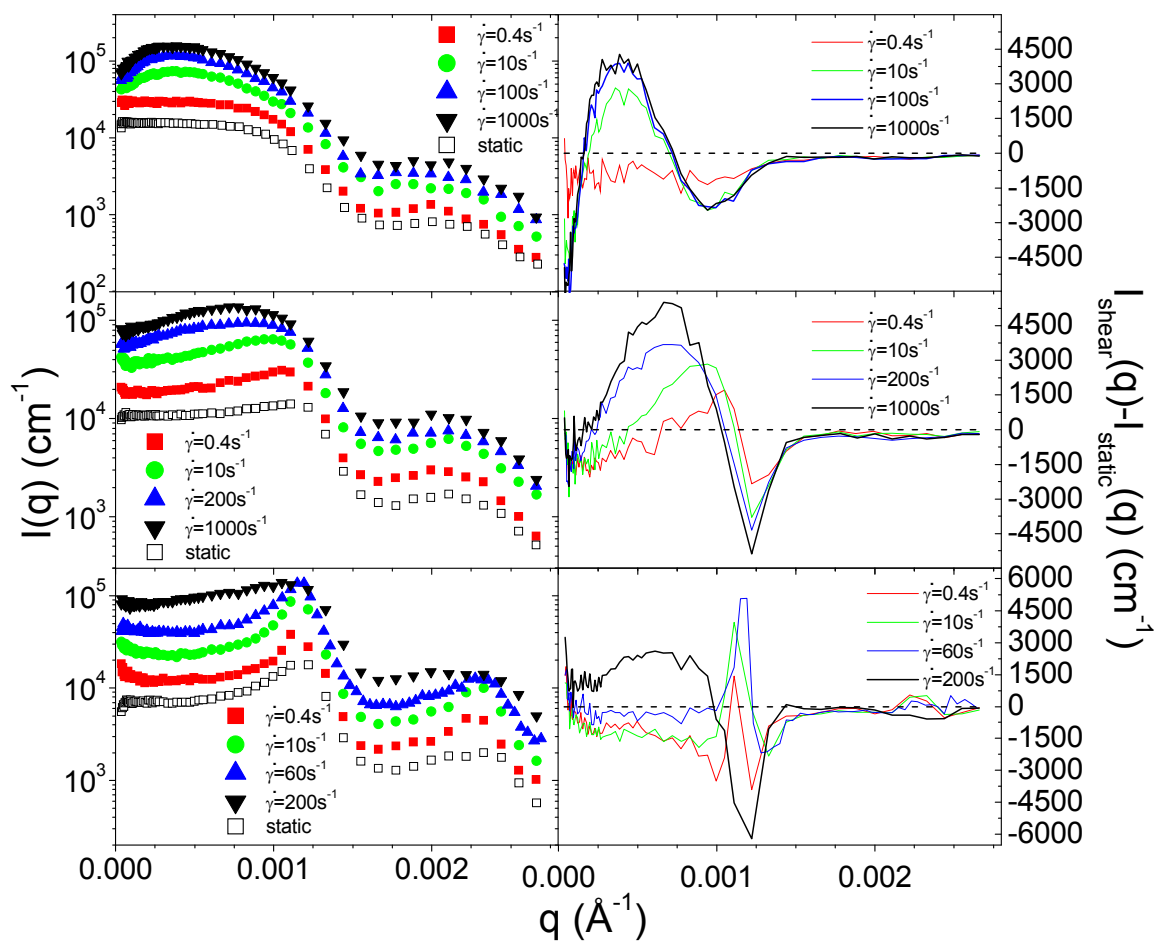


Figure 5.3 Flow-USANS measurements for low ($\phi=0.194$, top), moderate ($\phi=0.391$, middle) and high ($\phi=0.490$, bottom) concentration suspensions of SiO_2 in PEG. Left: $I(q)$ data under static conditions and at each shear rate, shifted by 2X, 4X, 6X, and 8X in order. Right: $I(q)$ data under shear subtracted from rest ($I(q)_{\text{static}}$).

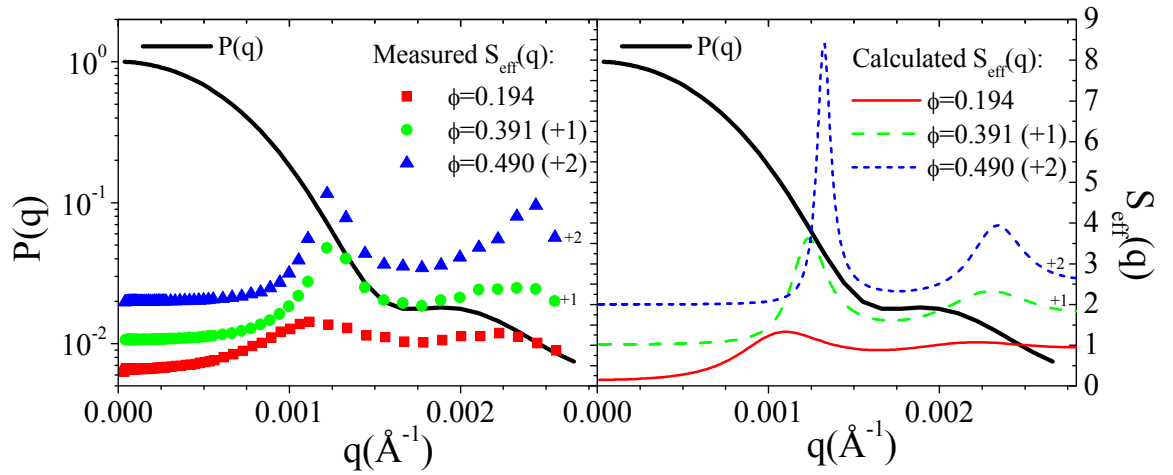


Figure 5.4 Particle form factor and measured effective smeared structure factors (left panel, shifted as indicated for clarity) under static conditions. The right panel shows the calculated effective structure factors (note- not smeared) for reference.

Figure 5.5 shows the measured effective structure factors under shear (left), as well as the difference between the structure factor under shear and that under static conditions (right), which accentuates the structural changes under shear. Generally, increases in the structure factor are seen at low q (below the nearest neighbor peak) with increasing shear rate, but a number of other subtle changes are seen. These structural changes and their cause are discussed below.

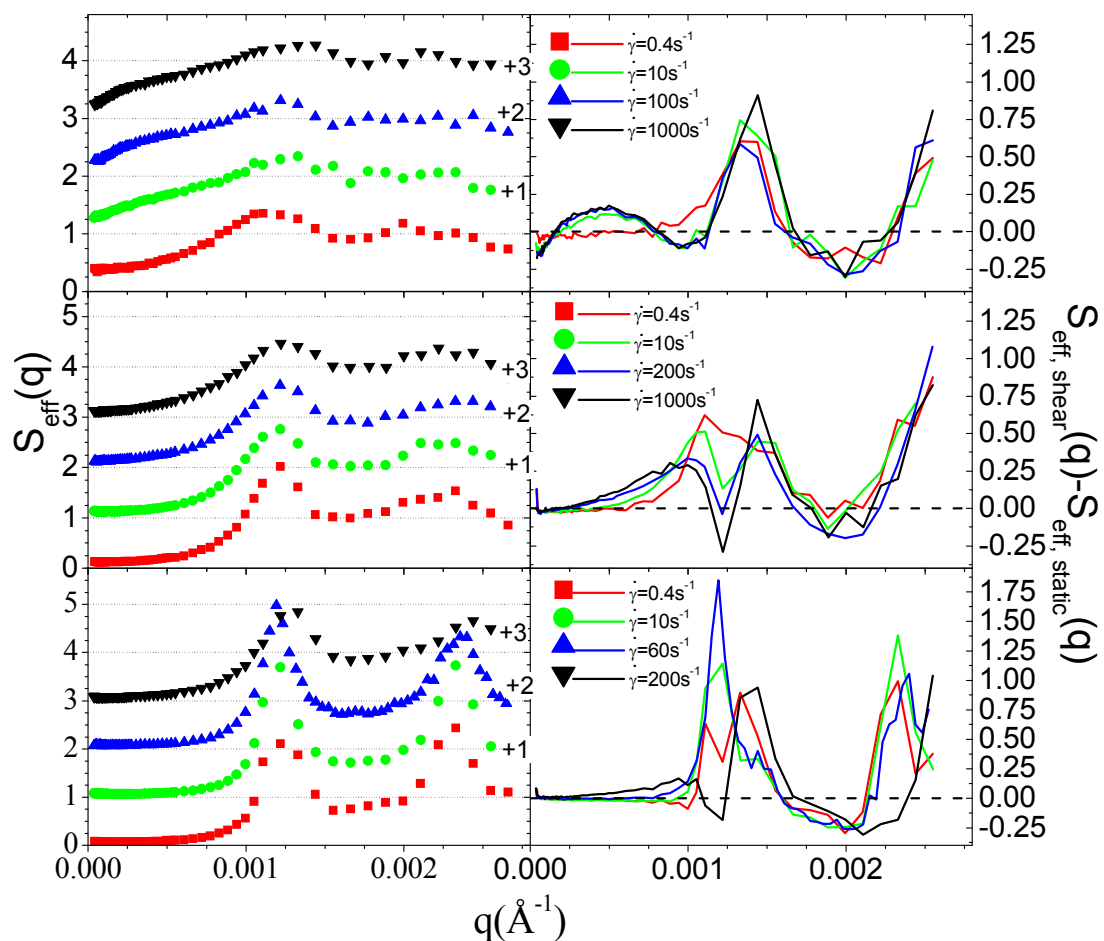


Figure 5.5 Left: Effective steady-shear structure factors measured via USANS on low ($\phi=0.194$, top), moderate ($\phi=0.391$, middle) and high ($\phi=0.490$, bottom) concentration suspensions of SiO_2 in PEG. Data progress from rest to high shear rates vertically and are shifted vertically with increasing shear rate for clarity. Right: Static structure factor with equilibrium structure factor subtracted to show growth of cluster peaks.

5.4 Discussion

5.4.1 Analysis of Flow-USANS Results

These results are similar to prior observations using SANS along the velocity gradient direction (radial or 1-3 plane) in literature and in Chapter 4 [15, 21, 23, 88], but these USANS measurements extend the range of observation to sufficiently low scattering vectors to capture the microstructure in the hydrocluster state at length scales sufficiently larger than the nearest neighbor distances for larger, 520 nm diameter particle suspensions.

To better elucidate the shear-induced structural changes, the right panels in Figure 5.3 show the subtraction of the intensity under shear minus that at rest. For the lowest concentration suspension, increasing shear flow leads to the development of a strong, broad correlation peak at $q_{\text{peak}} \sim 4 \times 10^{-4} \text{ \AA}^{-1}$. This broad peak is likely caused by cluster formation [94], with a characteristic length scale given by $2\pi/q_{\text{peak}} \sim 1500 \text{ nm}$, or about three particle diameters. Note that this is not a fractal-like structure forming as it is a clear peak in the scattering and not simply increased forward scattering. The minimum at higher q is due to a reduction in the equilibrium correlation peak in the structure factor, which is very weak at these low concentrations. Note that hydrocluster formation precedes the actual rise in the overall viscosity as the viscosity is comprised of a shear thinning component due to interparticle forces and a hydrodynamic component sensitive to the hydrocluster formation [21, 32]. The onset of clustering and shear thickening of the hydrodynamic component is expected to occur before the measurable rise in the total viscosity [21, 34, 87].

Similar results are observed for the medium concentration dispersion, but this loss in the equilibrium structure correlation peak is more evident; the peak

broadens and shifts to lower q progressively with increasing shear rate. Further, the peak positions are located at higher q than for the lowest concentration sample due to increased particle concentration, consistent with that seen in Chapter 4 via SANS.

A qualitative difference in behavior is observed for the most concentrated sample, where shearing greatly enhances the Bragg peak evident at equilibrium, which is consistent with shear-induced alignment of polycrystalline samples [111]. Further shearing leads to shear thickening, which is accompanied by a loss in order (large negative peak), and the formation of a cluster peak that is qualitatively similar to that observed for the lower two concentrations, but broader and lower in magnitude.

Figure 5.5 shows the effective structure factors under flow, which look similar in form to those at rest, but evolve systematically with applied shear rates. With increasing shear rate, the nearest neighbor peak shifts to higher q , indicating particles moving closer together, while a broad shoulder develops at lower q . To better illustrate the shear-induced microstructural changes, the right panel of Figure 5.5 shows the corresponding differences as the subtraction of these effective structure factors under flow minus the static values. Two features are clearly evident in the lowest concentration sample: flow enhances the structure peak corresponding to the nearest neighbor correlations, and high shear rates lead to the growth of a broad peak centered around $q_c^* \sim 4 \times 10^{-4} \text{ \AA}^{-1}$. This new peak not evident in the equilibrium structures indicates clusters with a characteristic cluster separation distance of $2\pi/q_c^* \sim 1500 \text{ nm}$ [94, 112]. The second, sharper peak, centered on $q_m^* \sim 1.4 \times 10^{-3} \text{ \AA}^{-1}$, indicates the center-to-center interparticle separation distance within a cluster of $2\pi/q_m^* \sim 450 \text{ nm}$, slightly smaller than the diameter of a particle, indicating that the particles are nearly close-packed (note, this value is approximate partly due to the

smearing effects present in the effective structure factor, discussed in more detail below). For the lowest concentration, $\phi=0.194$ sample, the higher q peak (nearest neighbor correlation) appears already at the lowest shear rate, but the cluster peak does not appear until 10 s^{-1} , at which point there is little change up to a shear rate of 1000 s^{-1} . Note that the shear viscosity is thinning at the lowest measured shear rate (0.4 s^{-1}) and only weakly shear thickening for the higher three shear rates ($10, 10^2, 10^3 \text{ s}^{-1}$). Also, at this concentration, the peak locations do not change with shear rate. Finally, large rearrangements are evident at this lower volume fraction in part because there is substantial free volume available to accommodate restructuring of the microstructure by flow.

At moderate concentration of $\phi=0.391$, a similar effect is observed, where the first peak in the structure factor broadens with increasing shear rate. This leads to a splitting in the subtracted pattern, as particle correlations strengthen at both lower q (cluster peak) and at higher q (close packing) relative to the liquid correlation peak at rest. Note that the structure factor at this concentration and low q is very low and so the magnitude of the cluster peak is small; the changes are more evident when examining the intensity directly (Figure 5.3). At the lowest shear rate, in the shear thinning regime, the primary feature is an increase in the magnitude of the correlation peak compared to static conditions. At the three highest shear rates, the viscosity reaches an intermediate shear plateau before gradually shear thickening. In this regime, a cluster peak forms with the associated shift of the nearest neighbor peak toward close packing. The magnitude of the restructuring under flow is less than that observed at the lower volume fraction as the particles in the fluid are concentrated, and so there is substantially less free volume available for restructuring. Nonetheless, relatively small

changes in microstructure can have substantial quantitative effects on the shear viscosity at these high concentrations.

Finally, for the most concentrated sample, the primary peak corresponds to a first order Bragg peak for a close packed structure at an effective volume fraction of ~ 0.6 . This peak continues to sharpen and grow with increasing shear rates, while the viscosity shows shear thinning. Only at the highest shear rate, which shows substantial shear thickening does the sample exhibit the traits observed for the liquid samples described previously, namely the formation of a cluster peak at low q and the commensurate enhancement of scattering intensity corresponding to a close-packed neighbor correlation. Ordering of the suspension into shear planes, observed via these measurements, leads to a lower viscosity fluid [113], whereas the hydroclustering seen at higher shear rates leads to a substantial increase in the hydrodynamic component of the viscosity [20, 35, 36, 44].

In Chapter 4, circular averaged radial SANS data of high and moderate concentration suspensions had similar peaks as those seen here. For the high concentration samples at $\phi \sim 0.53$, the peak was at 4.2 or $4.8 \times 10^{-3} \text{ \AA}^{-1}$, depending on the sample, with a corresponding secondary minimum at 6.0 or $6.6 \times 10^{-3} \text{ \AA}^{-1}$. For those 60 nm particles, these features correspond to a peak at $qa \sim 2.5$ - 2.9 and a minimum at $qa \sim 3.6$ - 4.0 . For the moderate concentration samples, the peak shifted to lower q with increasing applied shear, going from either 3.9 to $3.5 \times 10^{-3} \text{ \AA}^{-1}$ or 4.3 to $3.7 \times 10^{-3} \text{ \AA}^{-1}$. These scattering curves also had minima at 5.9 and $5.3 \times 10^{-3} \text{ \AA}^{-1}$, respectively. These peaks at concentrations of $\phi \sim 0.44$ are at $qa \sim 2.1$ - 2.3 , with secondary minima at 3.2 - 3.5 . In the USANS measurements shown here, the peak for the moderate concentration sample ($\phi \sim 0.4$) is at $1 \times 10^{-3} \text{ \AA}^{-1}$, shifting to $6 \times 10^{-4} \text{ \AA}^{-1}$

with increasing shear. For these 260 nm radius suspensions, that feature is a peak at $qa \sim 2.6$ -1.6. In addition, the secondary minimum seen in the moderate concentration sample by USANS is at $1.2 \times 10^{-3} \text{ \AA}^{-1}$, or $qa \sim 3.1$. These measurements are consistent between the SANS and USANS measurements, with the USANS giving slightly lower peak locations.

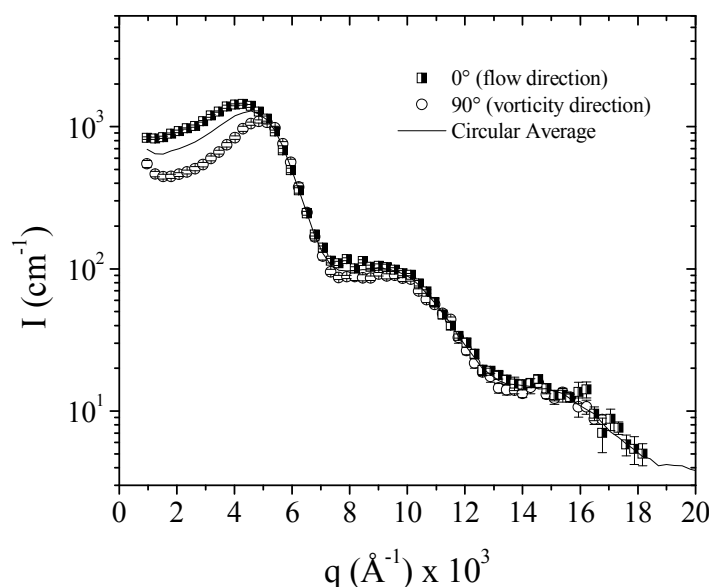


Figure 5.6 Rectangular and circular averaged scattered intensity as a function of wave vector from the $\phi=0.44$ sample of 60 nm suspensions tested in radial Rheo-SANS at 3981s^{-1} shows the expected difference between circularly averaged data and data averaged along either the flow or vorticity directions (USANS data is measured along the flow axis).

This difference in peak locations between SANS and USANS is explained better with the use of Figure 5.6, which shows rectangular averaged scattered intensity as a function of wave vector from the $\phi=0.44$ sample of 60 nm suspensions tested in

radial Rheo-SANS at 3981 s^{-1} , the full microstructural characterization of which is seen as Figures 4.43-4.46 in section 4.3.2.2. These rectangular averages are along either the horizontal or flow axis (0°), similar to the averaging done in the USANS experiment, or along the vertical or vorticity axis (90°). The peak heights quoted above from SANS measurements are averages over the whole detector and so are the circular averaged data given as the line in the figure, which includes contributions from both sets of points. However, the USANS measurement is an average along the flow direction, similar to the half filled squares in the figure. It can clearly be seen that in the SANS experiment, averages along the flow direction yield a larger peak at lower q than averages in the vorticity direction. Therefore, for concentrated suspensions under shear, averages along the flow direction, such as those measured via USANS, are expected to give peaks at lower q .

We also observe evidence for the loss of order upon shear thickening from a flowing, crystalline suspension ($\phi=0.490$), as originally proposed by Hoffman [37]. The mechanism for flow destabilization proposed by Hoffmann is hydrodynamic in origin (i.e., neighboring particles couple hydrodynamically due to fluctuations in position, leading to doublet rotation out of the flowing shear planes and disruption of the stratified flow). However, the mechanism of returning to a liquid-like structure under flow is insufficient to explain the magnitude of the increase in viscosity upon shear thickening [114] (although see [79] for a differing viewpoint). The measurements here, however, show that the large increase in stress is accompanied by the formation of hydroclusters [21, 25, 27, 28, 32, 33, 35, 36, 88, 115, 116], a microstructure with correlated density fluctuations that is distinctly different than that for a flowing liquid. Indeed, previous measurements, including those in Chapter 4,

have demonstrated a quantitative correlation between the hydroclustered microstructure of the shear thickened state and the shear rheology [23].

These USANS measurements show that reversible shear thickening is accompanied by correlated density fluctuations, denoted as hydroclusters, and that these hydroclusters are of finite extent and are comprised of fluctuations of closely packed particles. These results are in good qualitative agreement with simulations of flowing suspensions that include hydrodynamic interactions [25, 28, 35, 36, 115, 117], and are consistent with prior experimental measurements showing structural changes on the length scale of the nearest neighbor correlations upon shear thickening. The new results, however, are explicit demonstration of a cluster peak in the hydroclustered state, suggesting that hydroclusters are of finite extent and are highly correlated.

Finally, although USANS provides new and valuable evidence for the time-averaged structure of the hydroclustered state, the technique is limited in that it cannot provide information about the temporal nature of the fluctuations that are sometimes observed in shear thickening dispersions near the jamming transition [118]. Furthermore, unlike prior work where a quantitative 3-D reconstruction of the shear-thickened microstructure enabled quantitatively connecting the microstructure to the hydrodynamic and thermodynamic stresses [23, 66], the 1-D averaging of the USANS spectra prevents us from performing a similar quantitative analysis. Nonetheless, these results demonstrate new correlations arise in hydroclustered colloidal suspensions, and in conjunction with measurements in Chapter 4 indicate consistent structural deformations drive the rheology of suspensions of 60 and 260 nm radius spheres.

5.4.2 Experimental Limitations

5.4.2.1 Anisotropy Limitations from 1-d Detection

Attempts were made to develop real-space models to fit these complex structure factors under flow, but no successful, physically meaningful fits were achieved. This is most likely due to the highly anisotropic nature of the scattering at high shear rates [23, 33, 44, 88, 89], slit smearing, the limited vertical q range that the detector averages over, and possibly, multiple scattering. Therefore, we analyzed and discussed the results through the effective structure factors as shown in Figure 5.5. As previously mentioned, the measured effective structure factors would only equal the actual structure factor if there were no effects of instrument smearing, anisotropy, size polydispersity, or multiple scattering. In addition, understanding of the experimental setup and comparison to the SANS data from Chapter 4 indicates that the peak locations in USANS are lower bounds to the actual peak location. Regardless, these structural changes under shear seen via Flow-USANS are interesting from a qualitative standpoint. To understand the structure in more detail and gain more quantitative structural information, the approach seen in Chapter 4 utilizing smaller particles and the SANS experiment is preferred.

5.4.2.2 Multiple Scattering Effects

Two transmission measurements are taken in a USANS experiment. One measurement is the ratio of the intensity at zero angle, in the center of the rocking curve, of the sample compared to the empty cell, or T_{rock} . The other measurement is at large angle, T_{wide} , which measures transmission from all small angle scattering [60]. The ratio of the two, $T_{\text{rock}}/T_{\text{wide}}$ is the fraction of the beam that undergoes small angle scattering; multiple scattering can be ignored if this ratio is less than 0.9 [119]. The

measured transmission, seen in Table 5.3, varied from 0.843 to 0.899, indicating only a small amount of multiple scattering in measurements and therefore, no further corrections are applied to the data. Also, note that this ratio does not vary substantially or systematically with shear rate, indicating that the integrity of the sample is maintained during the flow-USANS experiments.

Table 5.3 Transmission measurements from USANS experiments.

ϕ	Shear rate (s^{-1})	T_{wide}	T_{rock}	T
0.194	0.4	0.702	0.616	0.877
0.194	10	0.701	0.602	0.859
0.194	100	0.702	0.604	0.860
0.194	1000	0.699	0.598	0.856
0.391	0.4	0.739	0.634	0.858
0.391	10	0.739	0.623	0.843
0.391	200	0.736	0.621	0.844
0.391	1000	0.734	0.620	0.845
0.490	0.4	0.760	0.656	0.864
0.490	10	0.759	0.646	0.852
0.490	60	0.757	0.643	0.850
0.490	200	0.757	0.646	0.853
0.194	Static cell	0.731	0.657	0.899
0.391	Static cell	0.759	0.662	0.873
0.491	0	0.784	0.694	0.885

5.5 Conclusions

Flow-USANS measurements under flow have been conducted for the first time to study the restructuring of the colloidal microstructure during shear thinning and shear thickening on length scales sufficient to elucidate the formation of

hydroclusters in particle sizes relevant to the body armor application discussed further in Chapter 7. These observations are consistent with the formation of hydroclusters in stable, near hard-sphere colloidal suspensions at high Péclet numbers. Further, we find the hydroclusters to be correlated density fluctuations of finite spatial extent in a shear thickening colloidal suspension. The hydroclusters are essentially close-packed. The breadth of the scattering cluster peak suggests a broad size range for these fluctuations, but a more detailed analysis from the flow-USANS measurement is not possible given the instrument limitations of slit smearing anisotropic structures. The structural measurements confirm expectations that hydroclusters are fluctuations in the form of transient, compact clusters as opposed to large, cell-spanning fractal-like aggregates, which would manifest as a continuous rise in scattering at low q rather than a scattering peak. In addition, the measurements compare well with prior optical and SANS measurements including those in Chapter 4, as well as simulation and theory showing that the hydrocluster formation precedes the rise in measured viscosity. We also demonstrate that, in agreement with prior work, an order-disorder transition may accompany shear thickening, but that it is not necessary for shear thickening, and that the shear thickened state after shear melting is marked by the presence of hydroclusters.

Chapter 6

EFFECTS OF PARTICLE SOFTNESS ON CONCENTRATED SUSPENSIONS RHEOLOGY

6.1 Introduction

One interesting rheological phenomenon in concentrated suspensions occasionally reported in the literature [37] but not often investigated is that of a second shear-thinning regime measured at stresses beyond the shear thickened state. Hoffman showed this behavior in the rheology of concentrated suspensions of discrete spherical particles (1.25 μm diameter poly (vinyl chloride) in di-octyl phthalate), shown in Figure 6.1. The viscosity versus rate graph (left) shows a discontinuous jump in the viscosity followed by a steady thinning at high stresses; the stress versus rate graph (right) shows there is a limiting stress at high shear rates. This second shear-thinning regime has not been studied previously in great detail and was sometimes dismissed as an artifact of rheological slip.

Theory [34] shows that the limiting suspension behavior in the shear thickening regime for hard-spheres is a constant viscosity irrespective of shear rate; this high-shear viscosity increases with particle concentration. Stokesian dynamics simulations support this conclusion although they have not directly calculated the behavior at extreme values of the Péclet number [24, 28]. Jamming theories suggest that the suspension stress should grow unbounded in the discontinuous shear thickening regime [120-123]. These predictions are obviously in conflict with the

aforementioned experiments. Knowledge of the limiting behavior of shear thickening suspensions is critical for engineering suspensions for applications in ballistic and protective materials as discussed further in Chapter 7 [124].

Much recent work has been done on the effects of softness in particle suspensions, from an experimental standpoint, supplemented by theoretical advances and simulations. Meeker et al. [125, 126] developed a theoretical model describing wall slip in concentrated suspensions of deformable particles based on elastohydrodynamic deformations of particles near a wall. This model successfully describes their data in the condition of significant wall slip. In addition, particle hardness effects on concentrated suspension rheology have been tested directly by measurements on agar microgel suspensions using varying agar concentration within the particle to give varying degrees of particle hardness [127]. These concentrated suspensions of deformable particles generally exhibited shear thinning behavior only, although the most concentrated suspension of the hardest particles did exhibit limited thickening. Additionally, the broadest treatment of concentrated, deformable particle suspensions would include suspensions where the dispersed phase is a liquid or gas. Such examples would include emulsions and foams, which typically do not exhibit shear thickening [1, 128, 129]. In contrast, concentrated emulsions are known to exhibit power law shear thinning for stresses above the yield stress, with a power law index ranging from $1/2$ to $1/3$ depending on volume fraction [130].

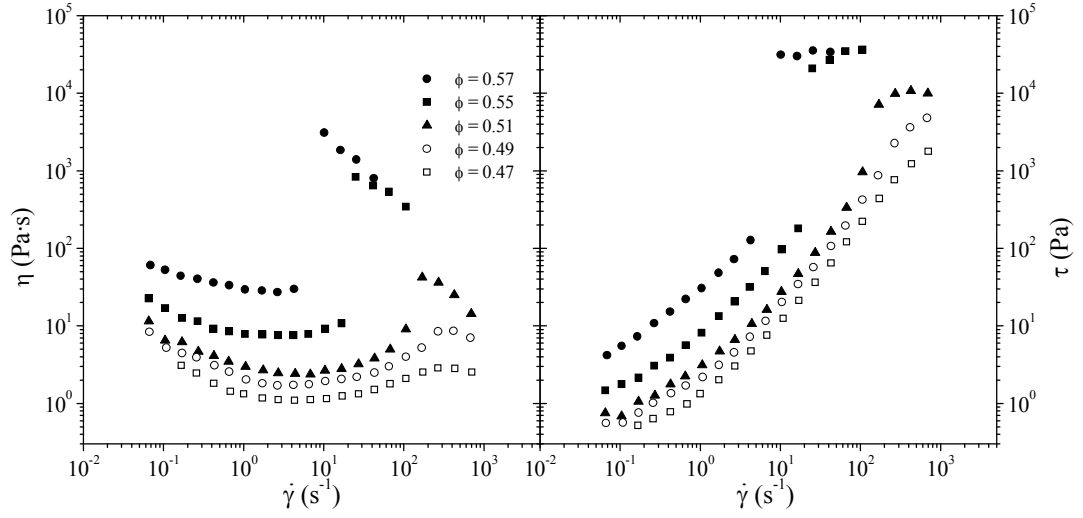


Figure 6.1 Viscosity versus shear rate data for concentrated suspensions of 1.25 μm diameter PVC spherical particles in di-octyl phthalate (DOP) from Hoffman [37].

The prior chapters of this thesis have tried to understand and quantify the microstructure and rheology of concentrated particle suspensions based on the treatment of the particles as hard, non-deformable particles, following prior theoretical and simulation work. In this chapter, we will look at the effects of particle hardness on the suspension rheology. In particular, we attempt to determine if, at the extremely high interparticle stresses achieved in the hydroclustered state, the stresses are sufficient to cause particle deformations and alter the high Péclet rheology. To accomplish this goal, we explore suspensions of particles typically considered to be “hard” particles, such as polymer spheres, as a model, elastically deformable particle suspension. The rheology of this deformable particle suspension will be compared to the data obtained on silica particle suspensions discussed throughout this thesis. We also compare with literature data for emulsions, microgels, polymer lattices and much

harder mineral particles. We propose that the limiting rheological behavior at high shear stresses is a real suspension property dictated by the particle mechanical properties. This hypothesis is tested by combining models for the hydrocluster theory of shear thickening with an elastohydrodynamic model for the lubrication forces acting between particles in the hydrocluster to develop a model for this limiting behavior. Comparisons to model system data for which we independently measure the particle hardness validate the model, which is further used to evaluate the effects of particle hardness on literature data.

6.2 Experimental

PMMA particles were chosen for this study due to their ease of synthesis, compatibility with PEG-based STF processing, expected lower hardness relative to SiO₂, and potential application in body armor materials (see Chapter 7). The PMMA particles were synthesized via a free-radical reaction of dilute methyl methacrylate monomer in mixed methanol and water solvent at 70°C for 3 hours [54], as discussed in section 2.3.2. The reaction materials were dialyzed against three separate batches of deionized water for at least 24 hours each. To produce the suspensions for rheology measurements, sufficient PEG-200 was added to achieve the desired particle volume fraction and then the water was removed by first heating while stirring at 60°C, then under vacuum at 60°C. Each suspension was prepared at the corresponding volume fraction from the same PMMA particle stock.

Atomic force microscopy measurements were performed as described in section 2.2.3, on dispersed particles dried on a glass slide. Rheological measurements were performed with a 20 mm 4° cone and plate geometry, and compared to those from a 20 mm roughened parallel plate geometry. Both upper and lower plates were

roughened by sandblasting. The sandblasting is intended to be a simple way to lower the effects of slip by decreasing the effect of any depletion effects near the wall [1, 131].

6.3 Results

6.3.1 PMMA Particle Characterization

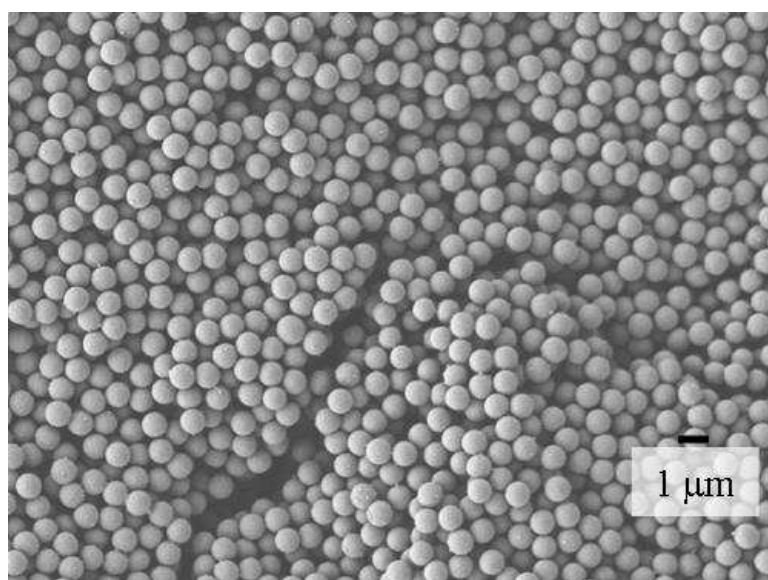


Figure 6.2 SEM micrograph of PMMA particles.

An SEM micrograph of the PMMA particles made for this study (Figure 6.2) shows the particles to be spherical and nearly monodisperse. Dynamic light scattering measurements of the particle hydrodynamic size in water gave a diameter of 1050 ± 110 nm. Note that, in this chapter, particles will be referred to by their diameter, to be consistent with the literature reports, rather than radius as in prior chapters.

6.3.2 Rheology

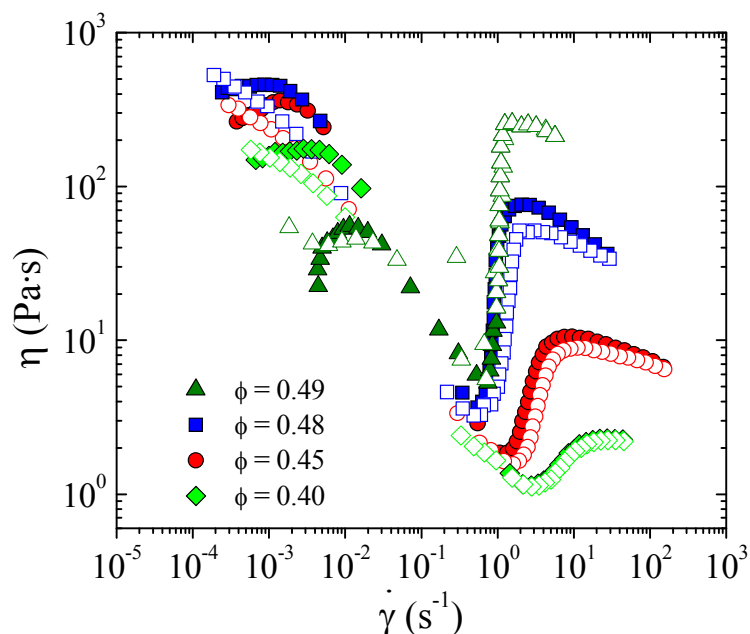


Figure 6.3 Steady shear rheological data for suspensions of 1.05 μm diameter PMMA spheres in PEG-200. The closed symbols are steady state sweeps at increasing shear stress and the open symbols are at decreasing shear stress.

Figure 6.3 shows the steady shear rheology of colloidal suspensions of PMMA particles in PEG-200 at four volume fractions. At the highest concentrations (0.49 and 0.48 volume fraction), these suspensions show apparent yielding and shear-thinning at low shear rates, followed by a nearly vertical rise in the viscosity at higher shear rates, marking the onset of nearly discontinuous shear thickening. The 0.45 and 0.40 volume fraction samples show similar yielding, thinning, and continuous shear thickening behavior. The highest concentration sample shows a plateau viscosity at high shear stresses beyond the discontinuous shear thickening. The other samples

show a second shear thinning regime at high shear rates. Open points on the plot indicate sweeps of decreasing stress directly following the increasing stress sweeps seen as closed points. Little hysteresis is observed at the high shear rates. However, significant hysteresis is seen at the low shear rates, indicative of measuring slip and yielding rather than actual shear thinning.

Figure 6.4 shows the steady shear rheology of the $\phi=0.48$ sample shown in Figure 6.3 as measured by a cone-and-plate geometry, compared to the same data measured by a sandblasted, roughened parallel plate geometry. If slip is significant and the roughening of the geometry successfully lowers the effect of wall slip, we would expect to see a significant increase in the apparent viscosity. There are increases in the apparent viscosity measured by roughened plates compared to the smooth cone and plate along the majority of the flow curve, but the general behavior and features including the shear thickening and post-thickening transition to shear thinning are the same. These deviations between the two geometries are consistent with the difference expected between cone and plate and parallel plate geometries for these non-Newtonian fluids, especially with consideration for the difficulty in zeroing the gap with the roughened plate geometry. Therefore, slip is unlikely to be the cause of the second shear thinning regime of the viscosity.

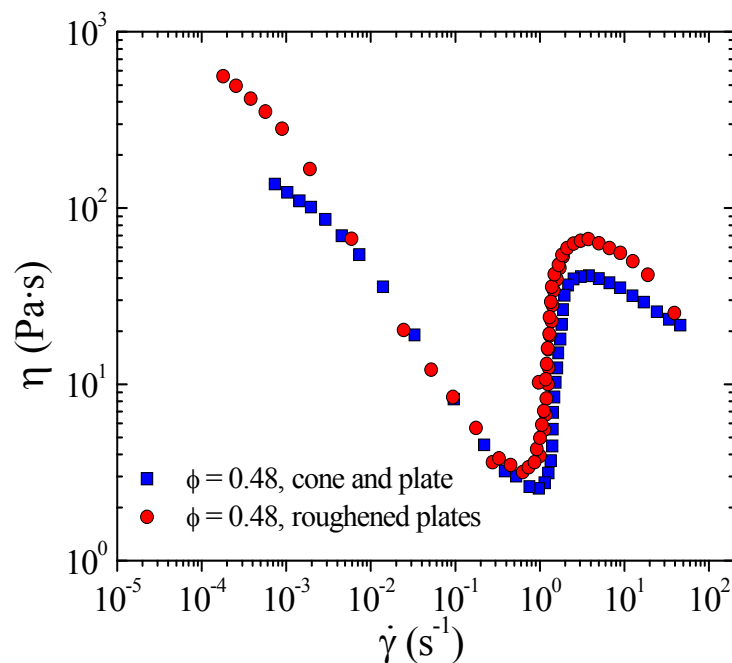


Figure 6.4 Comparison of steady shear rheology for PMMA particles in PEG-200 between cone and plate geometry and roughened parallel plates.

6.3.3 Particle Modulus

Measurements of the particle modulus are necessary for comparison of steady-shear rheology to the elastohydrodynamic model to be discussed in the next section. Modulus measurements were performed as explained in section 2.2.3. Figure 6.5 shows the force versus tip displacement data for AFM indentation on the PMMA (left) and SiO₂ (right) particles. As the tip extends toward the sample, the force is unchanging until the surface is reached. If there is an attraction between the tip and the sample, the force may drop as the surface is reached. When the tip is in contact with the sample, the force will begin to strongly rise with increasing displacement.

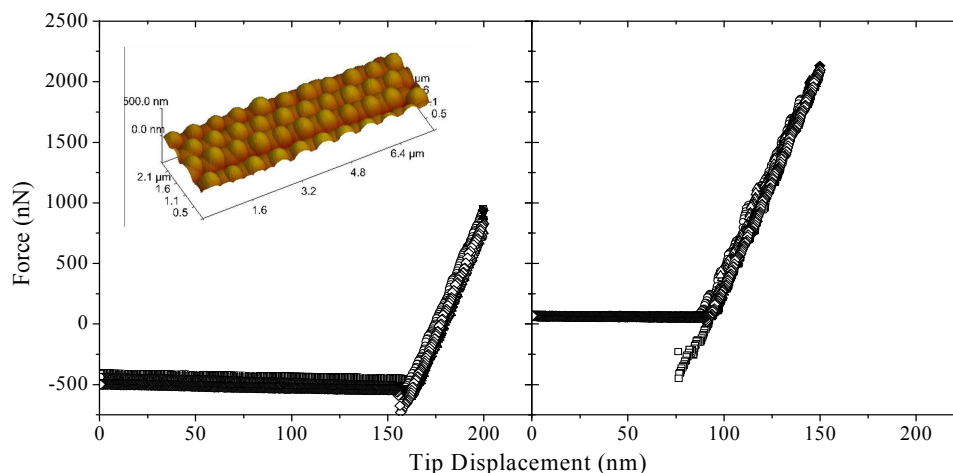


Figure 6.5 Raw force versus tip displacement AFM data for PMMA and SiO₂ spheres. Left) PMMA, with the particle surface height from AFM in tapping mode inset. Right) SiO₂ spheres. Closed symbols are the extension curve, open symbols are the retraction curve. Note: There are four representative data sets shown for each type.

Figure 6.6 shows deflection force as a function of indentation depth for indentation experiments on PMMA (left) and SiO₂ (right). The contact location and the tip deflection are subtracted from the tip displacement to yield the indentation seen as the abscissa in Figure 6.6. The deflection force shown as the ordinate in Figure 6.6 is the measured force shifted by the force at contact. The PMMA data, seen on the left in Figure 6.6 show little scatter over the four representative datasets shown. The SiO₂ data shown on the right has a little more scatter about a larger slope than the PMMA data (larger slope being higher modulus). In addition, the SiO₂ data shows multiple instances of an anomalous feature where, as the tip moves further into the sample, the deflection increases much faster, lowering the indentation distance with an increase in

deflection distance. This change in indentation depth can be up to 5 nm for the silica particles. This phenomenon is also seen in the PMMA samples, but less often and with decreases in the indentation depth of only one nm. This scatter is seen in the force versus displacement curves seen in Figure 6.5, but the force versus indentation depth curve appears especially noisy as oscillations in the tip deflection affect both the deflection force and indentation depth in the same manner, i.e., a large drop in the tip deflection alone will cause a drop in both. Note that, occasionally, during testing on the silica samples, indentation of the particle by the tip bent the AFM tip. The results shown here and those used to calculate the modulus are from indentation experiments with a tip that was not damaged during the experiment. No tip damage was seen with PMMA materials.

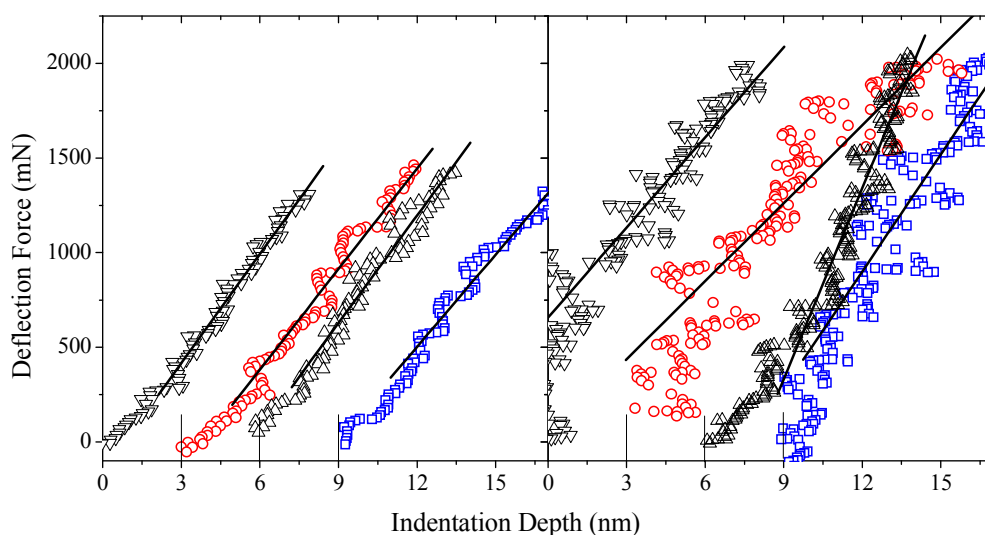


Figure 6.6 AFM deflection force versus indentation distance data used to calculate particle modulus. Left) PMMA spheres, Right) SiO₂ spheres. Curves are shifted by addition of 3, 6, and 9 nm for clarity. Lines indicate fit slope.

The final analysis of AFM experiments with corrections for the tip geometry based on the standard calibration material gave an elastic modulus of 2.9 ± 0.7 GPa for the PMMA particles, and 4.0 ± 1.5 GPa for the SiO₂ particles. Alternatively, under the assumption of Poisson's ratio being 0.5 already used to calculate the elastic modulus, the shear modulus would be 1.0 ± 0.2 GPa for the PMMA particles, and 1.3 ± 0.5 GPa for the SiO₂ particles. The values given for the moduli are the value \pm one standard deviation, where the error is solely that from the scatter in final analysis of multiple measurements (390 indentation measurements for PMMA and 51 indentation measurements for SiO₂) and does not include propagation of error from scatter in the original force versus indentation depth curve.

Table 6.1 summarizes the modulus data from the AFM data and literature sources for these materials. The calculated modulus for the PMMA is similar, but slightly lower than what is reported in the literature for bulk PMMA. This may be due to plasticization of the particles by the solvents used during the synthesis. It may also reflect the fact that we are probing the top few nanometers of the particles, which on any material may be mechanically different than the bulk material.

On the other hand, the values for silica nanoparticles are similar to that for the PMMA and an order of magnitude below that reported for bulk silica. The indentation depth used in measuring the modulus of the silica particles occurs within the particle's surface coating as measured in Chapter 3 via USANS and rheology. The AFM measurements of modulus are indeed consistent with a polymer-like surface coating. However, attempts to burn off the coating via a high temperature treatment (as discussed in sections 2.3.3 and 3.3) did not induce a statistically significant change in the measured particle modulus (4.4 ± 2.0 GPa from 224 measurements). Further work

is warranted to characterize the nanoscale surface mechanical properties of the silica particles, perhaps with stiffer probes, varying indentation depths, and the particles held in place on the substrate more rigidly. In these experiments, anomalous modulus measurements could result from the particles rotating or translating on impact from the AFM tip rather than being subjected to pure indentation. The only experimental check to assuage these concerns was to image the particles in tapping mode before and after the experiment to ensure that they had not translated or been pushed out of the plane. Further careful analysis of the error in fitting caused by anomalous features could improve the quality of the measurements on SiO₂ particles and therefore improve the agreement between measurements and literature. Nonetheless, although challenging, these pioneering studies of the nanoscopic surface mechanical properties provide reasonable values of the surface shear moduli for use in the following modeling of suspension rheology.

Table 6.1 Particle shear modulus data.

Material	Shear Modulus (GPa)	Source
SiO ₂ -a-quartz	44.3	[132]
b-SiO ₂	41.4	[132]
PMMA	2.14	[132]
PMMA	1.7	[133]
PMMA Particles	1.0 ± 0.2	AFM
SiO ₂ Particles	1.3 ± 0.5	AFM

6.4 Elastohydrodynamic Model

6.4.1 Model Development

The limiting shear rheology at high Péclet numbers, as discussed previously, is often seen to be a second shear-thinning regime at high shear stresses. This behavior is not typically seen by rheometric experiments for mineral based particles such as the silica particle dispersions seen in Chapter 3, but has been seen in literature for dispersions of polymer particles such as poly (vinyl chloride) in dioctyl phthalate [37] or poly (styrene/ethyl acrylate) in water [134]. As shown in the previous section, this limiting behavior is a real suspension property and not caused by rheometric slip. We hypothesize that this limiting behavior is a consequence of the stresses in the hydrocluster becoming sufficiently large such that particle elastic deformation limits the growth in suspension stress. This hypothesis is tested by developing a model for prediction of this limiting behavior, which is compared to rheological data from suspensions of varying particle mechanical properties. The model combines the hydrocluster theory of shear thickening with an elastohydrodynamic model for the lubrication forces acting between particles in the hydrocluster to develop a scaling argument for the dependence of the suspension stress

on particle properties in the regime where the rheological properties are controlled by these elastic particle deformations.

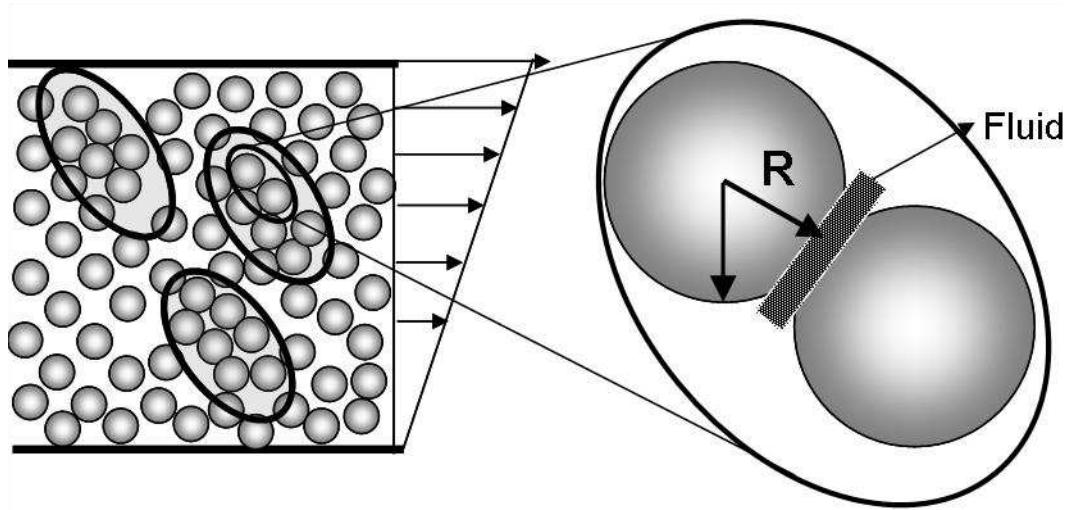


Figure 6.7 Proposed elastohydrodynamic deformation between two particles within a hydrocluster in a concentrated suspension.

As discussed previously and shown by neutron scattering (Chapters 4 and 5 and [23, 48]) and simulations [24, 25, 40, 42, 99], reversible shear thickening in colloidal suspensions is a consequence of hydrocluster formation, driven by hydrodynamic forces. We propose that at high enough stresses, particles in high stress regions of the hydroclusters will elastically deform, with a thin fluid layer between them, as depicted in Figure 6.7. We treat this phenomenon as an elastohydrodynamic deformation with Hertzian contact, similar to previous models of pastes that examined the deformation of a single particle near a wall [125, 126]. In fact, previous work identified that the elastic particle deformations which occur near a wall also likely

occur in the bulk of the fluid as jammed structures deform to pass each other [126]. Meeker et al. [126] argues that the stress resulting from the lubrication forces acting between an elastically deformable particle (with Hertzian contacts) and a hard wall scales as:

$$\sigma \sim \left(\frac{\eta_s V G_0}{a} \right)^{1/2} \left(\frac{G_0}{G_p} \right)^{1/6}, \quad (6.1)$$

where σ is the stress, η_s is the suspending fluid or medium viscosity, V is the velocity of the particle relative to the wall, a is the particle radius, G_0 is the particle shear modulus, and G_p is the particle elastic modulus. If we assume that $(G_0/G_p)^{1/6} \propto O(1)$, the limiting scaling of the stress as a function of shear rate becomes:

$$\sigma \sim (V/a)^{1/2} (\eta_s G_0)^{1/2} = \dot{\gamma}^{1/2} (\eta_s G_0)^{1/2}, \quad (6.2)$$

where we have identified the relative particle velocity with the applied shear rate. This can also be written in terms of a limiting suspension viscosity, η_{EH} , yielding a power-law shear-thinning behavior,

$$\eta_{EH} \sim \dot{\gamma}^{-1/2} (\eta_s G_0)^{1/2}. \quad (6.3)$$

Therefore, equation 6.3 predicts a second shear thinning regime at high stress within the hydroclustered fluid, with power law shear thinning with a slope of $1/2$ and the scale being a function of only the particle modulus and the solvent viscosity. The proportionality reflects an unknown constant, C_{EH} , as seen in equation 6.4,

$$\eta_{EH} = C_{EH} \dot{\gamma}^{-1/2} (\eta_s G_0)^{1/2}, \quad (6.4)$$

which accounts for the fraction of particles involved in elastohydrodynamic deformations within a hydrocluster. That is, only a fraction of the particles will be in high stress events at any moment, as shown by simulation [39, 99] and so, the model

represents an upper bounding limit of suspension rheology. That is, equations 6.2 and 6.3 provide an upper bound limit on the stress or viscosity, respectively at high shear rates in the post shear thickening, shear thinning regime. Hereafter, we will refer to this regime as the *elastohydrodynamic regime*. Note that this regime is anticipated to be a *universal* rheological behavior at high Péclet number (and low particle Reynolds number) for hydrodynamically interacting spheres as long as the stresses acting on a particle pair are sufficiently large to induce elastic (but not so large as to induce significant inelastic) particle deformation.

6.4.2 Elastohydrodynamic Model Predictions and Comparison to Data

In this section, we will compare the rheology of concentrated suspensions of varying particle hardness to the predictions from the model discussed in the prior section. We will first compare the model predictions using the modulus measurements shown in section 6.3.3 to the PMMA particle suspension rheology shown earlier in the chapter. Then we will compare the model predictions using the silica modulus measurements shown in section 6.3.3 to suspension rheology seen in Chapters 3 and 5 and similar suspensions from literature. Next, we will examine data from the literature on suspensions of polymer particles previously assumed to behave as hard particles. Then we will look at mineral particles from literature as an example of particles that are significantly harder than the polymer particles and have different shape. After that, we will compare the model to fumed silica suspension rheology seen in literature. Finally, in the discussion in the next section, we will show comparisons to more exotic “soft particle suspensions” such as suspensions of agar microgel particles with tunable hardness and emulsions stabilized by either surfactants or silica particles. Table 6.2

shows a summary of the modulus and viscosity parameters used in the elastohydrodynamic model in various figures.

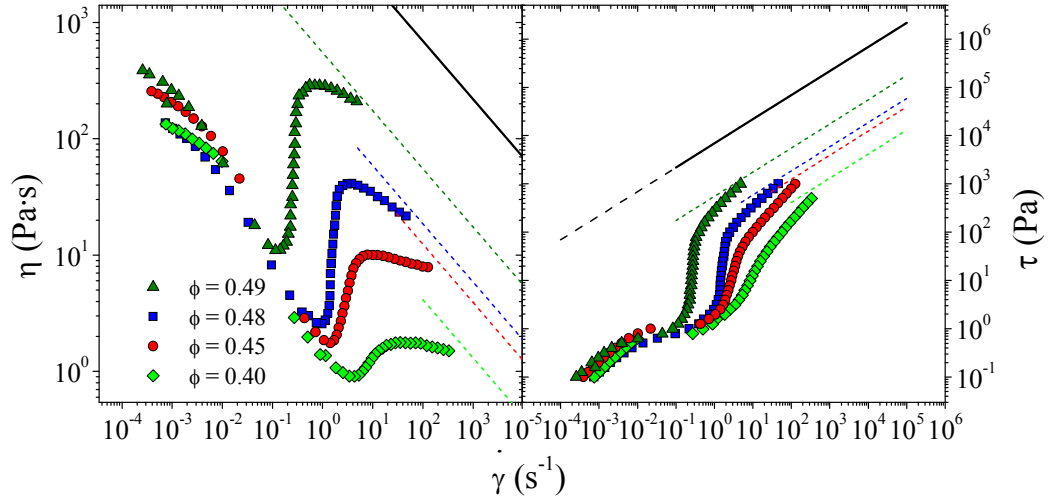


Figure 6.8 Elastohydrodynamic model compared to rheology data of 1.05 μm diameter PMMA spherical particle suspensions. Solid line is model (equation 6.3), with parameters seen in Table 6.2. Dotted lines are the model shifted by a constant to account for the volume fraction dependence in limiting stress.

Figure 6.8 shows the steady shear rheology data for the 1.05 μm diameter PMMA particles shown previously as Figure 6.3. The left pane of the figure shows the viscosity versus shear rate data shown previously. The right pane shows the stress as a function of shear rate. The stress plot shows that the limiting stresses at high shear scale approximately as the shear rate to the $\frac{1}{2}$ power, in reasonable agreement with the model (solid line). Note that the limiting stress curve shifts to higher stresses with increasing particle volume fraction, which is consistent with the expectation that the number of particle contacts under sufficiently high stress behavior may set the

prefactor. Another interesting observation that can easily be seen on the plot of shear stress versus shear rate is that all of these suspensions appear to begin the second shear thinning regime at the same critical value of stress (about 100 Pa); this critical stress for elastohydrodynamic deformations would be an interesting subject for future analysis.

The solid line indicates the model predictions obtained by replacing the proportionality with an equality (i.e., prefactor of one) at shear rates or stresses above the onset of shear thickening. This is the regime where the model is expected to provide a maximum stress or limiting viscosity behavior. The extension as a dashed line is simply to provide clarity and guide the eye, as the model is not anticipated to explain the suspension rheology for stresses or shear rates below shear thickening. The elastohydrodynamic model prediction is about one order of magnitude above the second shear thinning portion of the data, consistent with the expectations of the model providing an upper bound on the viscosity or stress as a function of shear rate. Dotted lines show how the model compares to the data with a prefactor dependent on volume fraction, adjusted to fit the data at the highest shear stresses.

The dependence of this prefactor on volume fraction is shown as Figure 6.9. The parameter does not appear to follow a simple volume fraction squared relationship as would be expected based on the relative likelihood of two particles coming into contact. The parameter instead appears to diverge as maximum packing is approached, increasing significantly at the highest concentration. As the dependence on volume fraction is larger than volume fraction squared, this indicates that multiple particles may be involved in the elastohydrodynamic deformation. The values of the

parameter in this limited volume fraction range vary from 0.006 at $\phi=0.40$ to a maximum of 0.07 at $\phi=0.49$.

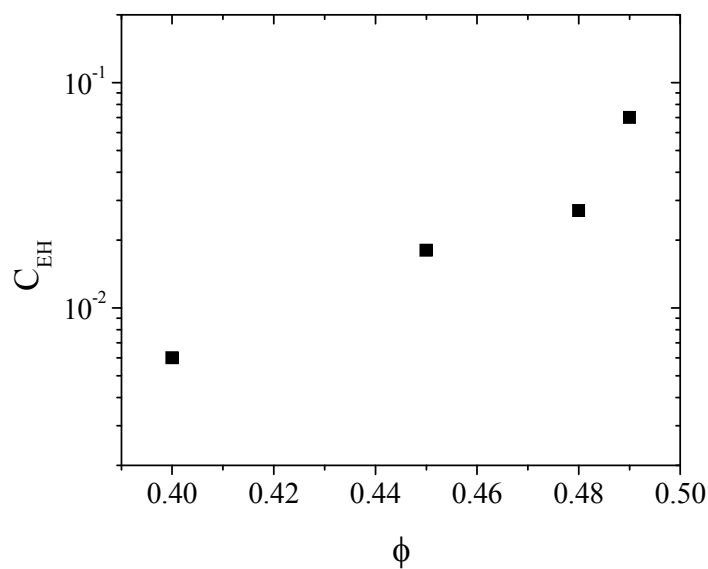


Figure 6.9 Elastohydrodynamic model prefactor fit to PMMA-PEG suspension data at various volume fractions.

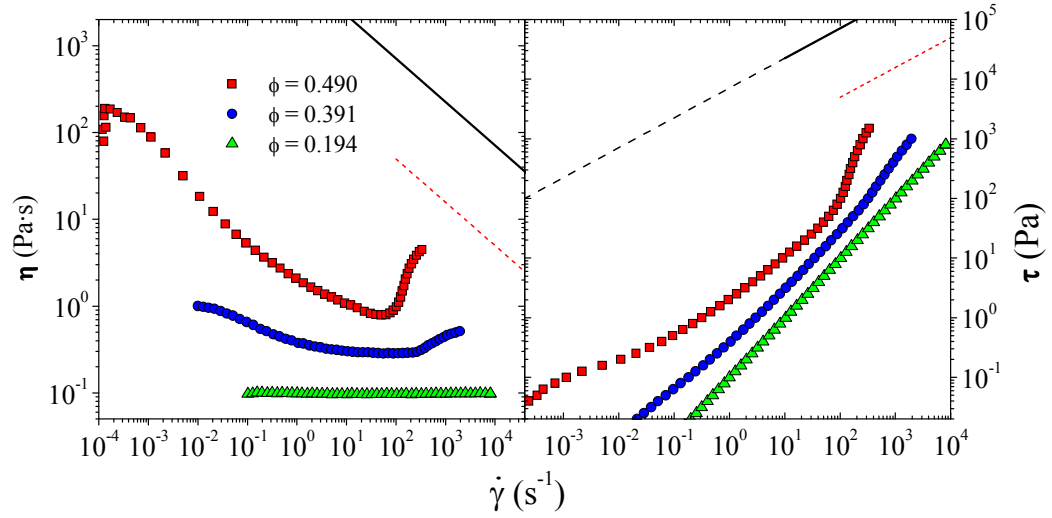


Figure 6.10 Elastohydrodynamic model compared to rheology data of 520 nm diameter silica spheres in PEG-200, seen in Chapters 3 and 5. The solid line indicates the model with C_{EH} of 1; the dotted line indicates the model with C_{EH} of 0.07, as seen for PMMA for $\phi=0.49$.

Figure 6.10 shows the silica suspension rheology as seen in Chapter 3 and 5 for 520 nm diameter SiO_2 suspensions in PEG-200. Figure 6.11 shows some nearly identical 450 nm diameter SiO_2 suspensions from Egres [16]. For these suspensions, shear thickening is observed with no limit of the stress versus rate curve at the highest measured stresses. The elastohydrodynamic model prediction is shown in the figure as the solid line, assuming a prefactor of 1 and using the measured shear modulus of 1.3 GPa. Also included is a dotted line for the model with a prefactor of 0.07 exhibited by the PMMA suspension at $\phi=0.49$. The model is multiple orders of magnitude above the data and so no thinning or plateau in viscosity due to elastohydrodynamic particle deformations would be expected in the range of shear rates accessible in the rheometer.

Figures 6.12 and 6.13 show a comparison of the elastohydrodynamic model to two sets of polymer particle suspensions from literature. Figure 6.12 shows the steady shear viscosity data for 1.25 μm PVC particles in dioctyl phthalate from Hoffman [37] previously shown in Figure 6.1. The elastohydrodynamic model prediction with a prefactor of one passes through the data for the highest concentration at the highest stresses in the elastohydrodynamic regime, providing an upper limiting bound. In addition, applying the prefactor of 0.07 from the PMMA suspensions at $\phi=0.47$, the model is slightly above the data at $\phi=0.47$ and goes through the data for $\phi=0.49$.

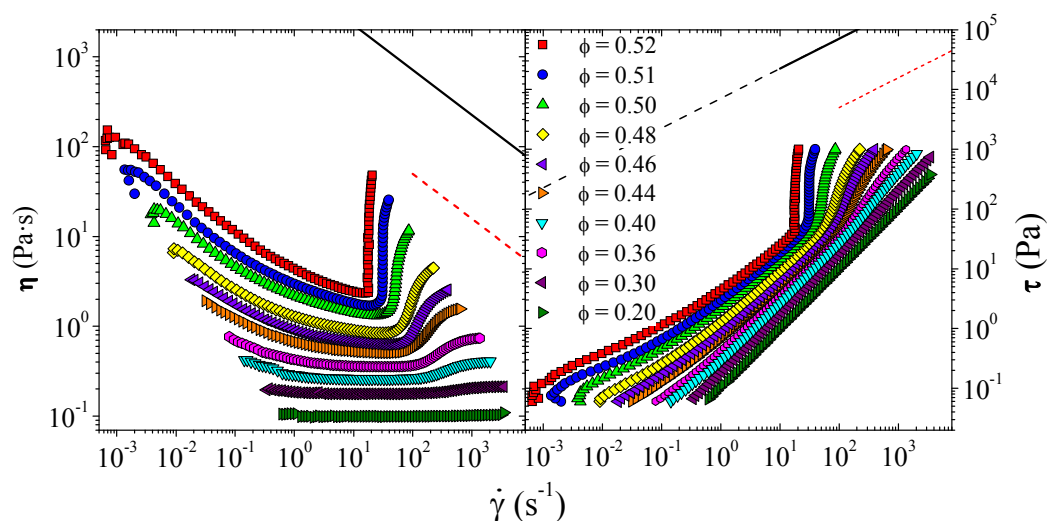


Figure 6.11 Elastohydrodynamic model compared to rheology data of SiO_2 sphere suspension rheology data (450 nm commercial SiO_2 in PEG-200 from Egres [16]). The solid line indicates the model with C_{EH} of 1; the dotted line indicates the model with C_{EH} of 0.07, as seen for PMMA for $\phi=0.49$.

Figure 6.13 shows poly(styrene-co-ethyl acrylate) spheres dispersed in water from Laun [134]. These suspensions shear thin, shear thicken, and show a limiting viscosity at high stresses. The model limiting prediction is less than one order of magnitude above the reported high shear stress and has a similar limiting slope. In addition, the model prediction using the prefactor from the PMMA suspension of 0.07 at $\phi=0.49$ goes through the data at $\phi=0.47$. Note that the elastic shear modulus of the particle is assumed to be polystyrene, which may be significantly harder than the copolymer used in making the particles, for which no modulus is reported.

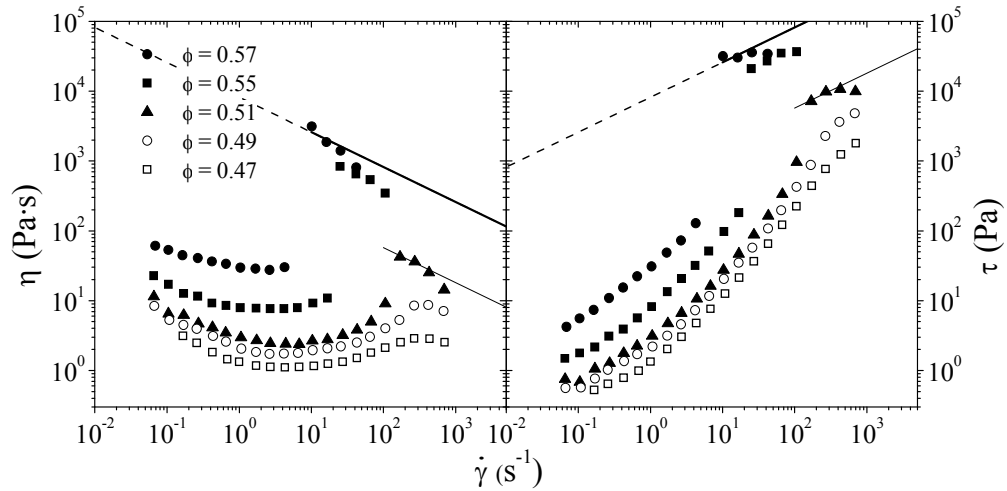


Figure 6.12 Elastohydrodynamic model compared to rheology data of 1.25 μm PVC particles in di-octyl phthalate (DOP) from Figure 4 of Hoffman [37]. The solid line indicates the model with C_{EH} of 1; the dotted line indicates the model with C_{EH} of 0.07, as seen for PMMA for $\phi=0.49$.

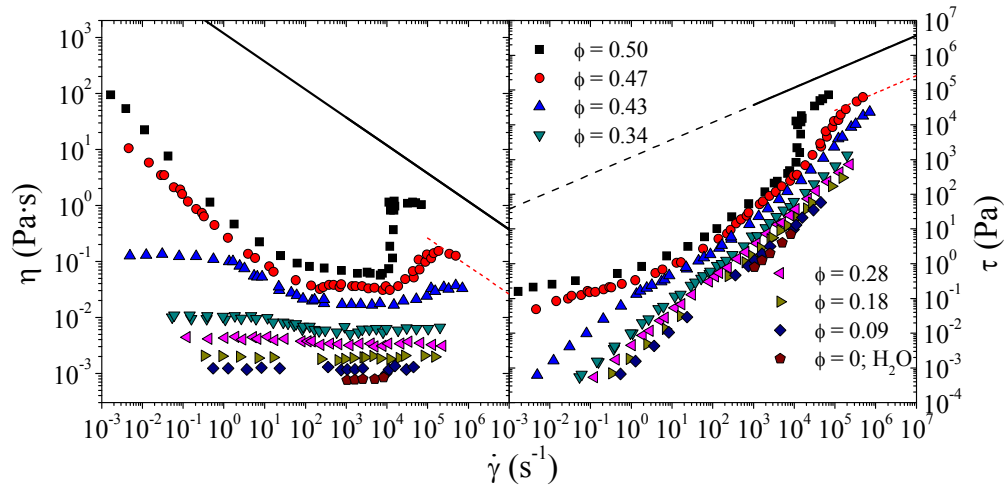


Figure 6.13 Elastohydrodynamic model compared to rheology data of poly(styrene/ethyl acrylate) spheres in water from Laun et al. [134]. The solid line indicates the model with C_{EH} of 1; the dotted line indicates the model with C_{EH} of 0.07, as seen for PMMA for $\phi=0.49$.

Figures 6.14 and 6.15 show the elastohydrodynamic model compared to the shear thickening rheology of mineral suspensions. It should be noted that the particles comprising these suspensions are not spherical, but rather rods and plates, respectively. At present it is not known how changing particle geometry will affect the elastohydrodynamic model as the geometry of the particle-particle contact will be different than that assumed in the model development.

Figure 6.14 shows shear rheology for suspensions of plate-like kaolin clay particles in water from Egres [16]. The data show strong shear thickening and no evidence of an elastohydrodynamic regime. The model prediction with a prefactor of one for these hard particle suspensions is about two to three times the maximum stress for the highest concentration sample with increasing deviation from the maximum measured stress for the lower volume fraction samples. Thus, insufficient stresses were reached in the experiments to probe the elastohydrodynamic regime.

Figure 6.15 shows steady shear rheology data for ellipsoidal particles of precipitated calcium carbonate (CaCO_3), from Egres et al. [41]. The model prediction with a prefactor of one lies just above the highest measured stresses for the most concentrated samples. These suspensions of colloidal clay particles show some evidence of the possible onset of elastohydrodynamic shear thinning at the highest volume fractions and stresses, consistent with their lower particle shear modulus.

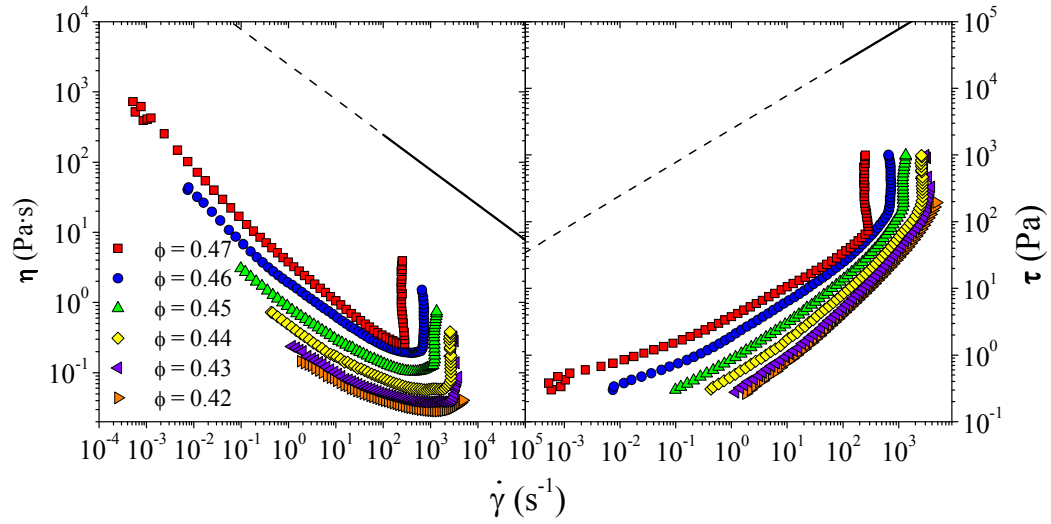


Figure 6.14 Elastohydrodynamic model compared rheology data of plate-like kaolin clay particle suspensions in water from Egres [16].

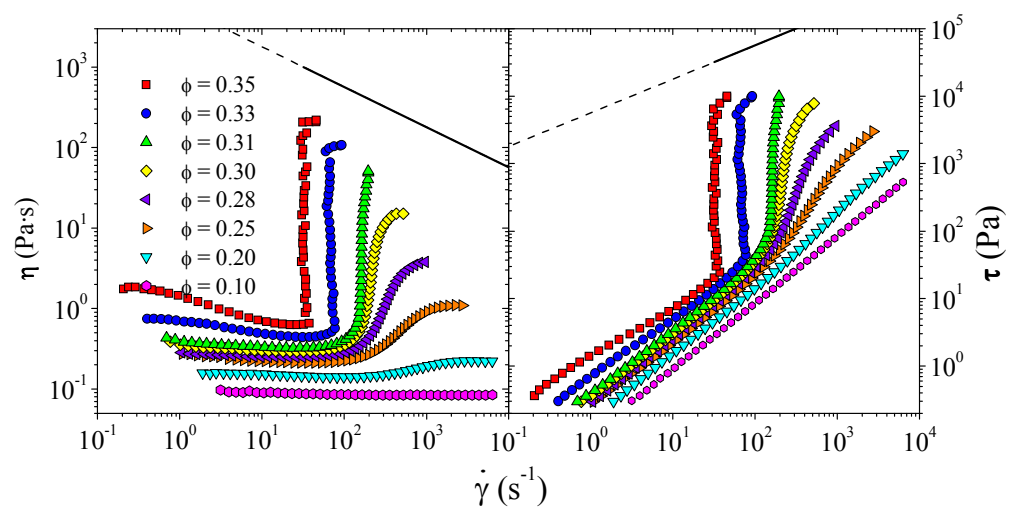


Figure 6.15 Elastohydrodynamic model compared rheology data of rod-like precipitated calcium carbonate (CaCO_3) (PCC) (aspect ratio 7:1) in water from Egres et al. [41].

Table 6.2 Summary of particle types, moduli, and solvent viscosities used in elastohydrodynamic model comparisons to data.

Figure	Data Source	Particle Type(diameter)	Solvent	Particle Modulus	Modulus Source	Solvent Viscosity (Pa-s)
6.8	Section 6.3.1	PMMA (1.05 μm)	PEG-200	0.97 GPa	PMMA-AFM	0.049
6.10	Chapter 3/5	SiO ₂ (520 nm)	PEG-200	1.03 GPa	SiO ₂ -AFM	0.049
6.11	Egres [16]	SiO ₂ (0.450 μm)	PEG-200	1.03 GPa	SiO ₂ -AFM	0.049
6.12	Hoffman [37]	PVC (1.25 μm)	Di-octyl phthalate	1.59 GPa	PVC – [132]	0.042
6.13	Laun [134]	Poly(styrene-co-ethyl acrylate) (0.250 μm)	Water	1.39 GPa	Polystyrene – [132]	0.001
6.14	Egres [16]	Kaolin Clay	Water	6 GPa	Kaolin – [135]	0.001
6.15	Egres [41]	Precip CaCO ₃	Water	32 GPa	CaCO ₃ – [132]	0.001
6.16	Raghavan [136]	Fumed Silica	PPG	10 ⁵ Pa	Fit using model	0.12
6.17	Adams [127]	Agar Microgel	Oil	185,89 kPa	Adams [127]	0.01
6.18	Wolf [137]	Pickering Emulsion	Water	10 ⁵ Pa	Fit using model	0.001

Figure 6.16 shows suspensions of fumed silica in poly(propylene glycol) (PPG) at concentrations ranging from 3 to 10 % silica by weight. These samples show weak shear thinning, followed by strong shear thickening, followed by the shear thinning indicative of the elastohydrodynamic effect. Similar rheological results have been seen for similar fractal particle suspensions by other researchers [10, 14]. Due to the fractal, porous nature of these particles, they exhibit shear thickening at these low concentrations, but the fractal nature also should lead to a low particle modulus compared to a solid particle. In fact, using the elastohydrodynamic model to

approximate the modulus, assuming a prefactor of one, gives a value of order 10^5 Pa, which is many orders of magnitude lower than that expected for bulk silica or that measured for the coated silica spheres here by AFM. This estimated modulus value increases by four orders of magnitude to 1 GPa if a prefactor of order 0.01 is included, consistent with the estimated volume fraction of these particles.

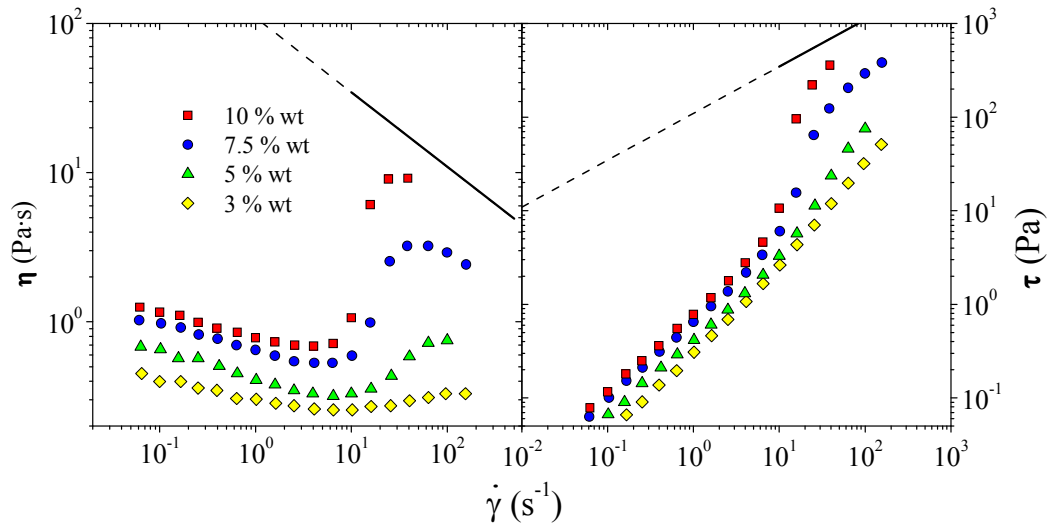


Figure 6.16 Elastohydrodynamic model compared rheology data of fumed silica suspensions in PPG from Raghavan et al. [136].

6.4.3 Discussion

Previous simulations and theory suggest that the limiting behavior of suspensions is a constant viscosity for continuous shear thickening and an unbounded stress for discontinuous shear thickening that leads to jamming. However, experiments on concentrated dispersions of polymer particles were seen to show a post-thickening

transition to thinning at rheometrically accessible shear stresses. The elastohydrodynamic model developed here provides an explanation for this discrepancy as well as providing a link between the particle's mechanical properties and the limit of suspension rheology at stresses beyond shear thickening. This regime where particle elastic deformations within the hydroclustered fluid control the rheology is termed the elastohydrodynamic regime.

AFM measurements of the particle hardness were used to estimate the particle elastic modulus of the model soft particles (PMMA) and silica particles used throughout this thesis. With no adjustable parameters, the model as developed provides an upper bound to the suspension rheology and is observed to lie above the measured data. Note that the silica suspensions, unlike the polymeric suspensions, did not exhibit any clear evidence of elastohydrodynamic shear thinning and the highest stresses probed did not approach those required to observe the effect, as predicted by the model.

We also examine literature data on shear thickening polymeric suspensions that exhibit post thickening shear thinning behavior and again observe that the model provides an upper bound for the measured rheology. The kaolin clay suspensions did not exhibit this post-thickening transition, which is expected and predicted by the model due to the high particle modulus relative to the measured shear stresses. The calcium carbonate dispersions had the largest modulus of the particles tested, but it did exhibit the possible onset of the elastohydrodynamic regime at high stresses. Here again, the data approach the limiting model predictions, so this behavior is consistent with the elastohydrodynamic model. It is noteworthy that the simple model is qualitatively consistent with the rheological data even for different particle

shapes. A comparison of the model to suspensions of fumed silica show post thickening shear thinning, possibly caused by deformations at stresses well below those expected for deformations in bulk silica, consistent with the particles having significantly increased flexibility due to their open, porous structure.

The prefactor in the model is fit to the PMMA data and applied to other data sets. The scaling of this prefactor with volume fraction does not follow a volume fraction squared relation as would be indicated by the likelihood of particle contacts. This prefactor appears to follow a relationship where it diverges with increasing volume fraction approaching maximum packing, although this constant is expected to be less than one. The prefactor value of 0.07 at $\phi=0.49$ does improve the model prediction for the data of Hoffman [37] and Laun et al. [134]. As the Hoffman data passes through the model at $\phi=0.57$, the prefactor is estimated to be order one at that concentration.

The elastohydrodynamic phenomenon described in this chapter is quite general, with applications beyond the relatively hard, discrete particles discussed so far. Numerous other examples of flowing, soft particle suspensions could potentially be affected by this elastohydrodynamic effect. For example, the basic theory comes from prior work on soft particle pastes. In fact, the prior work which developed the theory for slip near the wall noted the likelihood of these types of deformation occurring within the bulk material as well [125].

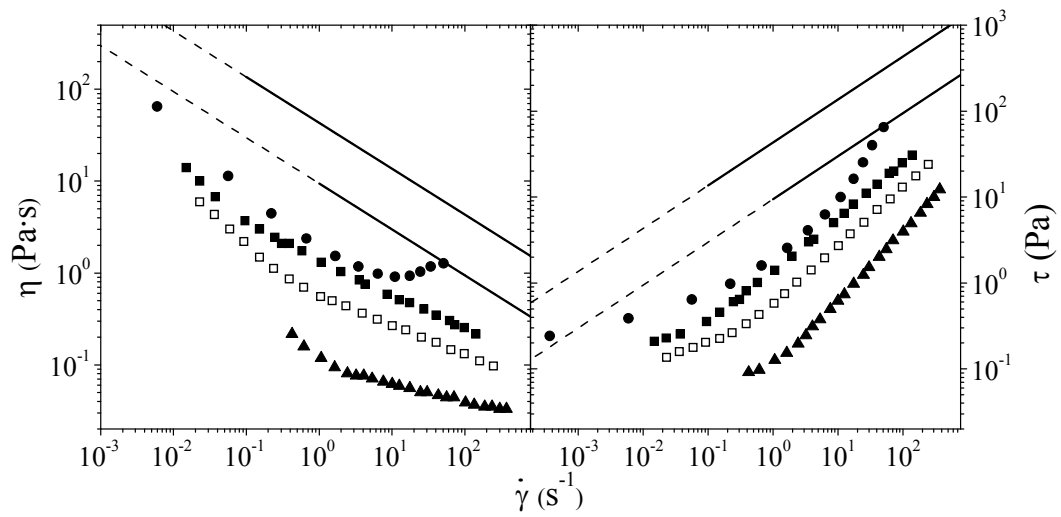


Figure 6.17 Steady shear rheology of concentrated suspensions of agar microgel particles of varying particle hardness from Adams et al. [127]. The rheology shows a regular shift to lower viscosity as the agar concentration and particle hardness are lowered. The lines are equation 6.3 with the modulus of 185 kPa and 8.9 kPa based on the particle moduli for the circles and squares, respectively.

Microgel particle suspensions are an example of concentrated, deformable particle suspensions. Adams et al. studied concentrated suspensions of agar-water microgel particles suspended in oil, at varying concentrations of agar within the particle which gives a tunable modulus [127]. The rheology measurements of the most concentrated of these suspensions at varying particle hardness are seen in Figure 6.17. At the highest agar concentration of 5%, the particle modulus was measured by Adams et al. to be 185 kPa, and the suspension was seen to shear thicken slightly; however, the softer particle suspensions continued to shear thin at stresses where the hardest particles shear thickened. The lines shown in the figure are the model with the assumption of the oil solvent viscosity as 0.01 Pa·s (not given in the reference), and the particle moduli as given in the article as 185 and 8.9 kPa for the two lines, based

on the two highest moduli particles represented as the circles and filled squares in the figure. The hardest particles shear thicken and the elastohydrodynamic model prediction is an order of magnitude above the stresses achieved in this experiment. The model predictions for the next hardest particles similarly provide an upper limiting bound to the rheology, which appears to shear thin with a power law index close to $\frac{1}{2}$. Thus, the behavior of the Agar suspensions is again consistent with the model predictions and it is intriguing that the power-law indices for the shear thinning suspensions is close to that predicted by elastohydrodynamics.

In addition, emulsions are another type of common, deformable particle suspensions that could show this effect. Wolf et al. present the shear viscosity of emulsions stabilized by silica particles (Pickering emulsions), which shear thickened and then thinned at stresses beyond the transition to thickening [137] (seen in Figure 6.18). Typically, emulsions do not exhibit shear thickening. In fact, Wolf et al. studied similar emulsions, stabilized by surfactants instead of solid particles. These surfactant-stabilized emulsions only exhibited shear thinning with no shear thickening. The shear thickening in Pickering emulsions is consistent with the elastohydrodynamic theory, in that the particle stabilized emulsions having sufficient rigidity to follow the hydrocluster mechanism as discussed previously, but the surfactant stabilized emulsions deform rather than thickening. Due to the ability of these emulsions to deform, they also show the post-thickening transition driven by elastohydrodynamic deformations. Utilizing the model compared to the secondary shear thinning seen in the elastohydrodynamic regime gives a first-pass estimate of the particle modulus for these Pickering emulsions as order 10^5 Pa, assuming the prefactor, C_{EH} is of order one.

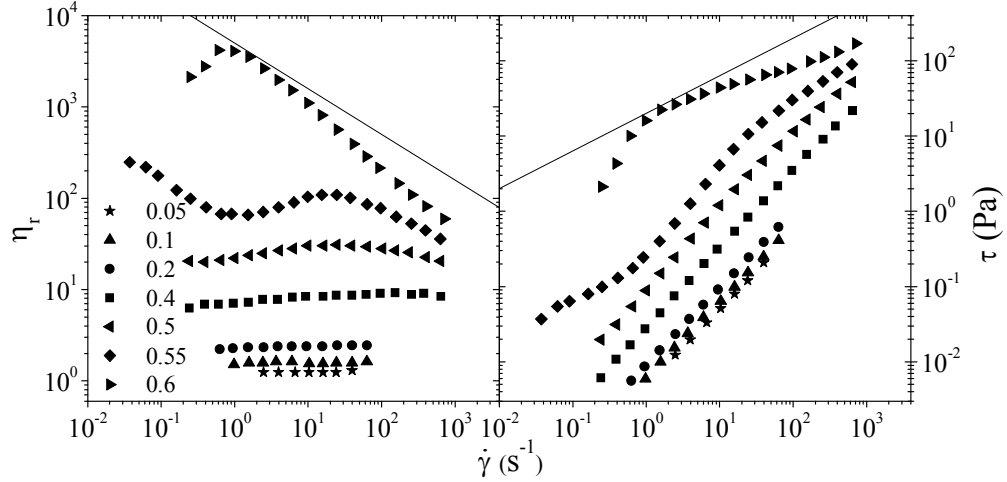


Figure 6.18 Steady shear rheology of Pickering emulsions from Wolf et al. [137]. The model line is shown with the $\eta_s=0.004$ Pa-s and $G_0=10^5$ Pa (fit to the data).

The model can also suggest why the surfactant stabilized emulsions do not show shear thickening. The surfactant stabilized emulsions are expected to have a much lower modulus and therefore, they may deform elastohydrodynamically to alleviate stress before they can shear thicken. Indeed, it has previously been hypothesized that emulsion droplet deformability leads to the absence of shear thickening [138], although no mechanistic model was presented.

6.5 Conclusions

Here, we developed a simple scaling model that describes how particle deformability can lead to a second-shear thinning regime beyond shear thickening, termed the elastohydrodynamic regime. This elastohydrodynamic model was tested

against particles of widely varying particle hardness from the literature as well as specially synthesized PMMA polymer colloid dispersions. Independent AFM measurements of the particle hardness were performed to provide the parameters necessary for the model. The elastohydrodynamic model is shown to successfully provide an upper bound to describe the terminal rheological behavior of polymer colloid dispersions at high shear rates.

In contrast, colloidal suspensions of mineral particles were observed not to show significant post-thickening shear thinning in rheometric experiments. Again, this is predicted by the model as the increased particle hardness would require higher stresses than those probed to reach the elastohydrodynamic regime.

As the elastohydrodynamic model may have more general applicability to model suspension rheology, we examined literature data for microgel particles of tunable modulus, which were shown to exhibit shear thickening for the hardest particles but not softer particles. This source of stress relaxation through elastohydrodynamic deformations could be the cause of the lack of thickening for the softer particles. Particle deformability in emulsions has been previously linked to the absence of shear thickening. Pickering emulsions, which would have significantly higher particle modulus compared to surfactant stabilized emulsions, were shown to shear thicken whereas surfactant stabilized emulsions did not. This difference between similar suspensions with harder particles showing thickening and softer particles showing only shear thinning is indicative of the elastohydrodynamic effect. Further work exploring higher shear stress behavior in mineral particle suspensions would prove useful in testing the universality of the elastohydrodynamic effect. Finally, we note that the dependence of high shear rheological properties as a function of particle

hardness is also relevant for use of these suspensions as body armor materials, as explored in Chapter 7.

Chapter 7

THE EFFECT OF PARTICLE HARDNESS ON SHEAR THICKENING FLUID COMPOSITES WITH PROTECTIVE FABRICS

7.1 Introduction

Concentrated suspensions show widely varying rheological properties, including yielding, shear thinning, and shear thickening [1, 6, 29, 40]. Shear thickening has been observed in industrial processing of concentrated suspensions, exhibiting orders-of-magnitude changes in viscosity with only slight changes in the flow kinematics [1, 6]. This shear thickening behavior can lead to sudden increases in flow resistance that can damage processing equipment and hinder materials processing.

More recently, shear thickening fluids (STF) have been used in combination with protective fabrics to improve their ballistic, stab, and puncture protective properties [2-5]. In general, it has been found that the addition of STF limits the mobility of yarns and filaments in the fabric, increasing the resistance of the fabric to damage mechanisms such as yarn pull-out and windowing. These observed behaviors suggest that fabric products such as soft body armor, protective safety wear, inflatables, and architectural fabrics could be made more robust through the incorporation of STF-fabrics.

Although there are a number of experimental studies on the behavior of STF-fabrics [2, 11, 12, 139-142], the existing literature provides only limited insight

into the detailed mechanisms by which the STF and fabric interact to produce globally beneficial properties. Comparisons of fabrics treated with particle-free Newtonian fluids showed little correlation between fluid viscosity and ballistic behavior [3]. For silica-based STFs added to aramid-based fabrics, the hard silica particles gouge and erode the surface of the softer aramid filaments in the vicinity of high applied stresses [11]. This fiber damage due to physical entrainment of particles could indicate that particle hardness relative to that of the fibers in the supporting fabric plays an important role in load transfer and fabric behavior. Other studies have shown that adding dry particles to fabrics results in similar improvements in performance to those observed for STF addition [5, 142, 143]. In addition, Bazhenov found that wetting Kevlar fabric with water lowered the friction, resulting in both lower pull-out resistance and lower ballistic performance [144]. Lee and coworkers performed a detailed experimental and numerical study on dry fabrics and fabric-resin composites which provides insight into the complex relationship between ballistic resistance, yarn mobility, and yarn breakage [145]. These results suggest that particle-fabric interactions play a significant role in the observed properties of STF-fabrics.

Further insights into the ballistic resistance behavior of woven fabrics can be derived from numerical studies [146-149]. In particular, frictional effects have been studied systematically by simulations. One study on the effects of inter-yarn friction showed failure primarily due to windowing and yarn pull-out at very low friction, maximum performance at moderate levels of friction due to the suppression of windowing, and reduced performance at high friction due to the loss of yarn pull-out as a failure mechanism [149]. Further studies showed that inter-yarn friction strongly

influences the penetration resistance of woven fabrics by spreading the load to additional yarns not directly impacted by the projectile [146, 147].

In this chapter, the detailed mechanisms of STF-fabric interaction are investigated through a systematic study of the effect of particle hardness and carrier fluid addition. Untreated aramid fabrics are compared to fabrics treated with: a control fluid, dry particles, or shear thickening fluid-particle suspensions. Both silica and poly(methyl methacrylate) (PMMA) particles are studied, to isolate particle entrainment effects and study the effect of particle hardness. To explore a range of fabric damage mechanisms, the fabric characterization experiments include yarn pull-out [67, 150-152], quasistatic puncture, and ballistic penetration experiments [2].

7.2 Experimental

Silica particles used in this study were commercially sourced, relatively monodisperse, nominally 500 nm in diameter, and have their particle and suspension properties characterized extensively as described in Chapters 3 and 5 [48]. Their density was measured by solution densitometry as 1.96 g/ml and the particle radius in PEG was measured by ultra small-angle neutron scattering to be 260 nm with 10% polydispersity, and confirmed by SEM and DLS (see section 3.5.1). The carrier fluid for SiO₂-STF and PMMA-STF was poly(ethylene glycol) (200 M_w PEG from Clariant, $\rho=1.12 \text{ g/cm}^3$, $\eta=0.049 \text{ Pa}\cdot\text{s}$), which was also used for the fluid treated PEG-Kevlar control sample. Fluid-particle STF dispersions for rheological testing were formulated by adding the particles to PEG and roll mixing overnight prior to testing. The steady shear rheology is shown in Figure 7.1 as viscosity versus applied stress and key features are summarized in Table 7.1. At 52 % particles by volume, the STF sample exhibits extreme shear thickening, which manifests as a nearly vertical viscosity versus

rate curve at high shear rates (inset). The Newtonian rheology of the PEG is shown for reference in Figure 7.1.

Table 7.1 Tabulated rheological parameters for suspensions used.

Particle type	SiO ₂	PMMA
Particle volume fraction (ϕ)	0.52	0.49
Particle weight fraction	0.64	0.51
Critical shear stress for shear thickening (Pa)	33.5	0.794
Critical viscosity at onset of shear thickening (Pa-s)	2.34	11.0
Critical shear rate for shear thickening (s ⁻¹)	14.4	0.115

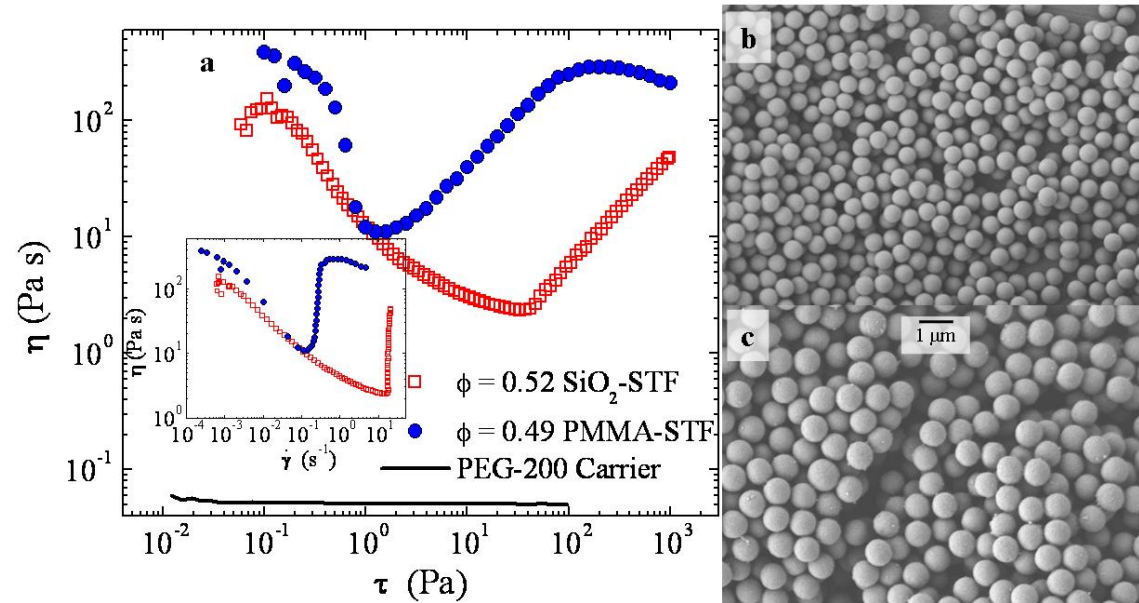


Figure 7.1 a) Steady shear rheology of shear-thickening suspensions used. SEM micrographs of b) commercial SiO₂ particles and c) lab produced PMMA particles.

PMMA particles were chosen for this study due to their ease of synthesis, compatibility with PEG-based STF processing, and expected lower hardness relative to SiO₂. The PMMA particles were synthesized via a free-radical reaction of dilute methyl methacrylate monomer in mixed methanol and water solvent at 70°C for 3 hours as discussed in section 2.3.2 [54]. To make sufficient PMMA particles for this study, two separate batches of approximately 1.5L total volume were used; the procedures for each were the same and the effective size determined from dynamic light scattering (DLS) was not significantly different. The reaction materials were dialyzed against three separate batches of deionized water for at least 24 hours each, and then concentrated via centrifugation to 31.5 % solids by weight before intercalation into fabric as discussed below or transfer into PEG for rheology measurements.

To produce a suspension for rheology measurements, sufficient PEG-200 was added to achieve an STF volume fraction of $\phi = 0.496$ (volume of PMMA normalized by total volume of PMMA and PEG) and then the water was removed by first heating while stirring at 60°C, then under vacuum at 60°C. This formulation of PEG-PMMA has been shown to exhibit shear thickening behavior (see Chapter 6) and its rheology is also shown in Figure 7.1. The particles produced had a density of 1.23 g/mL determined by solution densitometry in water by standard procedures assuming ideal mixing [89] and a diameter of 1050 ± 110 nm determined via DLS and confirmed via SEM. SEM micrographs of both particle types are also shown in Figure 7.1.

For in-fabric testing, the particles and/or carrier fluid were intercalated into sheets of JPS Composites (Anderson, SC) scoured Style 706 woven Kevlar fabric (600 denier KM2 yarns, plain-woven at 34×34 yarns per inch), with an areal density

of 180. g/m². In each case, the appropriate materials were diluted with ethanol, individual fabric sheets were dipped and held in the solution for at least one minute before being squeezed through rubber-coated nip rollers and hung to dry at room temperature. After air drying for at least 10 minutes, the fabric was dried in an oven at 60°C for 30 minutes to remove the ethanol and/or water co-solvents. The fabric was dry to the touch, even for the PEG, SiO₂-STF, and PMMA-STF materials which include PEG carrier fluid. Fabrics with PEG carrier had a uniform appearance; while PMMA– and SiO₂-coated fabrics without PEG appeared streaky with a whitened or slightly chalky appearance. If placed in contact with surfaces such as countertops or gloved hands, fabrics treated with the dried particle addition left a white residue of dry particles on the surface. In contrast, coated fabrics with PEG and particle STF suspension addition left no obvious residue on contact surfaces.

The mass or volume addition of each coating to the fabric can be controlled by tailoring the dilution ratio of coating to co-solvent in the dip bath. For the present study, we wish to compare coatings utilizing SiO₂ and PMMA particles, with and without PEG carrier fluid. A comparative series of coated fabrics could be formulated to maintain a consistent coating mass, coating volume, particle mass, or particle volume. We have chosen to design our experiment to compare fabrics with consistent particle volume addition. This selection is based on previous observations that sub-micron particles intercalate between fibers and yarns in the void space of the woven fabric [4, 5, 12, 142], so that a consistent particle volume addition should result in reasonably consistent geometric packing and fill of the particles in the coated fabrics. This geometric consistency allows for the most objective comparison of the effect of particle hardness and solvent addition on overall fabric performance. Other

comparisons, such as constant coating weight, could be more relevant to practical protective material design and would be valuable for additional study.

Six different fabric coatings, seen in Table 7.2, were compared: untreated (Neat), liquid control (PEG), dry PMMA (PMMA-dry), PMMA with PEG (PMMA-STF), dry SiO₂ (SiO₂-dry), and SiO₂ with PEG (SiO₂-STF). To achieve constant particle addition to the fabrics, dip baths for each particle-based coating were designed to a consistent ratio of total particle volume to co-solvent volume. This ratio ended up being 0.163 for the PMMA treatments and 0.173 for the SiO₂ treatments (the error came from a slight change in the PMMA particle density from the expected value from previous work). For the dry PMMA coating dip bath, ethanol was added to the concentrated particles in water (31.5 wt % solids) to achieve the desired particle:co-solvent volume ratio. For the PMMA-STF coating dip bath, an identical PMMA-water-ethanol dip bath was modified by adding sufficient PEG-200 to achieve an STF volume fraction of $\phi = 0.496$. For the dry SiO₂ coating dip bath, ethanol was added directly to the SiO₂ particles to achieve the desired particle:co-solvent volume ratio of 0.173. For the SiO₂-STF coating dip bath, an identical SiO₂-ethanol dip bath was modified by adding sufficient PEG-200 to achieve an STF volume fraction of $\phi = 0.52$. The PEG fabric (no particles) was produced using a bath with the same volume ratio of PEG to ethanol (0.217) as in the SiO₂-STF bath. For each case, the coating mass and volume additions as a percent add-on of the mass or volume of the fabric are summarized in Table 7.2.

Table 7.2 Data table of fabric treatment add-on and test results.

Treatment	Neat	PEG	PMMA-dry	PMMA-STF	SiO ₂ -dry	SiO ₂ -STF
Areal Density (gsm)	180	192±0.85	189±2.07	196±1.49	193±1.51	205±1.26
Weight Addition	-	6.55±0.47%	4.97±1.2%	9.16±0.83%	7.12±0.84%	14.0±0.72%
Total Volume Addition	-	8.42±0.61%	5.82±1.4%	11.2±1.0%	5.48±0.64%	13.3±0.69%
Particle Volume Addition	-	-	5.82±1.4%	5.58±0.51%	5.48±0.64%	6.92±0.36%
Fluid Volume Addition	-	8.42±0.61%	-	4.09±1.6%	-	4.09±1.9%
Yarn Pull-Out Data						
Loading Peak Force (N)	13.0±0.27	20.4±0.73	25.3±1.9	46.7±2.9	37.2±1.2	61.8±7.2
Loading Displacement (mm)	8.56±0.75	9.87±0.65	12.0±1.3	18.6±2.5	16.5±1.5	24.0±2.2
Plateau Force (N)	8.40±1.3	20.1±1.3	13.9±2.9	30.4±3.1	32.4±2.0	N/A
Plateau Location (mm)	8-60	19-64	12-60	21-66	16-62	N/A
Total Energy (J)	0.609±0.022	1.44±0.056	1.00±0.075	2.31±0.093	1.81±0.036	1.04±0.27
Spike Puncture Data						
Peak Force (N)	21.7±3.5	31.7±9.1	36.3±6.5	58.1±13	77.6±9.7	70.4±15
Failure Distance (mm)	8.19±0.43	7.83±0.84	8.99±0.48	9.71±0.46	10.3±0.63	10.3±1.1
Failure Energy (J)	50.0±11	71.1±28	91.4±24	163±48	215±43	193±49
Ballistic Data						
Ballistic V ₅₀ (m/s)	72.2±6.9	77.4±4.0	138±4.8	136±5.0	217±6.6	196±4.5

For each coating, two sheets of 38.1 cm × 38.1 cm fabric were produced for ballistic testing (later cut into 15.2 cm × 5.08 cm strips), one sheet of 25.4 cm × 20.3 cm fabric was produced for pull-out testing, and one sheet of 15.2 cm × 15.2 cm fabric, cut on a 45° bias, was produced for puncture testing (cut into two 15.2 cm × 7.62 cm pieces).

7.3 Results

7.3.1 Yarn Pull-Out Testing

All of the curves of force versus crosshead displacement for each material are shown in Figure 7.2; typical curves are compared more directly in Figure 7.3. In the neat, PEG, PMMA-dry, and PMMA-STF cases, the yarn uncrimps in a loading regime, shows a force plateau where the yarn pulls through the fabric weave, and then shows a steady force decay as the fiber pulls out of the weave. The peak force is generally noted at the end of the loading regime, but in the PEG-fabric the load increases slightly through the “plateau” region. In addition, the PMMA-STF fabric shows unique behavior of a significant drop (~30%) in load from the peak to the plateau. The extracted yarns appear to be in good condition, with little evidence of significant damage or fraying. In the SiO₂-dry case, the yarn tail is pulled partially through the weave (seen by the force plateau after fiber uncrimping), but generally breaks before the end of the tail enters the woven fabric. During pull-out for SiO₂-dry samples, the yarn becomes very frayed, and yarn fracture typically occurs on the pulled yarn at a position along its length that is still embedded inside the woven fabric. For SiO₂-STF fabrics, the yarn becomes very frayed and "fuzzy" during the uncrimping stage, but in most cases uncrimping appears to progress completely through the fabric.

Yarn fracture typically occurs after little or no yarn translation has occurred, with the fracture point again located on the pulled yarn at a location within the woven fabric. It is also interesting to note that ink marks on the pulled yarn appeared to "smear" as the yarn was pulled, indicating that individual filaments were being pulled at different rates. This observation implies that yarn failure is occurring gradually and at a filament-by-filament progression.

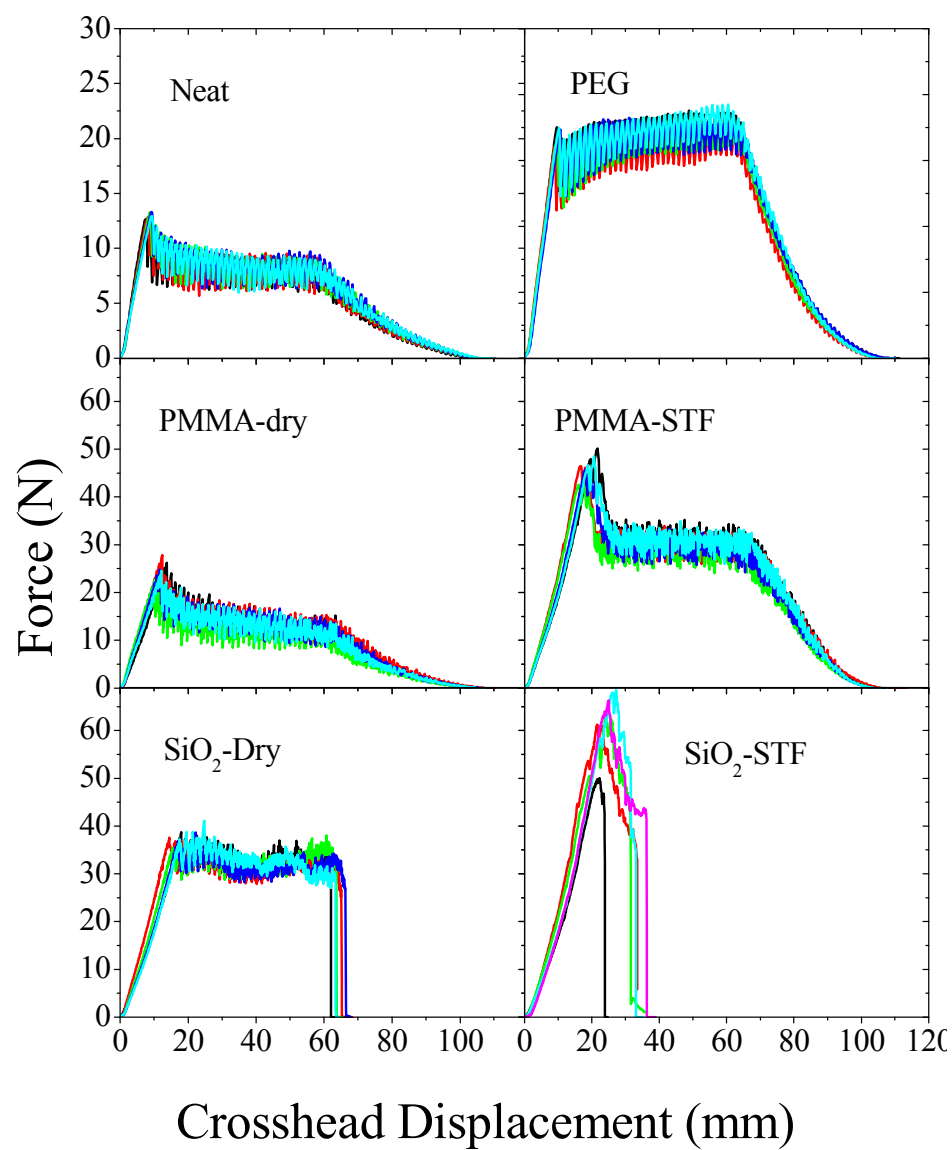


Figure 7.2 All curves of force versus crosshead displacement for yarn pull-out testing.

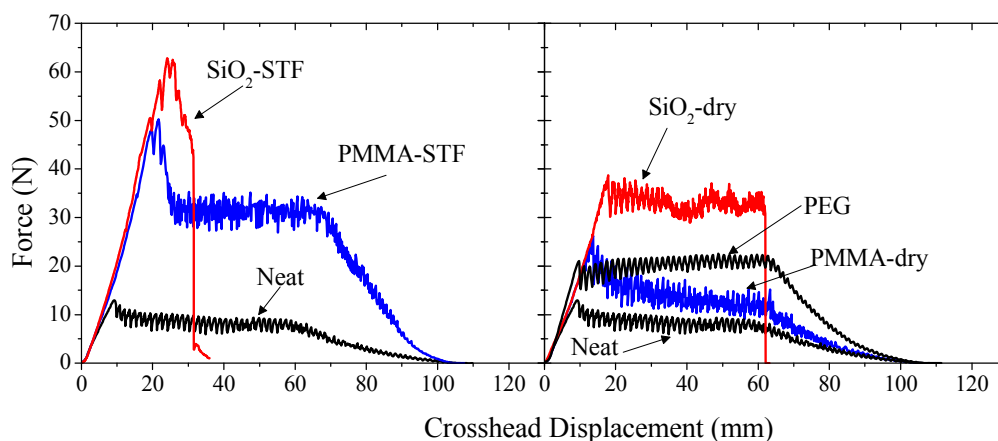


Figure 7.3 Typical force versus crosshead displacement curves from yarn pull-out testing for various fabric treatments.

Figure 7.4 and Table 7.2 compare the various fabrics in terms of loading peak force, loading displacement, and plateau force. Table 7.2 also includes the location of the plateau and the total integrated failure energy. All treated materials require higher forces to load and pull out the yarn than the neat material. In addition, the STF treated fabrics require significantly higher forces than the respective dry particle treated fabrics. The loading forces for the PMMA treated fabrics are also lower than the comparable SiO₂ treated fabrics. Note, however, that the PMMA-STF fabric, which showed no obvious fraying during pull-out, has a higher peak force than the SiO₂-dry fabric, which exhibited yarn breakage during pull-out. The PEG fabric has a slightly lower loading force than the PMMA-dry fabric, but a higher plateau force. This suggests that the liquid itself increases both the static friction (adhesion between yarns) and increases the dynamic friction, possibly due to viscous dissipation in the fabric.

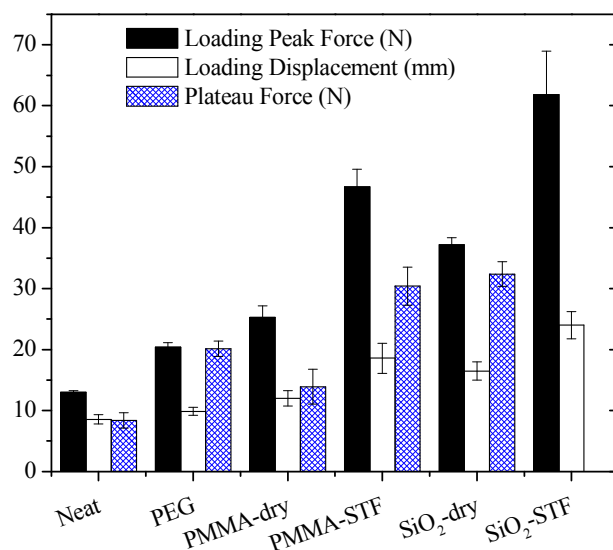


Figure 7.4 Yarn pull-out testing data for various fabric treatments. Error bars indicate one standard deviation above and below the average of five measurements. Note that no plateau is seen in the SiO₂-STF case due to yarn breakage and that the SiO₂-dry fabric plateau ends with yarn breakage.

SEM micrographs at low magnification for the fabrics after yarn pull-out can be seen in Figure 7.5. These images are oriented so that the direction of pull is upward, with the original extracted yarn position located at the center of the image. The yarns were fully extracted in the neat, PEG, and PMMA fabrics but not for the SiO₂ fabrics, where a significant fraction of the original pulled yarn filaments remain in the fabric. Figure 7.6 shows a higher magnification micrograph of either the cross-

yarn exposed by removal of a vertical yarn, or the yarn which was pulled in the SiO₂ cases. Areas of significant fiber scoring on large fractions of the yarn surface by the SiO₂ particles can be seen, but only limited fiber scoring is seen in the PMMA cases. Another key difference is that the SiO₂ particles all appear to be very spherical in shape, while many of the PMMA particles appear to have been flattened. This flattening of PMMA particles was not observed for virgin PMMA-treated fabrics, and therefore appears to be the direct result of the yarn pull-out process. The neat, PEG, and PMMA fabric weaves appear to have recovered to an orthogonal orientation after the pull-out experiment, whereas the high force on the SiO₂-STF fabric combined with the limited mobility has deformed the weave irreversibly such that the cross yarns have been displaced in the direction of yarn pull-out.

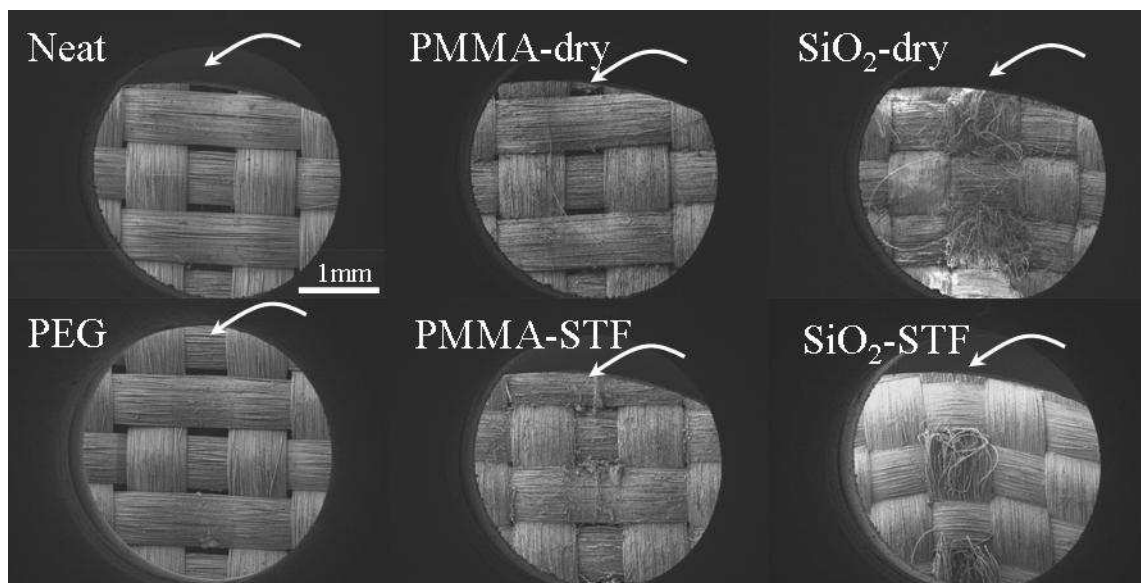


Figure 7.5 SEM micrographs of fabric from pull-out testing. The arrow indicates the former position of the extracted yarn, or in the SiO₂ cases, the fractured, pulled yarn.

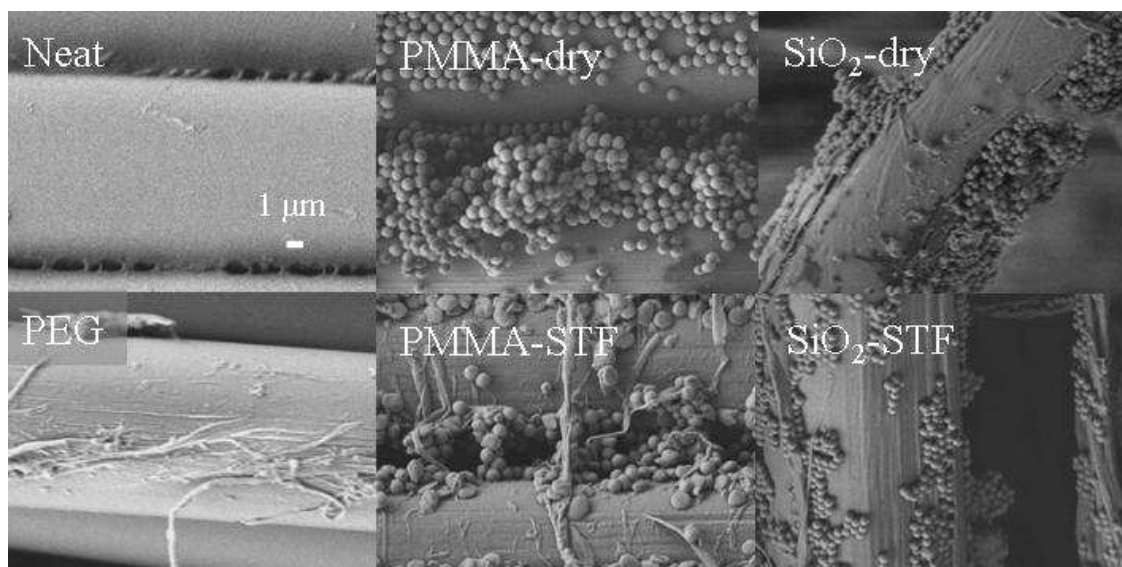


Figure 7.6 SEM micrographs of fabric from pull-out testing. The PMMA and particle-free fabrics show filaments of cross yarns, whereas SiO₂ fabrics show filaments from the pulled yarn.

7.3.2 Spike Puncture Testing

All curves of force versus displacement for the spike puncture testing for each material are shown in Figure 7.7; typical curves are compared in Figure 7.8.

Figure 7.9 summarizes the data in terms of peak force, displacement at failure, and integrated failure energy. Much of the variability seen in puncture testing is due to the woven nature of the fabric. The lowest penetration forces for a particular specimen

were observed when the spike initially contacted an interstitial position between yarns, leading to penetration primarily due to fabric "windowing" [11] (also referred to as "wedge through" [153]). Windowing refers to the spreading apart of yarns in a woven fabric, creating an open area through which an object can penetrate. In contrast, the highest penetration forces occurred when the spike first contacted the fabric at a yarn cross-over area, leading to a higher likelihood of yarn pull and fiber fracture with windowing during penetration. In spite of this variability, statistically significant differences in the energy and peak force were measured between the PMMA treated fabrics and the SiO₂ treated fabrics.

A significantly larger force, resulting in larger energy, was required to puncture the PMMA-STF fabric compared to the PMMA-dry fabric. As for the pull-out testing, the PEG fabric has similar peak force and failure energy compared to the PMMA-dry fabric. The SiO₂-STF fabric requires slightly less force to puncture than the SiO₂-dry fabric. The two SiO₂ materials have higher peak loads and failure energies than the PMMA-STF fabric. Figure 7.10 shows optical micrographs of the spike puncture testing. Kevlar yarns and fibrils were broken for the SiO₂ treated fabrics. In addition to fiber breakage, windowing of the fabric weave and splitting of the yarn into separate bundles of fibers both appear to be associated with fabric failure.

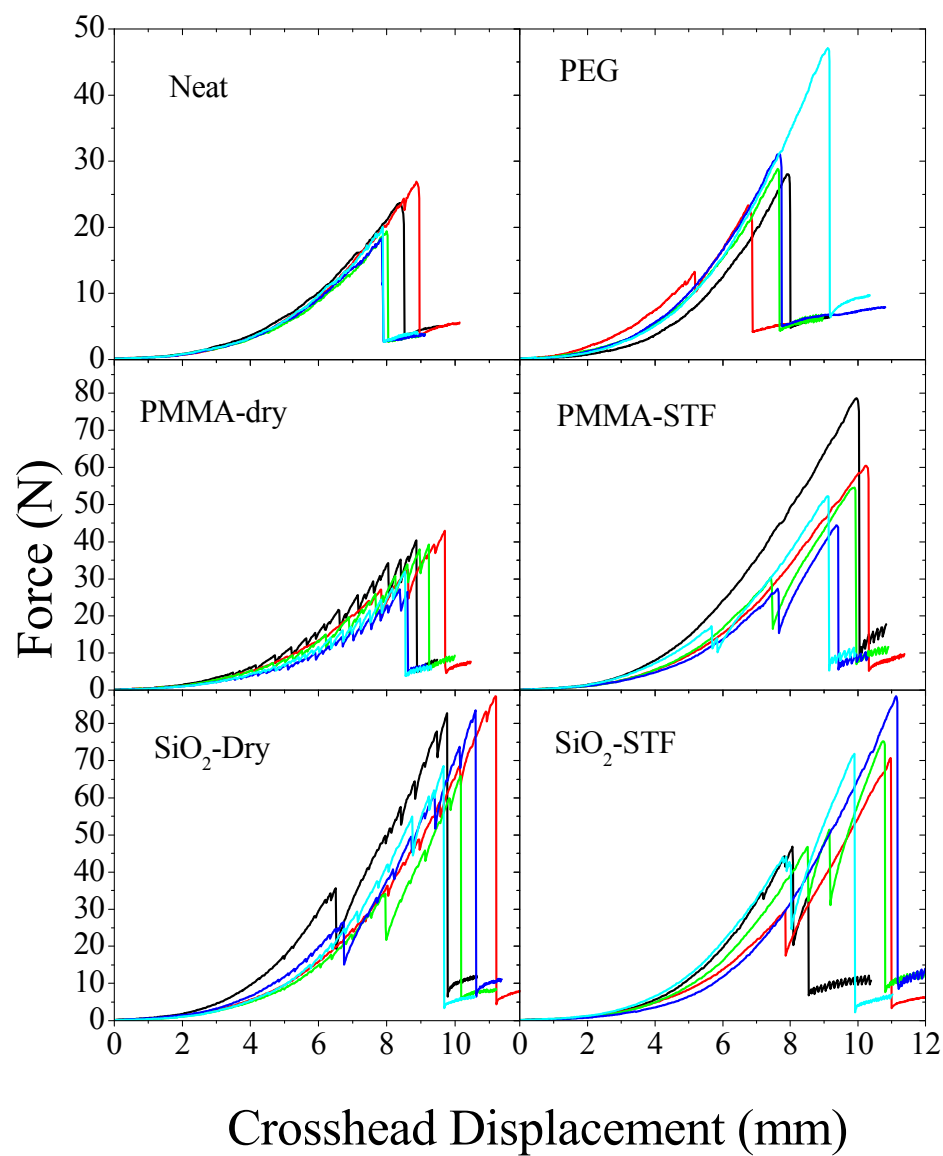


Figure 7.7 Force versus crosshead displacement for all curves in spike puncture testing.

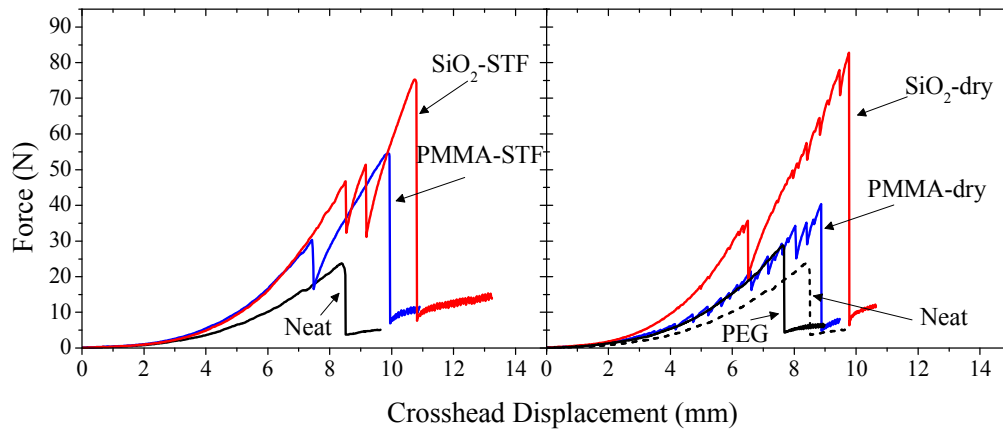


Figure 7.8 Typical force versus crosshead displacement curves for quasistatic spike puncture testing for various fabric treatments.

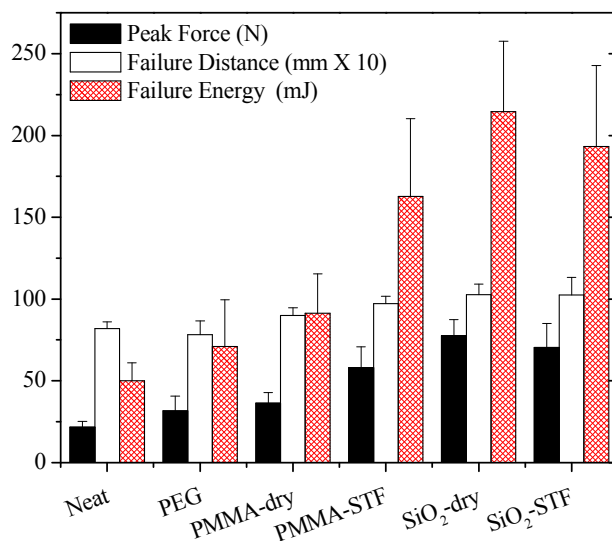


Figure 7.9 Spike puncture testing data for various fabric treatments. Error bars indicate one standard deviation above and below the average of five measurements. Units are chosen to accommodate data on one figure.

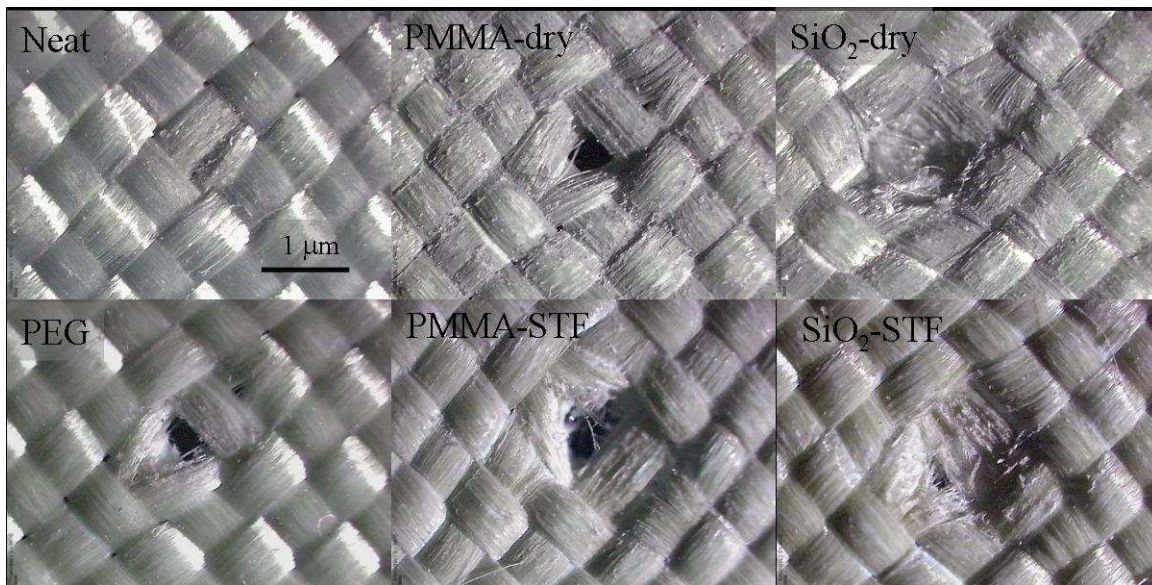


Figure 7.10 Optical micrographs of fabric from spike puncture testing.

7.3.3 Ballistic V_{50} Testing

The ballistic test results are shown in Figure 7.11. The V_{50} for the PMMA-dry and PMMA-STF fabric are both about 140 m/s, nearly double that of the neat and PEG fabrics. The SiO_2 -dry and SiO_2 -STF fabric both have a V_{50} over 195 m/s, about triple that of the neat fabric and about 50% higher than the PMMA fabrics. No significant difference is seen in the V_{50} between the PMMA fabrics, although the SiO_2 -dry fabric appears to show a slightly higher V_{50} than the SiO_2 -STF fabric. Since the failure energy is related to the velocity squared, the SiO_2 -fabrics have about one order of magnitude higher failure energy than the neat fabric. In Figure 7.12, which shows pictures of the failed fabrics, windowing is seen with limited yarn pull-out in the neat case. In the PEG and PMMA materials, significant yarn uncrimping and

extraction is evident (via ~2-3 cm long yarn loops pulled out at the damage zone). In addition, no yarn breakage is seen in the neat, PEG, or PMMA materials. In the SiO₂ materials, significant uncrimping is evident with very little yarn extraction, and the extracted fiber loops are much smaller (<0.5 cm). In addition, significant fiber breakage is seen for the SiO₂ materials. In the neat materials, yarn uncrimping and extraction does not appear to be significantly biased directionally; however, the PMMA and SiO₂ materials show only a limited damage zone in the horizontal direction but show uncrimping and fabric deformation over broader areas in the vertical direction. This bias in yarn uncrimping is consistent with the fixed boundaries in the horizontal direction limiting yarn pull-out and the free edges allowing pull-out in the vertical direction. The SiO₂ materials also show some tearing of the fabric weave at the fixed edge, far away from the impact point, which is not seen for the neat, PEG, or PMMA materials.

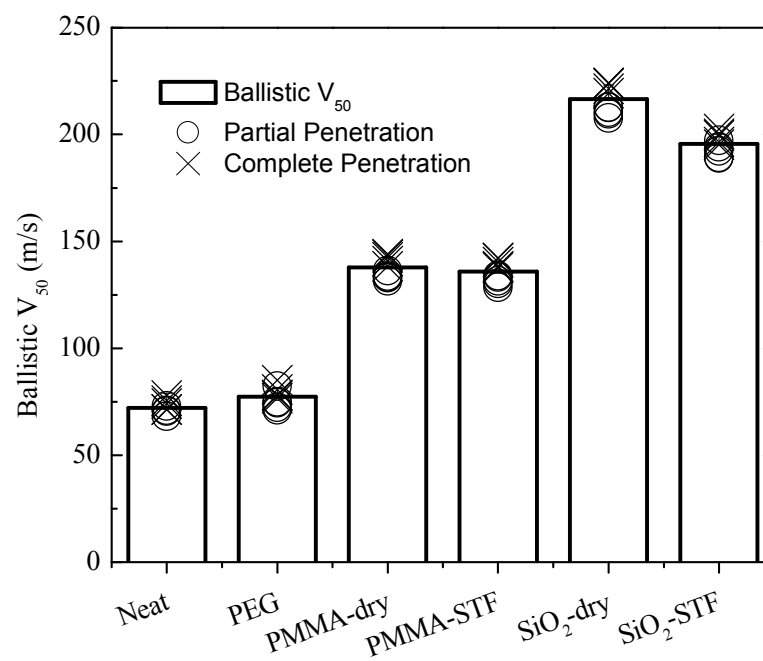


Figure 7.11 Ballistic V_{50} testing data for various fabric treatments.

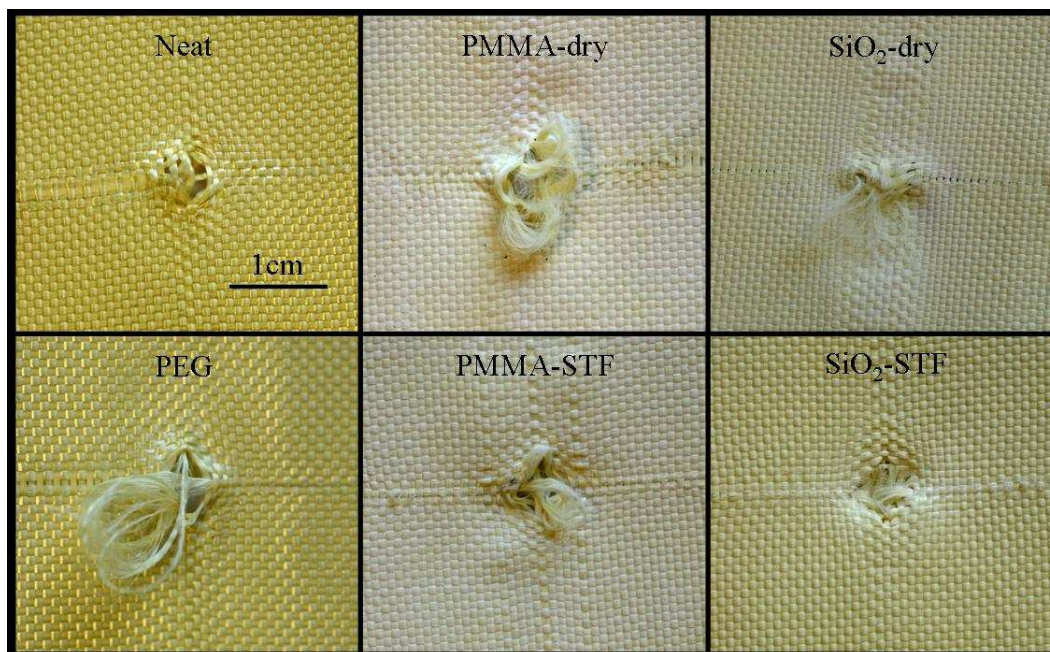


Figure 7.12 Front faces of fabric after ballistic testing. Yarn pull-out and windowing are seen in the Neat (left) and PMMA (center) fabrics, with fiber breakage and limited pull-out seen in the SiO₂ fabrics (right).

7.4 Discussion

The experiments performed in this study – yarn pull-out, quasistatic puncture, and ballistic penetration – explore a range of fabric defeat mechanisms including yarn uncrimping, yarn sliding and extraction, windowing, yarn and fiber compression, and fiber shear and tensile failure. These mechanisms can be broadly characterized as being dependent on either mechanical properties inherent to the yarn filaments or effects of mobility of the yarn or filament. For example, yarn sliding and

windowing are most directly modified by restricting the ability of fibers and yarns to reorganize and move relative to each other. In contrast, compression, shear, and transverse failure are more directly related to the mechanical properties of the Kevlar filaments.

The results of this study show that intercalation of particles into fabrics, whether dry or wetted, overall leads to a substantial increase in fabric resistance to yarn pull-out, puncture and ballistic penetration. It is unlikely that the intercalation of particles increases the inherent mechanical properties of the Kevlar filaments, as the particles are located primarily outside of the filaments and therefore should not provide mechanical reinforcement to the fiber. Therefore, these modifications to fabric behavior are most likely generated due to changes in the mobility-driven defeat mechanisms.

Particle hardness is shown here to be an important factor governing the behavior of particle-intercalated fabrics. All experiments showed a systematic increase in resistance for SiO₂ systems as compared to PMMA systems. If we accept the hypothesis that mobility mechanisms are primarily engaged in these experiments, then the harder particles must be more effective at reducing yarn and filament mobility. One obvious explanation for this behavior is that the harder particles are able to embed into the softer polymer filaments, leading to more direct mechanical coupling between fibers and particles. The SEM micrographs of this and previous studies [11] indicate that this mechanism is relevant. A different explanation would be that, under stress, the softer particles are more likely to accommodate loads through direct mechanical deformation. This accommodation could lead to less resistance to bulk compression and reorganization mechanisms, resulting in reduced effect on fabric mobility. This

second hypothesis is supported by the appearance of deformed PMMA particles after testing. The drop in pull-out load after the initial peak in the PMMA-STF-Kevlar, a feature unique to this treatment, could be symptomatic of these particle deformations. Further experiments are required to determine the relative importance of each of these mechanisms.

During yarn pull-out testing, yarn fracture was observed only for the treatments with SiO₂ particles. However, peak forces for the PMMA-STF pull-out case, in which complete yarn extraction was observed, are higher than the peak forces experienced by the SiO₂-dry case prior to yarn fracture. This result shows that the presence of harder particles can lead to a reduction in yarn and fiber mechanical properties under certain conditions. Direct characterization of the effect of particle intercalation on the tensile strength of yarns, although not reported in this study, could provide important insights into these mechanisms. It is likely that there are specific fabric applications where this fiber degradation due to the hard particles is detrimental, such that particle hardness may need to be tuned for optimal behavior. For example, it is reasonable to postulate that there exist particles with intermediate hardness between PMMA and SiO₂ that would result in higher pull-out resistance than PMMA, but would not induce premature yarn failure as observed for SiO₂-based coatings.

We should also acknowledge that the SiO₂ and PMMA particles are not identical in size (the PMMA particles are larger by a factor of 2), so there could be secondary effects due to particle size that limit the universality of our conclusions with respect to particle hardness. However, prior studies [4, 12] have shown that particle size plays only a minor role in fabric performance, as long as the particles are small enough to intercalate between filaments. Another recent study comparing 100 - 500

nm particles showed a slight increase in ballistic performance with decreasing particle size [3]. However, these observed differences do not appear to be significant enough to account for the behavioral differences we have observed between PMMA and silica systems.

The role of a fluid carrier in STF coatings, as compared to dry particle systems, is complex. In yarn pull-out testing, pure PEG addition increases both the static friction and dynamic friction as compared to the neat fabric. These effects lead to a moderate increase in puncture resistance, but little change in ballistic performance relative to the neat fabric. The combined addition of both fluid and particles as an STF formulation, compared to dry particle treatments, leads to a dramatic increase in yarn pull-out resistance for PMMA- and SiO₂- treated fabrics, and a significant improvement in puncture resistance for the PMMA-treated fabrics. However, the STF treatments lead to slight *decreases* in fabric performance relative to dry particle fabrics for both systems in ballistic testing and SiO₂ systems in puncture.

One possible explanation for these trends in behavior is that penetration behavior may not be optimized at maximum mobility restriction, but rather, at some intermediate degree of mobility. For example, for the fabric and projectile combination used in the present study, penetration is accommodated in neat fabrics by mobility mechanisms such as windowing and yarn pull-out. Therefore, higher mobility restriction is required. However, the yarn pull-out experiments show that SiO₂-STF coatings restrict yarn pull-out, leading to yarn failure with little extraction. In contrast, the SiO₂-dry composites showed the capacity for yarn extraction during yarn pull-out at high pull force. Therefore, under ballistic impact, the yarns in this fabric may be free to pull slightly, absorbing energy, lengthening the interaction time with the projectile,

and decreasing the severity of the instantaneous stresses on the yarns and filaments. Under this scenario, the very high pull-out resistance of the SiO₂-STF treatment is detrimental to overall penetration performance. This example underscores the important conclusion that a reduction in yarn mobility is not always beneficial; it is more likely that there exists an optimal degree of mobility for a given fabric and threat combination. The particle hardness, particle-to-fluid ratio, and coating-to-fabric ratio all provide means of tuning the performance of the coated fabric. This conclusion is supported by earlier numerical studies, which predicted that the ballistic resistance of a fabric would be highest at an optimal, intermediate yarn-yarn frictional value [144]. At this optimal value, fabric windowing is fully repressed, but enough slippage is permitted to reduce instantaneous stress concentrations in the vicinity of the impact.

On a more fundamental level, the results show that both frictional and viscous mechanisms may be relevant in these coated fabrics. For example, the behavior of the dry systems seems best described as a "frictional" effect, since no fluid is present. However, due to the very small size of the particles relative to the filament diameter and interstitial volumes, the dry coatings are more like a granular bed than a simple frictional coating [11]. Under this view, even the dry coatings will "flow" under deformation, and a simple surface friction model would be an incomplete representation of material behavior. Regarding viscous fluid effects, the yarn pull-out experiments in particular appear to show a strong effect due to the presence of the liquid carrier. It is particularly striking that the addition of PEG, without particles, leads to an increase in yarn pull-out resistance. It is not clear if this increase in resistance is due directly to viscous shear of the coating, or due to some indirect effect

such as reducing the ability of the yarns to compress to a cross-sectional shape that more easily accommodates yarn extraction.

While the results suggest that the rheological viscous coupling is certainly relevant, the specific role of the shear thickening rheology requires further investigation. The dramatic enhancement in yarn pull-out behavior for STF-treated fabrics relative to neat and dry particle treatments implies that the STF coatings do not simply behave as a linear combination of the constituents. Rather, the full rheological response of the STF fluids themselves must be considered. The strong shear thickening response for the STF fluids demonstrated in Figure 7.1 could lead to substantial load coupling between yarns and, hence, the extreme forces required for yarn pull-out. The detailed rheological response of PMMA-STF versus SiO₂-STF in Figure 7.1 could also be related to observed trends in their behaviors as coatings. The high shear rate shear thinning viscosity for the PMMA suspension is believed to be associated with particle deformations as seen in Chapter 6. These same particle deformations appear to also play a role in the reduced yarn pull-out force for these PMMA coatings.

One complicating factor in determining the role of STF rheology is that the extremely high surface area of the fabric could cause micro-scale segregation of fluid and particle phases. Since STF rheology is known to be highly sensitive to particle volume fraction, it is possible that the local composition and behavior of the coating varies relative to the original bulk STF properties. However, as noted above, the results cannot be explained by simply adding the properties of the PEG and dry particle treated samples, implying the presence of coupled physical effects. Furthermore, the physical appearance of the STF-treated fabrics shows none of the flaking and dustiness associated with the dry particle treated fabrics. These

observations suggest that particles are predominantly incorporated in the form of a colloidal dispersion and, given the compositions possible, that dispersion will exhibit shear thickening.

A second challenge in predicting in-situ rheological behavior is estimating stresses within the complex geometry of a woven fabric. The transitional behavior of an STF is fundamentally triggered by critical stress levels [15], rather than deformation rates, and these stresses are not limited to shearing [9, 154]. For example, it is possible that compression in a highly confined geometry can lead to high local stresses that induce STF transition. We can estimate characteristic stress levels for each of our experiments to determine the likelihood of a shear-thickening response.

As a first estimate, the characteristic stress for yarn pull-out is calculated as follows. Under the assumption that the yarn is pulled-out and fluid shear stress between the yarn and cross-yarns dominates over shear between adjacent yarns, the shear stress is the pull-out force normalized by the yarn-yarn sliding contact area. The geometry, ignoring the effects of yarn crimp, is shown in Figure 7.13. The value of the peak force from the PMMA-STF pull-out experiment, 46.7 N, is taken as a representative case. The normalization area for the shear stress is equal to the width of a yarn (determined from the 34 yarns per inch specification) multiplied by the intact woven length of the fabric, 5.08 cm:

$$\text{Area} = \left(\frac{1 \text{ inch}}{34 \text{ yarns}} \cdot \frac{0.0254 \text{ m}}{1 \text{ inch}} \right) \times 0.0508 \text{ m} = 3.8 \times 10^{-5} \text{ m}^2. \quad (7.1)$$

The stress is the peak force normalized by the area:

$$\text{Stress} = \frac{46.7 \text{ N}}{3.8 \times 10^{-5} \text{ m}^2} = 1.2 \times 10^6 \text{ Pa}. \quad (7.2)$$

This stress of 10^6 Pa is many orders-of-magnitude higher than the critical stress for shear thickening in these systems.

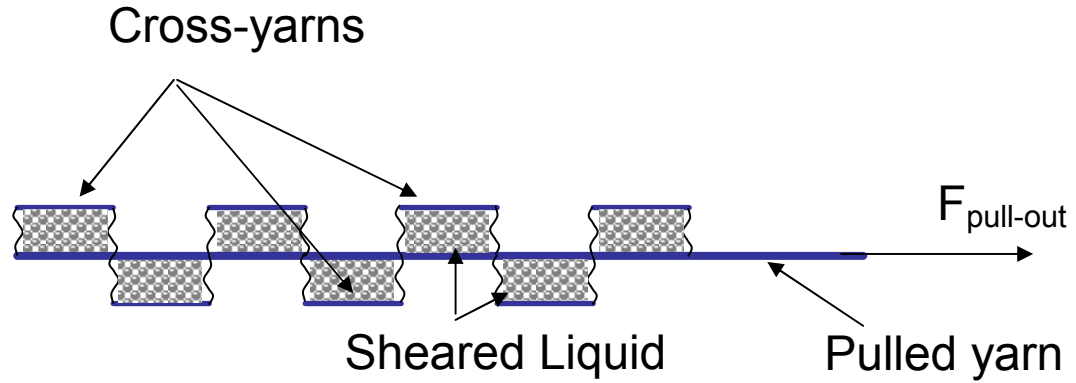


Figure 7.13 Diagram of shear stress calculations from pull-out experiment.

For the spike puncture experiment, an estimate of the compressional stress is the force normalized by the spike tip cross sectional area. From the NIJ Standard [68], the spike tip is 0.175" long and 0.075" wide at the base, giving a cone surface area of

$$\text{Area} = \pi \left(\frac{0.075 \text{ inch}}{2} \right) \times \sqrt{0.175^2 + \left(\frac{0.075}{2} \right)^2} \times \left(\frac{0.0254 \text{ m}}{1 \text{ inch}} \right)^2 = 1.4 \times 10^{-5} \text{ m}^2 \quad (7.3)$$

which would be the largest relevant area to normalize the force over, giving the most conservative estimate for stress. Using the peak force from spike puncture from PMMA-STF, 58.1N, as a representative value, an estimate of the stress is

$$\text{Stress} = \frac{58.1 \text{ N}}{1.4 \times 10^{-5} \text{ m}} = 4.1 \times 10^6 \text{ Pa} . \quad (7.4)$$

This stress of 10^6 Pa is also significantly greater than the critical stress for shear thickening in these systems.

For the ballistic experiments, the compressive stress on the fabric can be estimated by normalizing the deceleration force by the projectile area. This force is estimated by assuming that the projectile decelerates over one projectile length and that the deceleration force acts over an area equal to the cross-sectional area of the projectile. For a 5.59 mm diameter projectile with a mass of 0.692 g, at the V_{50} of PMMA-STF-Kevlar of 136 m/s, the projectile deceleration force can be written as

$$\text{Force} = \text{mass} \cdot \text{acc} = \text{mass} \frac{v^2}{2x} = 0.692 \times 10^{-3} \text{ kg} \cdot \frac{(136 \text{ m/s})^2}{2 \cdot (5.59 \times 10^{-3} \text{ m})} = 1140 \text{ N} . \quad (7.5)$$

The resulting deceleration stress can then be calculated as the force normalized by the projectile cross-sectional area:

$$\text{Stress} = \frac{1140 \text{ N}}{(1/4) \pi (5.59 \times 10^{-3} \text{ m})^2} = 46 \times 10^6 \text{ Pa} . \quad (7.6)$$

This stress of $\sim 10^7$ Pa is also significantly greater than the critical stress for shear thickening in these systems and an order of magnitude higher than the characteristic stresses estimated for either yarn pull out or puncture testing.

In summary, the estimate for the characteristic stress in each test is many orders of magnitude above the STF transitional stress measured in a rheometer. Therefore, the stresses encountered by the STFs intercalated in the small gaps between the fibers are likely to be sufficient to trigger shear thickening in all the tests performed on STF-fabrics. Future studies could search for signatures of shear thickening behavior in STF-fabrics by conducting puncture and pull-out experiments at varying loading rates.

Note that the experiments in this study included only single-layer, unbacked fabrics. While we expect many of these results to be broadly applicable, further testing is required to determine whether these conclusions apply to the performance of multilayer targets or unclamped targets on soft substrates.

On a practical level, and perhaps most importantly, there appears to be a major benefit to the liquid carrier in terms of handling and coating durability. The fabrics intercalated with dry particles tend to shed particles on most surfaces that they touch and even into free space if they are handled roughly. This behavior is not surprising, as there is no obvious binding force to keep the particles in contact with the fabric. In addition to dangers associated with nanoparticle emission into the environment, this shedding of particles suggests poor long-term durability of these coated fabrics. Their generally blotchy and non-uniform appearances also suggest the potential for inconsistent point-to-point behavior. In contrast, the particle-intercalated fabrics with liquid carriers look uniform and can be handled roughly and directly with little evidence of coating loss or transfer. This behavior suggests that the liquid carrier entrains the particles within the fabric through a capillary or wetting mechanism. From this practical viewpoint, the STF treatments appear to result in more durable and robust coatings, while providing puncture and pull-out performance comparable to or better than dry particle coatings. The presence of the liquid carrier also provides opportunity for incorporation of secondary functionalities, such as hydrophobicity or antimicrobial action.

7.5 Conclusions

The results of this chapter show that particle intercalation is an effective means to significantly modify the behavior of woven fabrics, primarily through a

decrease in yarn and fiber mobility. Harder particles tend to result in a greater reduction in mobility than softer particles, as they are more likely to mechanically engage filaments and less likely to accommodate stress via particle deformation. In addition, the inclusion of a liquid carrier with the intercalated particles tends to further restrict mobility, while dramatically improving the robustness and practicality of the coating. The results also show that, for some fabric performance metrics, a tuned level of mobility may be preferable to engineering extreme levels of restricted mobility. The estimates of the characteristic stresses and the results shown in this chapter demonstrate that studies of STF behavior at stresses and shear rates much greater than those accessible in a typical laboratory rheometer may be of additional value in understanding and tuning STF-fabric performance for specific applications. These studies complement the work investigating the role of particle hardness on the rheological properties of STFs in the prior chapter.

Chapter 8

CONCLUSIONS

The goal of this dissertation was to utilize novel microstructure measurements to provide insight into the structural changes that drive varied rheology in concentrated, colloidal suspensions. As mentioned previously, prior work has not been able to measure the structure via SANS directly in the shear plane, which is necessary for quantifying the structural changes that drive the shear thinning. In addition, prior work was limited to particle radii below 100 nm to measure microstructure. This thesis extends the prior experimental microstructure measurements by measuring directly in the shear plane, and extending measurements to suspensions of particles of 260 nm radius. In addition, improved microstructural understanding from these experiments led to development of a new model to describe the rheological behavior at high stresses within a hydrocluster. Finally, the use of these suspensions as treatments for Kevlar based woven fabric armor was also explored.

Chapter 3 shows the characterization of a series of chemically analogous, near hard-sphere, colloidal suspensions. SANS and USANS under static conditions indicate that these suspensions have non-hard-sphere interactions requiring an additional excluded volume shell of 5.6% of the radius. Rheological experiments confirm that these suspensions behave as near hard-spheres with this excluded volume as the shear thinning portion of the rheology fits the Cross model with parameters expected for hard-spheres. In addition, changing the solvent to the mixture used in SANS experiments did not appreciably affect the rheology.

Shear thickening was observed rheologically for a wide range of volume fractions, with increasing severity of thickening with increasing volume fraction. In addition, the scaling of the critical stress with particle size follows a particle size squared relationship and is exponential with respect to volume fraction. In addition, first normal stress differences were measured for some suspensions – the measured values under shear were negative and decreased in intensity with increasing shear rate, consistent with expectations from simulations. There have been only very limited experimental measurements of the first normal stress difference for Brownian near hard-sphere suspensions in the past.

Following full characterization of the rheology and equilibrium properties of these Brownian, near hard-sphere suspensions, Chapters 4 and 5 characterize the flow-induced microstructural changes. In Chapter 4, the structure of suspensions of the smaller (60 nm) particles characterized in Chapter 3 were examined via SANS in two planes of shear. The measurements in the 1-2 or flow-gradient plane of shear are the first measurements of their kind on suspensions and provide unique insight into the structure under shear. Qualitatively, the microstructure anisotropy matches that expected from Stokesian dynamics simulations and recent particle tracking microscopy experiments. In addition, the data provides evidence of clustering driving shear thickening.

A stress-SANS law from micromechanics theory provides the ability to convert structural measurements to relevant rheological parameters – both the thermodynamic and hydrodynamic components of the viscosity and normal stresses. The thermodynamic component of the viscosity is seen to show power law shear thinning, consistent with the rheology of the most concentrated suspensions. The

hydrodynamic component of the viscosity is seen to rise with increasing shear rate, consistent with the theory of hydrodynamically forced clustering driving shear thickening. Comparisons of the hydrodynamic component of the viscosity and the relevant harmonics between the two planes of shear confirm the use of the 1-2 plane geometry. Calculations of the first normal stress difference from SANS are compared to measured normal stresses for the first time and show excellent agreement.

Increased nearest neighbor scattered intensity with increasing shear rate, correlated to a rise in the hydrodynamic component of the viscosity, is measured for all near hard-sphere suspensions. Similar particles with a sticky hard-sphere interaction caused by a dense polymer coating show a decrease in this hydrodynamic viscosity at high shear rates. This result is consistent with the suppression of rheological shear thickening for this suspension and provides additional evidence that the hydroclusters drive thickening. For this sample, the polymer coating suppresses both the clustering and the thickening.

Structural changes, which are believed from theory and simulations to drive shear thickening, arise from increased particle correlations on the nearest neighbor length scale; these changes yield a subtle sharpening of the radial distribution at contact which can have significant effects on the rheology [24]. Increased nearest neighbor scattering was seen in the SANS measurements performed here, but the stress-SANS law is unable to account for the order of magnitude effects on the rheology. These large changes in rheological behavior can be caused by only small changes in the structure, represented by small changes in the scattering over a small length scale. The order of magnitude increase in the viscosity at high shear clearly can not be driven by a commensurate structural change which causes an order of

magnitude change in the scattered intensity. These large rheological changes can be driven by small structural changes through lubrication hydrodynamics, but this effect is not accurately captured by the simplified stress-SANS law. As such, while the SANS experiments and Stokesian dynamics simulations measure clustering, anisotropy, and shear thickening, they do not predict these order of magnitude changes in the viscosity. The nature of the divergence in viscosity seen in discontinuous and nearly discontinuous shear thickening still remains an important question for future research.

Ultra-small angle neutron scattering under shear flow was used to extend the measurements on suspensions via radial SANS to larger, 260 nm radius particles in Chapter 4. These experiments yield the new observation of cluster peaks seen via USANS, which are consistent with those seen via SANS and confirm the same hydroclustered structure drives the rheology of these larger particle suspensions. Due to the USANS measurement technique lacking the ability to measure structural anisotropy and due to the instrument smearing, the USANS results are limited and do not provide significant quantitative insight into the structure of concentrated suspensions. Using the SANS knowledge of the scattering anisotropy with the USANS measurements allows for a more accurate comparison of the peak locations between the two different measurements; with this insight, these results are consistent between the techniques on the chemically analogous suspensions of two different particle sizes.

Utilization of the insight on the microstructure within a hydrocluster allowed for development of an elastohydrodynamic model for particle elastic deformations within a hydrocluster that cause a second regime of shear thinning at stresses beyond the thickened state. Comparison of the model, combined with modulus

measurements via AFM nano-indentation, to the rheological data showed remarkable agreement. Further comparison of the model to literature suspensions of widely varying particle hardness from very hard mineral particles, to polymer particles which are typically considered non-deformable, to easily deformable microgel particles and liquid-liquid emulsions provided consistent insight into the high shear behavior of these suspensions. If we compare these suspensions to each other, with decreasing particle hardness the shear thickening was diminished, the peak viscosity in the thickened state decreased, and the second shear thinning regime became more prominent. In fact, shear thickening is completely suppressed if the particles become soft enough, as was seen in the microgel suspensions and emulsions. The microgel suspensions shear thickened only for the hardest particles and showed shear thinning over the entire shear rate range for the softer particles. Emulsions stabilized by particles shear thicken, whereas emulsion droplets stabilized by surfactants, which are particles with a more deformable interface, did not thicken. Deformation of the particles provides an additional mechanism for stress relief in flowing suspensions, not typically considered in the Stokesian dynamics simulations referenced earlier.

Finally, the use of these suspensions and the effects of particle hardness on the woven fabric composite armor performance were explored in Chapter 7. In particular, particle hardness was seen to play a key role in the lowering of yarn mobility to improve composite performance. In addition, since the shear thickening fluid suspension treatment provided significantly improved performance over the increase in performance from the dry particle treatment and little improvement was seen for the carrier fluid treated fabric, a synergistic effect provided by rheological coupling was observed. While shear thickening was not directly implicated in the

improved performance, estimates of the characteristic shear stress indicate that the fluid between yarns during a pull-out, stab, or ballistic experiment is at stresses well beyond measured shear thickening in rheometric experiments. Changing the particle hardness allows for tuning the yarn mobility, which could allow for a maximized level of performance as the ideal composite requires some level of yarn mobility to extend the interaction time between a threat and the composite.

These conclusions lead to some interesting areas for potential future work. The goal of these experiments was to provide additional insight into the structure-property relationships for concentrated, colloidal suspensions for use in various applications. The application explored here was woven fabric armor, which clearly benefitted from the addition of the colloidal suspension. Despite the measured improvement, it is not clear whether the suspension rheology truly controls this particular application. Regardless, many other applications, particularly in sandwich structure composites, will utilize shear thickening fluids for their tunable damping properties. Ability to predict and control rheological behavior will be paramount to rational design of these materials.

For the woven fabric composites shown here, clearly the characteristic stresses that the fluid undergoes during a stab or ballistic event are much higher than those achieved in the rheometer. Additional testing pushing the ability to measure the rheological behavior at higher applied stresses and shear rates will lead to improved understanding of the in-fabric behavior of these materials. Additionally, pushing the rheological testing of these materials to higher stresses and rates will allow for better testing of the elastohydrodynamic model proposed in Chapter 6.

Finally, the SANS and USANS measurements here were developed and applied on model colloidal suspensions. These should be considered novel techniques rather than merely new experiments, as these techniques to understand how colloidal interactions control the rheology of concentrated suspensions through the microstructure can be applied to many different materials with varying interparticle interactions. Some additional recent work has investigated the sticky sphere suspensions similar to some also presented in this thesis utilizing the 1-2 plane shear cell and can benefit from the method of analysis developed in this thesis.

Appendix A

NOMENCLATURE

Symbol	SI Units	Definition
a	[m]	Particle radius
A	[m ²]	Area of indentation (AFM)
A_1		First coefficient for critical stress correlation
A_2		Second coefficient for critical stress correlation
$A_{l,m}$		Spherical harmonic coefficients
A_{coating}		Particle surface coating weight fraction (TGA)
B	[m ⁻¹]	Incoherent background scattering intensity
B_{base}		Weight fraction lost in TGA experiment by uncoated particles
B_{coated}		Weight fraction lost in TGA experiment by coated particles
$[B_{l,m}^+(q)]$		Spherical harmonic coefficients in Cartesian coordinates
C_{hydro}	[N m ⁻² s]	Stress-SANS law coefficient for hydrodynamic viscosity
C_{thermo}	[N m ⁻² s]	Stress-SANS law coefficient for thermodynamic viscosity
C_1		Coefficient for suspension viscosity correlation (1st order)
C_2		Coefficient for suspension viscosity correlation (2nd order)
C_{EH}		Elastohydrodynamic prefactor
C_N		Configuration of all particles
D_0	[m ² s ⁻¹]	diffusion coefficient
ΔW_{empty}		Weight change in empty TGA crucible during experiment
E	[N m ⁻²]	Young's modulus
F_{indent}	[N]	Indentation force (AFM)

F_{tip}	[N]	Measured tip force in indentation experiment (AFM)
F_{contact}	[N]	Measured tip force at contact in indentation experiment (AFM)
F_z	[N]	Measured normal force under shear
$F_{z,0}$	[N]	Measured normal force at rest
G'	[N m ⁻²]	Elastic (storage) modulus
G''	[N m ⁻²]	Viscous (loss) modulus
$g(r)$		Radial distribution function
G_0	[N m ⁻²]	Particle shear modulus
G''_{min}	[N m ⁻²]	Minimum in G''
G_P	[N m ⁻²]	Particle elastic modulus
G'_{plateau}	[N m ⁻²]	Plateau (storage) modulus
H	[m]	Rheometer plate separation distance
h	[m]	Interparticle separation distance
$\hat{h}(q)$		Particle correlation function (spherical harmonics)
$\tilde{h}(q)$		Particle correlation function (Cartesian coordinates)
$I(q)$	[m ⁻¹]	Scattered neutron intensity
I_s	[m ⁻¹]	Instrument smeared scattered neutron intensity
I_{static}	[m ⁻¹]	Scattered neutron intensity under static conditions
I_{shear}	[m ⁻¹]	Scattered neutron intensity under shear
k_b	[m ² kg s ⁻² K ⁻¹]	Boltzmann's constant
K_h		Huggins Coefficient
l_b	[m]	Bjerrum length
l_{slip}	[m]	Rheometric slip length
m		Shear-thinning exponent (Cross model)
M	[N m]	Rheometer torque
N_1	[N m ⁻²]	First normal stress difference
N_2	[N m ⁻²]	Second normal stress difference
$P(q)$		Static form factor
$\overline{P(q,a,\sigma)}$		Particle form factor for polydisperse spheres
Pe		Péclet number (dimensionless shear rate)

p		Yield stress correlation exponent
q	$[m^{-1}]$	Scattering vector magnitude
\mathbf{q}	$[m^{-1}]$	Scattering vector
q_c^*	$[m^{-1}]$	Wave vector location of intercluster separation peak
q_m^*	$[m^{-1}]$	Wave vector location of interparticle separation peak
q_{peak}	$[m^{-1}]$	Wave vector location of cluster peak
q_x	$[m^{-1}]$	Scattering vector in the flow direction
q_y	$[m^{-1}]$	Scattering vector in the vorticity direction
q_z	$[m^{-1}]$	Scattering vector in the velocity gradient direction
R	$[m]$	Rheometer tool radius
R_h	$[m]$	Hydrodynamic radius
S	$[N\ m^{-3}]$	Stiffness from AFM measurement
$S(q)$		Static structure factor
$S_{eff}(q)$		Effective (measured) structure factor
$S_{eq}(q)$		Equilibrium (measured) structure factor
T	$[K]$	Temperature
t	$[m]$	Particle shell thickness
t_0	$[m]$	Shell thickness from Cross model zero shear viscosity
t_∞	$[m]$	Shell thickness from Cross model infinite shear viscosity
T_{rock}		Neutron transmission in the center of rocking curve (USANS)
T_{wide}		Neutron transmission at wide angles (USANS)
$W_{n,direction}$		Integration of n-fold symmetry in SANS spectra
$W_{2,1}$		Integration of cos-sin symmetry in SANS spectra (1-2 plane)
V_{50}	$[m\ s^{-1}]$	Velocity at which a projectile has a 50% chance of penetration
V_p	$[m^3]$	Volume of scattering object
\mathbf{v}		Flow velocity (direction)
v_{slip}	$[m\ s^{-1}]$	Rheometric slip velocity
Y		Yield stress correlation pre-factor
$Y_{l,m}$		Spherical harmonic irreducible tensor components
z	$[m]$	AFM stage vertical location

z_{indent}	[m]	Indentation depth (AFM)
$\alpha, \beta, \zeta_0, \zeta_2 (q)$		Spherical harmonic hydrodynamic functions
β		Adjustment parameter (AFM indentation)
Δh_{tip}	[m]	Tip deflection distance in indentation experiment (AFM)
$\Delta \lambda$	[m]	Neutron wavelength spread
Δq_v	[m ⁻¹]	Vertical scattering vector resolution (USANS)
$\Delta \rho$	[m ⁻²]	Neutron scattering contrast
ϕ		Volume fraction (calculated from density and weight fractions)
ϕ_{eff}		Effective volume fraction assuming proportional surface layer.
$\phi_{\text{eff,alt}}$		Effective volume fraction assuming constant surface layer.
$\phi_{\text{eff},0}$		Effective volume fraction from Cross model zero shear viscosity
$\phi_{\text{eff,inf}}$		Effective volume fraction from Cross model infinite shear viscosity
ϕ_m		Maximum packing volume fraction
$\phi_{v,\text{min}}$		Minimum effective volume fraction for yield stress
η	[N m ⁻² s]	Measured viscosity
η_0	[N m ⁻² s]	Zero-shear viscosity
η_∞	[N m ⁻² s]	Infinite-shear viscosity
η_{crit}	[N m ⁻² s]	Critical viscosity at the onset of shear thickening
η_{EH}	[N m ⁻² s]	Elastohydrodynamic limiting viscosity
η_r		Reduced viscosity
$\eta_{r,0}$		Reduced zero-shear viscosity
$\eta_{r,\infty}$		Reduced infinite-shear viscosity
$\eta_{r,\text{inf}}$		Reduced infinite-shear viscosity
$\eta_{r,0}^{\text{HS}}$		Reduced zero-shear viscosity expected for hard-spheres
$\eta_{\text{Hydro, equil}}$		Equilibrium hydrodynamic viscosity
κ	[m ⁻¹]	Inverse Debye-Hückel screening length
λ	[m]	Neutron wavelength
μ_s	[N m ⁻² s]	Solvent viscosity

ν		Poisson's ratio
ρ	$[\text{kg m}^{-3}]$	Mass density
$\rho(\text{SLD})$	$[\text{m}^{-2}]$	Neutron scattering length density
ρ_{HD}	$[\text{kg m}^{-3}]$	Particle hydrodynamic density
ρ_{num}		Particle number density
ρ_{particle}	$[\text{kg m}^{-3}]$	Particle density
ρ_{solvent}	$[\text{kg m}^{-3}]$	Solvent density
$\rho_{\text{suspension}}$	$[\text{kg m}^{-3}]$	Suspension density
θ		Scattering angle in flow-gradient plane
θ_{rad}		Scattering angle in flow-vorticity plane
$\theta^*(q)$		Thermodynamic stress integral (spherical harmonics)
σ	$[\text{N m}^{-2}]$	Interparticle stress
τ	$[\text{N m}^{-2}]$	Shear stress
τ_{b}		Baxter sticky parameter
τ_{crit}	$[\text{N m}^{-2}]$	Critical stress for shear thickening
τ_{Cross}		Cross-model critical stress (reduced)
τ_{hydro}	$[\text{N m}^{-2}]$	Hydrodynamic shear stress
τ_{R}	$[\text{N m}^{-2}]$	Rim shear stress
τ_{r}		Reduced shear stress
$\tau_{\text{r,yield}}$		Reduced yield stress
τ_{thermo}	$[\text{N m}^{-2}]$	Thermodynamic shear stress
τ_{yield}	$[\text{N m}^{-2}]$	Yield stress
Ω	$[\text{s}^{-1}]$	Rheometer cone angular velocity
Ψ_1		First normal stress difference coefficient
Ψ_2		Second normal stress difference coefficient
Ψ_{s}		Surface potential
$\dot{\gamma}$	$[\text{s}^{-1}]$	Measured shear rate
$\dot{\gamma}_{\text{apparent}}$	$[\text{s}^{-1}]$	Apparent shear rate
$\dot{\gamma}_{\text{crit}}$	$[\text{s}^{-1}]$	Critical shear rate for shear thickening
$\dot{\gamma}_{\text{true}}$	$[\text{s}^{-1}]$	True shear rate

Appendix B

ANALYSIS OF RHEOLOGICAL SLIP

Measurement of rheological slip was done by varying the gap in a parallel plate geometry, using the method of Yoshimura and Prudhomme [58] described in section 2.4.4. Additionally, but not shown, multiple samples of each type in the steady-shear measurements were done with at least two tools to ensure consistency between various tool geometries. Figure B.1 shows the apparent viscosity versus shear stress data for various plate gaps for a Newtonian viscosity standard (Cannon S8000). The apparent viscosity decreases with decreases in the tool gap – the lowest values are seen for the smallest tool gap. Analysis by the above method yields the values of the true shear rate and slip velocity versus reciprocal gap height seen in Figure B.2, with a slip velocity on the order of 10^{-6} m/s and a true shear rate of 0.433 s^{-1} at a rim shear stress, τ_R , of 10 Pa. Dividing the rim shear stress by the true shear rate gives a viscosity of 23.1 Pa-s, within 10% of the standard value and consistent with expectations.

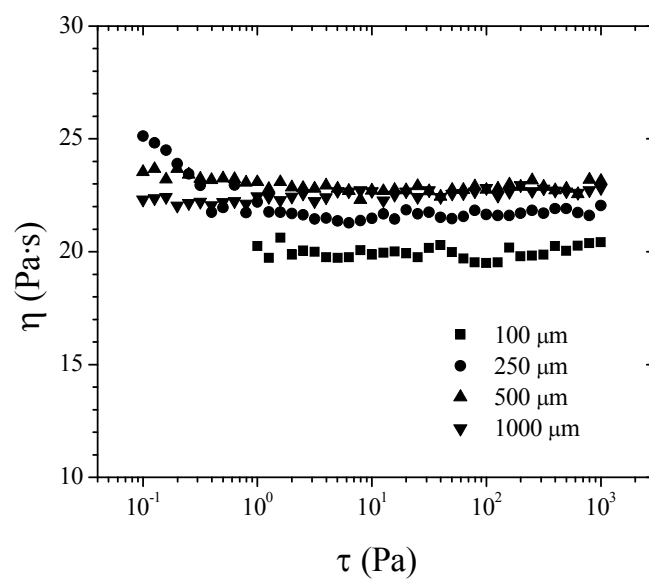


Figure B.1 Apparent viscosity measurements of a certified viscosity standard, Cannon S8000, used to validate slip measurements. The certified viscosity value is 21.355 Pa·s at 25°C.

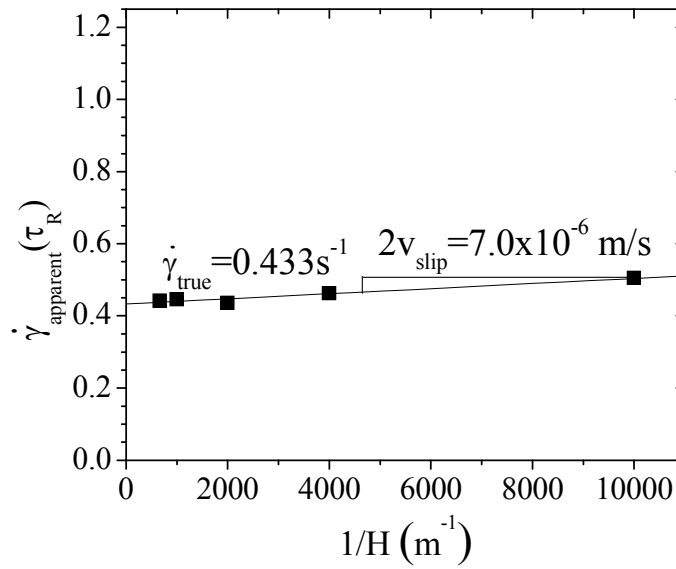


Figure B.2 Apparent shear rate versus reciprocal gap height for S8000 viscosity standard at a constant value of $\tau_R=10$ Pa yield the slip velocity and true shear rate.

Figure B.3 shows the apparent viscosity versus shear stress for the 60 nm silica dispersions in the solvent mixture of 30% PEG-600 and 70% ethylene glycol at $\phi=0.521$ measured at different gap heights. Decreasing the gap height is seen to consistently shift the apparent viscosity versus stress curve to lower viscosities, a total of almost one order of magnitude for a change in the gap from 2000 μm to 50 μm . Despite the order of magnitude change in the viscosity, the critical stress for shear thickening only changes from about 300 to 400 Pa with the same change in gap thickness. Thus, we confirm that the critical stress is relatively independent of gap thickness, as previously reported by Maranzano [59]. This behavior is indicative of the shear thickening being controlled by applied shear stress rather than shear rate.

Figure B.4 shows the slip analysis for the rheology data seen in Figure B.3 – specifically the apparent shear rate versus rim reciprocal gap height at various values

of the rim shear stress. The data at low gaps or high reciprocal gap heights show different behavior than those at high gaps, likely due to the influence of specific particles within the gap as the gap is less than 100 particle diameters. The data at the largest values of gap were not included in this slip analysis due to hysteresis in the measurements. The slope and intercept were determined from only the points at 500 and 250 μm gap. These calculations yield the values of the true shear rate and slip velocity seen in Figure B.5, and the slip lengths seen in Figure B.6. The slip length is seen to be about 15-25 μm at stresses in the shear-thinning regime, and 2-7 μm in the shear-thickened state.

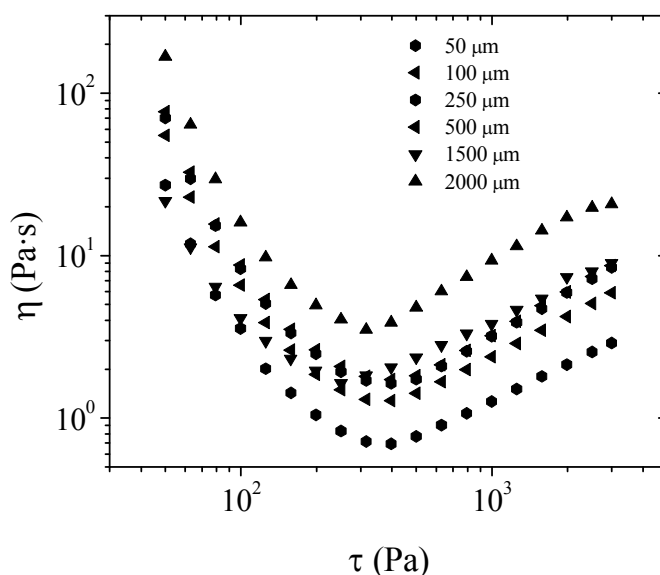


Figure B.3 Apparent viscosity versus applied stress for 60 nm silica dispersions at $\phi=0.521$ in solvent mixture of PEG-600 and ethylene glycol (70% ethylene glycol by weight). Measurements are at various gap heights in parallel plate geometry. Data shown are sweeps at increasing stress.

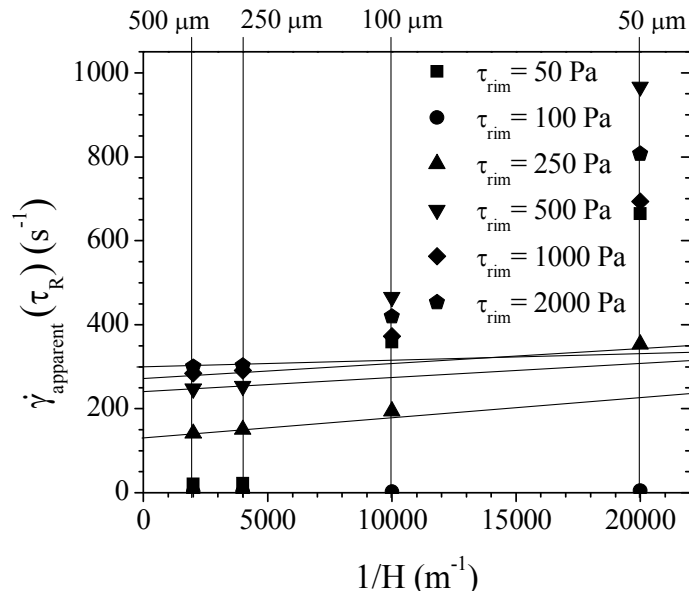


Figure B.4 Apparent shear rate at various values of the rim shear stress, plotted against reciprocal gap height for 60 nm silica dispersions at $\phi=0.521$ in solvent mixture of PEG-600 and ethylene glycol. Lines indicate slope and intercept calculated from the two points with the highest gap.

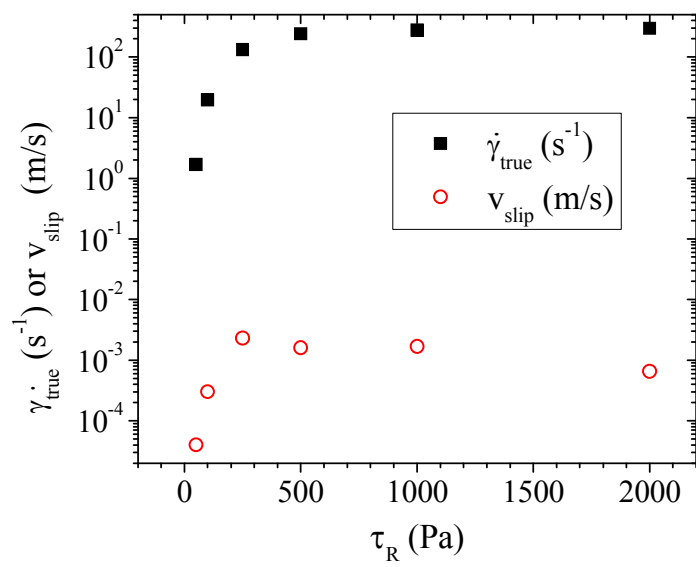


Figure B.5 True shear rate and slip velocity for 60 nm silica suspension in PEG-200 at various rim shear stresses.

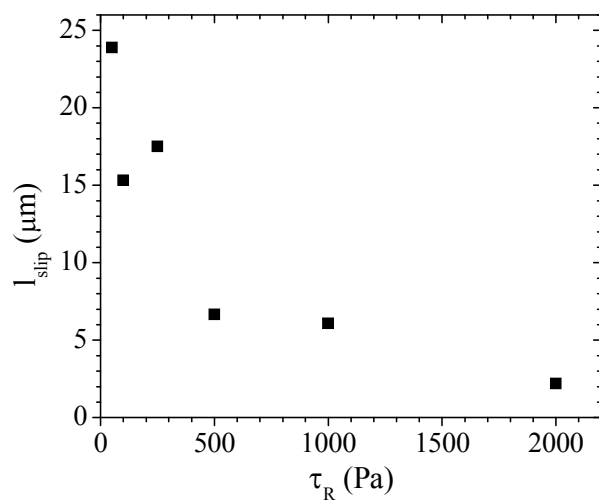


Figure B.6 Slip lengths as a function of rim shear stress.

Appendix C

EVALUATION OF STRUCTURE HOMOGENEITY ACROSS THE GAP VIA 1-2 PLANE FLOW-SANS

SANS experiments in the 1-2 plane of shear were also done with a smaller slit (0.1 mm) to collimate the beam and allow for resolution within the gap. Three locations within the gap were studied: near the inner rotating wall, in the center of the gap, and near the outer rotating wall. The steady shear rheology of the sample measured is shown as Figure C.1.

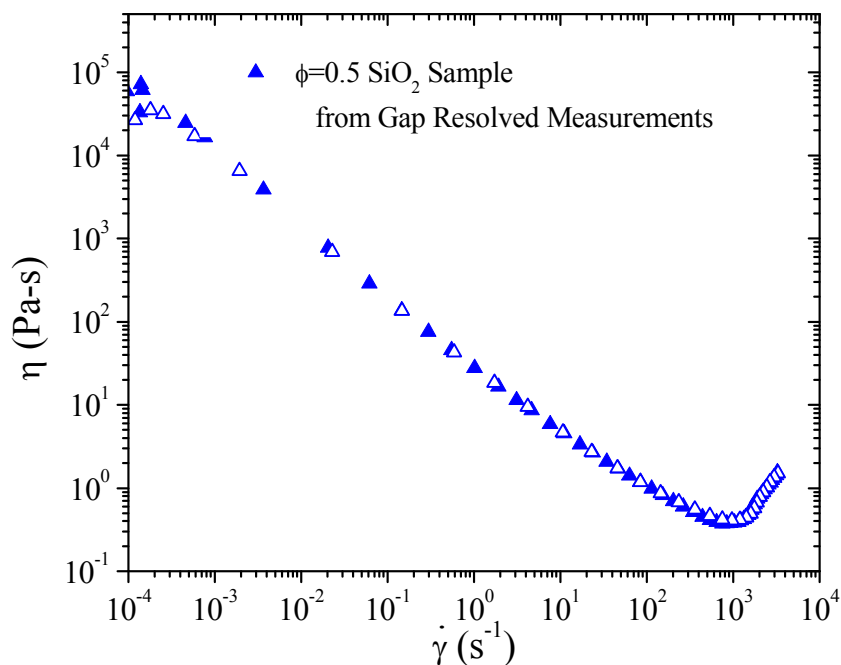


Figure C.1 Steady-shear rheology of $\phi=0.5$ SiO_2 sample tested in gap-resolved 1-2 plane flow-SANS experiments.

Figure C.2 shows the scattering results from the gap-resolved experiments. The center row shows the SANS spectra in the center of the gap. The top and bottom rows show the subtraction of the spectra in the center of the gap from that near the outer, fixed wall and the inner moving wall, respectively. Some small changes in the scattering are seen within the nearest neighbor ring. These differences are on the order of 10% of the intensity of the scattering in the nearest neighbor ring. In addition, they appear to be random fluctuations rather than having any systematic structure. There is no change in the difference spectra with shear rate, either. Therefore, there appears to be no significant or systematic change with gap position, at least for this data taken at shear rates in the shear-thinning regime of the rheology.

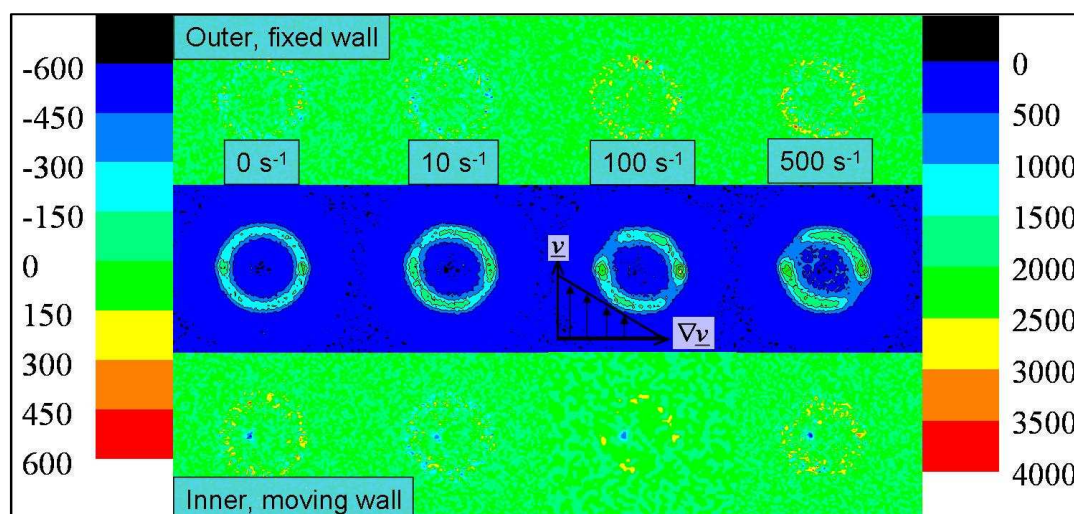


Figure C.2 Gap-resolved 1-2 plane Flow-SANS of concentrated suspensions at $\phi=0.50$. The top and bottom rows show subtraction of middle of gap SANS data from data near inner and outer cylinder, respectively (legend on left). The middle row is SANS spectra at middle of gap (legend on right).

Appendix D

ADDITIONAL PICTURES AND MICROGRAPHS OF FABRIC COMPOSITES

In this appendix, additional pictures and scanning electron micrographs of fabrics from experiments described in Chapter 7 will be presented.

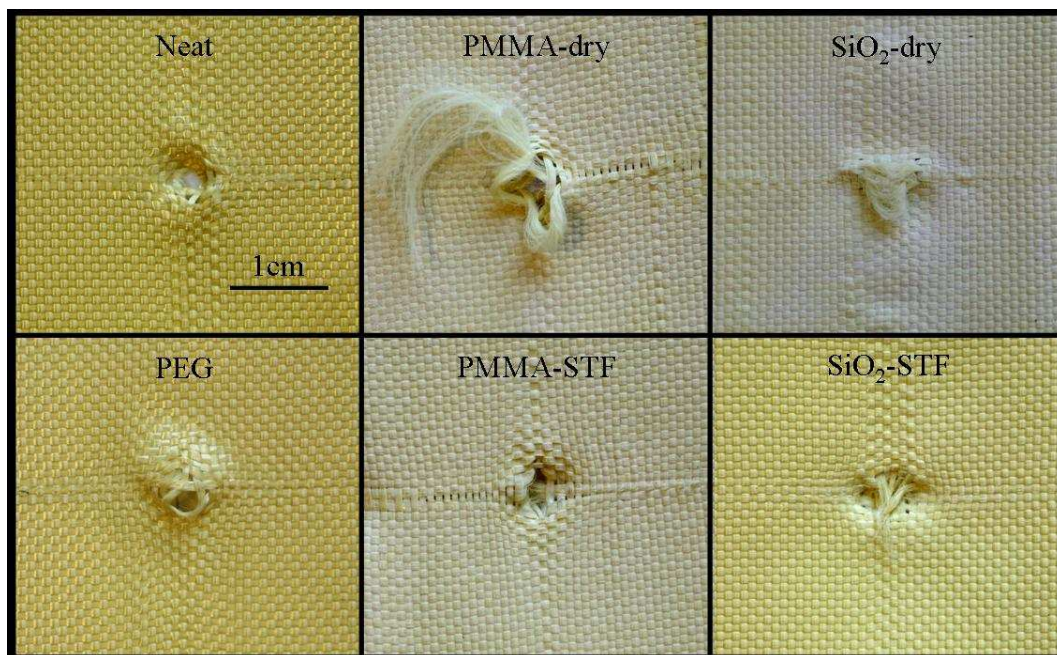


Figure D.1 Additional fabric photos from ballistic testing.

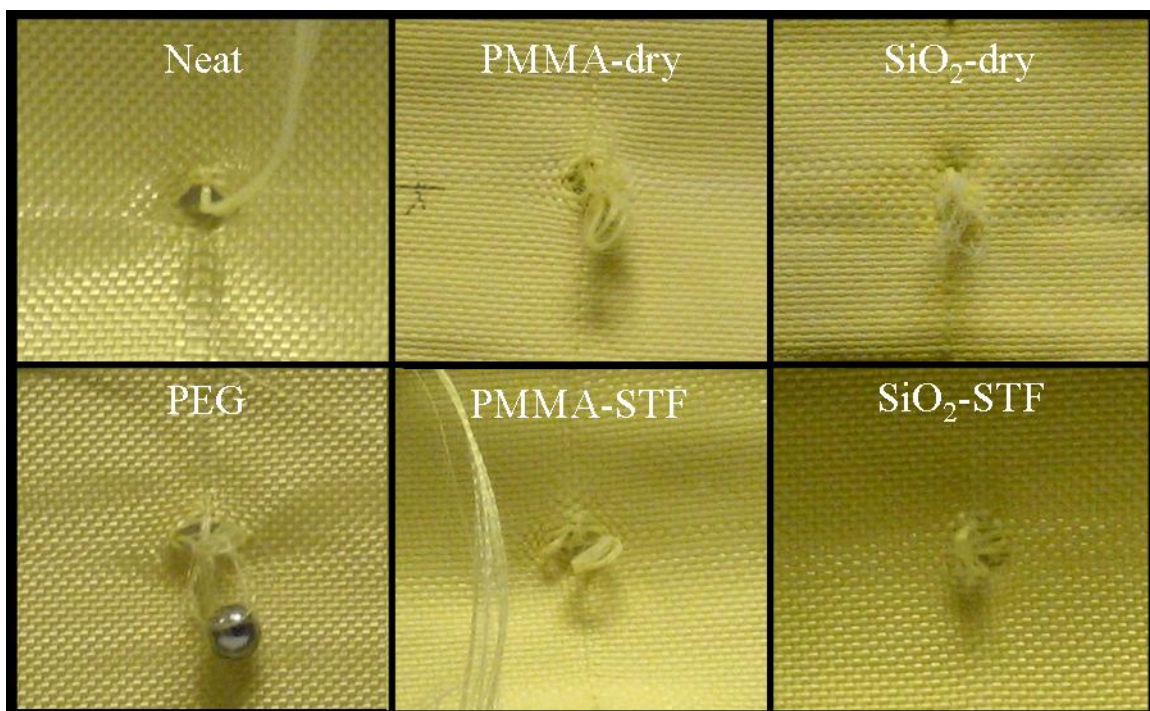


Figure D.2 Additional fabric photos from ballistic testing.

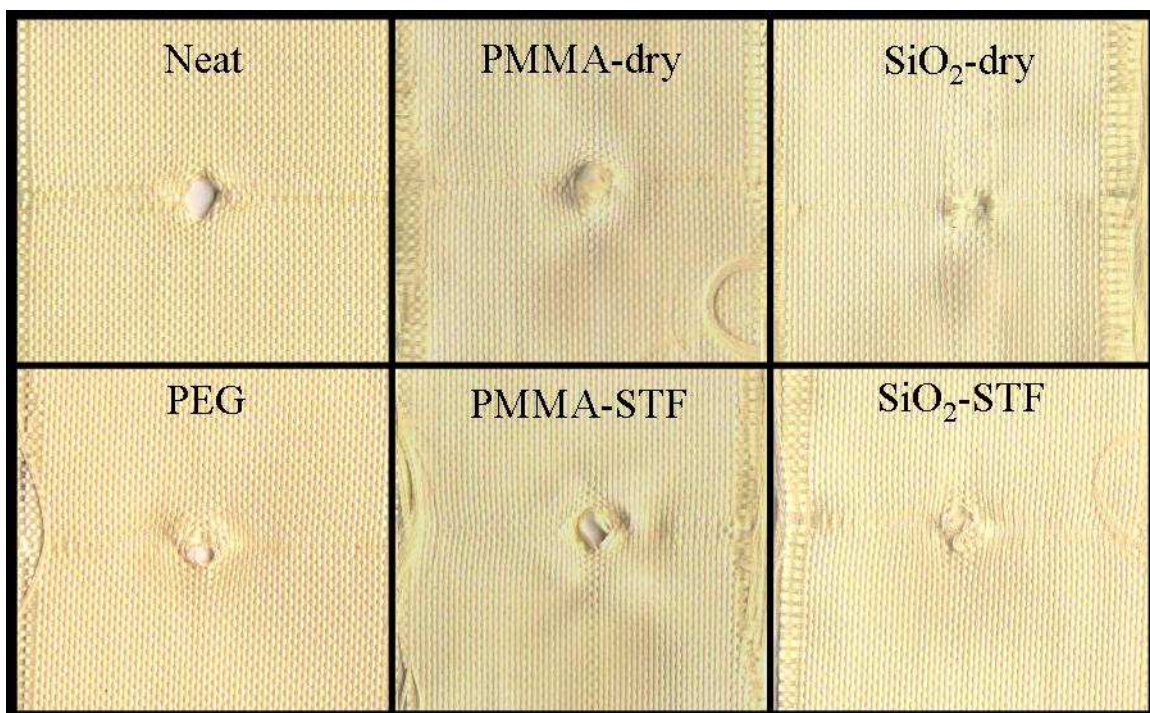


Figure D.3 Additional fabric photos from ballistic testing.

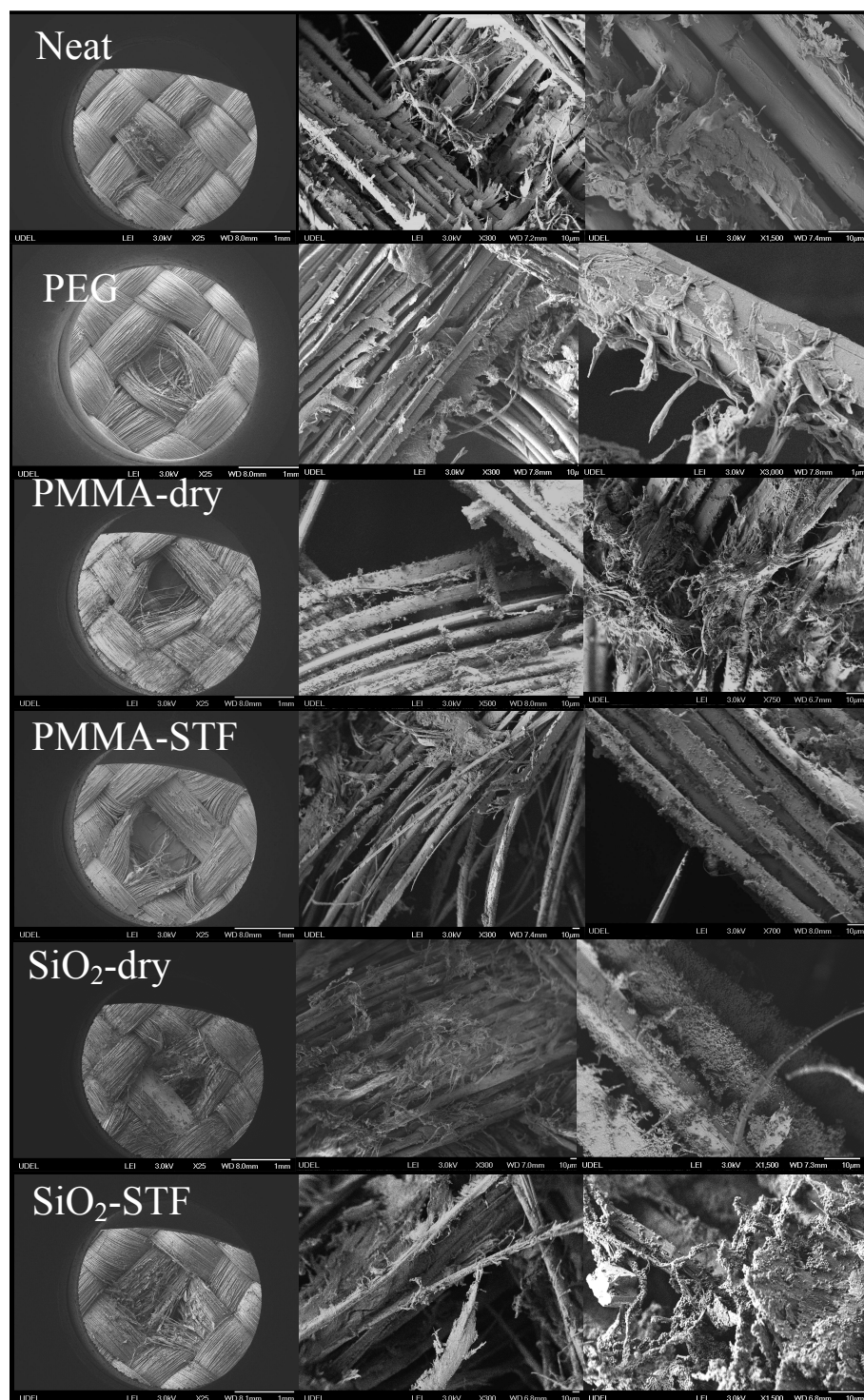


Figure D.4 Additional fabric scanning electron micrographs from spike testing.

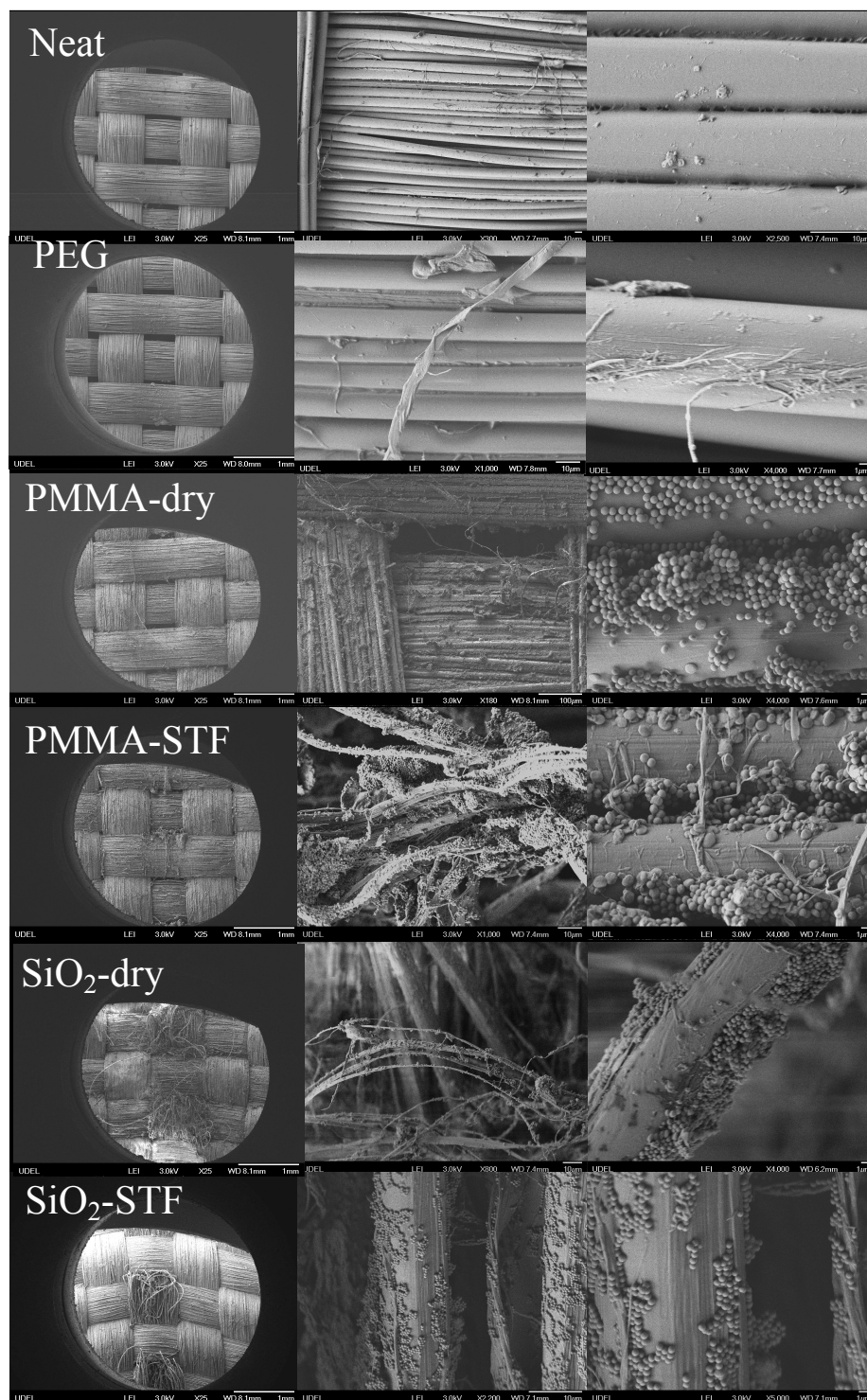


Figure D.5 Additional fabric scanning electron micrographs from yarn pull out testing.

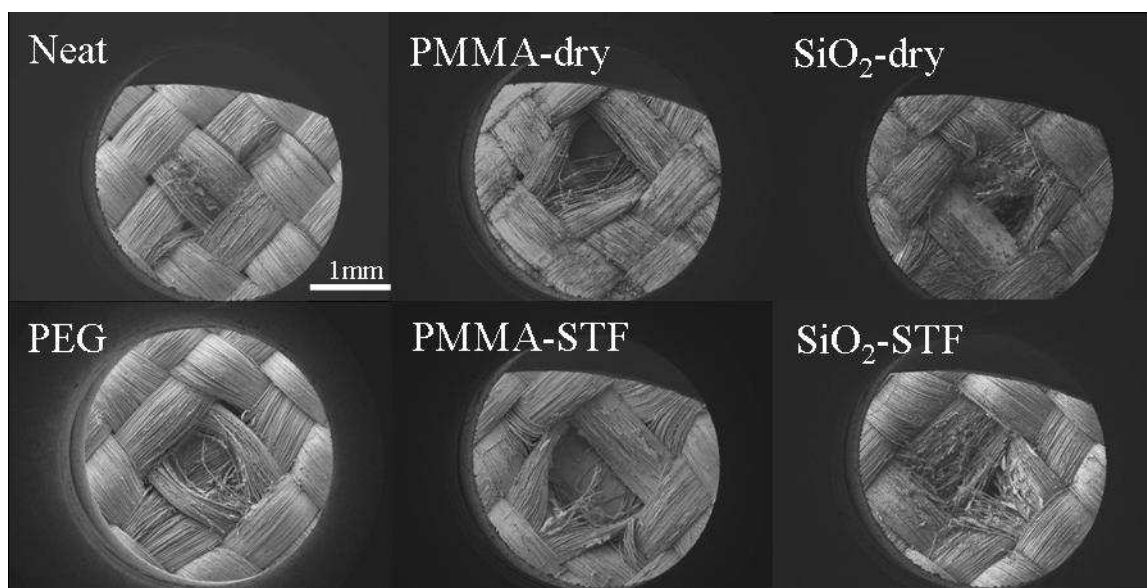


Figure D.6 Additional fabric scanning electron micrographs from spike testing.

BIBLIOGRAPHY

1. Barnes, H.A., *Shear-Thickening ("Dilatancy") in suspensions of nonaggregating solid particles dispersed in Newtonian liquids*. Journal of Rheology, 1989. **2**(33): p. 329-366.
2. Decker, M.J., et al. *Low Velocity Ballistic Properties of Shear Thickening Fluid (STF)-Fabric Composites*. in *22nd International Symposium on Ballistics*. 2005. Vancouver, BC.
3. Lee, B.-W., I.-J. Kim, and C.-G. Kim. *The influence of the particle size of silica on the ballistic performance of fabrics impregnated with silica colloidal suspension*. in *SEICO 09 SAMPE EUROPE 30th International Jubilee Conference and Forum*. 2009. Paris France.
4. Wetzel, E.D., et al. *The Effect of Rheological Parameters on the Ballistic Properties of Shear Thickening Fluid (STF)-Kevlar Composites*. in *8th International Conference on Numerical Methods in Industrial Forming Processes*. 2004. Columbus, OH.
5. Egres, R.G., et al. *Novel Flexible Body Armor Utilizing Shear Thickening Fluid (STF) Composites*. in *14th International Conference on Composite Materials*. 2003. San Diego, CA.
6. Beazley, K.M., *Industrial Aqueous Suspensions in Rheometry: Industrial Applications*, K. Walters, Editor. 1980, Research Studies Press: Chichester. p. 339-413.
7. Larson, R.G., *The Structure and Rheology of Complex Fluids*. 1998: Oxford University Press.
8. Lootens, D., et al., *Gelation, shear-thinning and shear-thickening in cement slurries*. Oil & Gas Science and Technology-Revue De L Institut Francais Du Petrole, 2004. **59**(1): p. 31-40.
9. Shenoy, S.S., N.J. Wagner, and J.W. Bender, *E-FiRST: Electric field responsive shear thickening fluids*. Rheol Acta, 2003. **42**: p. 287-294.
10. Fischer, C., et al., *Pre- and post-transition behavior of shear-thickening fluids in oscillating shear*. Rheologica Acta, 2007. **46**(8): p. 1099-1108.
11. Decker, M.J., et al., *Stab resistance of shear thickening fluid (STF)-treated fabrics*. Composites Science and Technology, 2007. **67**(3-4): p. 565-578.
12. Lee, Y.S., E.D. Wetzel, and N.J. Wagner, *The ballistic impact characteristics of Kevlar (R) woven fabrics impregnated with a colloidal shear thickening fluid*. Journal of Materials Science, 2003. **38**(13): p. 2825-2833.
13. Wagner, N.J. and J.W. Bender, *The role of nanoscale forces in colloid dispersion rheology*. Mrs Bulletin, 2004. **29**(2): p. 100-106.
14. Fischer, C., et al., *Dynamic properties of sandwich structures with integrated shear-thickening fluids*. Smart Materials and Structures, 2006. **15**(5): p. 1467-1475.

15. Bender, J.W. and N.J. Wagner, *Reversible shear thickening in monodisperse and bidisperse colloidal dispersions*. Journal of Rheology, 1996. **5**(40): p. 899-916.
16. Egres, R.G., *The Effects of Particle Anisotropy on the Rheology and Microstructure of Concentrated Colloidal Suspensions through the Shear Thickening Transition*, in *Department of Chemical Engineering*. 2005, University of Delaware: Newark.
17. Krishnamurthy, L.N. and N.J. Wagner, *Letter to the editor: Comment on "Effect of attractions on shear thickening in dense suspensions" [J. Rheology 48, 1321 (2004)]*. Journal of Rheology, 2005. **49**(3): p. 799-803.
18. Krishnamurthy, L.N., N.J. Wagner, and J. Mewis, *Shear thickening in polymer stabilized colloidal dispersions*. Journal of Rheology, 2005. **49**(6): p. 1347-1360.
19. Maranzano, B.J. and N.J. Wagner, *The effects of particle-size on reversible shear thickening of concentrated colloidal dispersions*. Journal of Chemical Physics, 2001. **114**(23): p. 10514-10527.
20. Maranzano, B.J. and N.J. Wagner, *The effects of interparticle interactions and particle size on reversible shear thickening: Hard-sphere colloidal dispersions*. Journal of Rheology, 2001. **45**(5): p. 1205-1222.
21. Bender, J.W. and N.J. Wagner, *Optical Measurement of the Contributions of colloidal forces to the rheology of concentrated suspensions*. Journal of Colloid and Interface Science, 1995. **172**(1): p. 171-184.
22. Egres, R.G., F. Nettesheim, and N.J. Wagner, *Rheo-SANS investigation of acicular-precipitated calcium carbonate colloidal suspensions through the shear thickening transition*. Journal of Rheology, 2006. **50**(5): p. 685-709.
23. Maranzano, B.J. and N.J. Wagner, *Flow-small angle neutron scattering measurements of colloidal dispersion microstructure evolution through the shear thickening transition*. Journal of Chemical Physics, 2002. **117**(22): p. 10291-10302.
24. Foss, D.R. and J.F. Brady, *Structure, diffusion and rheology of Brownian suspensions by Stokesian Dynamics simulation*. Journal of Fluid Mechanics, 2000. **407**: p. 167-200.
25. Melrose, J.R., J.H. vanVliet, and R.C. Ball, *Continuous shear thickening and colloid surfaces*. Physical Review Letters, 1996. **77**(22): p. 4660-4663.
26. Kaffashi, B., et al., *Elastic-like and viscous-like components of the shear viscosity for nearly hard sphere, Brownian suspensions*. Journal of Colloid and Interface Science, 1997. **187**(1): p. 22-28.
27. O'Brien, V.T. and M.E. Mackay, *Stress components and shear thickening of concentrated hard sphere suspensions*. Langmuir, 2000. **16**(21): p. 7931-7938.
28. Bossis, G. and J.F. Brady, *The Rheology of Brownian Suspensions*. Journal of Chemical Physics, 1989. **91**(3): p. 1866-1874.

29. Brady, J.F., *The Rheological Behavior of Concentrated Colloidal Dispersions*. Journal of Chemical Physics, 1993. **99**(1): p. 567-581.
30. Brady, J.F. and G. Bossis, *The Rheology of Concentrated Suspensions of Spheres in Simple Shear-Flow by Numerical-Simulation*. Journal of Fluid Mechanics, 1985. **155**(JUN): p. 105-129.
31. Morris, J.F. and J.F. Brady, *Self-diffusion in sheared suspensions*. Journal of Fluid Mechanics, 1996. **312**: p. 223-252.
32. D'Haene, P., J. Mewis, and G.G. Fuller, *Scattering Dichroism Measurements of Flow-Induced Structure of a Shear Thickening Suspension*. Journal of Colloid and Interface Science, 1993. **156**(2): p. 350-358.
33. Newstein, M.C., et al., *Microstructural changes in a colloidal liquid in the shear thinning and shear thickening regimes*. Journal of Chemical Physics, 1999. **111**(10): p. 4827-4838.
34. Bergenholtz, J., J.F. Brady, and M. Vicic, *The non-Newtonian rheology of dilute colloidal suspensions*. Journal of Fluid Mechanics, 2002. **456**: p. 239-275.
35. Brady, J.F. and J.F. Morris, *Microstructure of strongly sheared suspensions and its impact on rheology and diffusion*. Journal of Fluid Mechanics, 1997. **348**: p. 103-139.
36. Brady, J.F. and G. Bossis, *Stokesian Dynamics*. Annual Review of Fluid Mechanics, 1988. **20**: p. 111-157.
37. Hoffman, R.L., *Discontinuous and Dilatant Viscosity Behavior in Concentrated Suspensions .1. Observation of a Flow Instability*. Transactions of the Society of Rheology, 1972. **16**(1): p. 155-173.
38. Hoffman, R.L., *Discontinuous and Dilatant Viscosity Behavior in Concentrated Suspensions .2. Theory and Experimental Tests*. Journal of Colloid and Interface Science, 1974. **46**(3): p. 491-506.
39. Bossis, G. and J.F. Brady, *Self-Diffusion of Brownian Particles in Concentrated Suspensions under Shear*. Journal of Chemical Physics, 1987. **87**(9): p. 5437-5448.
40. Boersma, W.H., J. Laven, and H.N. Stein, *Computer-Simulations of Shear Thickening of Concentrated Dispersions*. Journal of Rheology, 1995. **39**(5): p. 841-860.
41. Egres, R.G. and N.J. Wagner, *The rheology and microstructure of acicular precipitated calcium carbonate colloidal suspensions through the shear thickening transition*. Journal of Rheology, 2005. **49**(3): p. 719-746.
42. Brady, J.F., *Computer simulation of viscous suspensions*. Chemical Engineering Science, 2001. **56**(9): p. 2921-2926.
43. Delhomme, J., *Onset of shear thickening in a simple fluid*. European Physical Journal E, 2004. **15**(1): p. 65-69.
44. Laun, H.M., et al., *Rheological and Small-Angle Neutron-Scattering Investigation of Shear-Induced Particle Structures of Concentrated Polymer*

- Dispersions Submitted to Plane Poiseuille and Couette-Flow*. Journal of Rheology, 1992. **36**(4): p. 743-787.
45. Shenoy, S.S. and N.J. Wagner, *Influence of medium viscosity and adsorbed polymer on the reversible shear thickening transition in concentrated colloidal dispersions*. Rheologica Acta, 2005. **44**(4): p. 360-371.
 46. Lionberger, R.A. and W.B. Russel, *Microscopic theories of the rheology of stable colloidal dispersions*. Advances in Chemical Physics, Vol 111, 2000. **111**: p. 399-474.
 47. Wagner, N.J., G.G. Fuller, and W.B. Russel, *The Dichroism and Birefringence of a Hard-Sphere Suspension under Shear*. Journal of Chemical Physics, 1988. **89**(3): p. 1580-1587.
 48. Kalman, D.P. and N.J. Wagner, *Microstructure of shear-thickening concentrated suspensions determined by flow-USANS*. Rheologica Acta, 2009. **48**(8): p. 897-908.
 49. Russel, W.B., D.A. Saville, and W.B. Schowalter, *Colloidal Dispersions*. 1989: Cambridge University Press.
 50. Kline, S.R., *Reduction and analysis of SANS and USANS data using IGOR Pro*. Journal of Applied Crystallography, 2006. **39**: p. 895-900.
 51. Vanlandingham, M.R., et al., *Relating elastic modulus to indentation response using atomic force microscopy*. Journal of Materials Science Letters, 1997. **16**(2): p. 117-119.
 52. Vanlandingham, M.R., et al., *Nanoscale indentation of polymer systems using the atomic force microscope*. Journal of Adhesion, 1997. **64**(1-4): p. 31-59.
 53. Hutter, J.L. and J. Bechhoefer, *Calibration of Atomic-Force Microscope Tips (Vol 64, Pg 1868, 1993)*. Review of Scientific Instruments, 1993. **64**(11): p. 3342-3342.
 54. Shim, S.E., et al., *Preparation of ultra fine poly(methyl methacrylate) microspheres in methanol-enriched aqueous medium*. Macromolecular Research, 2004. **12**(2): p. 240-245.
 55. Vanhelden, A.K., J.W. Jansen, and A. Vrij, *Preparation and Characterization of Spherical Monodisperse Silica Dispersions in Non-Aqueous Solvents*. Journal of Colloid and Interface Science, 1981. **81**(2): p. 354-368.
 56. Macosko, C.W., *Rheology Principles, measurements and applications*. 1994: Wiley-VCH.
 57. Chow, M.K. and C.F. Zukoski, *Gap Size and Shear History Dependencies in Shear Thickening of a Suspension Ordered at Rest*. Journal of Rheology, 1995. **39**(1): p. 15-32.
 58. Yoshimura, A. and R.K. Prudhomme, *Wall Slip Corrections for Couette and Parallel Disk Viscometers*. Journal of Rheology, 1988. **32**(1): p. 53-67.
 59. Maranzano, B.J., *Rheology and Microstructure of Concentrated Near Hard Sphere Colloidal Dispersions at the Shear Thickening Transition*, in *Department of Chemical Engineering*. 2001, University of Delaware: Newark.

60. Barker, J.G., et al., *Design and performance of a thermal-neutron double-crystal diffractometer for USANS at NIST*. Journal of Applied Crystallography, 2005. **38**: p. 1004-1011.
61. Kim, M.H. and C.J. Glinka, *Ultra small angle neutron scattering study of the nanometer to micrometer structure of porous Vycor*. Microporous and Mesoporous Materials, 2006. **91**(1-3): p. 305-311.
62. Liberatore, M.W., et al., *Spatially resolved small-angle neutron scattering in the 1-2 plane: A study of shear-induced phase-separating wormlike micelles*. Physical Review E, 2006. **73**(2): p. 020504-1-4.
63. Schulz, G.V., A. Scholz, and R.V. Figini, *Analyse Zweier Charakteristischer Verteilungen Von Polystyrol Durch Kolonnenfraktionierung*. Makromolekulare Chemie, 1962. **57**: p. 220-240.
64. Ackerson, B.J., et al., *Comparison of Small Shear-Flow Rate Small Wave Vector Static Structure Factor Data with Theory*. Journal of Chemical Physics, 1989. **90**(6): p. 3250-3253.
65. Amante, J.M., *Investigation of shear thickening in charge stabilized colloidal dispersions*, in *Chemical Engineering*. 1998, University of Delaware: Newark.
66. Wagner, N.J. and B.J. Ackerson, *Analysis of Nonequilibrium Structures of Shearing Colloidal Suspensions*. Journal of Chemical Physics, 1992. **97**(2): p. 1473-1483.
67. Kirkwood, K.M., et al., *Yarn pull-out as a mechanism for dissipating ballistic impact energy in Kevlar((R)) KM-2 fabric - Part I: Quasi-static characterization of yarn pull-out*. Textile Research Journal, 2004. **74**(10): p. 920-928.
68. *Stab resistance of personal body armor - National Institute of Justice Standard - NIJ0115.00*. 2000.
69. Bodt, B.A. and H.B. Tingey, *Design and Estimation for Small Sample Sensitivity Testing*. Naval Research Logistics, 1990. **37**(6): p. 875-892.
70. Cross, M.M., *Rheology of Non-Newtonian Fluids - a New Flow Equation for Pseudoplastic Systems*. Journal of Colloid Science, 1965. **20**(5): p. 417-437.
71. Russel, W.B. and M.C. Grant, *Distinguishing between dynamic yielding and wall slip in a weakly flocculated colloidal dispersion*. Colloids and Surfaces a-Physicochemical and Engineering Aspects, 2000. **161**(2): p. 271-282.
72. Dekruif, C.G., et al., *Hard-Sphere Colloidal Dispersions - Viscosity as a Function of Shear Rate and Volume Fraction*. Journal of Chemical Physics, 1985. **83**(9): p. 4717-4725.
73. Cheng, Z.D., et al., *Nature of the divergence in low shear viscosity of colloidal hard-sphere dispersions*. Physical Review E, 2002. **65**(4): p. 041405-1-8.
74. Baxter, R.J., *Percus-Yevick Equation for Hard Spheres with Surface Adhesion*. Journal of Chemical Physics, 1968. **49**(6): p. 2770-2774.

75. Cichocki, B. and B.U. Felderhof, *Diffusion-Coefficients and Effective Viscosity of Suspensions of Sticky Hard-Spheres with Hydrodynamic Interactions*. Journal of Chemical Physics, 1990. **93**(6): p. 4427-4432.
76. Krishnamurthy, L.N. and N.J. Wagner, *The influence of weak attractive forces on the microstructure and rheology of colloidal dispersions*. Journal of Rheology, 2005. **49**(2): p. 475-499.
77. Boersma, W.H., J. Laven, and H.N. Stein, *Shear Thickening (Dilatancy) in Concentrated Dispersions*. Aiche Journal, 1990. **36**(3): p. 321-332.
78. Bergenholtz, J. and N.J. Wagner, *The Huggins Coefficient for the Square-Well Colloidal Fluid*. Industrial & Engineering Chemistry Research, 1994. **33**(10): p. 2391-2397.
79. Hoffman, R.L., *Explanations for the cause of shear thickening in concentrated colloidal suspensions*. Journal of Rheology, 1998. **42**(1): p. 111-123.
80. Brady, J.F. and M. Vicic, *Normal Stresses in Colloidal Dispersions*. Journal of Rheology, 1995. **39**(3): p. 545-566.
81. Helgeson, M.E., N.J. Wagner, and D. Vlassopoulos, *Viscoelasticity and shear melting of colloidal star polymer glasses*. Journal of Rheology, 2007. **51**(2): p. 297-316.
82. Stellbrink, J., et al., *Partial structure factors in star polymer/colloid mixtures*. Applied Physics A, 2002. **74**: p. S355-S357.
83. Lindner, P. and R.C. Oberthur, *Apparatus for the Investigation of Liquid-Systems in a Shear Gradient by Small-Angle Neutron-Scattering (SANS)*. Revue De Physique Appliquee, 1984. **19**(9): p. 759-763.
84. Ackerson, B.J., et al., *Neutron-Scattering from Charge Stabilized Suspensions Undergoing Shear*. Journal of Chemical Physics, 1986. **84**(4): p. 2344-2349.
85. Johnson, S.J., C.G. Dekruif, and R.P. May, *Structure Factor Distortion for Hard-Sphere Dispersions Subjected to Weak Shear-Flow - Small-Angle Neutron-Scattering in the Flow-Vorticity Plane*. Journal of Chemical Physics, 1988. **89**(9): p. 5909-5921.
86. Vanderwerff, J.C., et al., *Neutron-Scattering from Dense Colloidal Dispersions at High Shear Rates - the Deformation of the Structure Factor in the Shear Plane*. Physica A, 1990. **165**(3): p. 375-398.
87. Gopalakrishnan, V. and C.F. Zukoski, *Effect of attractions on shear thickening in dense suspensions*. Journal of Rheology, 2004. **48**(6): p. 1321-1344.
88. Watanabe, H., et al., *Nonlinear rheology and flow-induced structure in a concentrated spherical silica suspension*. Rheologica Acta, 1998. **37**(1): p. 1-6.
89. Lee, Y.S. and N.J. Wagner, *Rheological properties and small-angle neutron scattering of a shear thickening, nanoparticle dispersion at high shear rates*. Industrial and Engineering Chemistry Research, 2006. **45**(21): p. 7015-7024.
90. Bossis, G. and J.F. Brady, *Dynamic Simulation of Sheared Suspensions .1. General-Method*. Journal of Chemical Physics, 1984. **80**(10): p. 5141-5154.

91. Bossis, G., J.F. Brady, and C. Mathis, *Shear-Induced Structure in Colloidal Suspensions .1. Numerical-Simulation*. Journal of Colloid and Interface Science, 1988. **126**(1): p. 1-15.
92. Helgeson, M.E., et al., *Relating shear banding, structure, and phase behavior in wormlike micellar solutions*. Soft Matter, 2009. **5**(20): p. 3858-3869.
93. Helgeson, M.E., et al., *Rheology and spatially resolved structure of cetyltrimethylammonium bromide wormlike micelles through the shear banding transition*. Journal of Rheology, 2009. **53**(3): p. 727-756.
94. Stradner, A., et al., *Equilibrium cluster formation in concentrated protein solutions and colloids*. Nature, 2004. **432**(7016): p. 492-495.
95. Eberle, A.P.R., et al., *Temperature-Dependent Nanostructure of an End-Tethered Octadecane Brush in Tetradecane and Nanoparticle Phase Behavior*. Langmuir. **26**(5): p. 3003-3007.
96. Menon, S.V.G., V.K. Kelkar, and C. Manohar, *Application of Baxter Model to the Theory of Cloud Points of Nonionic Surfactant Solutions*. Physical Review A, 1991. **43**(2): p. 1130-1133.
97. Lionberger, R.A. and W.B. Russel, *A Smoluchowski theory with simple approximations for hydrodynamic interactions in concentrated dispersions*. Journal of Rheology, 1997. **41**(2): p. 399-425.
98. Sriram, I., *Active microrheology of colloidal suspensions*, in Department of Chemical Engineering. 2010, University of Delaware: Newark.
99. Melrose, J.R. and R.C. Ball, *"Contact networks" in continuously shear thickening colloids*. Journal of Rheology, 2004. **48**(5): p. 961-978.
100. Woutersen, A., R.P. May, and C.G. Dekruif, *The Shear-Distorted Microstructure of Adhesive Hard-Sphere Dispersions - a Small-Angle Neutron-Scattering Study*. Journal of Rheology, 1993. **37**(1): p. 71-88.
101. Wagner, N.J. and W.B. Russel, *Light-Scattering Measurements of a Hard-Sphere Suspension under Shear*. Physics of Fluids A: Fluid Dynamics, 1990. **2**(4): p. 491-502.
102. Tomita, M. and T.G.M. Vandeven, *The Structure of Sheared Ordered Lattices*. Journal of Colloid and Interface Science, 1984. **99**(2): p. 374-386.
103. Scirocco, R., J. Vermant, and J. Mewis, *Shear thickening in filled Boger fluids*. Journal of Rheology, 2005. **49**(2): p. 551-567.
104. Bhatia, S.R., *Ultra-small-angle scattering studies of complex fluids*. Current Opinion in Colloid and Interface Science, 2005. **9**(6): p. 404-411.
105. Hoekstra, H., et al., *Multi length scale analysis of the microstructure in sticky sphere dispersions during shear flow*. Langmuir, 2005. **21**(24): p. 11017-11025.
106. Hoekstra, H., et al., *Rheology and structure of suspensions in liquid crystalline hydroxypropylcellulose solutions*. Langmuir, 2002. **18**(15): p. 5695-5703.

107. Versmold, H., C. Dux, and S. Musa, *On the structure of charge stabilized polymer dispersions*. Journal of Molecular Liquids, 2002. **98-9**: p. 145-162.
108. Versmold, H., S. Musa, and A. Bierbaum, *Concentrated colloidal dispersions: On the relation of rheology with small angle x-ray and neutron scattering*. Journal of Chemical Physics, 2002. **116**(6): p. 2658-2662.
109. Versmold, H., et al., *Shear-induced structure in concentrated dispersions: Small angle synchrotron X-ray and neutron scattering*. Langmuir, 2001. **17**(22): p. 6812-6815.
110. Versmold, H., et al., *Stacking structure of concentrated shear ordered dispersions by two scattering methods*. Langmuir, 2005. **21**(10): p. 4324-4327.
111. Chen, L.B., et al., *Rheological and Microstructural Transitions in Colloidal Crystals*. Langmuir, 1994. **10**(8): p. 2817-2829.
112. Groenewold, J. and W.K. Kegel, *Anomalously large equilibrium clusters of colloids*. Journal of Physical Chemistry B, 2001. **105**(47): p. 11702-11709.
113. Rastogi, S.R., N.J. Wagner, and S.R. Lustig, *Microstructure and rheology of polydisperse, charged suspensions*. Journal of Chemical Physics, 1996. **104**(22): p. 9249-9258.
114. Laun, H.M., R. Bung, and F. Schmidt, *Rheology of Extremely Shear Thickening Polymer Dispersions (Passively Viscosity Switching Fluids)*. Journal of Rheology, 1991. **35**(6): p. 999-1034.
115. Phung, T.N., J.F. Brady, and G. Bossis, *Stokesian Dynamics simulation of Brownian suspensions*. Journal of Fluid Mechanics, 1996. **313**: p. 181-207.
116. Maranzano, B.J., et al., *Surface charge of 3-(trimethoxysilyl) propyl methacrylate (TPM) coated Stober silica colloids by zeta-phase analysis light scattering and small angle neutron scattering*. Langmuir, 2000. **16**(26): p. 10556-10558.
117. Catherall, A.A., J.R. Melrose, and R.C. Ball, *Shear thickening and order-disorder effects in concentrated colloids at high shear rates*. Journal of Rheology, 2000. **44**(1): p. 1-25.
118. Lootens, D., H. Van Damme, and P. Hebraud, *Giant stress fluctuations at the jamming transition*. Physical Review Letters, 2003. **90**(17).
119. Schelten, J. and W. Schmatz, *Multiple-Scattering Treatment for Small-Angle Scattering Problems*. Journal of Applied Crystallography, 1980. **13**(Aug): p. 385-390.
120. Holmes, C.B., et al., *Glass transitions and shear thickening suspension rheology*. Journal of Rheology, 2005. **49**(1): p. 237-269.
121. Holmes, C.B., M. Fuchs, and M.E. Cates, *Jamming transitions in a schematic model of suspension rheology*. Europhysics Letters, 2003. **63**(2): p. 240-246.
122. Head, D.A., A. Ajdari, and M.E. Cates, *Rheological instability in a simple shear-thickening model*. Europhysics Letters, 2002. **57**(1): p. 120-126.

123. Head, D.A., A. Ajdari, and M.E. Cates, *Jamming, hysteresis, and oscillation in scalar models for shear thickening*. Physical Review E, 2001. **64**(6).
124. Kalman, D.P., et al., *Effect of Particle Hardness on the Penetration Behavior of Fabrics Intercalated with Dry Particles and Concentrated Particle-Fluid Suspensions*. ACS Applied Materials & Interfaces, 2009. **1**(11): p. 2602-2612.
125. Meeker, S.P., R.T. Bonnecaze, and M. Cloitre, *Slip and flow in soft particle pastes*. Physical Review Letters, 2004. **92**(19).
126. Meeker, S.P., R.T. Bonnecaze, and M. Cloitre, *Slip and flow in pastes of soft particles: Direct observation and rheology*. Journal of Rheology, 2004. **48**(6): p. 1295-1320.
127. Adams, S., W.J. Frith, and J.R. Stokes, *Influence of particle modulus on the rheological properties of agar microgel suspensions*. Journal of Rheology, 2004. **48**(6): p. 1195-1213.
128. Tadros, T.F., *Fundamental Principles of Emulsion Rheology and Their Applications*. Colloids and Surfaces a-Physicochemical and Engineering Aspects, 1994. **91**: p. 39-55.
129. Kraynik, A.M., *Foam Flows*. Annual Review of Fluid Mechanics, 1988. **20**: p. 325-357.
130. Mason, T.G., *New fundamental concepts in emulsion rheology*. Current Opinion in Colloid & Interface Science, 1999. **4**(3): p. 231-238.
131. Buscall, R., J.I. McGowan, and A.J. Mortonjones, *The Rheology of Concentrated Dispersions of Weakly Attracting Colloidal Particles with and without Wall Slip*. Journal of Rheology, 1993. **37**(4): p. 621-641.
132. Levy, Bass, and Stern, eds. *Handbook of Elastic Properties of Solids, Liquids, and Gases*. Vol. III: Elastic Properties of Solids: Biological and Organic Materials, Earth and Marine Sciences. 2001, Academic Press.
133. Brandrup, J., E. Immergut, and E. Grulke, *Polymer Handbook*. 1999, New York: John Wiley & Sons.
134. Laun, H.M., *Rheological Properties of Aqueous Polymer Dispersions*. Angewandte Makromolekulare Chemie, 1984. **123**(Aug): p. 335-359.
135. Vanorio, T., M. Prasad, and A. Nur, *Elastic properties of dry clay mineral aggregates, suspensions and sandstones*. Geophysical Journal International, 2003. **155**(1): p. 319-326.
136. Raghavan, S.R. and S.A. Khan, *Shear-thickening response of fumed silica suspensions under steady and oscillatory shear*. Journal of Colloid and Interface Science, 1997. **185**(1): p. 57-67.
137. Wolf, B., et al., *Shear thickening of an emulsion stabilized with hydrophilic silica particles*. Journal of Rheology, 2007. **51**(3): p. 465-478.
138. Saiki, Y., C.A. Prestidge, and R.G. Horn, *Effects of droplet deformability on emulsion rheology*. Colloids and Surfaces a-Physicochemical and Engineering Aspects, 2007. **299**(1-3): p. 65-72.

139. Egres, R.G., et al. *Stab resistance of shear thickening fluid (STF)-Kevlar composites for body armor applications*. in *24th Army Science Conference*. 2004.
140. Egres, R.G., et al., *Stab performance of shear thickening fluid (STF)-Kevlar composites for body armor applications*. SAMPE 2005. 2005, Long Beach, CA.
141. Rosen, B.A., et al. *Multi-Threat Performance of Kaolin-Based Shear Thickening Fluid (STF)-Treated Fabrics*. in *SAMPE*. 2007. Baltimore, MD.
142. Tan, V.B.C., T.E. Tay, and W.K. Teo, *Strengthening fabric armour with silica colloidal suspensions*. *International Journal of Solids and Structures*, 2005. **42**(5-6): p. 1561-1576.
143. Mahfuz, H., et al., *Enhanced stab resistance of armor composites with functionalized silica nanoparticles*. *Journal of Applied Physics*, 2009. **105**(6).
144. Bazhenov, S., *Dissipation of energy by bulletproof aramid fabric*. *Journal of Materials Science*, 1997. **32**(15): p. 4167-4173.
145. Lee, B.L., et al., *Penetration failure mechanisms of armor-grade fiber composites under impact*. *Journal of Composite Materials*, 2001. **35**(18): p. 1605-1633.
146. Duan, Y., et al., *Modeling friction effects on the ballistic impact behavior of a single-ply high-strength fabric*. *International Journal of Impact Engineering*, 2005. **31**(8): p. 996-1012.
147. Duan, Y., et al., *A numerical investigation of the influence of friction on energy absorption by a high-strength fabric subjected to ballistic impact*. *International Journal of Impact Engineering*, 2006. **32**(8): p. 1299-1312.
148. Scott, B.R. *The penetration of compliant laminates by compact projectiles*. in *18th Int. Symp. Ball.* . 1999. San Antonio, TX.
149. Zeng, X.S., V.B.C. Tan, and V.P.W. Shim, *Modelling inter-yarn friction in woven fabric armour*. *International Journal for Numerical Methods in Engineering*, 2006. **66**(8): p. 1309-1330.
150. Kirkwood, J.E., et al., *Yarn pull-out as a mechanism for dissipating ballistic impact energy in Kevlar((R)) KM-2 fabric - Part II: Predicting ballistic performance*. *Textile Research Journal*, 2004. **74**(11): p. 939-948.
151. Shockey, D.A., D.C. Erlich, and J.W. Simons, *Improved Barriers to Turbine Engine Fragments: Interim Report III, DOT/FAA/AR-99/8-III*. 2001.
152. Shockey, D.A., et al., *Improved Barriers to Turbine Engine Fragments: Interim Report IV, DOT/FAA/AR-99/8-IV*. 2002.
153. Cheeseman, B.A. and T.A. Bogetti, *Ballistic impact into fabric and compliant composite laminates*. *Composite Structures*, 2003. **61**(1-2): p. 161-173.
154. Nam, C.H., et al. *Ballistic and Rheological Properties of STFs Reinforced by Short Discontinuous Fibers*. in *SAMPE*. 2005. Long Beach, CA.